ADVANCES IN THE INTEGRATION OF BRAIN-MACHINE INTERFACES AND ROBOTIC DEVICES

EDITED BY: Luca Tonin, Emanuele Menegatti and Damien Coyle

PUBLISHED IN: Frontiers in Robotics and AI and Frontiers in Neuroscience

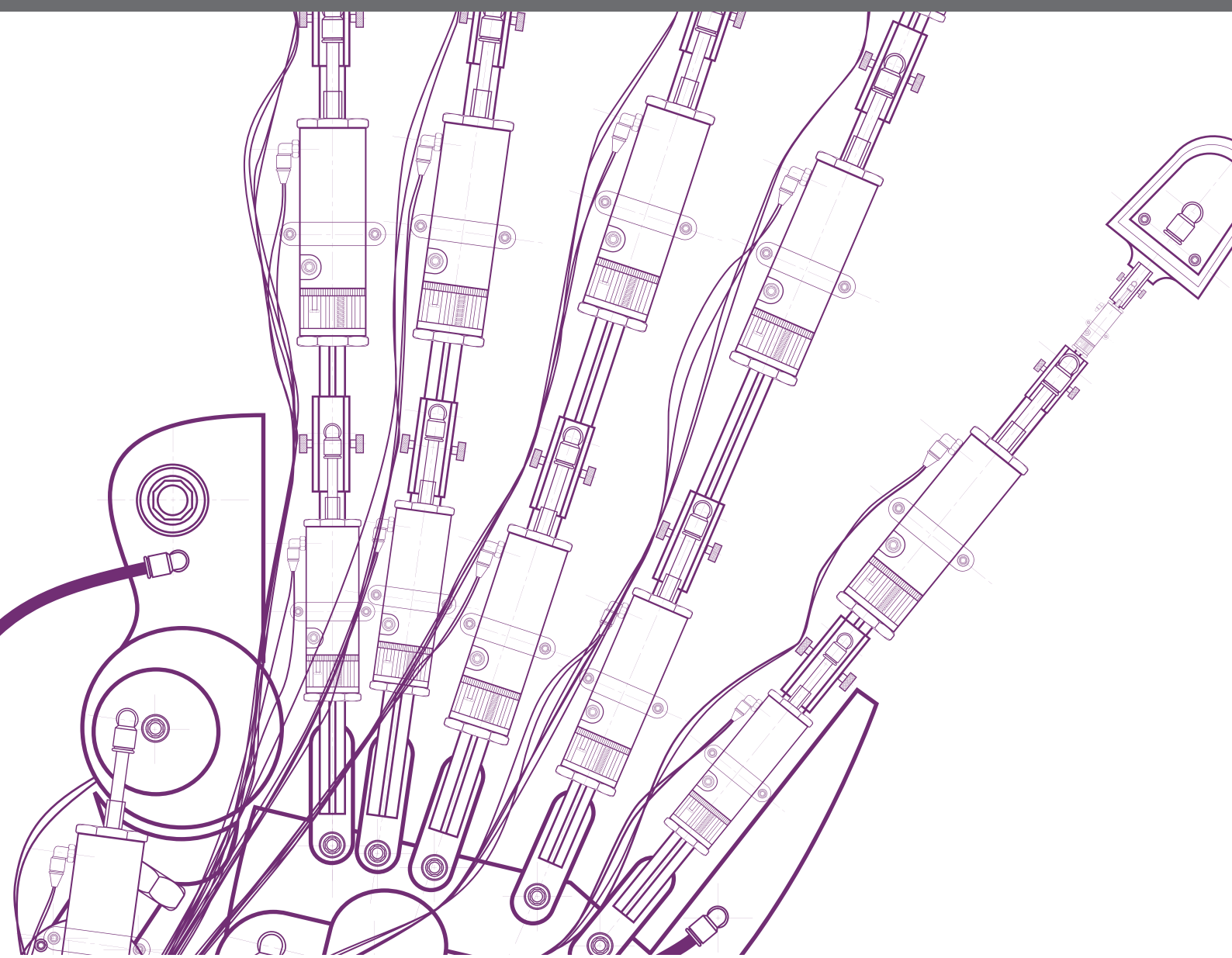

frontiers Research Topics

frontiers

ISSN 1664-8714
ISBN 978-2-88966-673-7
DOI 10.3389/978-2-88966-673-7

About Frontiers

Frontiers is more than just an open-access publisher of scholarly articles: it is a pioneering approach to the world of academia, radically improving the way scholarly research is managed. The grand vision of Frontiers is a world where all people have an equal opportunity to seek, share and generate knowledge. Frontiers provides immediate and permanent online open access to all its publications, but this alone is not enough to realize our grand goals.

Frontiers Journal Series

The Frontiers Journal Series is a multi-tier and interdisciplinary set of open-access, online journals, promising a paradigm shift from the current review, selection and dissemination processes in academic publishing. All Frontiers journals are driven by researchers for researchers; therefore, they constitute a service to the scholarly community. At the same time, the Frontiers Journal Series operates on a revolutionary invention, the tiered publishing system, initially addressing specific communities of scholars, and gradually climbing up to broader public understanding, thus serving the interests of the lay society, too.

Dedication to Quality

Each Frontiers article is a landmark of the highest quality, thanks to genuinely collaborative interactions between authors and review editors, who include some of the world's best academicians. Research must be certified by peers before entering a stream of knowledge that may eventually reach the public - and shape society; therefore, Frontiers only applies the most rigorous and unbiased reviews.
Frontiers revolutionizes research publishing by freely delivering the most outstanding research, evaluated with no bias from both the academic and social point of view. By applying the most advanced information technologies, Frontiers is catapulting scholarly publishing into a new generation.

What are Frontiers Research Topics?

Frontiers Research Topics are very popular trademarks of the Frontiers Journals Series: they are collections of at least ten articles, all centered on a particular subject. With their unique mix of varied contributions from Original Research to Review Articles, Frontiers Research Topics unify the most influential researchers, the latest key findings and historical advances in a hot research area! Find out more on how to host your own Frontiers Research Topic or contribute to one as an author by contacting the Frontiers Editorial Office: frontiersin.org/about/contact

ADVANCES IN THE INTEGRATION OF BRAIN-MACHINE INTERFACES AND ROBOTIC DEVICES

Topic Editors:
Luca Tonin, University of Padua, Italy
Emanuele Menegatti, University of Padua, Italy
Damien Coyle, Ulster University, United Kingdom

Citation: Tonin, L., Menegatti, E., Coyle, D., eds. (2021). Advances in the Integration of Brain-Machine Interfaces and Robotic Devices. Lausanne: Frontiers Media SA.
doi: 10.3389/978-2-88966-673-7

Table of Contents

frontiers in Robotics and AI

EDITORIAL
published: 10 March 2021
doi: 10.3389/frobt.2021.653615

Editorial: Advances in the Integration of Brain-Machine Interfaces and Robotic Devices

Luca Tonin[1]*, *Emanuele Menegatti*[1] and *Damien Coyle*[2]

[1]Department of Information Engineering, University of Padua, Padua, Italy, [2]Intelligent Systems Research Centre, School of Computing, Engineering and Intelligent Systems, Ulster University, Derry, United Kingdom

Keywords: Brain-machine interface, robotics, shared-control, human-robot interaction, assistive devices

Editorial on Research Topic

Advances in the Integration of Brain-Machine Interfaces and Robotic Devices

Recent advances in noninvasive Brain-Machine Interfaces (BMIs) have demonstrated the potential impact of directly interfacing the brain with machines. The ultimate translational goal of BMI systems is to enable people suffering from severe motor disabilities to control a new generation of neuroprostheses and, thus, (re)gain their own independence.

Many studies have already demonstrated the feasibility of the BMI technology with different kinds of assistive devices, designed to restore communication (e.g., virtual keyboard) or to enable the control of robotic applications (e.g., wheelchairs, telepresence robots, robotic arms, and drones). However, despite great progress, the integration of the BMI and robotics is still in its infancy and translational impact is low.

The BMI community has predominantly focused on exploring novel algorithms to decode the user's intentions from neural patterns with a focus on enhancing the robustness and the reliability of the BMI system. However, the process of how the estimated intentions of the user are translated by the intelligent robotic device into real and daily-based situations is often neglected. This largely affects the translational impact of the BMI technology. The latest advances in the field of robotics may help address this challenge by exploiting novel human–robot interaction theories and by providing insights and solutions from a new and different perspective.

This special topic sought original contributions that explicitly take into account the cross-cutting aspects in BMI and robotics research including but not limited to BMI control of navigation robots, BMI control of robotic prosthetic limbs, BMI-driven assistive technology for end users, translational aspects in BMI-controlled devices, shared-control strategies for the BMI, contextualized robotic behaviors, long-term human–robot interaction (BMI–robot interaction), semi-autonomous robot behaviors, evaluation of BMI-driven robotics in real-world scenarios, and real-time detection of possible targets in real-world scenarios. All typologies of closed-loop BMI systems (e.g., based on exogenous stimulation or self-paced paradigms) were solicited if they focused on the integration of BMI and robotics devices. We are pleased with the interest in the topic and the collection of studies presented, which include two state-of-the-art reviews, one on neural driven rehabilitation robotics for lower limb gait rehabilitation and another human affective states when interfacing with robotic devices, as well as five novel studies investigating a range of BMI robotic learning scenarios and signal decoding in invasive and noninvasive BMIs, all of which highlight opportunities and challenges to advance the integration of Brain-Machine Interfaces and Robotic devices.

In their review, Alirmardani and Hiraki focused on the current employment of BMIs in human–robot interaction applications. They illustrated the state of the art of passive BMIs and the current challenges to monitor and decode cognitive load, attention level, perceived errors, and emotional states in real time.

Edited and reviewed by:
Mikhail Prokopenko,
The University of Sydney, Australia

***Correspondence:**
Luca Tonin
luca.tonin@dei.unipd.it

Specialty section:
This article was submitted to Computational Intelligence in Robotics, a section of the journal Frontiers in Robotics and AI

Received: *14 January 2021*
Accepted: *21 January 2021*
Published: *10 March 2021*

Citation:
Tonin L, Menegatti E and Coyle D (2021) Editorial: Advances in the Integration of Brain-Machine Interfaces and Robotic Devices. Front. Robot. AI 8:653615. doi: 10.3389/frobt.2021.653615

Kim et al. investigated the influence and the effect of human supervision on robot learning during pick-and-place tasks. In the proposed experimental scenario, two human–robot interfaces were provided: the first one based on human gestures to decode the human's intent and the second based on error-related potentials to provide the human's intrinsic feedback of the performed robot action. They demonstrated that such a human–robot interaction promoted robotic learning and the concurrent online adaptation, especially when prior knowledge about the task was provided.

Monitoring robot behavior through the evaluation of possible mistakes may be not the only way to foster the learning process of intelligent devices. Wirth et al. showed the possibility of exploiting a single-trial P300-based BMI to discriminate when a virtual robot has reached a predefined destination during navigation tasks. They proposed this approach as part of a learning-based system to enhance the efficacy and efficiency of BMI-driven applications for navigation.

Similarly, Kolkhorst et al. showed that a robotic agent could improve the usability of an event-related potential BMI by obviating the traditional need of an external screen for stimulus presentation. They exploited a robotic arm to present stimuli by highlighting objects in a realistic environment with a laser pointer. The proposed classification method, based on specialized classifiers in the Riemann tangent space, reported not only high accuracy but also robustness to both heterogeneous and homogeneous objects.

Beyond exploiting the "human-in-the-loop" approach to monitor robot behaviors, BMI systems can be also used to directly control the movement of robotic actuators. While most studies to date demonstrated the feasibility of mentally driving a single assistive device, Huang et al. proposed a hybrid BMI system to control an integrated wheelchair-robotic arm system. A motor imagery BMI was used to deliver navigation commands to the wheelchair and an electrooculogram-based interface for the control of the robotic arm. Interestingly, the system allows the users to voluntarily renew the classification parameters during online operations by means of a specific sequence of commands.

In Kim et al., authors proposed a new decoding algorithm based on deep canonical correlation analysis and neuronal firing rate activities that improves the kinematic reconstruction in a 2D arm reaching task performed by nonhuman primates. The algorithm was designed to identify the best kinematics-related canonical variables of neuronal activity via deep learning–based approaches. As highlighted in the study, the prediction of kinematic parameters of a prosthetic device from neural activities can have profound consequences in BMI clinical applications.

Finally, Lennon et al. conducted a systematic review of the current state of the art and limitations of neural driven robotic gait devices in stroke rehabilitation. Despite identifying a limited number of promising studies to date, the review highlighted wide heterogeneity in the reporting and the purpose of neurobiosignal utilization during robotic gait training after a stroke and the lack of standardized protocols. A quick reference guide (the DESIRED Checklist) is proposed to identify a minimum reporting data set as a standard for future studies in order to maximize the translational impact of the technology.

In summary, in the BMI field, the role of the robotic intelligence is often underestimated by relegating the robotic device to a mere actuator of the user's commands. This collection highlighted challenges to be addressed and potential solutions, standards to adhere to when undertaking studies, and the importance of further investigating the potential bidirectional human–robot interactions in BMI applications in order to improve the overall efficiency of these novel interfaces and to design a new generation of neuroprosthetic devices.

AUTHOR CONTRIBUTIONS

All authors listed have made a substantial, direct, and intellectual contribution to the work and approved it for publication.

Conflict of Interest: The authors declare that the research was conducted in the absence of any commercial or financial relationships that could be construed as a potential conflict of interest.

frontiers in Neuroscience

ORIGINAL RESEARCH
published: 22 November 2019
doi: 10.3389/fnins.2019.01243

An EEG-/EOG-Based Hybrid Brain-Computer Interface: Application on Controlling an Integrated Wheelchair Robotic Arm System

Qiyun Huang[1], *Zhijun Zhang*[1], *Tianyou Yu*[1], *Shenghong He*[2] *and Yuanqing Li*[1]*

[1] Center for Brain Computer Interfaces and Brain Information Processing, South China University of Technology, Guangzhou, China, [2] MRC Brain Network Dynamics Unit, Nuffield Department of Clinical Neurosciences, University of Oxford, Oxford, United Kingdom

Most existing brain-computer Interfaces (BCIs) are designed to control a single assistive device, such as a wheelchair, a robotic arm or a prosthetic limb. However, many daily tasks require combined functions which can only be realized by integrating multiple robotic devices. Such integration raises the requirement of the control accuracy and is more challenging to achieve a reliable control compared with the single device case. In this study, we propose a novel hybrid BCI with high accuracy based on electroencephalogram (EEG) and electrooculogram (EOG) to control an integrated wheelchair robotic arm system. The user turns the wheelchair left/right by performing left/right hand motor imagery (MI), and generates other commands for the wheelchair and the robotic arm by performing eye blinks and eyebrow raising movements. Twenty-two subjects participated in a MI training session and five of them completed a mobile self-drinking experiment, which was designed purposely with high accuracy requirements. The results demonstrated that the proposed hBCI could provide satisfied control accuracy for a system that consists of multiple robotic devices, and showed the potential of BCI-controlled systems to be applied in complex daily tasks.

Keywords: brain-computer interface (BCI), hybrid BCI, electroencephalogram (EEG), electrooculogram (EOG), wheelchair, robotic arm

OPEN ACCESS

Edited by:
Damien Coyle,
Ulster University, United Kingdom

Reviewed by:
Jing Jin,
East China University of Science and Technology, China
Keum-Shik Hong,
Pusan National University, South Korea

***Correspondence:**
Yuanqing Li
auyqli@scut.edu.cn

Specialty section:
This article was submitted to Neuroprosthetics, a section of the journal Frontiers in Neuroscience

Received: *09 March 2019*
Accepted: *04 November 2019*
Published: *22 November 2019*

Citation:
Huang Q, Zhang Z, Yu T, He S and Li Y (2019) An EEG-/EOG-Based Hybrid Brain-Computer Interface: Application on Controlling an Integrated Wheelchair Robotic Arm System. Front. Neurosci. 13:1243. doi: 10.3389/fnins.2019.01243

1. INTRODUCTION

An Electroencephalogram (EEG)-based brain-computer interface (BCI) records electrical signals of brain cells from scalp and translates them into various communication or control commands (Wolpaw et al., 2000). Common modalities used in EEG-based BCIs include steady-state visual evoked potentials (SSVEP) (Cheng et al., 2015), event-related potentials (ERPs) (Blankertz et al., 2011; Jin et al., 2017), and mu (8–12 Hz)/beta (18–26 Hz) rhythms related to motor imagery (MI) (Lafleur et al., 2013).

A main focus of the EEG-based BCIs is to combine them with existing assistive devices, such as a prosthesis or a wheelchair, to support motor substitution of the user's limb functions, e.g., the grasping function and the walking function (Millán et al., 2010). While SSVEP- and ERP-based

BCIs only provide discrete commands, MI-based ones can generate nearly continuous outputs in real time, which makes them a good fit for manipulating assistive devices that require highly accurate and continuous control. Several purely MI-based BCIs have been developed to realize basic control of external devices (Wolpaw and McFarland, 2004; Lafleur et al., 2013; Meng et al., 2016). However, MI-based BCIs still suffer from limited number of distinguishable MI tasks (Yu et al., 2015).

To overcome the limitation of using a single MI paradigm, many excellent works have been established in recent years to realize multidimensional control of external devices by combining the MI with other EEG modalities (Rebsamen et al., 2010; Long et al., 2012; Li et al., 2013; Bhattacharyya et al., 2014; Ma et al., 2017) or other bioelectrical signals (Punsawad et al., 2010; Jun et al., 2014; Witkowski et al., 2014; Ma et al., 2015; Soekadar et al., 2015; Minati et al., 2016), i.e., using a hybrid brain-computer interfaces (hBCIs) (Pfurtscheller et al., 2010; Hong and Khan, 2017). For example, in Long et al. (2012) and Li et al. (2013) the user continuously controlled the direction (left/right turn) of a wheelchair using the left- or right- imagery, and used the P300 potential and SSVEP to generate discrete commands, such as acceleration/deceleration and stopping; in Ma et al. (2017), the users generated MI to control the moving of a robotic arm, and stop it by detecting the P300 potential.

Other than with different EEG modalities, MI can also be combined with other bioelectrical signals, such as Electrooculogram (EOG) signals and functional near infrared spectroscopy (fNIRS) (Khan and Hong, 2017), to build a hBCI. EOG signals are generated by eye movements and usually maintain a higher signal-to-noise ratio (SNR) compared with EEG signals (Maddirala and Shaik, 2016). In Witkowski et al. (2014), MI-related brain activities were translated into continuous hand exoskeleton-driven grasping motions which could be interrupted by EOG signals, aiming to enhancing the reliability and safety of the overall control. In Soekadar et al. (2015), Soekadar et al. demonstrated that the inclusion of EOG in a MI-based hand exoskeleton system could significantly improve the overall performance across all participants.

Prior studies have well-demonstrated the feasibility of using an hBCI to control a single assistive device, such as a wheelchair or a robotic arm. However, it is still unknown whether multiple devices can be integrated together and controlled by a single hBCI. Such integration is challenging because it requires higher control accuracies (i.e., the positional accuracy and the angular accuracy) and more control degrees than a single BCI-controlled device system. Also, the time and efforts consumed to control an integrated system are usually higher than that of any of its single component, which may reduce the reliability. In this study, we integrate a wheelchair and a robotic arm into a unified system, aiming to help the user move from a random place to approach and grasp a target object which is also randomly placed far away from the user. A novel hBCI based on EEG (the MI paradigm) and EOG signals is proposed to control the system. Specifically, for the wheelchair, users can continuously steer the wheelchair left/right by imagining left/right hand movements. Users generate discrete wheelchair commands, such as moving forward and backward and stopping, by implementing eye blinks and eyebrow movements. For the robotic arm, the eye blinks and eyebrow movements are utilized along with two cameras in a shared control mode. There were 22 healthy subjects participated in a MI training session, after which five of them (with accuracy over 80%) were asked to complete a tricky self-drinking task using the proposed system. The experimental results showed that the proposed hBCI could provide satisfied accuracy to control the integrated system and had the potential to help users complete daily tasks.

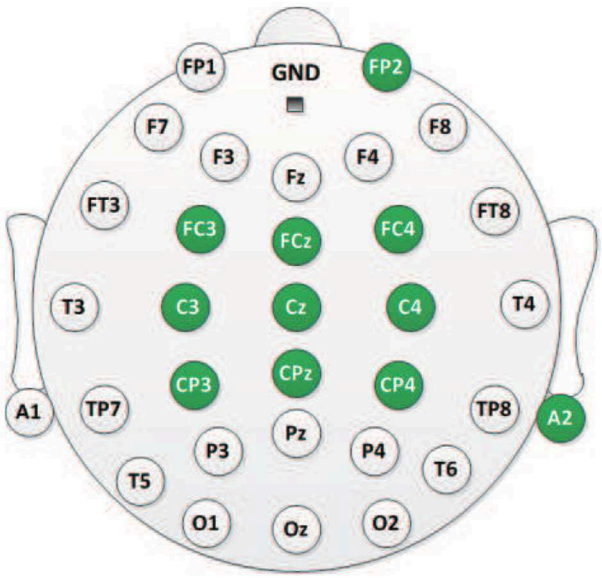

FIGURE 1 | The 10–20 electrode distribution of a 32-channel Quik-cap. Eleven electrodes (green color) are employed in this study.

The remainder of this paper is organized as follows: section 2 is the methodologies, including the signal acquisition, the system framework and the hBCI; sections 3 and 4 describe the experiments and present the results; further discussions are included in section 5; and section 6 concludes the paper.

2. METHODS

2.1. Signal Acquisition

As shown in **Figure 1**, the EEG signals are recorded from nine electrodes ("FC3," "FCz," "FC4," "C3," "Cz," "C4," "CP3," "CPz," and "CP4") attached on a 32-channel Quik-cap and amplified by a SynAmps2 amplifier [Neuroscan Compumeidcs, USA] with a sampling rate of 250 Hz. One electrode attached on the forehead ("FP2") is used to record the EOG signals which are resulted from eye movements. The amplifier is grounded on the forehead, and "A2" is the reference electrode which is placed near the right ear lobe. The impedances between the scalp and all electrodes are maintained below 5 kΩ.

2.2. System Components

The system consists of into two parts: (i) the control unit; and (ii) the execution unit. The control unit is a novel hBCI that

processes the recorded EEG and EOG signals and translates them into various control commands. The execution unit is an integrated wheelchair robotic arm system which was built to help paralyzed people in Huang et al. (2019). As shown in **Figure 2B**, the hardware components include a laptop to present the GUI, a wheelchair [0.8 × 0.6 m, UL8W, Pihsiang Machinery Co. Ltd.], a six-degree intelligent robotic arm [JACO6 DOF-S, Kinova Robotics] and two motion-sensing cameras [Kinect v2, Microsoft].

2.3. GUI and Control Strategy

The graphical user interface (GUI) of the hBCI consists of two separate panels: (i) the wheelchair panel (**Figure 3A**); and (ii) the robotic arm panel (**Figure 3B**). When the system is turned on, the wheelchair panel is presented. As shown in **Figure 3A**, the progress bar is used to control the wheelchair direction. The value of the bar represents the classification result of the user's left-right MI imagery. Two green lines are set at somewhere on the left and right sides of the bar as the left and right threshold, respectively. Initially, the value of the progress bar is 0 and the bar stops in the middle. The user can grow the bar to the left/right side by continuously imagining left/right hand movement. As long as the value of the bar exceeds the left/right threshold, the wheelchair is continuously turned to the left/right at an angular velocity of $0.1\pi/s$ (18°/s) (see details in the *EEG signals processing* section).

In the wheelchair panel, there are nine buttons placed around the progress bar that flash one by one in a predefined sequence. The interval between the onset of two continuous button flashes is 100 ms. Thus, the period of a complete round (i.e., each button flashes once) is 900 ms. To select a target button, the user first performs an intended blink in response to a flash of the target button. The system detects the intended blink and pre-selects a potential target button according to the timing of blinking. Next, if the pre-selected button is correct, the user needs to raise his/her eyebrows once to verify it. Only when a button is pre-selected and verified can the corresponding command be triggered (see details in the *EOG signals processing* section). The "Move" and "Back" buttons represent moving forward and backward at 0.2 m/s, respectively. The "Stop" button is used to stop the moving and turning of the wheelchair immediately. Other buttons in the wheelchair panel are active only when the wheelchair is stopped. For example, the user can increase/decrease the left and right threshold values by selecting the "+"/"−" buttons on the left and right sides, and renew the MI classification parameters (see details in the *EEG signals processing* section). The "Switch" button is used to switch the GUI to the robotic arm panel.

In the robotic arm panel, there are 6 buttons which flash one by one with an interval of 150 ms, as shown in **Figure 3B**. Thus, the round period is also 900 ms. The three object buttons ("Item 1," "Item 2," and "Item 3") represent three target objects that can be grasped. Once the user selects an object button, the two cameras (Camera A and B) would return the coordinates of the object as well as the user's mouth to the robotic arm, and then the arm automatically plan the path to grasp the target and bring it to the user's mouth. The "Init" button is used to initiate the arm's internal parameters and move it to the home position. After the target has been brought to the mouth, the user can select the "Back" button to ask the arm to put the target back automatically. The "Switch" button is used to switch to the wheelchair panel. The system flowchart is illustrated in **Figure 2A**.

2.4. EEG Signals Processing

A supervised machine learning process was implemented to process the multichannel EEG signals, which included two parts: (i) the offline model training process; and (ii) the online classification process. In the offline model training process, each user was asked to complete several left/right hand MI tasks. The recorded and labeled (left or right) EEG signals from the nine electrodes ("FC3," "FCz," "FC4," "C3," "Cz," "C4," "CP3," "CPz," and "CP4") were first referenced with the signals from "A2." Then, the signals were band-pass filtered around 8–30 Hz (α and β bands). For the feature extraction, the common spatial pattern (CSP) method was applied. Specifically, a covariance matrix was achieved by the following formula:

$$R_i = \frac{X_i \times X_i{}^T}{trace(X_i \times X_i{}^T)} \tag{1}$$

where $X_i \in R^{M\times N}$ denotes the filtered EEG data matrix of the i_{th} trial, M is the number of channels (9 in this case), N is the number of samples in each trial.

Then, the covariance matrixes that belong to the same class (left or right) were added up as SUM_l or SUM_r. The goal of CSP was to find a spatial filter $W \in R^{m\times N}$ (m is the order of the spatial filter) that maximized the band power difference between SUM_l and SUM_r, and this W could be constructed using the eigenvectors of SUM_l and SUM_r (Li and Guan, 2008). The MI feature used in this study was defined in MATLAB as below:

$$F_i = log\frac{diag(W \times R_i \times W^T)}{sum(diag(W \times R_i \times W^T))} \tag{2}$$

where $F_i \in R^{m\times m}$ denotes the MI feature of the EEG data of the i_{th} trial. Further, the features of all trials and their labels were used to learn a MI classifier based on the support vector machine (SVM) algorithm.

In the online classification process, the MI classifier evaluated a 2-s real-time EEG data epoch every 0.2 s, and generated a score c, which represents the comparative similarity between the input data epoch and the two classes. The mean score for the idle state (i.e., when the user did not imagine) was termed as the idle score C_{idle}. Each newly generated score c was compared to C_{idle}, and the result was used to steer the wheelchair as below:

$$\text{Turn left: } \begin{cases} c < C_{idle} \\ |c - C_{idle}| > TH_l \end{cases} \tag{3}$$

$$\text{Turn right: } \begin{cases} c > C_{idle} \\ |c - C_{idle}| > TH_r \end{cases} \tag{4}$$

where TH_l and TH_r denote the left and right threshold, respectively. As mentioned in the *GUI and control strategy* section, once the "Renew" button was selected when the wheelchair was stopped, the system updated C_{idle} by averaging

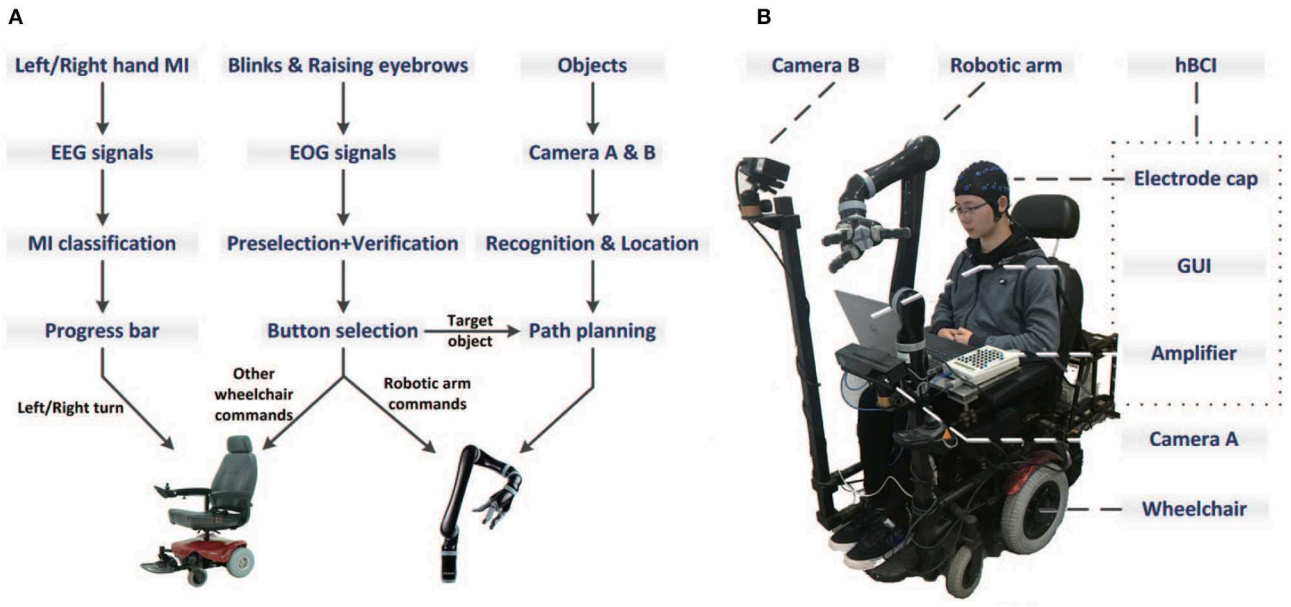

FIGURE 2 | The system flowchart **(A)** and the basic components **(B)** which include the hBCI, a wheelchair, a six-degree intelligent robotic arm and two motion-sensing cameras.

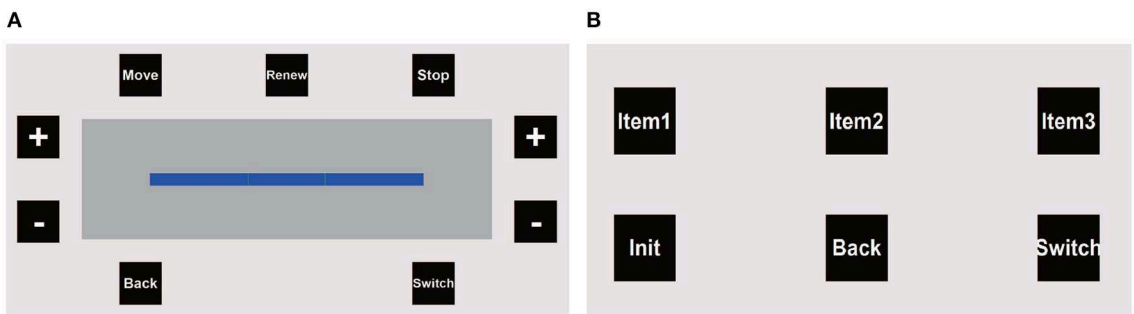

FIGURE 3 | The GUI of the proposed hBCI consists of two separate panels: the wheelchair panel **(A)** and the robotic arm panel **(B)**.

the scores of the next 3 s, during which the user was supposed to be in the idle state. If C_{idle} was renewed, the threshold values TH_l and TH_r also needed to be adjusted, which could be realized by selecting the "+"/"−" buttons on the wheelchair panel, as shown in **Figure 3A**.

2.5. EOG Signals Processing

To select a button on the GUI, users were asked to perform two kinds of eye movements: one intended blink and one eyebrow raising movement. Specifically, after each button flash, the algorithm evaluated a 600-ms EOG data epoch (i.e., 150 samples) which started from the onset of that flash to examine whether it contains an intended blink. A blink was detected and recognized as intended if two conditions were satisfied: (i) The 600-ms data epoch passed a multi-threshold waveform check (as described in Huang et al., 2018), which implied that there was a blink waveform (either intended or unintended) contained in this epoch; (ii) The detected blink waveform was regarded as intended if it was occurred within a certain delay window after the flash onset, and also the peak of the waveform should passe an intended amplitude threshold, as shown in **Figure 4**. The second condition was based on experimental observations: although the response time to a flash varied among individuals, it was relatively stable for a particular user (e.g., 280–320 ms after the flash), and intended blinks usually had a higher amplitude than unintended ones due to the more strong eye movement. For example, if a blink waveform with enough amplitude was detected about 280 ms after the flash onset of "MOVE," it would be recognized as an intended blink in response to "MOVE." For other buttons, the delay should be extended or shortened by at least 100 ms due to the button flash interval.

However, there was still a possibility that an unintended blink was mistakenly detected to be intended. Thus, a verification process was implemented to further exclude the unintended

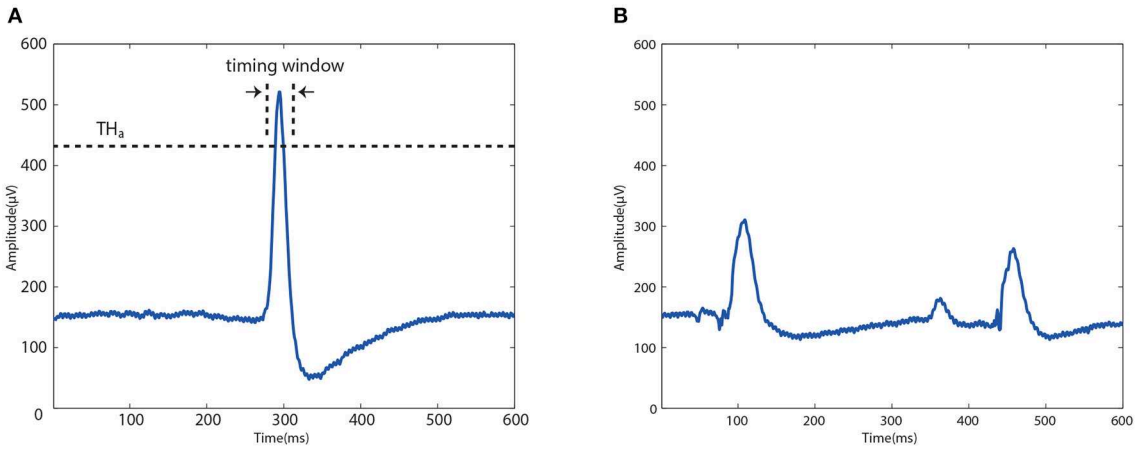

FIGURE 4 | Typical EOG waveform of an intended blink **(A)** and unintended blinks **(B)**. The peak of the intended waveform should be located within a predefined timing window and pass an amplitude threshold TH_a.

inference. Specifically, when an intended blink was detected in the EOG epoch after a button flash, the system just preselected the button and highlighted it in blue as feedback without any command activated. The user was asked to judge the feedback and raise eyebrows to verify if it was what he/she wanted. Only when a button was preselected and verified, was the corresponding command triggered. The detection algorithm for the eyebrow raising movement was similar with the multi-threshold waveform check used in the blink detection, which aimed to recognize different eye movements by checking particular waveform parameters, such as the amplitude, the speed (i.e., the differential value) and the duration of the movement (Huang et al., 2019).

3. EXPERIMENTS

Twenty-two healthy subjects (6 female and 16 males, aged between 22 and 37 years) participated in a MI-based training session and an EOG-based training session without actual control of the wheelchair and the robotic arm. The MI-based training session was designed to help subjects learn and improve the ability of voluntarily modulating the sensorimotor EEG in the motor cortex by performing left-right hand MI task; The EOG-based training session was supposed to help subjects learn how to select a flashing button using the proposed EOG paradigm. Next, five of the 22 subjects with satisfied performance were asked to complete a mobile self-drinking experiment. The experiments were approved by the Ethics Committee of Sichuan Provincial Rehabilitation Hospital. Written informed consent for experiments and the publication of individual information was obtained from all subjects.

3.1. MI-Based Training Session

All of the 22 subjects participated in a MI-training section on each of three different days in 2 weeks, each section consists of three sessions (i.e., nine sessions for each subject). Each MI-training session consisted of an offline run without feedback and an online run with feedback. In an offline run, the subjects performed 40 random left-/right-hand MI trials according to the cue presented on screen. A trial began with a 5-s rest period, in which subjects relaxed and remained in an idle state. Then, a fixation cross was presented at the center of the screen for 2 s, prompting subjects to concentrate on the upcoming task cue. After the cross disappeared, an arrow randomly pointed to either the left or the right was appeared for 5 s. Subjects were asked to imagine the movement of the left or right hand, as indicated by the cue arrow. The recorded EEG data were then used to build a classifier and calculate the offline MI classification accuracy based on a 10-fold cross validation process.

It has been reported that feedback paradigm can enhance MI training (Yu et al., 2015). Thus, after each offline run, subjects completed an online run with visual feedback. Specifically, the subject was asked to change the state of the progress bar by performing left-/right-hand MI task. The left/right MI thresholds were set properly in this session to separate the bar into left, middle (idle), and right parts, ensuring that the subject could effectively control the bar to switch between the three parts. Any out-of-control situation implied the need of adjustment in the rest MI-training sessions, such as adjustment of the imagined hand movement. Subjects with an offline MI classification accuracy over 80% and showed a good control effect of the progress bar were selected to participate in the following experiments.

3.2. EOG-Based Training Session

In this session, five of the 22 subjects with satisfied MI performance were selected to complete 3 EOG-based training sessions, each of which consisted of 30 trials. In a trial, a random target button on the wheelchair panel was first highlighted in blue for 2 s. Then, all buttons started flashing as described in the *GUI* section. Subjects were asked to perform blinks and eyebrow movements to select the target button as soon as possible. The break between two continuous trials was 2 s. After the three sessions, each subject was asked to keep in the idle state for 10 min

during which he/she just relaxed. Indicators, such as the selection accuracy, the selection delay and the false positive rate (FPR), were calculated to evaluate the EOG performance of the system.

3.3. Mobile Self-Drinking Experiment

Five of the 22 subjects that completed both the MI- and EOG-based training sessions participated in this experiment. As shown in **Figures 5A,B**, in an indoor experimental field (8 × 5 m), several obstacles were placed between the starting point and a randomly placed table, on which there were two different bottles with a straw and some water in each of them. To complete an experimental run, subjects were asked to control the system to complete three concatenated tasks: (i) Driving the system from the starting point to reach the table through the obstacles; (ii) Manipulating the robotic arm to grasp a target bottle, drink water with the straw and then put the bottle back; (iii) Driving the system to go through obstacles and a door (width: 1.15 m). Each subject completed three runs with the proposed hBCI.

4. RESULTS

4.1. MI Training Results

In this study, each of the 22 subjects completed 9 MI training sessions. According to the binominal test theory, a significant statistical difference is supported if the p-value is smaller than 0.0056 (0.05/9). We use the following formula in MATLAB to calculate the p-value:

$$p = 1 - cdf('bino', a, num, 0.5) \tag{5}$$

where num is the number of trials in a session (40 in this case), and a is the number of the correctly predicted trials in a session. By this formula, we can achieve that a should be larger than 27 to ensure that p-value is smaller than 0.0056. Thus, the smallest required number of correct trials in a session is 28, which means the accuracy is around 70% (28/40). Considering the high control precisions required in this study, we set 80% as a minimum passing accuracy to invite potential subjects to participate in more MI training sessions.

According to the experimental results, five of the 22 subjects achieved a highest accuracy above 80% in an optimal session, as shown in **Table 1**. The average accuracies and standard deviations of these five subjects are presented in **Figure 6**. Among them, two subjects (S1 and S2) had prior experience with the MI paradigm, and the other three (S3, S4, and S5) were the first time to perform MI tasks. The highest MI accuracies for these five selected subjects in an optimal session were higher than 80%, and the average accuracies for each of them were higher than 70%. For the two subjects with prior MI experience, the highest accuracies were 95 and 100%, respectively. Except for the five selected subjects, six of the 22 subjects did not generate accuracy higher than random level (70% in this case, determined by the binominal test) in any session, which implied that no significant modulations of the sensorimotor rhythms were observed among them. The rest eleven subjects achieved a highest accuracy between 70 and 80% in an optimal session, which was higher than random level but might not be satisfied to realize a reliable control.

4.2. EOG Training Results

As shown in **Table 1**, all of the five subjects participated in this session could achieve an EOG accuracy (the highest value of all sessions) above 95% for the button selection task. The average EOG accuracy for these subjects was 96.2 ± 1.3%, which demonstrated that the individual variance of the proposed EOG paradigm was much smaller than that of the MI paradigm. According to the results, it took 1.3 ± 0.3 s in average to generate a command through the EOG paradigm, which was faster than that proposed in some EOG-based state-of-the-art works (typically 2–3 s) (Ma et al., 2015; Huang et al., 2018). In this study, the FPR was evaluated without the verification process, aiming to verify the effectiveness of the proposed method based on the peak amplitude and timing (see details in the *EOG signals processing* section to distinguish intended and unintended blinks. For these five subjects, the average FPR was 1.5 ± 1.2 events/min. Since a healthy person with normal eye movements usually performed 10–20 unintended blinks per minute, the probability that an unintended blink was mistakenly regarded as an intended one in this work was ∼7.5–15%. This probability was considered to be acceptable since there was a verification process (i.e., raising eyebrows) after the blink recognition, which could ensure that the error recognition of unintended blinks would not result in any output command.

4.3. Mobile Self-Drinking Experiment Results

The average number of collisions for each subject in the three concatenated tasks (Task 1: reaching the table; Task 2: grasping the bottle to drink and put it back; Task 3: passing the door) in this experiment were illustrated in **Table 2**. For Task 2, a failed grasp was counted as a collision. According to the results, S1 successfully completed the three runs without any collision. S2 completed the first two tasks in all three runs but failed to pass through the door in one run. Thus, the average number of collisions for S2 to complete a run of Task 3 was around 0.3. S4 completed Task 1 without any collision, and generated 1/0.3 collisions averagely in Task 2/Task 3. For S3 and S5, the average numbers of collisions in Task 1 were 1.3 and 1.7, respectively, which might be resulted from the relatively unstable direction control of the wheelchair.

5. DISCUSSION

Previous wheelchair systems controlled by BCIs were generally tested by asking the subject to drive the wheelchair from one place to another without accurate requirements of the distance and direction control accuracy. In this study, the subjects need to accurately control and stop the wheelchair in front of a table with a certain distance range and direction. Otherwise the grasping task will fail. Thus, a main purpose of this work is to prove that a hybrid BCI can provide satisfied control precisions (both the distance and direction) for the wheelchair and the robotic arm to handle tricky daily tasks.

In this study, the moving task was concatenated with the grasping task. To ensure a successful grasp, the target bottle has

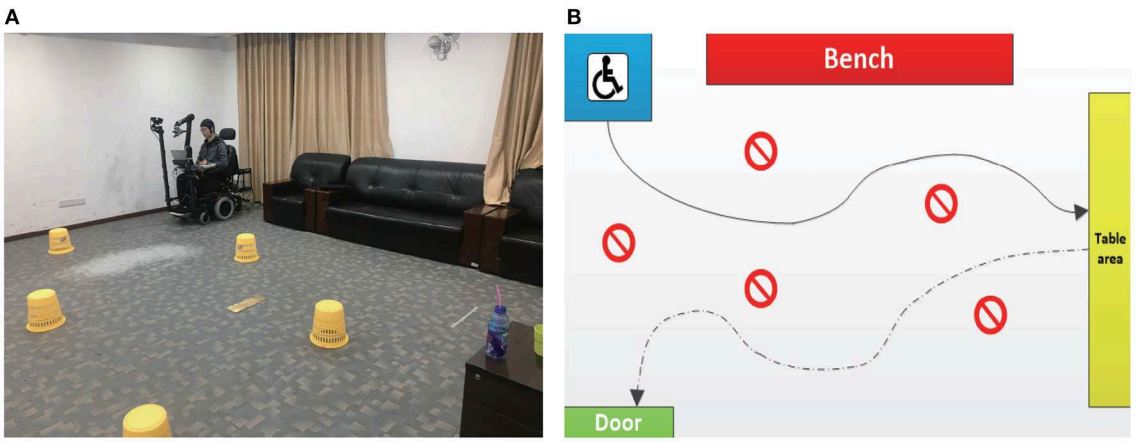

FIGURE 5 | (A) The actual view of the experimental field. **(B)** A typical route that a subject (S1) drove through during the experiment.

TABLE 1 | Results of the five subjects in the MI-/EOG-Based sessions.

Subjects	Gender	Age	MI accuracy (%)	EOG accuracy (%)	EOG RT (s)	EOG FPR (events/min)
S1	Male	25	95	95	1.4	1.5
S2	Male	33	100	95.3	1.3	3.5
S3	Male	27	82.5	97.7	1.8	1.5
S4	Male	25	80	97.5	1.1	0.2
S5	Male	26	82.5	95.5	1.1	1
Mean ± SD	/	/	88±8.9	96.2±1.3	1.3±0.3	1.5±1.2

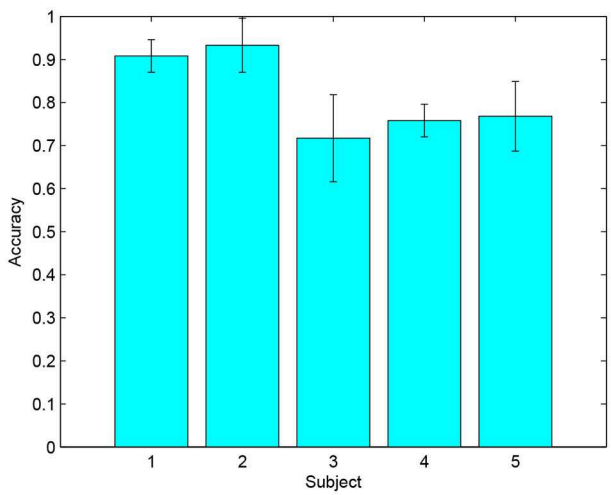

FIGURE 6 | The average accuracies and standard deviations of the five selected subjects in the 9 MI training sessions.

TABLE 2 | Results of the mobile self-drinking experiment.

Subjects	Task 1	Task 2	Task 3
S1	0	0	0
S2	0	0	0.3
S3	1.3	0.3	0.7
S4	0	1	0.3
S5	1.7	1	0
Mean	0.6	0.5	0.7

to be located within a limited rectangular space 0.4 m ahead of Camera A (length: 0.8 m; width: 0.4 m; height: 0.6 m). Thus, the required positional accuracy of this task is 0.4 m. There are no reports of any BCI-controlled wheelchair systems achieving such accuracy. In this study, considering that the wheelchair speed is 0.2 m/s and the stop RT is ∼1.15 s, the proposed system achieves a positional accuracy of 0.23 m, which is satisfied compared with the required accuracy. Moreover, since the proposed system generates nearly continuous directional control outputs, the user can accurately adjust the wheelchair to ensure it is facing almost directly to the target. According to the experimental results, three of the five subjects successfully completed the Task 1 of the mobile self-drinking experiment, and all of the five subjects completed Task 2 and Task 3 with no more than 1 collision in average, which demonstrated the proposed hBCI provided sufficient accuracies to control the integrated system.

In the proposed hybrid BCI, we attempt to use the EOG signals to handle the out-of-control problem of MI-based systems, which

is caused by the time-varying characteristic of the EEG signals and is more serious in an integrated system task, since it usually consumed more time and efforts than a single device task does. Specifically, users could select the corresponding buttons through the EOG paradigm to renew the MI parameter C_{idle} using real-time EEG signals and adjust the left/right turning threshold TH_l and TH_r. To renew C_{idle}, the user first stopped the wheelchair and then perform eye movements to select the "Renew" button. After the button was selected, the user kept in idle state for at least 10 s. The algorithm averaged the scores during this period and used it as an offset compensation for C_{idle}. Moreover, if some unreliable issues caused an offset in the left/right classification, the user could increase/decrease the left/right threshold with a step of 0.2 by selecting the "+"/"−" buttons on the wheelchair panel. According to the observations during the experiments, the three subjects without prior MI experience (S3, S4, and S5) could extend the time of effective control through this strategy, which supported that this strategy might be a feasible solution to utilize the reliability of EOG signals to overcome the time-varying characteristic of the EEG signals.

For subjects maintaining normal eye movements, EOG may be a better choice for developing HMIs since it usually has a higher signal-to-noise ratio. However, EOG-based HMIs can only provide discrete commands, which hurts the control precision in scenarios that require continuous control, such as the direction control of the wheelchair. Compared with EOG, the motor imagery (MI) paradigm used in BCI has a better real-time response performance (usually a few hundreds of millisecond). In this work, the timing window length of an EEG signal epoch for the MI classification was 2 s, and the interval between the starting points of two temporal adjacent epochs was 0.2 s (i.e., the algorithm generated a MI classification result for every 0.2 s). Moreover, the left/tigh threshold conditions were applied to further smooth the outputs. Other wheelchair commands and all of the robotic arm commands were generated by EOG.

Other functions of the wheelchair, such as moving forward/backward and stopping, can be realized in a discrete control mode. Thus, we used an EOG-based button selection paradigm similar with the one proposed in Huang et al. (2018). In Huang et al. (2018), users performed 3-4 blinks to select a button and resulted in a RT of 3.7 s. In this study, users performed one blink and one eyebrow movement for button selection, and the average RT was reduced to ∼1.4 s. For the robotic arm, since the required positional accuracy of a grasping task usually reaches centimeter-level, it is challenging to use a single BCI to realize the full control of the arm. Therefore, we implemented a shared control mode to combine the intelligence of the robotic arm with the EOG paradigm. Once the user selects a button which represents a target bottle, the robotic arm automatically plans the path between the target object and the user's mouth according to the accurate coordinates obtained by the two cameras.

6. CONCLUSION

In this paper, a novel hBCI based on EEG and EOG was presented for the control of an integrated assistive system, which consisted of a wheelchair and a robotic arm, aiming to help users move from a random place and grasp a target object that is placed far away. Users steered the wheelchair left/right by performing motor imagery of the left/right hand, and generated other wheelchair or robotic arm commands by implementing two kinds of eye movements (blinking and raising eyebrows). Five subjects were asked to use the system to complete a mobile self-drinking experiment, which included several tricky tasks, such as avoiding obstacles, grasping a target bottle and passing through a door. The experimental results demonstrated that the proposed hBCI could provide satisfied control accuracy for controlling an integrated assistive system to complete complex daily tasks. In a future work, we will improve the hBCI paralyzed patients and expand its application range in the medical rehabilitation process.

DATA AVAILABILITY STATEMENT

The raw data supporting the conclusions of this manuscript will be made available by the authors, without undue reservation, to any qualified researcher.

ETHICS STATEMENT

This study was carried out in accordance with the recommendations of the Ethics Committee Regulations, the Ethics Committee of Sichuan Provincial Rehabilitation Hospital with written informed consent from all subjects. All subjects gave written informed consent in accordance with the Declaration of Helsinki. The protocol was approved by the Ethics Committee of Sichuan Provincial Rehabilitation Hospital.

AUTHOR CONTRIBUTIONS

YL and QH came up with the main idea of this work, and QH realized it, completed the experiments, and wrote the paper with help from YL. ZZ and QH worked together to realize the pattern recognition part for the robotic arm control. TY provided kind help for building the MI training paradigm. SH provided the helpful advices for the hybrid wheelchair control strategy.

FUNDING

This work was supported by the National Key Research and Development Program of China under Grant 2017YFB1002505, the National Natural Science Foundation of China under Grant 61633010, the Guangdong Natural Science Foundation under Grant 2014A030312005, and the Key R&D Program of Guangdong Province, China under grant 2018B030339001.

REFERENCES

Bhattacharyya, S., Konar, A., and Tibarewala, D. N. (2014). Motor imagery, P300 and error-related EEG-based robot arm movement control for rehabilitation purpose. *Med. Biol. Eng. Comput.* 52, 1007–1017. doi: 10.1007/s11517-014-1204-4

Blankertz, B., Lemm, S., Treder, M., Haufe, S., and Müller, K. R. (2011). Single-trial analysis and classification of ERP components–a tutorial. *IEEE Trans. Neural Syst. Rehabil. Eng.* 56, 814–825. doi: 10.1016/j.neuroimage.2010.06.048

Cheng, X., Wang, Y., Nakanishi, M., Gao, X., Jung, T. P., and Gao, S. (2015). High-speed spelling with a noninvasive brain-computer interface. *Proc. Natl. Acad. Sci. U.S.A.* 112, 6058–6067. doi: 10.1073/pnas.1508080112

Hong, K. S., and Khan, M. J. (2017). Hybrid brain computer interface techniques for improved classification accuracy and increased number of commands: a review. *Front. Neurorobot.* 11:35. doi: 10.3389/fnbot.2017.00035

Huang, Q., Chen, Y., Zhang, Z., He, S., Zhang, R., Liu, J., et al. (2019). An EOG-based wheelchair robotic arm system for assisting patients with severe spinal cord injuries. *J. Neural Eng.* 16:026021. doi: 10.1088/1741-2552/aafc88

Huang, Q., He, S., Wang, Q., Gu, Z., Peng, N., Li, K., et al. (2018). An EOG-based human-machine interface for wheelchair control. *IEEE Trans. Biomed. Eng.* 65, 2023–2032. doi: 10.1109/TBME.2017.2732479

Jin, J., Zhang, H., Ian, D., Wang, X., and Cichocki, A. (2017). An improved P300 pattern in BCI to catch user's attention. *J. Neural Eng.* 14:036001. doi: 10.1088/1741-2552/aa6213

Jun, J., Zongtan, Z., Erwei, Y., Yang, Y., and Dewen, H. (2014). Hybrid brain-computer interface (BCI) based on the EEG and EOG signals. *Biomed. Mater. Eng.* 24, 2919–2925. doi: 10.3233/BME-141111

Khan, M. J., and Hong, K. S. (2017). Hybrid EEG-fNIRS-based eight-command decoding for BCI: application to quadcopter control. *Front. Neurorobot.* 11:6. doi: 10.3389/fnbot.2017.00006

Lafleur, K., Cassady, K., Doud, A., Shades, K., Rogin, E., and He, B. (2013). Quadcopter control in three-dimensional space using a noninvasive motor imagery-based brain-computer interface. *J. Neural Eng.* 10:046003. doi: 10.1088/1741-2560/10/4/046003

Li, Y., and Guan, C. (2008). Joint feature re-extraction and classification using an iterative semi-supervised support vector machine algorithm. *Mach. Learn.* 71, 33–53. doi: 10.1007/s10994-007-5039-1

Li, Y., Pan, J., Wang, F., and Yu, Z. (2013). A hybrid BCI system combining P300 and SSVEP and its application to wheelchair control. *IEEE Trans. Biomed. Eng.* 60, 3156–3166. doi: 10.1109/TBME.2013.2270283

Long, J., Li, Y., Wang, H., Yu, T., Pan, J., and Li, F. (2012). A hybrid brain computer interface to control the direction and speed of a simulated or real wheelchair. *IEEE Trans. Neural Syst. Rehabil. Eng.* 20, 720–729. doi: 10.1109/TNSRE.2012.2197221

Ma, J., Zhang, Y., Cichocki, A., and Matsuno, F. (2015). A novel EOG/EEG hybrid human-machine interface adopting eye movements and ERPs: application to robot control. *IEEE Trans. Biomed. Eng.* 62, 876–888. doi: 10.1109/TBME.2014.2369483

Ma, T., Li, H., Deng, L., Yang, H., Lv, X., Li, P., et al. (2017). The hybrid BCI system for movement control by combining motor imagery and moving onset visual evoked potential. *J. Neural Eng.* 14:026015. doi: 10.1088/1741-2552/aa5d5f

Maddirala, A. K., and Shaik, R. A. (2016). Removal of EOG artifacts from single channel EEG signals using combined singular spectrum analysis and adaptive noise canceler. *IEEE Sens. J.* 16, 8279–8287. doi: 10.1109/JSEN.2016.2560219

Meng, J., Zhang, S., Bekyo, A., Olsoe, J., Baxter, B., and He, B. (2016). Noninvasive electroencephalogram based control of a robotic arm for reach and grasp tasks. *Sci. Rep.* 6:38565. doi: 10.1038/srep38565

Millán, J. D. R., Rupp, R., Múller-Putz, G. R., Murray-Smith, R., Giugliemma, C., and Tangermann, M. (2010). Combining brain-computer interfaces and assistive technologies: state-of-the-art and challenges. *Front. Neurosci.* 4:161. doi: 10.3389/fnins.2010.00161

Minati, L., Yoshimura, N., and Koike, Y. (2016). Hybrid control of a vision-guided robot arm by EOG, EMG, EEG biosignals and head movement acquired via a consumer-grade wearable device. *IEEE Access* 4, 9528–9541. doi: 10.1109/ACCESS.2017.2647851

Pfurtscheller, G., Allison, B. Z., Brunner, C., Bauernfeind, G., Solis-Escalante, T., Scherer, R., et al. (2010). The hybrid BCI. *Front. Neurosci.* 4:3. doi: 10.3389/fnpro.2010.00003

Punsawad, Y., Wongsawat, Y., and Parnichkun, M. (2010). Hybrid EEG-EOG brain-computer interface system for practical machine control. *Int. Conf. IEEE Eng. Med. Biol.* 24, 2919–2925. doi: 10.1109/IEMBS.2010.5626745

Rebsamen, B., Guan, C., Zhang, H., Wang, C., Teo, C., Ang, M., et al. (2010). A brain controlled wheelchair to navigate in familiar environments. *IEEE Trans. Neural Syst. Rehabil. Eng.* 18, 590–598. doi: 10.1109/TNSRE.2010.2049862

Soekadar, S. R., Witkowski, M., Vitiello, N., and Birbaumer, N. (2015). An EEG/EOG-based hybrid brain-neural computer interaction (BNCI) system to control an exoskeleton for the paralyzed hand. *Biomed. Eng.* 60, 199–205. doi: 10.1515/bmt-2014-0126

Witkowski, M., Cortese, M., Cempini, M., Mellinger, J., Vitiello, N., and Soekadar, S. R. (2014). Enhancing brain-machine interface (BMI) control of a hand exoskeleton using electrooculography (EOG). *J. Neuroeng. Rehabil.* 1:165. doi: 10.1186/1743-0003-11-165

Wolpaw, B. R., Birbaumer, N., Heetderks, W. J., McFarland, D. J., Peckham, P. H., Schalk, G., et al. (2000). Brain-computer interface technology: a review of the first international meeting. *IEEE Trans. Neural Syst. Rehabil. Eng.* 8, 164–173. doi: 10.1109/TRE.2000.847807

Wolpaw, J. R., and McFarland, D. J. (2004). Control of a two-dimensional movement signal by a noninvasive brain-computer interface in humans. *Proc. Natl. Acad. Sci. U.S.A.* 101, 17849–17854. doi: 10.1073/pnas.0403504101

Yu, T., Xiao, J., Wang, F., Zhang, R., Gu, Z., Cichocki, A., et al. (2015). Enhanced motor imagery training using a hybrid BCI with feedback. *IEEE Trans. Biomed. Eng.* 62, 1706–1717. doi: 10.1109/TBME.2015.2402283

Conflict of Interest: The authors declare that the research was conducted in the absence of any commercial or financial relationships that could be construed as a potential conflict of interest.

frontiers in Neuroscience

ORIGINAL RESEARCH
published: 11 February 2020
doi: 10.3389/fnins.2020.00066

"You Have Reached Your Destination": A Single Trial EEG Classification Study

Christopher Wirth, Jake Toth and Mahnaz Arvaneh*

Automatic Control and Systems Engineering Department, University of Sheffield, Sheffield, United Kingdom

Studies have established that it is possible to differentiate between the brain's responses to observing correct and incorrect movements in navigation tasks. Furthermore, these classifications can be used as feedback for a learning-based BCI, to allow real or virtual robots to find quasi-optimal routes to a target. However, when navigating it is important not only to know we are moving in the right direction toward a target, but also to know when we have reached it. We asked participants to observe a virtual robot performing a 1-dimensional navigation task. We recorded EEG and then performed neurophysiological analysis on the responses to two classes of correct movements: those that moved closer to the target but did not reach it, and those that did reach the target. Further, we used a stepwise linear classifier on time-domain features to differentiate the classes on a single-trial basis. A second data set was also used to further test this single-trial classification. We found that the amplitude of the P300 was significantly greater in cases where the movement reached the target. Interestingly, we were able to classify the EEG signals evoked when observing the two classes of correct movements against each other with mean overall accuracy of 66.5 and 68.0% for the two data sets, with greater than chance levels of accuracy achieved for all participants. As a proof of concept, we have shown that it is possible to classify the EEG responses in observing these different correct movements against each other using single-trial EEG. This could be used as part of a learning-based BCI and opens a new door toward a more autonomous BCI navigation system.

Keywords: EEG, classification, BCI, human machine interaction, neurophysiology, P300, navigation, target recognition

OPEN ACCESS

Edited by:
Damien Coyle,
Ulster University, United Kingdom

Reviewed by:
Yongtian He,
University of Houston, United States
Didem Gokcay,
Middle East Technical University, Turkey

****Correspondence:***
Christopher Wirth
cwirth1@sheffield.ac.uk

Specialty section:
This article was submitted to Neuroprosthetics, a section of the journal Frontiers in Neuroscience

Received: *03 September 2019*
Accepted: *16 January 2020*
Published: *11 February 2020*

Citation:
Wirth C, Toth J and Arvaneh M (2020) "You Have Reached Your Destination": A Single Trial EEG Classification Study. Front. Neurosci. 14:66. doi: 10.3389/fnins.2020.00066

1. INTRODUCTION

Studies concerning robotic movement and navigation tasks have previously used electroencephalography (EEG) to investigate the brain's responses to observing correct and erroneous movements. These studies have shown that it is possible to classify the responses to correct movements against erroneous ones on a single-trial basis (Chavarriaga et al., 2014; Iturrate et al., 2015; Zander et al., 2016; Kim et al., 2017). Furthermore, a few recent studies have demonstrated the feasibility of using such correct-vs-error classification as feedback for reinforcement-learning-based Brain-Computer Interfaces (BCI) (Iturrate et al., 2015; Zander et al., 2016; Kim et al., 2017). Additionally, some studies have shown that different erroneous conditions can be classified against each other (Iturrate et al., 2010; Spüler and Niethammer, 2015; Wirth et al., 2019). These interesting advances have created the possibility of systems in which machines can

control the low-level action decisions in order to navigate semi-autonomously toward a target, with feedback provided via implicit communication with a user through brain signals spontaneously generated while observing the task (Iturrate et al., 2015; Zander et al., 2016).

However, none of these previous studies have investigated whether it is possible to classify EEG responses to different types of correct actions against each other. In most navigation tasks, it is crucial not only to know that you are moving in the correct direction, but also to recognize when you have reached your destination. As such, it is highly important to consider whether there are significant neurophysiological differences between the brain's responses to observing different correct movements: those that get closer to a target, compared to those that actually reach it.

To address this question, we evaluated data from a virtual robotic navigation task. Participants were asked to observe a virtual robot, represented by a cursor, navigating in a 1-dimensional space and attempting to reach a target. We then investigated the EEG responses to movements that reached the target (hereafter referred to as the "TR condition," short for "target reached"), in contrast to the responses to movements toward the target, but not reaching it (hereafter referred to as the "TT condition," short for "toward target").

To explore neurophysiologicial distinctions between the TT condition and the TR condition, we used time domain features to compare the latency and amplitude of key features of the event related potentials (ERPs). We also examined the spatial distribution of EEG responses to each condition, using topographical maps.

Our main focus was on the P300: a positive peak in an ERP at ∼300 ms (Smith et al., 1970; Picton, 1992), known to be elicited in the brain when a subject recognizes a target stimulus in a sequence containing both target and non-target stimuli (Polich et al., 1991, 1996; Picton, 1992). The P300 has been successfully utilized in BCI, notably in spelling devices (Farwell and Donchin, 1988; Sellers and Donchin, 2006; Krusienski et al., 2008; Gugera et al., 2009; Fazel-Rezai et al., 2012). In these cases, the "target" stimulus is the specific character the user wishes to type. Each potentially desired character is typically highlighted a number of times, with each time being referred to as a "subtrial." These subtrials are then averaged to increase the robustness of classification (Farwell and Donchin, 1988; Sellers and Donchin, 2006; Lotte et al., 2007; Krusienski et al., 2008; Gugera et al., 2009; Fazel-Rezai et al., 2012). Similar systems have also been developed for the control of robots (Lüth et al., 2007; Bell et al., 2008; Johnson et al., 2010; Bhattacharyya et al., 2014), cursors (Polikoff et al., 1995; Li et al., 2010; Kanoh et al., 2011), and wheelchairs (Rebsamen et al., 2006; Iturrate et al., 2009).

Unlike these previous studies utilizing the P300 for robotic control, and similar applications, in our study each stimulus (i.e., each movement) was only presented once, and so our classification phase required single-trial classification. Single-trial P300 classification is challenging, due in part to the low signal-to-noise ratio of EEG data (Jansen et al., 2004; Lotte et al., 2007), hence many systems presenting a number of subtrials. One study investigated the effects of different numbers of subtrials, and, while high accuracy was achieved with many subtrials, classification accuracy of <50% was reported based on a single subtrial, and 3 subtrials were required to achieve over 60% accuracy (Lenhardt et al., 2008). More recently, studies focusing on single-trial P300 classification have shown success, with some reporting accuracies over 80% (Finke et al., 2009; Korczowski et al., 2015; Lin et al., 2017). These studies were classifying the presence of a P300 against its absence. Our goal was to differentiate the P300s elicited in response to two slightly different desired actions. This presents an extra challenge, as we can expect the signals of the conditions to be more similar to each other.

In one previous study, one version of a task presented 80% standard stimuli and 20% target stimuli with all targets being identical to each other, while another version presented 80% standard stimuli and 20% target stimuli, with a pool of 25 different target stimuli; the latter case was found to elicit a broader P300 (Breton, 1988). While the responses to the different target stimuli were not compared to one another, this finding suggests that the P300 is affected by how often a specific stimulus appears in a task. Indeed, other literature has reported that P300 amplitude increases for larger target-to-target intervals (Gonsalvez and Polich, 2002). As well as this, the P300 has been shown to be associated with positive outcomes (Hajcak et al., 2005), and its amplitude has been shown to be affected by reward magnitude (Yeung and Sanfey, 2004; Sato et al., 2005; Wu and Zhou, 2009).

In this study, the desired stimulus is either a movement toward the target or, in cases when the virtual robot is adjacent to the target location, a movement that reaches the target. We hoped to identify and exploit differences between responses to these stimuli, arising from both the experimental differences (i.e., reaching the target occurs less frequently than other correct moves) and the participants' cognitive response to the two conditions (i.e., reaching the target may be considered more important than other correct moves). We then aimed to use the identified neurophysiological differences in order to classify the EEG responses to the two conditions against each other on a single-trial basis.

In order to classify responses to the conditions against each other, we implemented a stepwise linear discriminant analysis strategy, using time domain features from six electrode sites to generate subject-specific classification models. A second publicly available data set (Chavarriaga and Millán, 2010), gathered from participants observing a similar 1-dimensional navigation paradigm, was used to further validate the efficacy of the classification strategy. We tested our approach using data from 10 healthy young adults from the first task, and a further five healthy young adults from the second task.

2. METHODS

This study uses data from two tasks. Neurophysiological analysis and single-trial classification were performed on data from Task 1. These data were recorded at the University of Sheffield, UK. Data from a Task 2 were used in order to further validate the single-trial classification section of the study.

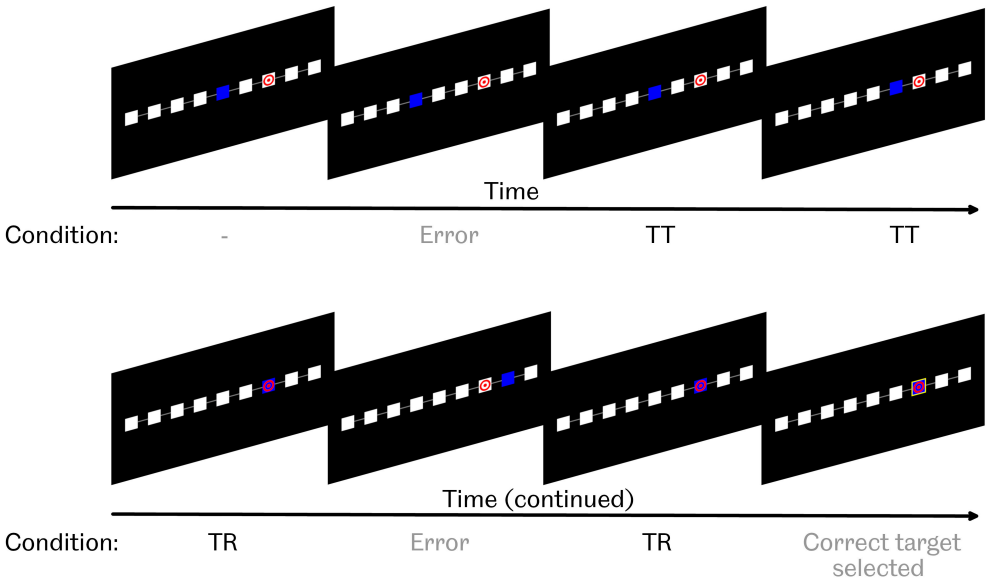

FIGURE 1 | Task 1 paradigm. Participants were asked to observe as a blue cursor attempted to navigate toward, and select, a marked target square. If the cursor was on the target, possible actions were either to select it by drawing a yellow box around the square, or take 1 step away from the target. If the cursor was not on the target, possible actions were either to move 1 step toward the target, move 1 step further away from the target, or erroneously select the current square as the target by drawing a yellow box around it. "TT" condition refers to "toward target," i.e., movements toward, but not reaching, the target. "TR" condition refers to "target reached," i.e., movements that did reach the target.

This was an open access data set, obtained under a Creative Commons Attribution—Non Commercial—No Derivatives 4.0 International license, based on a study by Chavarriaga and Millán (2010).

2.1. Participants

Ten healthy adults (4 female, 6 male, mean age 27.30 ± 8.31) were recruited to participate in Task 1. All of these participants were included in all aspects of the study. All participants had normal or corrected-to-normal vision. They reported no history of psychiatric illness, head injury, or photosensitive epilepsy. Written informed consent was provided by all participants before testing began. All procedures were in accordance with the Declaration of Helsinki, and were approved by the University of Sheffield Ethics Committee in the Automatic Control and Systems Engineering Department.

Six healthy adults (1 female, 5 male, mean age 27.83 ± 2.23) performed Task 2. 1 participant was excluded from this study as too few trials were available after artifact rejection.

2.2. Experimental Setup

2.2.1. EEG Setup

For Task 1, eight channels of EEG were recorded at 500 Hz using an Enobio 8 headset. The electrode sites recorded were Fz, Cz, Pz, Oz, C3, C4, P07, and PO8. A further reference electrode was placed on the earlobe.

For Task 2, 64 channels of EEG were recorded at 512 Hz using a BioSemi ActiveTwo system, and were referenced to the common average. Electrodes were placed using the 10–20 system.

2.2.2. Task 1

In Task 1, participants were seated in front of a screen and asked to observe a computer controlled cursor. Participants were presented with nine squares, arranged in a horizontal line, on a black background, as seen in **Figure 1**. The cursor's current square was colored blue. The target square was identified by a red bullseye symbol on a white background. All other squares were plain white.

At the beginning of each run, the cursor appeared 2 or 3 squares away from the target location, either to the left or the right. Every 2 s, either the cursor would move to an adjacent square, or a yellow box would be drawn around the cursor's current position in order to identify that the computer believed that it had reached the target. Such target identification could occur correctly or erroneously. Actions occurred with preset probabilities, which depended on whether or not the cursor was on the target. These probabilities are shown in **Table 1**.

After the target was identified, either correctly or erroneously, the run finished and the screen was cleared. After 5 s, the next run began. A beep sounded 1 s before the start of each run. Participants were asked to refrain from movement and blinking during each run, but told that they could move and blink freely between runs, while the screen was blank. This process repeated until the end of the block, with each block lasting ∼4 min.

Each participant performed a single session of observations. Participants were asked to observe blocks, with breaks of as long as they wished between blocks, until they reported their concentration levels beginning to decrease. Most participants observed six blocks of trials. However, two participants observed only 2 blocks. On average, Task 1 participants observed a total of

TABLE 1 | Action probabilities for Tasks 1 and 2.

Task	Cursor location	Action	Probability
Task 1	Not on target	Move toward target	0.7
		Move further from target	0.2
		Identify location as target	0.1
	On target	Identify location as target	0.67
		Step off target	0.33
Task 2	Not on target	Move toward target	0.8
		Move further from target	0.2

Note that each run in Task 2 ended once the cursor reached the target. As such there were no moves from an on-target position in Task 2. In both tasks, both TT and TR conditions occurred as a result of "move toward target" actions. If these actions occurred when the cursor was adjacent to the target, the result would be reaching the target (i.e., TR condition). If the cursor was not adjacent to the target prior to the action, the result would be moving closer to the target, but not reaching it (i.e., TT condition).

149.2 ± 40.0 (mean ± standard deviation) TT condition trials, and 82.3 ± 20.0 TR condition trials.

2.2.3. Task 2

In Task 2, participants were similarly asked to observe the 1-dimensional movement of a computer-controlled cursor. Twenty locations were arranged in a horizontal line across a screen. The cursor was displayed as a green square. The target was displayed as a blue square when it appeared to the left of the cursor, or a red square when it appeared to the right of the cursor.

At the beginning of a run, the target was drawn no more than three positions away from the cursor. Every 2 s, the cursor would move either toward or away from the target with preset probabilities, shown in **Table 1**. Unlike Task 1, no target identification was required by the computer. Instead, each run ended when the cursor reached the target. After this, the cursor stayed in its existing location, and a new target was drawn, again no more than three positions away from the cursor. This process repeated until the end of the block, with each block lasting 3 min.

Participants each performed two sessions of observations. Each session consisted of 10 blocks. The number of days between sessions varied between participants, from a minimum of 50 days to a maximum of more than 600 days. On average, Task 2 participants observed a total of 620.2 ± 10.6 TT condition trials, and 277.7 ± 14.1 TR condition trials.

2.3. Neurophysiological Analysis

Data from Task 1 were used for neurophysiological analysis. As we did not have control over the experimental paradigm for Task 2, and so did not have a precisely detailed picture of how the stimuli were presented, we opted not to perform neurophysiological analysis on Task 2 data, instead using these only to further validate the classification phase of this study.

Raw data from Task 1 were resampled to 64 Hz, and then band-pass filtered from 1 to 10 Hz, using a zero-phase Butterworth filter. TT and TR Trials were extracted from a time window of 0 to 1,000 ms, relative to the movement of the cursor. All extracted trials were baseline corrected relative to a period of 200 ms immediately before the movement of the cursor. Artifact rejection was performed by discarding any trials in which the range between the highest and lowest amplitudes, in any channel, was $>100\mu$V.

Grand average time domain event related potential (ERP) data were plotted using the extracted trials, showing the mean voltage ± 1 standard error, comparing responses to the TT condition with those to the TR condition.

Peak analysis was performed in order to identify the latencies at which the P300 occurred in the ERP data. Visual inspection of time domain ERP and topographical plots indicated that the highest P300 amplitude in this study occurred at electrode site Cz, and that there was a difference in P300 amplitudes in response to the two conditions at this site. As such, Cz was chosen as the most suitable channel for peak analysis. This peak analysis was carried out on the grand average ERP for responses to each condition. Subsequently, the P300 was identified as the highest positive peak, occurring between 200 and 500 ms. This time window was selected based on a visual inspection of the grand average time-domain data. To check for statistically significant differences in peak latencies, the same analysis was carried out to find the P300 peak in the average responses of each individual participant, for both conditions. According to one-sample Kolmogorov-Smirnov tests, we could not assume the data to be normally distributed. Therefore, a Wilcoxon signed-rank test was performed to compare the peak latencies identified for the two conditions.

To check whether there was a statistically significant difference in peak amplitude between responses to the two conditions, the mean amplitude was calculated in the responses the average responses of each individual participant, in a time window from 200 to 500 ms in order to encapsulate the full breadth of the P300. According to one-sample Kolmogorov-Smirnov tests, we could not assume the data to be normally distributed. Therefore, a Wilcoxon signed-rank test was performed to compare the amplitudes identified for the two conditions.

Topographical maps were then plotted for responses to each condition, using a 50 ms window surrounding the P300 latency (from peak −25 ms to peak +25 ms) as identified in the pooled data from all trials of both conditions combined. All topographical maps used the same scale, from the minimum value to the maximum values across all grand averages.

2.4. Single-Trial Classification

Single-trial classification was performed on data from both tasks. The same classification protocol was followed for both data sets, and is described in this section.

2.4.1. Pre-processing and Feature Extraction

Data from six electrode sites were used for single-trial classification: Fz, Cz, Pz, Oz, PO7, and PO8. These channels were selected based on visual inspection of grand average time domain ERPs, and considering prior knowledge related to these sites. The P300 has shown to peak in midline electrodes (Polich et al., 1997), and posterior sites, such as PO7 and PO8 are associated with visual processing (Deutsch et al., 1988; Wolber and Wascher, 2005; Schneider et al., 2012). As with the neurophysiological analysis, data were resampled at 64 Hz, trials were baseline corrected to a period of 200 ms immediately before presentation

of the stimulus, and artifact rejection was performed to remove any trials with a range of $>100\mu$V between the highest and lowest amplitude in any channel. For the classification phase, data were band-pass filtered between 1 and 32 Hz. This band was selected after visual inspection of event-related spectral perturbation (ERSP) data which showed that, while most activity occurred at low frequencies, some potentially useful activity was also present in higher frequencies (see **Supplementary Figure 1**). Trials were extracted from 200 to 700 ms relative to the movement of the cursor. This window was selected based on visual inspection of grand average time domain ERPs. Selecting this window results in 33 samples per channel. Thus, in total, each trial was represented by 198 (6×33) features.

Previous literature has suggested that a minimum of 20 trials are required to provide stability in the P300 (Cohen and Polich, 1997). As such, we implemented a minimum cut-off of 20 artifact-free trials per class, in order to ensure we had enough data to produce a reliable training set. One participant was excluded from the single-trial classification phase of this study due to this cutoff.

2.4.2. Classification With Stepwise Linear Discriminant Analysis

In order to classify the data based on the most relevant subset of features, stepwise linear discriminant analysis was chosen as our classification approach, as previous literature has shown this strategy to be effective at both feature selection and classification of both P300 (Donchin et al., 2000; Krusienski et al., 2006, 2008; Sellers and Donchin, 2006; Lotte et al., 2018) and motion-onset visual evoked potential (mVEP) EEG data (Guo et al., 2008). An individual classification model was generated for each participant, using only the data from that individual participant's responses to the task. Firstly, for a given participant, an initial subset of features was selected. The amplitudes of the training trials for each condition were compared in each feature (i.e., each combination of channel and time point) using an unequal variances t-test. Features whose p-value was <0.05 were included in the initial feature set. The stepwise procedure was then performed to select which features would be included in the final model. At each step, a regression analysis was performed on models with and without each feature, producing an F-statistic with a p-value for each feature. If the p-value of any feature was <0.05, the feature with the smallest p-value would be added. Otherwise, if the p-value of any features already in the model had risen to > 0.10 at the current step, the feature with the largest p-value would be removed from the model. This process continued until no feature's p-value reached the thresholds for being added to, or removed from, the model. If no features were added to the model at all, a single feature with the smallest p-value would be selected. Training and test trials were then reduced to the selected features.

The training set for the condition with the fewest training trials was oversampled in order to ensure that training occurred with an equal number of trials per condition. A linear classification model was then trained and tested. All classifiers were trained and tested using leave-one-out cross validation. To test statistical significance of the classification, a right-tailed Fisher's exact test was performed on the confusion matrix of each participant's results. In order to test whether the classification was significant at a group level, individual p-values were combined into a group p-value using Fisher's method (Loughin, 2004; Heard and Rubin-Delanchy, 2018).

3. RESULTS

3.1. Neurophysiological Distinctions

In the responses to both conditions, grand average time domain ERPs showed a broad P300 peak, as can be seen in **Figure 2A**. **Figures 2B,C** show examples of time domain ERPs from individual participants (1 and 10, respectively). In both conditions, the shape of the broad P300 featured a peak shortly prior to 300 ms, followed by a slight drop in amplitude, and then a secondary peak, shortly after 400 ms. In responses to the TR condition, the earlier peak was found to have the highest amplitude, at a latency of 265 ms. The secondary peak marked the highest amplitude in grand average responses to the TT condition, with a latency of 420 ms. However, the Wilcoxon signed-rank test did not find a significant difference between the P300 peak latencies of responses to the two conditions ($p = 0.81$).

A distinction was seen between the P300 amplitudes of responses to the two conditions. The TR condition was observed to elicit a P300 with a greater amplitude than that generated in response to the TT condition. The Wilcoxon signed-rank test comparing the amplitudes of the two conditions, based on a time window from 200 to 500 ms in order to encapsulate the breadth of the P300, found this difference in amplitude to be statistically significant ($p = 0.004$).

Grand average time domain data for all eight electrode sites recorded for Task 1 are shown in **Supplementary Figure 2**.

Topographical maps plotted at the P300 peak latency showed the main activation to occur in the central midline, in response to both conditions, as can be seen in **Figure 3**.

We observed some features in the ERP responses to both conditions which may be related to motion-onset visual evoked potentials (mVEP). Such mVEPs occur when users percieve the beginning of movement of an object or symbol on a screen (Kuba et al., 2007; Guo et al., 2008; Marshall et al., 2013; Beveridge et al., 2019). Three main peaks have been identified in mVEP: a positive peak (P1), followed by a negative deflection (N2), then another positive peak with a latency of 240–500 ms (Kuba et al., 2007; Guo et al., 2008; Marshall et al., 2013; Beveridge et al., 2019), which has been described as a P2 (Kuba et al., 2007; Guo et al., 2008; Marshall et al., 2013) or P300 (Beveridge et al., 2019). The movements considered in this study were instantaneous steps from one location to the next. However, along with the P300, small P1 and N2 peaks were visible, with latencies of 78 and 125 ms, respectively, relative to the movement of the cursor. These peaks did not appear to differ between responses to the two conditions.

3.2. Classification

3.2.1. Classification of Task 1

The classification accuracies of each individual participant of Task 1 are shown in **Table 2**. The mean overall accuracy for all Task 1 participants was 66.5%. The mean accuracy for the TT

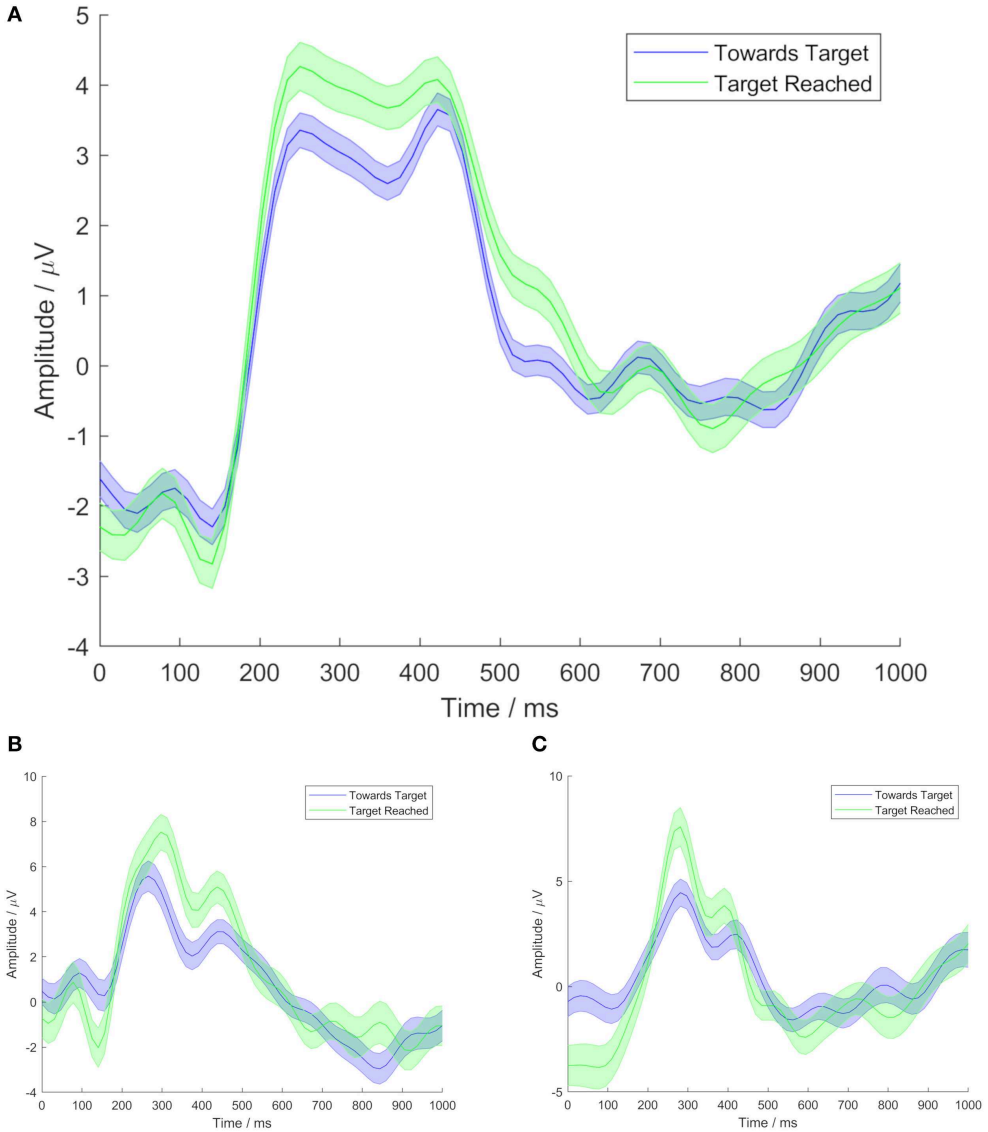

FIGURE 2 | Time domain ERPs at electrode site Cz, from Task 1. Time shown is relative to movement of the cursor. Central lines represent mean signals. Shaded areas cover 1 standard error. Blue lines show TT condition data. Green lines show TR condition data. **(A)** Shows grand average data from all Task 1 participants, **(B)** shows data from participant 1, and **(C)** shows data from participant 10.

condition was 68.8%, and the mean accuracy for the TR condition was 62.4%. Statistically significant separation of the conditions ($p < 0.05$) was found for all Task 1 participants. At a group level, the classification results for Task 1 were found to be statistically significant ($p = 2.8 \times 10^{-54}$).

3.2.2. Classification of Task 2

The classification accuracies of each individual participant of Task 2 are shown in **Table 3**. The mean overall accuracy for all Task 2 participants was 68.0%. The mean accuracy for the TT condition was 70.5%, and the mean accuracy for the TR condition was 61.0%. As with Task 1, statistically significant separation of the conditions ($p < 0.05$) was found for all Task 2 participants. At a group level, the classification results for Task 2 were found to be statistically significant ($p = 9.6 \times 10^{-62}$).

4. DISCUSSION AND CONCLUSION

4.1. Neurophysiological Distinctions Between the Conditions

In this study, the key neurophysiological difference that we identified between the two conditions was in the amplitude of the P300. The amplitude of the P300 was found to be greater in response to the TR condition (i.e., movements that reached the target) than the TT condition (i.e., movements that were correct, but did not reach

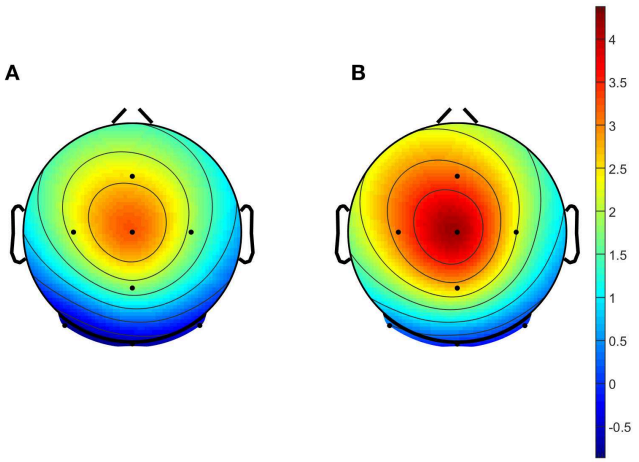

FIGURE 3 | Grand average topographical maps of Task 1 data. Maps were plotted based on a 50 ms window surrounding the peaks identified as P300 from grand average data across all participants, and both conditions. Plots shown represent **(A)** responses to the TT condition, and **(B)** responses to the TR condition.

the target). This distinction was found to be statistically significant ($p = 0.004$).

As discussed in section 1, a number of studies have reported that P300 amplitude is affected by reward magnitude (Yeung and Sanfey, 2004; Sato et al., 2005; Wu and Zhou, 2009). It should be noted that, in this study, participants were not directly rewarded based on the virtual robot's performance. However, it is certainly feasible that they regarded moves that reached the target as being more important than moves that did not reach it, which could be considered analogous to the TR condition having a higher reward magnitude. Reports have been mixed regarding the effects of valence on the P300. Some studies have reported amplitude being affected by positive valence (Cano et al., 2009; Wu and Zhou, 2009), while others have reported valence either having no effect (Carretié et al., 1997; Yeung and Sanfey, 2004), or an effect only in the case of negative valence (Conroy and Polich, 2007). P300 amplitude has also been shown to be dependent on whether feedback was expected or unexpected (Hajcak et al., 2005), and on target-to-target interval, with amplitude increasing when targets appeared less frequently (Gonsalvez and Polich, 2002).

Taking into consideration previous findings on the P300, and the experimental setup of our task, there are a number of potential causes of this increase in amplitude for responses to the TR condition, compared to the TT condition. It may represent a cognitive response recognizing that a move that reaches the target is a more important step than other correct moves. Alternatively, while this study was designed as a navigation observation task, it could also conceptually be considered as an oddball paradigm. That is to say, the TR condition occurs less frequently than the TT condition. Therefore, it is possible that the increased P300 amplitude is due to the relative rarity of the TR condition. It is quite possible that the difference in amplitude may be the result of a combination of these factors.

We also briefly investigated frontal theta power, and asymmetry in alpha power, as these have been reported to vary with regard to valence (Reuderink et al., 2013). However, no significant differences in these markers were identified between the conditions. It is certainly feasible that participants would not have had a strong emotional reaction to reaching the target. In Task 1, the goal was not fully achieved until the target was not only reached but also identified. Furthermore, users knew they were not controlling the virtual robot, and were not rewarded if it performed well. It may be interesting to investigate whether these valence markers indicate different reactions in future on-line experiments, in which participants' responses affect the actions of the virtual robot.

4.2. Single-Trial Classification

Previous studies have successfully classified the brain's responses to correct movements against responses to erroneous movements in navigation tasks, such as the ones explored in this study. The original study for which the data of Task 2 were generated reported classification accuracy of 75.8 and 63.2% for the correct and erroneous movement classes, respectively (Chavarriaga and Millán, 2010). Another study reported correct vs. erroneous movement classification accuracy, in three similar navigation tasks, of 73.8, 72.5, and 74.3% (Iturrate et al., 2015). It is reasonable to expect that the classification of two different correct movements against each other would be more challenging than the classification of correct movements against erroneous ones; we would expect to see more pronounced differences in the brain's responses in the latter case.

In this study, classifying EEG responses to correct movements toward the target (but not reaching it) against responses to movements that reached the target, we achieved mean overall classification accuracy of 66.5 and 68.0% for the two tasks. Indeed, these were only slightly below the levels previously reported for erroneous vs. correct movements in similar tasks. Interestingly, overall accuracy reached a high of 83.7% in the best case. Crucially, statistically significant separation of the two conditions ($p < 0.05$) was achieved for all participants from both tasks, and highly significant separation of the classes was shown at the group level ($p = 2.8 \times 10^{-54}$ and $p = 9.6 \times 10^{-62}$ for the Task 1 and Task 2, respectively).

As a proof of concept, we have shown that it is possible to classify responses to these two classes of correct movement against each other using single-trial EEG. As discussed in section 2.4.2, we chose to apply stepwise linear discriminant analysis in this study, as it has previously been shown to be successful in classifying similar data types (Donchin et al., 2000; Krusienski et al., 2006, 2008; Sellers and Donchin, 2006; Guo et al., 2008; Lotte et al., 2018). However, it is possible that other methodologies, which could be explored in future, may be able to provide further increases in classification accuracy. In potential future systems, classifications of the human observer's EEG responses could be used to guide the movement of a real or virtual robot, with the user being explicitly rewarded for good performance of the robot. In such systems, adding information from more frontal electrodes may be able to provide an increase in classification accuracy, as the frontal cortex has been shown to

TABLE 2 | Single-trial classification results of Task 1 data.

Subject	# TT trials	# TR trials	Mean # Features selected	TT accuracy (%)	TR accuracy (%)	Overall accuracy (%)	*p*-value
1	162	86	35.0	64.8	55.8	61.7	1.4×10^{-3}
2	73	40	44.8	68.5	60.0	65.5	3.1×10^{-3}
3	157	93	10.3	60.5	51.6	57.2	4.2×10^{-2}
4	163	89	50.9	76.1	70.8	74.2	4.1×10^{-13}
5	63	39	30.4	65.1	53.8	60.8	4.7×10^{-2}
6	155	88	6.3	67.7	63.6	66.3	1.9×10^{-6}
7	154	85	16.6	59.7	52.9	57.3	4.0×10^{-2}
8	156	81	15.9	67.3	61.7	65.4	1.7×10^{-5}
9	145	76	40.0	73.1	72.4	72.9	7.5×10^{-11}
10	169	89	37.7	85.2	80.9	83.7	5.0×10^{-26}
Mean	**139.7**	**76.6**	**28.8**	**68.8**	**62.4**	**66.5**	**All < 0.05, group *p*-value:** $p = 2.8 \times 10^{-54}$

Overall accuracy calculated as the percentage of trials, of either class, correctly classified. Number of features selected calculated as the mean of all iterations of leave-one-out cross-validation.

TABLE 3 | Single-trial classification results of Task 2 data.

Subject	# TT trials	# TR trials	Mean # Features selected	TT accuracy (%)	TR accuracy (%)	Overall accuracy (%)	*p*-value
1	448	105	44.3	75.0	60.0	72.2	1.9×10^{-11}
2	585	180	89.2	74.2	66.7	72.4	7.3×10^{-23}
3	259	128	64.7	67.6	60.9	65.4	8.4×10^{-8}
4	201	93	31.5	61.7	51.6	58.5	2.2×10^{-2}
5	603	250	71.8	74.0	66.0	71.6	1.4×10^{-27}
Mean	**419.2**	**151.2**	**60.3**	**70.5**	**61.0**	**68.0**	**All < 0.05, group *p*-value:** $p = 9.6 \times 10^{-62}$

Overall accuracy calculated as the percentage of trials, of either class, correctly classified. Number of features selected calculated as the mean of all iterations of leave-one-out cross-validation.

code prediction and reward (Schultz et al., 1997; Schultz, 2001; McClure et al., 2004).

4.3. Implications for BCI

The P300 has a history of successful use in BCI, as discussed in section 1. In particular, there have been many studies, dating back over 30 years, regarding the use of P300 signals in BCI spelling devices (Farwell and Donchin, 1988; Sellers and Donchin, 2006; Krusienski et al., 2008; Gugera et al., 2009; Fazel-Rezai et al., 2012). These systems have often been able to improve the robustness and accuracy of their classifications by using paradigms that allowed each stimulus to be presented multiple times, and the responses to be averaged. P300-based BCIs have also been created for other applications, such as video games (Finke et al., 2009; Kaplan et al., 2013), virtual reality (Bayliss, 2003), and control of robots (Lüth et al., 2007; Bell et al., 2008; Johnson et al., 2010; Bhattacharyya et al., 2014), cursors (Polikoff et al., 1995; Li et al., 2010; Kanoh et al., 2011) and wheelchairs (Rebsamen et al., 2006; Iturrate et al., 2009). Furthermore, the P300 has been utilized alongside other modalities, such as motor imagery (Su et al., 2011) and steady-state visual evoked potentials (SSVEP) (Yin et al., 2013) to create hybrid BCIs (Pfurtscheller et al., 2010; Müller-Putz et al., 2011; Amiri et al., 2013). The navigation scenarios presented in this study provided a further challenge compared to many previous P300-related systems, as each stimulus (i.e., movement) was only presented once. This was an important aspect of the paradigm, as we wished to simulate the observation of real navigation, with a view to future applications in which classifications could be made solely based on users' responses to the actions they observe. In such real navigation, each action occurs only once. While accurate single-trial P300 classification is challenging due to the low signal-to-noise ratio of EEG (Jansen et al., 2004; Lotte et al., 2007), some recent studies have shown that it can be achieved. One study using a video game context reported mean offline classification accuracy of 85%, and online accuracy of 66% (Finke et al., 2009). Another study

reported single trial P300 classification accuracy of 70% (Jansen et al., 2004). In other cases, the area under the receiver operating characteristic curve (AUC) was reported for various possible classifier parameters, rather than the classification accuracy for a specific trained and optimized model. An AUC of over 0.8 has been reported for many participants (Korczowski et al., 2015; Lin et al., 2017). In this study, rather than classifying a condition eliciting a P300 against a condition that did not elicit a P300, we were classifying two P300-generating conditions against each other. As such the fact that statistically significant separation of two different correct conditions was achieved for all participants is encouraging for the use of the P300 in single-trial BCI scenarios.

In recent years, there have been interesting advances in BCIs based on signals that are generated spontaneously in the brain, without the need of a conscious effort to generate them on the part of the user. These systems, making use of implicit communication, have been described in two groups, referred to as "reactive BCI," in which a spontaneous response is triggered by a stimulus, and "passive BCI," whereby arbitrary mental states are measured (Zander et al., 2010, 2014; Zander and Köthe, 2011). Some particularly interesting recent studies have been those exploring reactive BCI in robotic movement and navigation tasks. Classification of error-related potentials (ErrP) in order to differentiate correct movements from erroneous ones has been combined with reinforcement learning in order to allow machines to perform a desired action (Kim et al., 2017) or navigate toward a desired target (Chavarriaga and Millán, 2010; Iturrate et al., 2015; Zander et al., 2016). By obtaining more detailed information from spontaneously generated signals, we can provide these systems with more context, and allow them to learn more efficiently and act more appropriately. The ability to classify when a target has been reached specifically and separately from other correct movements, as has been demonstrated in this study, would be an important aspect of a navigation system, and thus could enhance the usability and effectiveness of navigation-based BCI.

4.4. Conclusion

In this study, we compared the ERPs generated in EEG data, in response to observing two types of correct movements by a virtual robot: those that moved the robot closer to the target without reaching it, and those in which the robot reached the target. We were able to show that both correct movement conditions elicited a P300, and we identified a significantly higher P300 amplitude in cases in which the target was reached.

Interestingly, we were able to classify the responses to these two types of correct actions against each other with mean overall accuracies of 66.5 and 68.0% for two tasks, achieving statistically significant separation of the conditions for all participants. This single-trial classification could be used as part of a learning-based BCI, and opens a new door toward a more autonomous BCI navigation system.

DATA AVAILABILITY STATEMENT

The raw data supporting the conclusions of this article will be made available by the authors, within 3 years, once further experiments have concluded, to any qualified researcher.

ETHICS STATEMENT

The studies involving human participants were in accordance with the Declaration of Helsinki, and were reviewed and approved by University of Sheffield Ethics Committee in the Automatic Control and Systems Engineering Department. The participants provided their written informed consent to participate in this study.

AUTHOR CONTRIBUTIONS

MA conceived the study, supervised the work, and contributed to writing the paper. JT performed the data collection for Task 1. CW designed Task 1, performed the neurophysiological analysis and single-trial analysis, and wrote the paper.

FUNDING

This research was supported by University of Sheffield, United Kingdom, and a Doctoral Training Partnership Scholarship from the Engineering and Physical Sciences Research Council (EPSRC).

SUPPLEMENTARY MATERIAL

The Supplementary Material for this article can be found online at: https://www.frontiersin.org/articles/10.3389/fnins.2020.00066/full#supplementary-material

REFERENCES

Amiri, S., Fazel-Rezai, R., and Asadpour, V. (2013). A review of hybrid brain-computer interface systems. *Adv. Hum. Comput. Interact.* 2013, 1–8. doi: 10.1155/2013/187024

Bayliss, J. (2003). Use of the evoked potential p3 component for control in a virtual apartment. *IEEE Trans. Neural Syst. Rehabil. Eng.* 11, 113–116. doi: 10.1109/TNSRE.2003.814438

Bell, C. J., Shenoy, P., Chalodhorn, R., and Rao, R. P. N. (2008). Control of a humanoid robot by a noninvasive brain-computer interface in humans. *J. Neural Eng.* 5, 214–220. doi: 10.1088/1741-2560/5/2/012

Beveridge, R., Wilson, S., Callaghan, M., and Coyle, D. (2019). Neurogaming with motion-onset visual evoked potentials (mVEPs): adults versus teenagers. *IEEE Trans. Neural Syst. Rehabil. Eng.* 27, 572–581. doi: 10.1109/TNSRE.2019.2904260

Bhattacharyya, S., Konar, A., and Tibarewala, D. N. (2014). Motor imagery, P300 and error-related EEG-based robot arm movement control for rehabilitation purpose. *Med. Biol. Eng. Comput.* 52, 1007–1017. doi: 10.1007/s11517-014-1204-4

Breton, F., Ritter, W., Simson, R., and Vaughan, H. G. Jr. (1988). The N2 component elicited by stimulus matches and multiple targets. *Biol. Psychol.* 27, 23–44. doi: 10.1016/0301-0511(88)90003-8

Cano, M. E., Class, Q. A., and Polich, J. (2009). Affective valence, stimulus attributes, and p300: color vs. black/white and normal vs. scrambled images. *Int. J. Psychophysiol.* 71, 17–24. doi: 10.1016/j.ijpsycho.2008.07.016

Carretié, L., Iglesias, J., García, T., and Ballesteros, M. (1997). N300, P300 and the emotional processing of visual stimuli. *Electroencephalogr. Clin. Neurophysiol.* 103, 298–303. doi: 10.1016/S0013-4694(96)96565-7

Chavarriaga, R., and Millán, J. D. R. (2010). Learning from EEG error-related potentials in noninvasive brain-computer interfaces. *IEEE Trans. Neural Syst. Rehabil. Eng.* 18, 381–388. doi: 10.1109/TNSRE.2010.2053387

Chavarriaga, R., Sobolewski, A., and Millán, J. D. R. (2014). Errare machinale EST: the use of error-related potentials in brain-machine interfaces. *Front. Neurosci.* 8:208. doi: 10.3389/fnins.2014.00208

Cohen, J., and Polich, J. (1997). On the number of trials needed for P300. *Int. J. Psychol.* 25, 249–255. doi: 10.1016/S0167-8760(96)00743-X

Conroy, M. A., and Polich, J. (2007). Affective valence and P300 when stimulus arousal level is controlled. *Cogn. Emot.* 21, 891–901. doi: 10.1080/02699930600926752

Deutsch, G., Bourbon, W. T., Papanicolaou, A. C., and Eisenberg, H. M. (1988). Visuospatial tasks compared via activation of regional cerebral blood flow. *Neuropsychologia* 26, 445–452. doi: 10.1016/0028-3932(88)90097-8

Donchin, E., Spencer, K., and Wijesinghe, R. (2000). The mental prosthesis: assessing the speed of a p300-based brain-computer interface. *IEEE Trans. Rehabil. Eng.* 8, 174–179. doi: 10.1109/86.847808

Farwell, L., and Donchin, E. (1988). Talking off the top of your head: toward a mental prosthesis utilizing event-related brain potentials. *Electroencephalogr. Clin. Neurophysiol.* 70, 510–523. doi: 10.1016/0013-4694(88)90149-6

Fazel-Rezai, R., Allison, B. Z., Guger, C., Sellers, E. W., Kleich, S. C., and Kübler, A. (2012). P300 brain computer interface: current challenges and emerging trends. *Front. Neuroeng.* 5:14. doi: 10.3389/fneng.2012.00014

Finke, A., Lenhardt, A., and Ritter, H. (2009). The mindgame: a P300-based brain-computer interface game. *Neural Netw.* 22, 1329–1333. doi: 10.1016/j.neunet.2009.07.003

Gonsalvez, C. J., and Polich, J. (2002). P300 amplitude is determined by target-to-target interval. *Psychophysiology* 39, 388–396. doi: 10.1017/S0048577201393137

Gugera, C., Dabana, S., Eric Sellers, C. H., Krausza, G., Carabalonac, R., Gramaticac, F., et al. (2009). How many people are able to control a P300-based brain-computer interface (BCI)? *Neurosci. Lett.* 462, 94–98. doi: 10.1016/j.neulet.2009.06.045

Guo, F., Hong, B., Gao, X., and Gao, S. (2008). A brain-computer interface using motion-onset visual evoked potential. *J. Neural Eng.* 5, 477–485. doi: 10.1088/1741-2560/5/4/011

Hajcak, G., Holroyd, C. B., Moser, J. S., and Simons, R. F. (2005). Brain potentials associated with expected and unexpected good and bad outcomes. *Psychophysiology* 42, 161–170. doi: 10.1111/j.1469-8986.2005.00278.x

Heard, N. A., and Rubin-Delanchy, P. (2018). Choosing between methods of combining *p*-values. *Biometrika* 105, 239–246. doi: 10.1093/biomet/asx076

Iturrate I., Montesano L., and Minguez, J. (2010). "Robot reinforcement learning using eeg-based reward signals," in *Proceedings IEEE International Conference on Robotics and Automation (ICRA'10)* (Anchorage, AK), 4822–4829. doi: 10.1109/ROBOT.2010.5509734

Iturrate, I., Antelis, J. M., Kübler, A., and Minguez, J. (2009). A noninvasive brain-actuated wheelchair based on a P300 neurophysiological protocol and automated navigation. *IEEE Trans. Robot.* 25, 614–627. doi: 10.1109/TRO.2009.2020347

Iturrate, I., Chavarriaga, R., Montesano, L., Minguez, J., and Millán, J. D. R. (2015). Teaching brain-machine interfaces as an alternative paradigm to neuroprosthetics control. *Sci. Rep.* 5:13893. doi: 10.1038/srep13893

Jansen, B. H., Allam, A., Kota, P., Lachance, K., Osho, A., and Sundaresan, K. (2004). An exploratory study of factors affecting single trial P300 detection. *IEEE Trans. Biomed. Eng.* 51, 975–978. doi: 10.1109/TBME.2004.826684

Johnson, G. D., Waytowich, N. R., Cox, D. J., and Krusienski, D. J. (2010). "Extending the discrete selection capabilities of the P300 speller to goal-oriented robotic arm control," in *3rd IEEE RAS and EMBS International Conference on Biomedical Robotics and Biomechatronics* (Tokyo), 572–575.

Kanoh, S., Miyamoto, K., and Yoshinobu, T. (2011). "A P300-based BCI system for controlling computer cursor movement," in *Proceedings of 33th Annual International Conference of the IEEE Engineering in Medicine and Biology Society (EMBC)* (Boston, MA), 6405–6408.

Kaplan, A., Shishkin, S., Ganin, T., Basyul, I., and Zhigalov, A. (2013). Adapting the P300-based brain-computer interface for gaming: a review. *IEEE Trans. Comput. Intell. AI Games* 5, 141–149. doi: 10.1109/TCIAIG.2012.2237517

Kim, S. K., Kirchner, E. A., Stefes, A., and Kirchner, F. (2017). Intrinsic interactive reinforcement learning–using error-related potentials for real world human–robot interaction. *Sci. Rep.* 7:17562. doi: 10.1038/s41598-017-17682-7

Korczowski, L., Congedo, M., and Jutten, C. (2015). "Single-trial classification of multi-user P300-based brain-computer interface using riemannian geometry," in *Proceedings of 37th Annual International Conference of the IEEE Engineering in Medicine and Biology Society (EMBC)* (Milan), 1769–1772.

Krusienski, D. J., Sellers, E., Mcfarland, D., Vaughan, T., and Wolpaw, J. (2008). Toward enhanced P300 speller performance. *J. Neurosci. Methods* 167, 15–21. doi: 10.1016/j.jneumeth.2007.07.017

Krusienski, D. J., Sellers, E. W., Cabestaing, F., Bayoudh, S., McFarland, D. J., Vaughan, T. M., et al. (2006). A comparison of classification techniques for the P300 speller. *J. Neural Eng.* 3, 299–305. doi: 10.1088/1741-2560/3/4/007

Kuba, M., Kubová, Z., Kremláček, J., and Langrová, J. (2007). Motion-onset VEPs: Characteristics, methods, and diagnostic use. *Vision Res.* 47, 189–202. doi: 10.1016/j.visres.2006.09.020

Lenhardt, A., Kaper, M., and Ritter, H. (2008). An adaptive P300-based online brain-computer interface. *IEEE Trans. Neural Syst. Rehabil. Eng.* 16, 121–130. doi: 10.1109/TNSRE.2007.912816

Li, Y., Long, J., Yu, T., Yu, Z., Wang, C., Zhang, H., et al. (2010). An EEG-based BCI system for 2-D cursor control by combining mu/beta rhythm and P300 potential. *IEEE Trans. Biomed. Eng.* 57, 2495–2505. doi: 10.1109/TBME.2010.2055564

Lin, Z., Zeng, Y., Tong, L., Zhang, H., Zhang, C., and Yan, B. (2017). Method for enhancing single-trial P300 detection by introducing the complexity degree of image information in rapid serial visual presentation tasks. *PLoS ONE* 12:e0184713. doi: 10.1371/journal.pone.0184713

Lotte, F., Bougrain, L., Cichocki, A., Clerc, M., Congedo, M., Rakotomamonjy, A., et al. (2018). A review of classification algorithms for EEG-based brain-computer interfaces: a 10 year update. *J. Neural Eng.* 15:031005. doi: 10.1088/1741-2552/aab2f2

Lotte, F., Congedo, M., Lécuyer, A., Lamarche, F., and Arnaldi, B. (2007). A review of classification algorithms for EEG-based brain-computer interfaces. *J. Neural Eng.* 4, R1–R13. doi: 10.1088/1741-2560/4/2/R01

Loughin, T. M. (2004). A systematic comparison of methods for combining *p*-values from independent tests. *Comput. Stat. Data Anal.* 47, 467–485. doi: 10.1016/j.csda.2003.11.020

Lüth, T., Ojdanić, D., Ola Friman, O. P., and Gräser, A. (2007). "Low level control in a semi-autonomous rehabilitation robotic system via a brain-computer interface," in *IEEE 10th International Conference on Rehabilitation Robotics* (Noordwijk), 721–728.

Marshall, D., Coyle, D., and Wilson, S. (2013). "Motion-onset visual evoked potentials for gaming: a pilot study," in *24th IET Irish Signals and Systems Conference* (Letterkenny), 56.

McClure, S. M., York, M. K., and Montague, P. R. (2004). The neural substrates of reward processing in humans: the modern role of fmri. *Neuroscientist* 10, 260–268. doi: 10.1177/1073858404263526

Müller-Putz, G. R., Breitwieser, C., Cincotti, F., Leeb, R., Schreuder, M., Leotta, F., et al. (2011). Tools for brain-computer interaction: a general concept for a hybrid bci. *Front. Neuroinform.* 5:30. doi: 10.3389/fninf.2011.00030

Pfurtscheller, G., Allison, B. Z., Brunner, C., Bauernfeind, G., Solis-Escalante, T., Scherer, R., et al. (2010). The hybrid BCI. *Front. Neurosci.* 4:30. doi: 10.3389/fnpro.2010.00003

Picton, T. W. (1992). The P300 wave of the human event-related potential. *J. Clin. Neurophysiol.* 9, 456–479. doi: 10.1097/00004691-199210000-00002

Polich, J., Alexander, J. E., Baue, L. O., Kuperman, S., Morzorati, S., O'Connor, S. J., et al. (1997). P300 topography of amplitude/latency correlations. *Brain Topogr.* 9, 275–282. doi: 10.1007/BF01464482

Polich, J., Brock, T., and W.Geisler, M. (1991). P300 from auditory and somatosensory stimuli: probability and inter-stimulus interval. *Int. J. Psychophysiol.* 11, 219–222. doi: 10.1016/0167-8760(91)90015-P

Polich, J., Ellerson, P. C., and Cohen, J. (1996). P300, stimulus intensity, modality, and probability. *Int. J. Psychophysiol.* 23, 55–62. doi: 10.1016/0167-8760(96)00028-1

Polikoff, J. B., Bunnell, H. T., and Borkowski, W. J. (1995). "Toward a P300-based computer interface," in *RESNA'95 Annual Conference* (Vancouver, BC), 178–180.

Rebsamen, B., Burdet, E., Guan, C., Zhang, H., Teo, C. L., Zeng, Q., et al. (2006). "A brain-controlled wheelchair based on P300 and path guidance," in *1st IEEE/RAS-EMBS International Conference on Biomedical Robotics and Biomechatronics* (Pisa), 1101–1106.

Reuderink, B., Mühl, C., and Poel, M. (2013). Valence, arousal and dominance in the EEG during game play. *Int. J. Auton. Adapt. Commun. Syst.* 6, 45–62. doi: 10.1504/IJAACS.2013.050691

Sato, A., Yasuda, A., Ohira, H., Miyawaki, K., Nishikawa, M., Kumano, H., et al. (2005). Effects of value and reward magnitude on feedback negativity and P300. *Neuroreport* 16, 407–411. doi: 10.1097/00001756-200503150-00020

Schneider, D., Beste, C., and Wascher, E. (2012). On the time course of bottom-up and top-down processes in selective visual attention: an EEG study. *Psychophysiology* 49, 1660–1671. doi: 10.1111/j.1469-8986.2012.01462.x

Schultz, W. (2001). Book review: reward signaling by dopamine neurons. *Neuroscientist* 7, 293–302. doi: 10.1177/107385840100700406

Schultz, W., Dayan, P., and Montague, P. R. (1997). A neural substrate of prediction and reward. *Science* 275, 1593–1599. doi: 10.1126/science.275.5306.1593

Sellers, E. W., and Donchin, E. (2006). A P300-based brain-computer interface: initial tests by als patients. *Clin. Neurophysiol.* 117, 538–548. doi: 10.1016/j.clinph.2005.06.027

Smith, D., Donchin, E., Cohen, L., and Starr, A. (1970). Auditory averaged evoked potentials in man during selective binaural listening. *Electroencephalogr. Clin. Neurophysiol.* 28, 146–152. doi: 10.1016/0013-4694(70)90182-3

Spüler, M., and Niethammer, C. (2015). Error-related potentials during continuous feedback: using EEG to detect errors of different type and severity. *Front. Hum. Neurosci.* 9:155. doi: 10.3389/fnhum.2015.00155

Su, Y., Qi, Y., Xun Luo, J., Wu, B., Yang, F., Li, Y., et al. (2011). A hybrid brain-computer interface control strategy in a virtual environment. *J. Zhejiang Univ. Sci. C* 12, 351–361. doi: 10.1631/jzus.C1000208

Wirth, C., Dockree, P. M., Harty, S., Lacey, E., and Arvaneh, M. (2019). Towards error categorisation in BCI: single-trial EEG classification between different errors. *J. Neural Eng.* 17:016008. doi: 10.1088/1741-2552/ab53fe

Wolber, M., and Wascher, E. (2005). The posterior contralateral negativity as a temporal indicator of visuo-spatial processing. *J. Psychophysiol.* 19, 182–194. doi: 10.1027/0269-8803.19.3.182

Wu, Y., and Zhou, X. (2009). The P300 and reward valence, magnitude, and expectancy in outcome evaluation. *Brain Res.* 1286, 144–122. doi: 10.1016/j.brainres.2009.06.032

Yeung, N., and Sanfey, A. G. (2004). Independent coding of reward magnitude and valence in the human brain. *J. Neurosci.* 24, 6258–6264. doi: 10.1523/JNEUROSCI.4537-03.2004

Yin, E., Zhou, Z., Jiang, J., Chen, F., Liu, Y., and Hu, D. (2013). A novel hybrid BCI speller based on the incorporation of SSVEP into the P300 paradigm. *J. Neural Eng.* 10:026012. doi: 10.1088/1741-2560/10/2/026012

Zander, T. O., Brönstrup, J., Lorenz, R., and Krol, L. R. (2014). "Towards BCI-based implicit control in human-computer interaction," in *Advances in Physiological Computing*, eds S. H. Fairclough and K. Gilleade (London: Springer London), 67–90.

Zander, T. O., and Köthe, C. (2011). Towards passive brain-computer interfaces: applying brain-computer interface technology to human-machine systems in general. *J. Neural Eng.* 8:025005. doi: 10.1088/1741-2560/8/2/025005

Zander, T. O., Kothe, C., Jatzev, S., and Gaertner, M. (2010). "Enhancing human-computer interaction with input from active and passive brain-computer interfaces," in *Brain-Computer Interfaces: Applying Our Minds to Human-Computer Interaction*, eds D. S. Tan and A. Nijholt (London: Springer London), 181–199.

Zander, T. O., Krol, L. R., Birbaumer, N. P., and Gramann, K. (2016). Neuroadaptive technology enables implicit cursor control based on medial prefrontal cortex activity. *Proc. Natl. Acad. Sci. U.S.A.* 113, 14898–14903. doi: 10.1073/pnas.1605155114

Conflict of Interest: The authors declare that the research was conducted in the absence of any commercial or financial relationships that could be construed as a potential conflict of interest.

frontiers in Robotics and AI

ORIGINAL RESEARCH
published: 31 March 2020
doi: 10.3389/frobt.2020.00038

A Robust Screen-Free Brain-Computer Interface for Robotic Object Selection

Henrich Kolkhorst[1,2,3*†], *Joseline Veit*[1†], *Wolfram Burgard*[2,3,4] *and Michael Tangermann*[1,2,3*]

[1] Brain State Decoding Lab, Department of Computer Science, University of Freiburg, Freiburg im Breisgau, Germany, [2] Autonomous Intelligent Systems, Department of Computer Science, University of Freiburg, Freiburg im Breisgau, Germany, [3] Cluster of Excellence BrainLinks-BrainTools, University of Freiburg, Freiburg im Breisgau, Germany, [4] Toyota Research Institute, Los Altos, CA, United States

Brain signals represent a communication modality that can allow users of assistive robots to specify high-level goals, such as the object to fetch and deliver. In this paper, we consider a screen-free Brain-Computer Interface (BCI), where the robot highlights candidate objects in the environment using a laser pointer, and the user goal is decoded from the evoked responses in the electroencephalogram (EEG). Having the robot present stimuli in the environment allows for more direct commands than traditional BCIs that require the use of graphical user interfaces. Yet bypassing a screen entails less control over stimulus appearances. In realistic environments, this leads to heterogeneous brain responses for dissimilar objects—posing a challenge for reliable EEG classification. We model object instances as subclasses to train specialized classifiers in the Riemannian tangent space, each of which is regularized by incorporating data from other objects. In multiple experiments with a total of 19 healthy participants, we show that our approach not only increases classification performance but is also robust to both heterogeneous and homogeneous objects. While especially useful in the case of a screen-free BCI, our approach can naturally be applied to other experimental paradigms with potential subclass structure.

Keywords: brain-machine interface, screen-free brain-computer interface, subclass structure, human-robot interaction, event-related potentials, service robots

OPEN ACCESS

Edited by:
Luca Tonin,
University of Padova, Italy

Reviewed by:
Muhammad Jawad Khan,
National University of Sciences and Technology (NUST), Pakistan
Andrés Úbeda,
University of Alicante, Spain

***Correspondence:**
Henrich Kolkhorst
kolkhorst@informatik.uni-freiburg.de
Michael Tangermann
michael.tangermann@blbt.uni-freiburg.de

†These authors have contributed equally to this work

Specialty section:
This article was submitted to Computational Intelligence in Robotics, a section of the journal Frontiers in Robotics and AI

Received: *02 December 2019*
Accepted: *05 March 2020*
Published: *31 March 2020*

Citation:
Kolkhorst H, Veit J, Burgard W and Tangermann M (2020) A Robust Screen-Free Brain-Computer Interface for Robotic Object Selection. Front. Robot. AI 7:38. doi: 10.3389/frobt.2020.00038

1. INTRODUCTION

Robotic service assistants can help impaired users gain autonomy by performing physical tasks, such as fetching objects or serving a meal. While the robots should perform low-level actions without supervision, the human should be able to exert high-level control, such as deciding which object to fetch and deliver. Non-invasive brain signals can be used to deliver such control commands—especially for users who cannot reliably communicate using other modalities. For example, event-related potentials (ERPs) form one class of possible control signals from electroencephalography (EEG). Traditionally, computer screens with graphical user interfaces present stimuli in order to elicit ERP responses and to map brain responses to application commands. However, the required association between elements of the user interface and objects or actions in the real world can be ambiguous (e.g., in the presence of multiple identical objects).

Yet user goals in human–robot interaction are often related to tangible objects of the environment that the robot can manipulate. Hence, interaction with objects offers an alternative to screen-based selection. For instance, the robot can highlight candidate objects in the environment

using a laser pointer as introduced in Kolkhorst et al. (2018). The ERP responses elicited by each laser highlighting allow to identify the target of a user's visual attention among multiple candidate objects (c.f., **Figure 1**). This novel approach avoids the indirection of an additional screen and permits changing environments while utilizing the robot that is needed anyhow for user assistance. Screen-free object selection was shown to work reliably in an online setting in Kolkhorst et al. (2018). Yet, the original evaluation was limited to candidate objects that shared similar surface properties and consequently looked similar upon illumination with the laser.

In more realistic application environments, possible candidate objects have *heterogeneous* optical properties. These could affect the elicited brain responses and lead to different ERP distributions across objects. In screen-based brain-computer interfaces (BCIs), such heterogeneous stimuli could be considered a—correctable—design flaw. In contrast, a high variance in surfaces and therefore stimuli is inherent to an in-the-scene highlighting approach and cannot be easily mitigated by modifying the experimental paradigm. Instead, it is desirable to address this problem from a machine-learning perspective.

One strategy is to treat each object—corresponding to a partition of the original classification task—as a separate subclass problem. A simple method would be to train separate classifiers for each subclass (e.g., object). However, as such a specialization entails reduced training data, it may be detrimental when applied to objects with similar optical properties. A more data-efficient treatment of subclass structure has been proposed by Höhne et al. (2016). While using traditional mean electrode potentials as ERP features, the authors proposed to regularize each subclass classifier toward other subclasses.

In this work, we address the problem of heterogeneous subclasses in the context of screen-free BCIs by training subclass-regularized classifiers in a Riemannian-geometry framework. Our contributions are threefold: First, we show that different object and stimulation properties lead to heterogeneous EEG responses in a screen-free BCI. Second, we propose to use subclass-regularized linear discriminant analysis (LDA) classifiers in a centered Riemannian tangent space to handle this heterogeneity. This can be viewed as a weighted incorporation of data from other subclasses. Third, we show on data from experiments with 19 participants observing homogeneous and heterogeneous stimuli that our approach improves classification performance compared to subclass-specific as well as subclass-agnostic classifiers while not deteriorating performance for non-relevant subclass information. Our improvements also hold for small amounts of training data.

This paper extends our earlier conference contribution (Kolkhorst et al., 2019b) in several ways: We corroborate the results of our earlier pilot study (which included 6 participants) on data from 19 participants. Additionally, we propose to center subclasses using parallel transport and regularize each classifier toward other objects rather than applying separate object-specific classifiers—allowing a more efficient use of data. We also provide a more comprehensive description of the approach and an extended discussion.

After reviewing related work in section 2, we describe our experimental paradigm—using a robot equipped with a laser pointer to elicit ERPs for candidate objects—in section 3.1. Subsequently, we explain our approach to handle subclass information in a Riemannian-geometry classification framework in section 3.2. After reporting results both regarding neurophysiology of responses and classification performance in section 4, we close with a discussion and conclusion in sections 5 and 6.

2. RELATED WORK

As non-invasive brain-computer interfaces promise to offer communication capabilities to users who cannot reliably

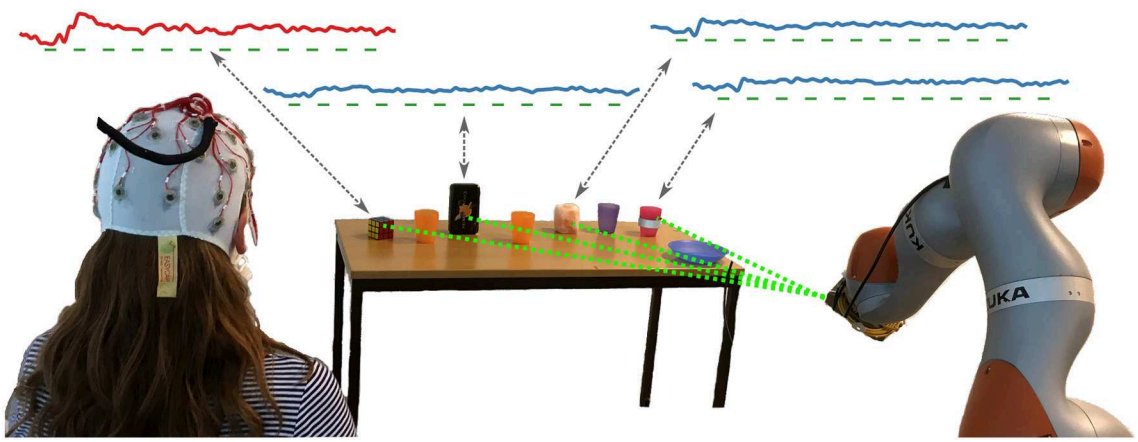

FIGURE 1 | Setup of our screen-free BCI: While the user attends to her goal object (the Rubik's cube in this example), the robot sequentially highlights candidates in the environment using a laser pointer mounted adjacent to the end effector. As depicted by the grand averages in the top, the EEG responses to the highlighting stimuli (marked by green bars) differ between the target object of the user (the Rubik's cube, red curve) and the other non-targets (blue curves). However, the optical properties cause dissimilar responses across objects for both classes. Our approach is able to robustly handle these differences in brain responses when predicting the user goal from the EEG response to each highlighting.

use other modalities, a wide range of command-and-control applications has been investigated. While multiple signal categories such as mental imagery can provide information, here we focus on experimental paradigms utilizing event-related potentials in response to a presented stimulus. Examples include spelling using visual (Sellers and Donchin, 2006; Hübner et al., 2017; Nagel and Spüler, 2019), auditory (Schreuder et al., 2010) or tactile (van der Waal et al., 2012) information and control of devices (Tangermann et al., 2009). In order to classify individual ERP responses, mean electrode potentials in suitable time intervals after the stimulus can be combined with linear classification methods (Blankertz et al., 2011). Recently, approaches based on deep learning (Schirrmeister et al., 2017; Behncke et al., 2018; Lawhern et al., 2018) or covariance representations leveraging Riemannian geometry (Barachant et al., 2013; Barachant and Congedo, 2014; Congedo et al., 2017) have gained popularity—both for ERPs and other signal classes—and can be considered state of the art.

Since the stimulus presentation is key for reliable analysis and classification of ERPs, consistent differences in presentation also affect the distribution of elicited ERPs. For example, variations in the target-to-target interval or habituation effects have been found to cause non-identically distributed ERP responses and affect classification performance (Citi et al., 2010; Hübner and Tangermann, 2017). These aspects can be viewed as *subclasses* of the data. Höhne et al. addressed the subclass structure in neuroimaging applications by training separate LDA classifiers for each subclass while regularizing them toward other subclasses using multi-target shrinkage (Bartz et al., 2014; Höhne et al., 2016). In principle, adapting subclass-specific classifiers to other subclasses can also be interpreted as a special case of transfer learning (e.g., Jayaram et al., 2016), which aims to improve performance by leveraging data from related tasks or datasets. In the context of Riemannian geometry (unsupervised), parallel transport of covariance matrices to a common point on the manifold (Zanini et al., 2018; Yair et al., 2019) as well as additional (supervised) geometric transformations (Rodrigues et al., 2019) have been proposed to reduce the differences in distributions between related datasets.

In the context of human-robot interaction—e.g., with service robots—the user should typically be able to deliver (high-level) commands to the robot (e.g., which object to fetch). Different modalities such as screens, speech (e.g., Shridhar and Hsu, 2018) or manually marking target objects using a laser pointer (Gualtieri et al., 2017) can be used to deliver these commands. However, impaired users might not be able to reliably control the robot using common modalities.

Brain signals as a feedback modality have also been used for command-and-control scenarios in robotics environments, e.g., to control wheelchairs or telepresence robots (Iturrate et al., 2009; Leeb et al., 2015), in fetch-and-carry tasks (Burget et al., 2017) or for grasp selection (Ying et al., 2018). These approaches typically use screens for stimulus presentation. While approaches based on mental imagery do not strictly require stimulus presentation, they would be limited in practice to only a small number of different commands in the absence of a mediating user interface.

A smaller number of publications utilized informative EEG signals from users who were passively observing a moving robot. Examples include the identification of erroneous actions (Salazar-Gomez et al., 2017; Behncke et al., 2018) or user preferences for robot motion (Iwane et al., 2019; Kolkhorst et al., 2019a). While this allows to infer user judgment of robotic actions, it requires the robot to first perform a candidate action (e.g., moving to the object with the highest prior probability). As goals of the user will often be outside of the robot's workspace, this strategy is typically more time-consuming than screen-based strategies. In addition, robotic motion is not instantaneous, which lowers the classification performance obtainable from event-locked evoked signals. Consequently, highlighting of objects with a laser pointer can be viewed as a combination of a natural user task with the ability to query many candidates and the precise stimulus timing known from traditional ERP paradigms.

3. MATERIALS AND METHODS

In this section, we describe our screen-free BCI setup with heterogeneous objects as well as the data collection process. Subsequently, we present the covariance-based classification pipeline and specifically our approach to subclass-regularized classification of ERP signals in the Riemannian tangent space.

3.1. Screen-Free Stimulus Presentation Using Highlighting in the Environment

The idea of our screen-free BCI is to keep the user's attention on the environment while presenting stimuli—eliciting informative event-related potentials that allow decoding of the user goal. In our setup, the stimuli are presented by highlighting candidate objects with a laser pointer, which results in a temporally precise onset and an—ideally—salient stimulus.

3.1.1. Experimental Setup for Robotic Object Selection

In order to highlight the candidate objects of the user, we used a KUKA iiwa robotic arm with a 1 mW green laser pointer mounted next to the end effector. As depicted in **Figure 1**, in our experiments the robot was positioned in front of a table with objects. Since robot movements are needed to orient the laser pointer to different objects, the robot highlighted the same object multiple times in a sequence lasting 3 s before switching to the next. For each highlighting, the laser pointer was turned on for 100 ms.

Highlighting poses for the robot were determined based on the positions of objects in the scene (in our ROS implementation, we expect a TF coordinate frame (Foote, 2013) for each object). In pilot experiments, we obtained these positions from a vision-based object detector and tracker (SimTrack, Pauwels and Kragic, 2015), which allows for the scene to change between different highlighting sequences. In the EEG experiments, we fixed object positions to reduce potential failures due to tracking errors. We obtained the desired robot configuration for highlighting an object based on the kinematics of the robot by minimizing required joint motion during the transition from the previous

highlighting configuration while requiring the beam direction of the laser pointer to intersect with the object's position.

As depicted in **Figure 1**, we used eight candidate objects as potential user goals: four *homogeneous* ones with similar surfaces (the same as in Kolkhorst et al., 2018), and four *heterogeneous* ones, for which we used everyday objects with differing optical surface properties. The different appearances of the highlightings with a laser pointer are depicted in **Figure 2**. The homogeneous objects (using obj. 1 as a representative) consisted of semi-transparent plastic, resulting in a salient spatially confined point. Despite varying shape, all homogeneous objects (three plastic cups and a plate; see **Figure 1**) resulted in similar stimulus intensities upon highlighting.

The heterogeneous objects caused different appearances of the laser upon illumination. Two objects (obj. 5 and obj. 6) induced large and salient points, whereas the laser points on obj. 7 and obj. 8 were less salient. Note that the materials and shapes of objects affected multiple optical properties. For example, obj. 5 (and, to a lesser degree, obj. 6) partially reflected the light, leading to an additional visible spot on the surface of the table. Although optical properties differed between objects, the effects (e.g., reflections) are not necessarily detrimental as they may increase stimulus salience. For an additional impression of the experiment setup and the appearance of stimuli, we refer the reader to the **Supplementary Video**.

We acquired the brain signals using a cap holding $N_c = 31$ Ag/AgCl gel-based passive EEG electrodes (EasyCap) positioned according to the extended 10–20 system (Chatrian et al., 1985, see **Figure S2**) with a nose reference. We kept channel impedances below 20 kΩ. The amplifier (Brain Products BrainAmp DC) sampled the EEG signals at 1 kHz.

3.1.2. Experiments and Datasets

In this work, we report results from experiments with 19 healthy participants. The recorded EEG data is publicly available (Kolkhorst et al., 2020). Following the Declaration of Helsinki, we received approval by the Ethics Committee of the University Medical Center Freiburg and obtained written informed consent from participants prior to the session.

Each experiment consisted of multiple trials, in which the user had a constant goal object and four candidate objects (either the homogeneous or the heterogeneous ones) were highlighted. Each trial consisted of three repetitions, where one repetition corresponds to highlighting each candidate object in turn with a 3 s stimulus sequence. A schematic overview of the experiment structure can be found in **Figure S1**. We performed online experiments, i.e., after each trial we provided visual feedback on the decoded target object of the user. For the online feedback, we used a classifier without subclass handling which was trained at the beginning of the experiment (see Kolkhorst et al., 2018 for details on the online setup).

We asked the participants to put themselves in the condition of a user of an assistive robotic arm and that they could decide which object the robot should fetch by *attending* the object. We instructed participants to attend the goal object throughout the trial. While we did not mandate it, we expect that most participants maintained visual focus on the goal (i.e., used overt attention). We asked participants to sit relaxed and to minimize eye movements during a trial. In order to support the performance evaluation, we determined the goal object according to the experimental protocol and gave it as a cue to the participant prior to the start of every trial.

To investigate the influence of different object types and show applicability to varying stimulus-onset asynchronies (SOAs, the time between the start of subsequent laser highlightings), we performed three series of experiments: In the first, sessions with 7 participants were each split equally into two conditions: In each trial, either the four heterogeneous objects were highlighted using an SOA of 250 ms (the corresponding data is subsequently denoted by HET1) or the homogeneous objects were highlighted, also with an SOA of 250 ms (denoted by HOM1). In the second series with 6 participants—which has previously been used in Kolkhorst et al. (2019b)—each session was split into trials with heterogeneous objects and 250 ms SOA (HET2), and trials with homogeneous objects and an SOA of 500 ms (HOM2). The third

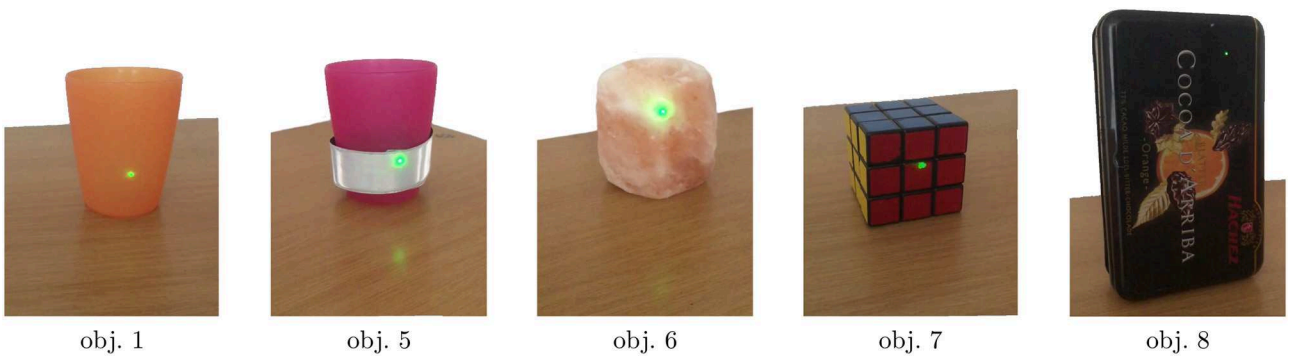

FIGURE 2 | Close-up photos of candidate objects during highlighting in our experiments. The differing optical properties cause dissimilar appearances (using identical laser pointer illumination). Object 1 is a representative of the homogeneous objects (see **Figure 1** for all objects), for which the highlighting appears similar. Objects 5 to 8 correspond to the heterogeneous objects. Note the reflection on the table surface for objects 5 and 6, and the low salience of the laser point at the top right of object 8.

series with 6 participants was originally described in Kolkhorst et al. (2018) and contains solely trials with the homogeneous objects and an SOA of 500 ms (HOM3). Hence, objects and stimulus parameters are identical between HET1 and HET2 as well as between HOM2 and HOM3. The SOAs affect the overlap between ERP responses to subsequent stimuli. Differences in SOA lead to variations in discriminability of individual stimuli, information transfer rate as well as usability (c.f., Höhne and Tangermann, 2012).

Each individual highlighting k can be associated with the target or non-target class $y(k) \in \{\mathrm{t}, \mathrm{nt}\}$. We investigated different definitions for subclasses of stimuli: The prime categorization is the mapping of stimuli to object instances $o(k) \in \{1, \ldots, 8\}$. Since we performed multiple sequential highlightings for a single object before moving to the next, we can also identify each highlighting with the position within the stimulus sequence $q(k) \in \{1, \ldots, 12\}$. As we expect most variation between the first and subsequent stimuli, stimulus positions can be aggregated to $\tilde{q}(k)$ with $\tilde{q}(k) = \mathit{initial}$ if $q(k) = 1$ and $\tilde{q}(k) = \mathit{subsequent}$ for $q(k) > 1$. For a more general notation, we use j to denote the index of a subclass (i.e., representing a value of either o, q or $\tilde{q}$ in this paradigm) and use N_{sub} for the number of subclasses (i.e., the number of unique values of j for a given subclass definition). The index set $\mathcal{K}_j$ denotes the indices of highlightings belonging to this subclass. The number of highlightings for each of the data subsets and for each subclass in the different experiment conditions can be found in **Table 1**.

3.2. EEG Decoding

Identifying the goal object of the user reduces to a binary classification problem on the EEG data: Since we know the highlighted object for each brain response, we want to decode whether the user attended the highlighted object (for which we expect a *target* response) or not (*non-target* response). Hence, the target object can be predicted by choosing the object for which the target scores of the corresponding highlightings are highest. **Figure 3** shows the overall processing pipeline for selecting the target from multiple candidates in the scene.

We use a classification pipeline based on Riemannian geometry: Covariances matrices of each time window are used as a signal representation, projected into the tangent space (TS) and classified using linear discriminant analysis (LDA). In order to handle heterogeneous subclasses in the data, we investigated three different classification approaches (as illustrated in **Figure 4**): The simplest way is to ignore subclass information and train classifiers on the pooled data (***TS+LDA***). Alternatively, specialized classifiers can be trained separately for each subclass (***sep. TS+LDA***). Third, we propose to perform subclass-specific centering and train specialized classifiers that are regularized toward other subclasses (***cTS+reg-LDA***), utilizing the full data.

3.2.1. Segmentation and Preprocessing

As depicted in **Figure 3**, we perform preprocessing steps before estimating covariances: We filter the continuous EEG to the range of 0.50 Hz to 16 Hz before downsampling to 100 Hz. For classification, we extract one time window $\boldsymbol{X}_k \in \mathbb{R}^{N_c \times N_t}$ of 1 s duration for each highlighting k, starting at the onset of the laser light ($N_t = 101$). To remove offsets, we subtract the mean activity of the preceding 200 ms. Note that most windows contain the response to multiple stimuli (four in the case of 250 ms SOA, two in the case of 500 ms). We reject windows in which the peak-to-peak amplitude exceeded 100 µV in any channel.

To capture the temporal course of the ERPs, we follow Barachant and Congedo (2014) and augment each window $\boldsymbol{X}_k$ with prototype responses. This leads to a block structure of the covariance that also captures temporal information: Aside from the covariance of the measured signal, two blocks correspond to the cross-covariance of the signal with the ERP prototypes, providing information on the phase difference of signal and prototypes. As prototypes, we use the Euclidean mean $\bar{\boldsymbol{X}}_i$ of responses for the target and non-target classes in the training data ($i \in \{\mathrm{t}, \mathrm{nt}\}$). To reduce dimensionality, we project the data based on spatial filtering components obtained from xDAWN decompositions (Rivet et al., 2009). We select two components per class corresponding to the largest eigenvalues, resulting in filter matrices $\boldsymbol{W}_i \in \mathbb{R}^{2 \times N_c}$. This leads to augmented windows

$$\tilde{\boldsymbol{X}}_k = \begin{pmatrix} \boldsymbol{W}_{\mathrm{t}} \bar{\boldsymbol{X}}_{\mathrm{t}} \\ \boldsymbol{W}_{\mathrm{nt}} \bar{\boldsymbol{X}}_{\mathrm{nt}} \\ \boldsymbol{W}_{\mathrm{t}} \boldsymbol{X}_k \\ \boldsymbol{W}_{\mathrm{nt}} \boldsymbol{X}_k \end{pmatrix} \in \mathbb{R}^{N_{c'} \times N_t} \tag{1}$$

with $N_{c'} = 8$ surrogate channels out of which the first four are the prototypes (these are constant across windows).

TABLE 1 | Dataset Characteristics: Number of participants and stimuli for the different datasets, grouped by subclass definition.

Subclass	**n/a**			**Obj (o)**			**Stim ($\tilde{q}$)**		
obj. type	**het**	**hom**		**het**	**hom**		**het**	**hom**	
SOA	**250 ms**	**250 ms**	**500 ms**	**250 ms**	**250 ms**	**500 ms**	**250 ms**	**250 ms**	**500 ms**
No. of participants	13	7	12	13	7	12	13	7	12
Targets/subclass	864	864	648	216;216;216;216	216;216;216;216	162;162;162;162	72;792	72;792	108;648
Non-targets/subclass	2,592	2,592	1,938	648;648;648;648	648;648;648;648	484;484;484;484	216;2,376	216;2,376	323;1,938

The group consisting of the first three columns (the subclass denoted by "n/a") corresponds to the complete data, while the other two groups correspond to the data when using objects ("obj", o) or stimulus position ("stim", $\tilde{q}$) as a subclass definition. The columns for heterogeneous objects with an SOA of 250 ms apply to datasets Het1 *and* Het2*, homogeneous objects with an SOA of 250 ms to* Hom1 *and the columns for homogeneous objects with an SOA of 500 ms to* Hom2 *and* Hom3*. The number of stimuli per subclass are separated by semicolons and correspond to a single experiment session. Note that the number of stimuli per subclass is uniform in the case of objects while it varies for the two subclasses based on $\tilde{q}$ ("stim").*

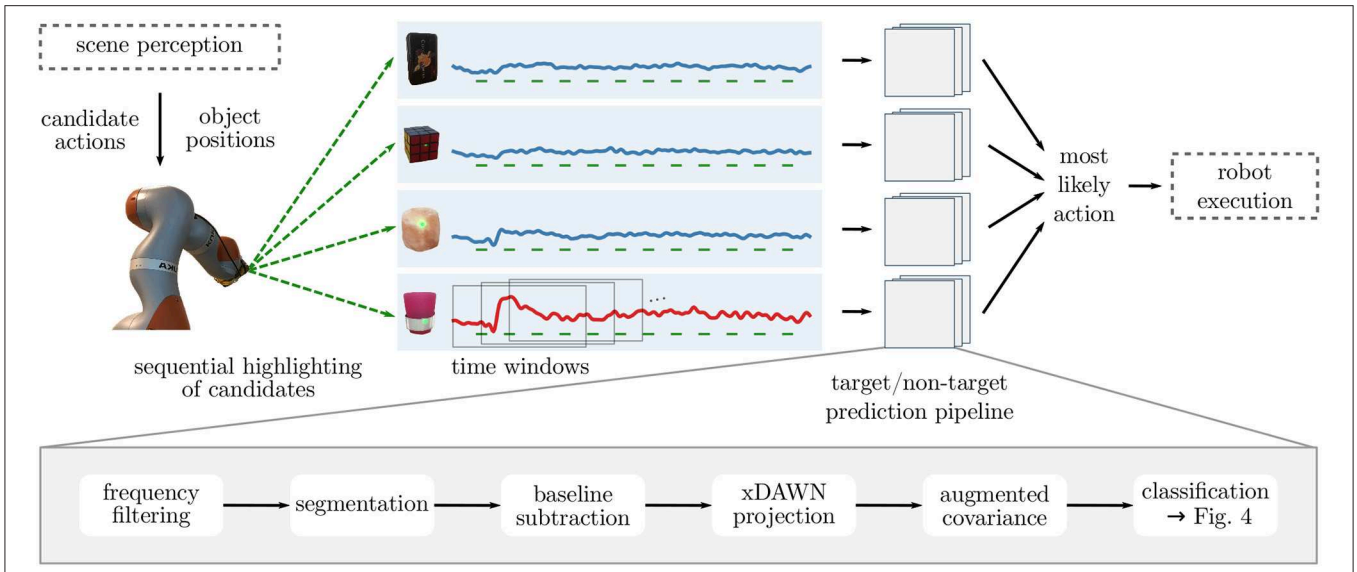

FIGURE 3 | Overall architecture of the screen-free BCI: In order to identify user intentions, candidate objects—corresponding to possible actions of the robot—are highlighted sequentially. Time windows aligned to each stimulus are preprocessed and their covariance representation is used for classification (see lower part of the figure and **Figure 4**). Based on the predicted probabilities that the user attended the object in a given time window (i.e., whether it was the target), the most likely candidate is identified and the appropriate action is taken. In a future application setting, we see this pipeline combined with scene perception and object manipulation (marked by dashed boxes). In this work, however, we fixed candidate objects and gave purely visual feedback on the decoded target object rather than executing a grasp.

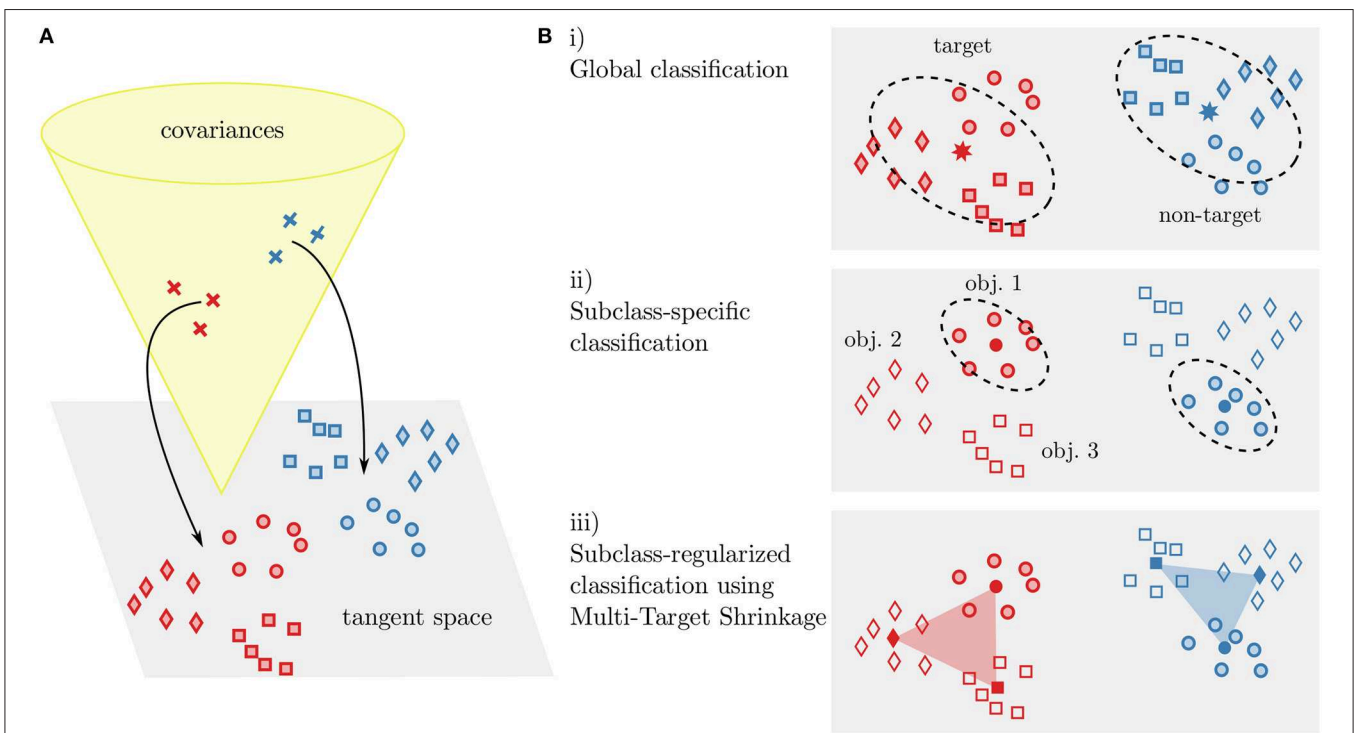

FIGURE 4 | Illustration of our covariance-based classification approaches. Covariances $\boldsymbol{C}_k \subset \mathcal{S}_{++}$ are projected into the Riemannian tangent space $\mathcal{T}_{\boldsymbol{C}^m}$ **(A)**. In the tangent space, classification is performed using linear discriminant analysis **(B)**. Either a single classifier is trained on the data (i, corresponding to *TS+LDA*), separate classifiers are trained for each subclass (ii, *sep. TS+LDA*), or the class means of subclass-specific classifiers are regularized toward other subclasses (iii, *cTS+reg-LDA*). This can be seen as a weighted inclusion of data from other subclasses. Note that for the latter case, we also perform centering by parallel transport of the members of each subclass in covariance space. In the figure, classes (target and non-targets) are indicated by color and subclasses (object instances) by different markers.

3.2.2. Covariance-Based Decoding Pipeline

In this section, we give a brief description of our Riemannian geometry-based classification pipeline. For more details and motivation, we refer the reader to Pennec et al. (2006), Congedo et al. (2017), and Yger et al. (2017). For each augmented time window $\tilde{\boldsymbol{X}}_k$ (i.e., each highlighting event), we calculate window-wise covariances $\boldsymbol{C}_i \in \mathcal{S}_{++}(N_{c'})$ that lie in the cone of $N_{c'} \times N_{c'}$ symmetric positive-definite matrices. Note that we regularize covariances using analytically determined shrinkage (Ledoit-Wolf). While Euclidean distances are ill-suited in $\mathcal{S}_{++}$ (c.f., Yger et al., 2017)—hindering the use of standard classification approaches—each element $\boldsymbol{C}^{\text{ref}}$ of the manifold can be associated with a tangent space $\mathcal{T}|_{\boldsymbol{C}^{\text{ref}}}$ at this point (Barachant et al., 2013).

Covariance matrices $\boldsymbol{C}$ are mapped to their tangent space representation $\boldsymbol{S}$ using $\text{Logm}_{\boldsymbol{C}^{\text{ref}}}(\boldsymbol{C}) = \text{logm}\left((\boldsymbol{C}^{\text{ref}})^{-1/2}\boldsymbol{C}(\boldsymbol{C}^{\text{ref}})^{-1/2}\right)$. Here logm denotes the matrix logarithm. The matrix logarithm and the square root of a matrix $\boldsymbol{C} \in \mathcal{S}_{++}$ can be calculated by applying the corresponding scalar operation to the elements of the diagonal matrix $\boldsymbol{\Lambda}$ obtained from the decomposition $\boldsymbol{C} = \boldsymbol{Q}\boldsymbol{\Lambda}\boldsymbol{Q}^T$. As a reference point, we use the Fréchet mean $\boldsymbol{C}^m$ of the training data with regard to the affine-invariant Riemannian metric (c.f., Congedo et al., 2017). The reverse operation—mapping from $\mathcal{T}|_{\boldsymbol{C}^{\text{ref}}}$ to $\mathcal{S}_{++}$—is denoted by $\text{Expm}_{\boldsymbol{C}^{\text{ref}}}$.

While not necessarily positive definite, tangent space matrices $\boldsymbol{S} \in \mathcal{S}(N_{c'})$ are symmetric and can hence be vectorized into $\mathbf{s} \in \mathbb{R}^{N_{c'}(N_{c'}-1)/2}$ (c.f., Barachant et al., 2013). In principle, an arbitrary classifier can be used in the tangent space. In this work, we choose linear discriminant analysis (LDA). Note that in preliminary tests we found LDA to yield a classification performance similar to logistic regression [which was used in Kolkhorst et al. (2018)]. The weight vector of an LDA is given by $\boldsymbol{w}_{\text{LDA}} = \boldsymbol{C}_{\text{LDA}}^{-1}(\boldsymbol{\mu}_{\text{t}} - \boldsymbol{\mu}_{\text{nt}})$ for class means $\boldsymbol{\mu}_{\text{t}}$, $\boldsymbol{\mu}_{\text{nt}}$ and the total within-class covariance matrix $\boldsymbol{C}_{\text{LDA}}$. This classification pipeline—training a single classifier on the training data—is denoted by *TS+LDA*.

3.2.3. Classifiers for Subclasses

In order to handle the heterogeneous subclasses in the data (primarily different objects), we explore the use of separate classifiers for each subclass. These can either be separate (using only data from a single subclass) or include regularization toward other subclasses (i.e., incorporating data from other subclasses).

As a first approach, we train separate subclass-specific classifiers (similar to Kolkhorst et al., 2019b). We apply the same classification approach as described above, but only on the data $\{\boldsymbol{X}_k \mid k \in \mathcal{K}_j\}$ of the corresponding subclass j. The Fréchet mean $\boldsymbol{C}_j^m$ of the covariances belonging to j is used as the reference point for the tangent space projection of each subclass. Similarly, LDA classifiers are trained separately, leading to N_{sub} classifiers per participant. This classification pipeline is denoted by *sep. TS+LDA*.

3.2.3.1. Subclass-regularized LDA

As a second way to leverage the subclass information, we adapt the regularization approach proposed by Höhne et al. (2016) (denoted by RSLDA in their paper): Rather than calculating the class means $\boldsymbol{\mu}_{\text{t}}, \boldsymbol{\mu}_{\text{nt}}$ for the LDA classifier of subclass j only on the subset of the data corresponding to $\mathcal{K}_j$, data from other subclasses $j' \neq j$ is also used by calculating a weighted class mean.

This can be formalized as multi-target shrinkage of the mean (MTS, Bartz et al., 2014; Höhne et al., 2016): For the classifier of subclass j, the shrunk mean of class i can be obtained by a convex combination of the corresponding class's means on all subclasses.

$$\boldsymbol{\mu}_{i,j}^{MTS}(\boldsymbol{\alpha}) = \left(1 - \sum_{j' \neq j} \alpha_{j'}\right) \boldsymbol{\mu}_{i,j} + \sum_{j' \neq j} \alpha_{j'} \boldsymbol{\mu}_{i,j'} \tag{2}$$

Here, $\boldsymbol{\mu}_{i,j} = \sum_{\{k \in \mathcal{K}_j | y(k)=i\}} \mathbf{s}_k$ corresponds to the mean of the vectorized tangent space representations of the given class and subclass. The coefficients $\boldsymbol{\alpha}$ can be obtained by minimizing the expected mean square error, leading to a quadratic program based on the variance and bias of the different means. Intuitively, weights for other subclasses j' should be small if distances between subclass means are large or if there is a high variance in the samples of j' for the given class. For details, we refer the reader to Bartz et al. (2014) and Höhne et al. (2016).

3.2.3.2. Parallel transport of subclasses

In order to regularize $\boldsymbol{\mu}_{i,j}$ toward the class mean of another subclass $\boldsymbol{\mu}_{i,j'}$, both should be located in the same tangent space. However, in the case of separate subclass classifiers, the reference points would also differ: The first class mean would be located in $\mathcal{T}|_{\boldsymbol{C}_j^m}$, while the second would be in $\mathcal{T}|_{\boldsymbol{C}_{j'}^m}$. One possibility to address this would be to map the mean tangent vectors back into the manifold $\mathcal{S}_{++}$ before projecting them in the correct tangent space:

$$\boldsymbol{\mu}_{i,j}^{MTS}(\boldsymbol{\alpha}) = \left(1 - \sum_{j' \neq j} \alpha_{j'}\right) \boldsymbol{\mu}_{i,j} + \sum_{j' \neq j} \alpha_{j'} \, \text{Logm}_{\boldsymbol{C}_j^m} \text{Expm}_{\boldsymbol{C}_{j'}^m} \boldsymbol{\mu}_{i,j'} \tag{3}$$

As an alternative, we center each subclass using parallel transport on $\mathcal{S}_{++}$ before tangent space projection, which has previously been proposed in the context of transfer learning (c.f., Zanini et al., 2018; Yair et al., 2019): A symmetric positive definite matrix (e.g., of subclass j) can be transported along the geodesic from $\boldsymbol{C}_j^m$ to the identity using $\Gamma_{\boldsymbol{C}_j^m \to \boldsymbol{I}}(\boldsymbol{C}) = (\boldsymbol{C}_j^m)^{-1/2}\,\boldsymbol{C}\,(\boldsymbol{C}_j^m)^{-1/2}$. Afterwards, $\boldsymbol{C}_j^m = \boldsymbol{I}$ for all subclasses j and the matrix logarithm and matrix exponential in Equation 3 cancel since all means are located in the same tangent space. Hence, Equation 3 reduces again to Equation 2. We denote the resulting classification pipeline—consisting of centering subclasses using parallel transport combined with subclass-regularized LDA classifiers—with *cTS+reg-LDA*.

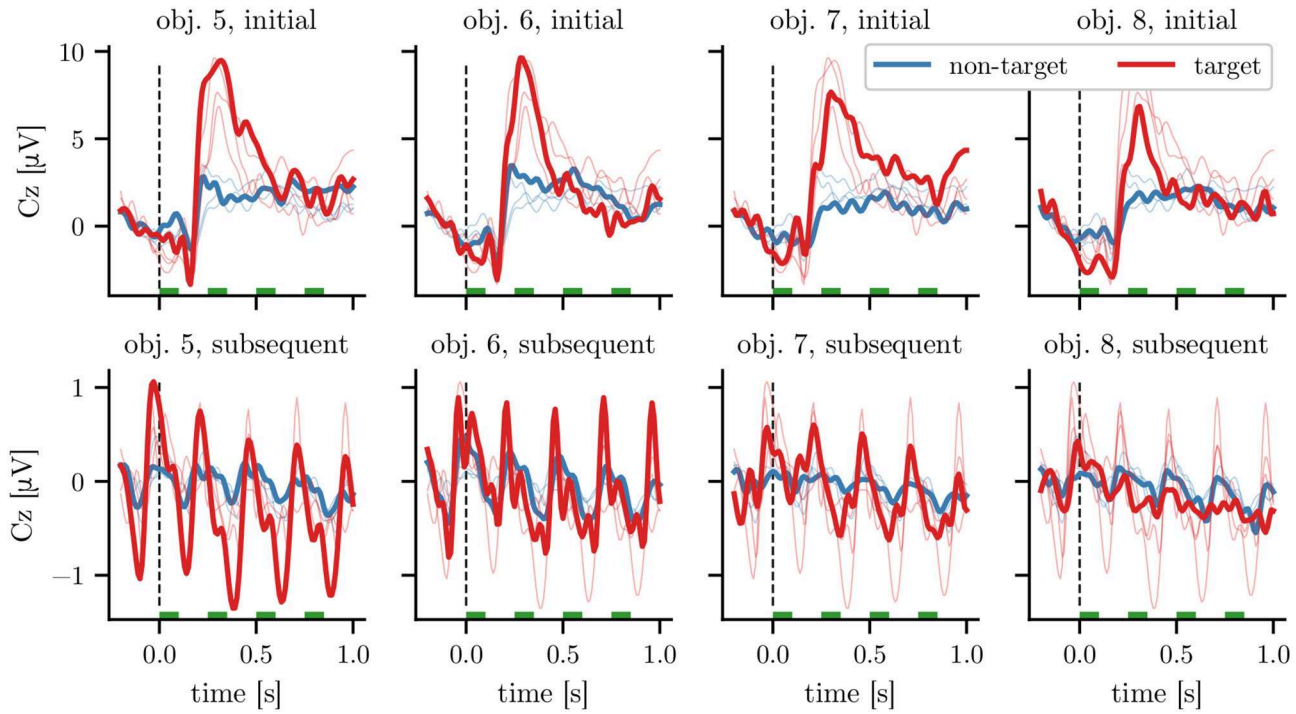

FIGURE 5 | Grand average responses at electrode Cz for heterogeneous objects. Each column corresponds to the responses to the highlighting of a single object. The top row depicts the response to the initial stimulus of a 3 s stimulation sequence, while the bottom row depicts the average response to the 11 subsequent ones (see **Figure 1** for averages over the full stimulation sequence). Time 0 corresponds to the onset of highlighting, with all stimulation intervals marked with green bars. For ease of comparison, the averages for other objects of the same row are shown with thin lines. The averages are calculated on the combined data of the 13 participants of datasets HET1 and HET2 using an SOA of 250 ms. The target (non-target) averages are calculated based on 234 (702) and 2,574 (7,722) time windows for the plots in the top and bottom row, respectively (before artifact rejection).

An overview of all classification approaches can be found in **Figure 4**.

3.2.4. Evaluation

For each participant, classifiers were trained and tested in a five-fold chronological cross-validation. In order to evaluate the influence of data set size, we also report results on 33 % of the data (we used the first of three repetitions in each trial). Note that due to the interleaved design, data for both different objects and dataset sizes is temporally balanced within each experiment session. We evaluated the classification performance using the area under the receiver operating characteristic (AUC). The decoding pipeline was implemented in Python, building upon MNE-Python (Gramfort et al., 2013), scikit-learn (Pedregosa et al., 2011) and pyRiemann (Barachant and Congedo, 2014).

4. RESULTS

In this section, we report participants' feedback on the paradigm before describing the influence of subclasses—different objects and position in stimulation sequence—on the elicited ERPs. Subsequently, we report classification performances for the different proposed subclass handling strategies.

4.1. Behavioral Feedback From Participants

In order to get insight into the feasibility and usability of the screen-free approach from a user perspective, we gathered feedback from participants in post-session questionnaires. Participants reported that the task induced a low stress level (24 ± 19 on a visual analog scale from "relaxed," which is represented by 0, to "stressed," represented by 100) and required low mental demand (24 ± 16 on a scale from "easy" to "demanding"). While answers reveal medium required effort (46 ± 25 on a scale from "few" to "much"), verbal feedback from participants indicated that this was influenced by our instruction to avoid blinking. Overall, participants were satisfied with their task performance (76 ± 19 on a scale from "unsatisfied" to "satisfied"). Answers of individual participants can be found in **Figure S3**.

4.2. Grand Average Responses to Laser Highlighting

The highlighting of objects with a laser pointer elicited various event-related potentials (ERPs) starting approximately 100 ms after stimulus onset. Similar to common screen-based visual ERP paradigms, responses appear to be a combination of early sensory and later cognitive components (c.f., Blankertz et al.,

TABLE 2 | Performance of the different classification approaches on the evaluated datasets.

	Obj. type	het		hom			
	SOA	250 ms		250 ms		500 ms	
	data size	33%	100%	33%	100%	33%	100%
Subclass	classifier						
n/a	TS+LDA	0.79 ± 0.09	0.82 ± 0.07	0.88 ± 0.07	0.91 ± 0.06	0.79 ± 0.10	0.84 ± 0.07
Obj (o)	sep. TS+LDA	0.76 ± 0.08	0.83 ± 0.06	0.80 ± 0.11	0.89 ± 0.07	0.71 ± 0.09	0.80 ± 0.08
	cTS+reg-LDA	**0.82 ± 0.08**	**0.86 ± 0.05**	**0.89 ± 0.06**	**0.92 ± 0.05**	0.79 ± 0.10	**0.85 ± 0.07**
Stim ($\tilde{q}$)	sep. TS+LDA	0.78 ± 0.08	0.82 ± 0.07	0.87 ± 0.07	0.91 ± 0.05	0.78 ± 0.09	0.84 ± 0.06
	cTS+reg-LDA	0.79 ± 0.09	0.82 ± 0.07	0.88 ± 0.07	0.92 ± 0.06	**0.80 ± 0.10**	0.85 ± 0.07

*Rows correspond to different classifiers, trained on the given subclass definition ("n/a" corresponds to training a single subclass-agnostic classifier). Columns correspond to the different datasets (see **Table 1** for the sample counts using 100 % of the data). Performance is reported as the mean and standard deviation of the area under the receiver operating characteristic (AUC, higher is better). For each dataset, the bold AUC values highlight the classifier with the best performance.*

2011). Class-discriminative differences between target and non-target responses could be observed from approximately 200 ms after the onset of highlighting.

Looking separately at the grand average ERPs for different objects and stimulus positions within the sequence on the combined data of HET1 and HET2 as depicted in **Figure 5**, we can observe *heterogeneous responses* to these different subclasses: First, the initial highlighting of each sequence (depicted in the top row) resulted in an ERP with a higher amplitude—specifically around 300 ms, which is in line with the expected P300 response for target stimuli—than subsequent highlightings (bottom row; note the different axis limits). Second, we find that the ERPs differed between the four heterogeneous objects, both in amplitude and waveform. For example, amplitudes of both target and non-target ERPs for obj. 7 and obj. 8 were smaller than for the other objects. We observed, that latencies for obj. 8 varied stronger between participants than for other objects (data not shown). In contrast, differences in waveform between objects were smaller for the homogeneous objects in HOM1, HOM2, and HOM3, while the amplitude differences between the responses corresponding to first and subsequent stimuli are consistent with the differences for heterogeneous ones. The corresponding grand average plots for dataset HOM1 can be found in **Figure S4**.

4.3. Classification Results

Next, we investigate the classification performance on individual time windows corresponding to a single highlighting event. After comparing the subclass-agnostic classification performance (*TS+LDA*) on different object types, we report results on using separate subclass-specific classifiers (*sep. TS+LDA*) and the proposed subclass-regularized classifiers (*cTS+reg-LDA*).

First, we investigate how the difference between homogeneous and heterogeneous objects translates into classification performance. For this, the data of the 7 participants in datasets HET1 and HOM1 is well-suited, since they observed both heterogeneous and homogeneous objects with an SOA of 250 ms. We find that classification using the *TS+LDA* pipeline (i.e., disregarding subclass information) worked well for all participants and would be adequate for control. Yet on the time windows corresponding to heterogeneous objects, this pipeline achieved an AUC of 0.82 compared to 0.91 for homogeneous objects. This shows that the heterogeneity of objects described in the previous subsection also translates into reduced classification performance (see **Table 2** for results on the different data subsets).

Using separate classifiers (*sep. TS+LDA*) for every object o to handle the heterogeneity, we observe improvements when ample training data is available: As depicted in **Figure 6A**, AUC performance on HET1 and HET2 (13 participants) improved slightly to 0.83 compared to 0.82 for the object-agnostic classifier when training on 100 % of the data. However, these improvements vanished if not enough (subclass-specific) training data was available: Using only 33 % of the data, performance dropped to 0.76 for separate subclass-specific classifiers compared to 0.79 for the subclass-agnostic classification. This reflects the smaller amount of training data (c.f., **Table 1**).

Using the proposed subclass-regularized classifiers in a centered tangent space (*cTS+reg-LDA*), we can observe improved performance over the baseline classifiers in the presence of heterogeneous objects: As the regularization takes into account information of other subclasses (i.e., objects o), *cTS+reg-LDA* resulted in gains over *TS+LDA* on the reduced data (mean AUC of 0.82 vs. 0.79) and the full data (0.86 vs. 0.82, a stronger improvement than *sep. TS+LDA*). Equally important, the proposed approach is also applicable to data where we do not expect a strong subclass structure: As depicted in **Figure 6**, when training subclass-regularized object classifiers on the full data of homogeneous objects, the proposed approach achieved a mean AUC of 0.87 and slightly outperformed *TS+LDA*, whereas training separate classifiers resulted in a drop to 0.83.

Using the stimulus positions $\tilde{q}$ as subclasses resulted in smaller effects: For *sep. TS+LDA*, we observed performance similar to a global classifier on the full data and a small deterioration on 33 % of the data. On the other hand, *cTS+reg-LDA* performed better or on the same level as *TS+LDA* when using the stimulus position ($\tilde{q}$) as subclasses. Detailed results for the separate subclasses and datasets can be found in **Table 2**.

Examining individual participants (as depicted in panel B of **Figure 6**), classification results using *cTS+reg-LDA* with

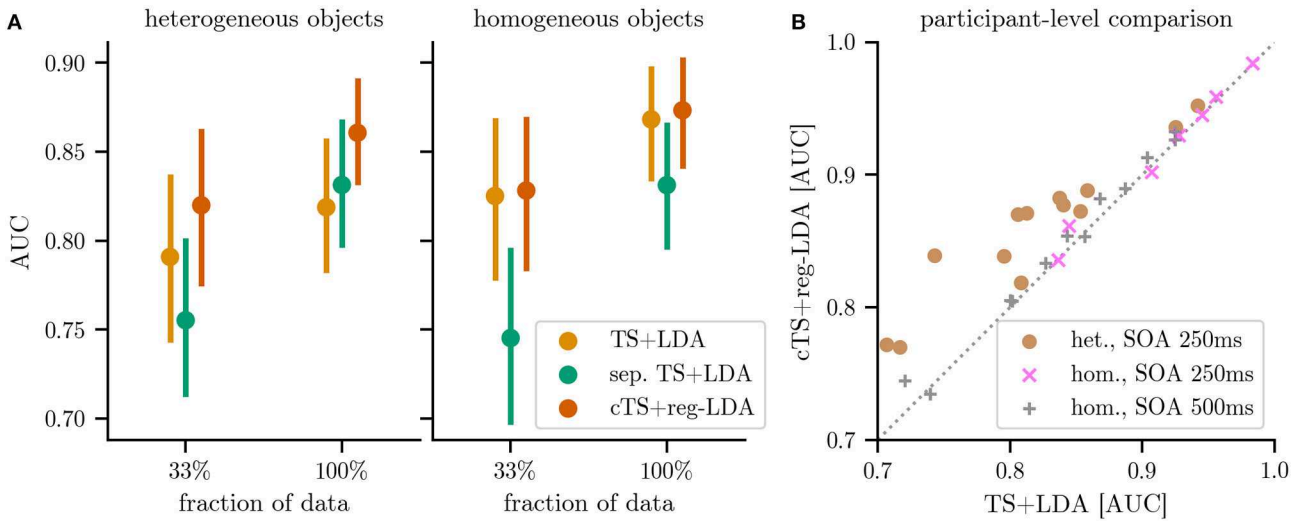

FIGURE 6 | Performance of the different classification pipelines for classifying individual responses: Riemannian tangent space classification ignoring subclass information (*TS+LDA*), separate tangent space classifiers for each subclass (*sep. TS+LDA*) and the proposed separate subclass-regularized classifiers in centered tangent spaces (*cTS+reg-LDA*). For the latter two approaches, each object corresponds to a separate subclass. **(A)** shows the results for heterogeneous objects (combining the 13 participants of datasets HET1 and HET2) and for homogeneous objects (combining the 19 participants of datasets HOM1, HOM2, and HOM3). **(B)** plot compares the performance of *cTS+reg-LDA* and *TS+LDA* on the level of individual participants (colors indicate differing object types and SOA). Markers above the diagonal indicate that the proposed *cTS+reg-LDA* outperforms *TS+LDA*. Results are reported using the area under the receiver operating characteristic (AUC, higher is better) and error bars correspond to bootstrapped 95 % confidence intervals. Detailed results can be found in **Table 2**.

objects as subclasses were better than the ones using *TS+LDA* for all 13 participants in the case of heterogeneous objects (HET1 and HET2) as well as for 14 of 19 participants in the case of homogeneous objects (HOM1, HOM2, and HOM3). For heterogeneous objects, the proposed approach resulted in a median absolute improvement in AUC of 0.04 across participants (minimal and maximal improvements of 0.01 and 0.10, respectively). To test the significance of differences in AUC between *cTS+reg-LDA* and *TS+LDA* in the presence of different object types and SOAs, we used a two-sided Wilcoxon signed-rank test at significance level $\alpha = 0.05$ with a conservative Holm-Bonferroni correction. We can reject the null hypothesis both for heterogeneous objects with an SOA of 250 ms (adjusted $p = 0.004$) and—interestingly—also for homogeneous objects with an SOA of 500 ms ($p = 0.030$). We could not reject it for the 7 participants in the setting with homogeneous objects and an SOA of 250 ms ($p = 0.398$). As expected, effect sizes are larger in the presence of heterogeneous objects than for homogeneous ones (c.f., **Figure 6**).

The weights $\boldsymbol{\alpha}$ of the subclass regularization allow introspection into the classification: As depicted in **Figure 7**, the weights for heterogeneous objects show a clear block structure, with obj. 5 and obj. 6 as well as obj. 7 and obj. 8 being regularized to each other—reflecting similarities in the optical properties (c.f., **Figure 2**) and average responses (c.f., **Figure 5**). The classifier means for the non-target class were regularized more than the target ones. Regularization toward other subclasses was stronger when only 33 % of data was available. When applying *cTS+reg-LDA* to homogeneous objects, we also observed larger weights for other subclasses, indicating a smaller influence of the subclass structure on the classifier means (c.f., **Figure S5**).

5. DISCUSSION

Building a screen-free BCI for robotic object selection by highlighting objects in the environment removes a level of indirection for the user. However, this benefit in terms of usability comes at the price of reduced stimulus homogeneity: When optical properties across candidate objects vary—as frequently encountered in real-world environments—the differences in appearance of the laser highlighting result in different feature distributions. While this can partly be attributed to a varying salience of stimuli, it is hard to mitigate by modifying the experimental design since we do not want to constrain or exchange the objects. In principle the laser parameters could be automatically adapted to different surfaces, yet this would pose a substantial challenge in practice. Whereas vision-based approaches can model optical properties such as the diffuse reflectance of surfaces (e.g., Krawez et al., 2018), we encountered combinations of translucency as well as diffuse and specular reflections.

Hence, we decided to approach this problem from a machine-learning perspective by modeling object instances as subclasses and training separate subclass-regularized classifiers that combine data from different subclasses in a weighted manner. We achieved strong performance gains by combining multi-target shrinkage of the mean (as proposed in Höhne et al., 2016) with both subclass-specific centering using parallel

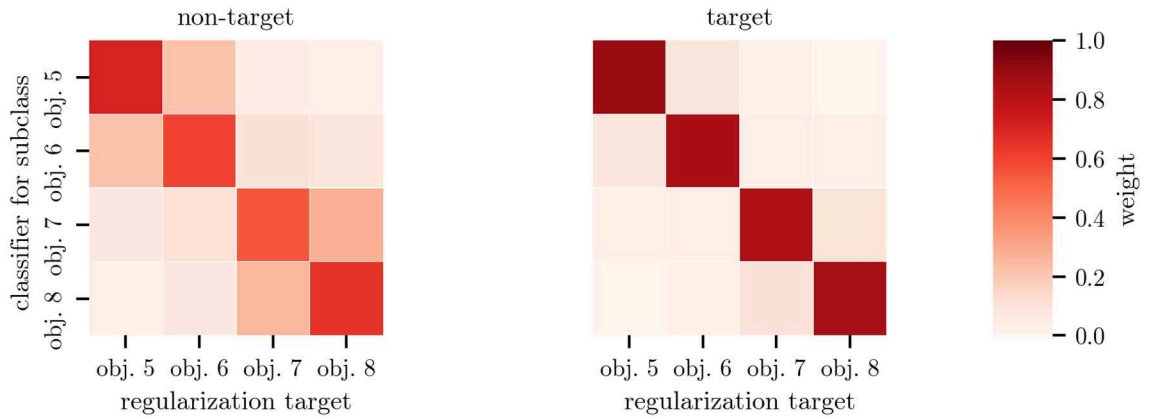

FIGURE 7 | Mean regularization weights α for heterogeneous objects. Each row corresponds to the weights of a single subclass-specific classifier. On the left, regularization weights for the mean of the non-target class are shown whereas the corresponding weights for the target class are shown on the right. Entries can be viewed as sample weights of the data of the corresponding subclass. Note the object similarities indicated by the block structure in this figure compared to the stimulus appearances in **Figure 2**. The weights have been averaged across all participants of datasets HET1and HET2 with classifiers trained on 100 % of the data.

transport and the state-of-the-art performance of covariance-based Riemannian tangent space classifiers. Our approach is applicable to arbitrary subclasses and experimental paradigms. Note that the information about subclasses (e.g., objects) is readily available at test time. We found that the proposed pipeline significantly outperformed the baseline in the case of relevant subclasses, while being robust to irrelevant subclasses. Notably, we could observe smaller performance gains even when distributions do not substantially differ between subclasses (e.g., homogeneous objects). Performance did not deteriorate in the presence of a large amount of subclasses (e.g., for every position q in the stimulus sequence, data not shown). The effect sizes—gains of three or more points in AUC compared to ignoring the subclass information—were substantial and are relevant in practical applications. Introspection of the learned regularization weights (**Figure 7**) as a measure of subclass similarity mirrors the differences in visual appearance of the highlighting (**Figure 2**). While ERP amplitudes differed based on the position of a stimulus in the sequence (initial vs. subsequent), using this as a subclass resulted in smaller improvements in classification performance. This indicates that the Riemannian classification pipeline may be more robust to changes in amplitude rather than ERP waveform.

Exploring possible alternative classification approaches, in additional experiments (data not shown), we found the proposed specialized (i.e., subclass-regularized) classifiers to achieve higher classification performance than using subclass-specific normalization with a global classifier: While we found that subclass-specific centering of covariance matrices using parallel transport already improved classification, performance was lower than using our proposed approach (especially with sufficient training data). While additional geometric transformations [such as rotation to another subset of the data as proposed by Rodrigues et al. (2019)] could in principle be an alternative to the convex combination of subclass means, we observed reduced performance on our data. Applying subclass-regularized LDA on features based on mean electrode potentials in suitable time intervals (as reported in Höhne et al., 2016; results not shown) performed consistently worse than using Riemannian tangent space features (which matches the results in Kolkhorst et al., 2018).

A limitation of our current approach is the assumption that we have observed all subclasses in the training data. While this would likely not hold in practice, the subclass of a novel object could be assigned either based on visual similarity to known objects or using proximity of EEG signals in covariance space. Generally, it could be useful to use clusters of objects with similar optical properties as subclasses in the presence of a large number of objects. While we performed the analyses in this paper in an offline manner, the approach is applicable online. Compared to the subclass-agnostic classifiers during the online experiments (c.f., Kolkhorst et al., 2018), the additional computational burden of centering matrices is small, hence we are confident that results would translate to an online application.

The use of screen-free stimuli is not limited to specific stimulation parameters. In this work, we opted for stimulation aimed at eliciting ERPs as different candidate objects were highlighted sequentially rather than in parallel. The two representative SOAs in our experiments indicated robustness to different stimulus parameters. It would also be interesting to evaluate parallel screen-free stimuli with a higher frequency—more closely resembling broadband (Thielen et al., 2015) or steady-state (e.g., Chen et al., 2015) visual evoked potentials—as it is likely that different optical properties would also induce heterogeneous responses in such a setting. In this work, we used a constant stimulation sequence length for simplicity, yet information transfer rate could be increased by committing to a goal once a required confidence has been reached (i.e., dynamic stopping), which would also increase robustness to non-control states (Schreuder et al., 2013; Nagel and Spüler, 2019).

The proposed *cTS+reg-LDA* classification approach is also applicable outside of our screen-free BCI setting. While here the problem of non-identically distributed ERP responses induced by subclasses is especially relevant, subclasses are also frequently

encountered in traditional, screen-based visual or auditory stimulus presentation. For example, varying locations of stimuli or different target-to-target intervals can also lead to dissimilar subclasses (c.f., Höhne et al., 2016; Hübner and Tangermann, 2017). Furthermore, the small improvements of our approach on homogeneous objects indicate that subclass information can be helpful even when no differences between subclasses are expected. Based on the found robustness it can be applied without risking a decline in classification performance.

Considering screen-free stimulus presentation in general, we view it as a building block that can be integrated into assistive human–robot interaction scenarios. Given that a robot is available to assist the user, it can also be used to present stimuli corresponding to possible assistive actions. As examples, it can be adapted to arbitrary goals that are related to spatial locations (e.g., where to place objects or how to avoid an obstacle) or it could be used for interactive teaching of the robot (e.g., where to grasp an object). Illuminating objects with a robot makes screen-free stimuli feasible in a changing environment with novel objects, as opposed to using active light sources on candidates. Combining the screen-free BCI with computer vision and manipulation modules (c.f., **Figure 3**), we envision that candidate (manipulation) actions are determined based on detected object affordances or anticipated user commands in a scene (e.g., Kaiser et al., 2016; Koppula and Saxena, 2016). As actions can be translated to appropriate highlightings of the corresponding objects, our BCI paradigm can then be used to choose between the candidates. Consequently, a screen-free BCI can be seen as a disambiguation module giving users direct control in a shared-autonomy setting.

6. CONCLUSION

In this work, we presented a screen-free brain-computer interface for an object selection task that allows robust decoding of user goals. Using the robot to present stimuli by highlighting objects in the environment with a laser pointer avoids the indirection of a graphical user interface but results in heterogeneous responses to objects in realistic environments. Our approach addresses this by training specialized classifiers for the object subclasses that are regularized based on the data of other objects.

In extensive experiments with 19 participants, we show that different optical properties of candidate objects induced distinct distributions of the corresponding brain responses. We find that our approach significantly improved classification performance in the presence of heterogeneous objects while not deteriorating in the presence of homogeneous ones. This increased robustness enables the application of screen-free BCIs in more diverse environments.

For future work, it would be interesting to also incorporate vision-based information on stimulus similarity for novel objects as well as increase communication bandwidth and applicability by using dynamic stimulus sequences and hierarchical goal selection.

DATA AVAILABILITY STATEMENT

The dataset recorded for this study (Freiburg Screen-free BCI for Robotic Object Selection: EEG Dataset) is publicly available at http://dx.doi.org/10.17605/OSF.IO/JZS7D.

ETHICS STATEMENT

The studies involving human participants were reviewed and approved by the Ethics Committee of the University Medical Center Freiburg. The participants provided their written informed consent prior to participating in this study.

AUTHOR CONTRIBUTIONS

HK and MT contributed conception and design of the study. WB and MT acquired funding. HK and JV performed the EEG experiments, implemented software, and performed the analyses. HK wrote the original draft. JV, WB, and MT reviewed and edited the draft.

FUNDING

This work was (partly) supported by BrainLinks-BrainTools, Cluster of Excellence funded by the German Research Foundation (DFG, grant number EXC 1086). Additional support was received from the German Federal Ministry of Education and Research (BMBF) under contract number 01IS18040B-OML, the DFG under INST 39/963-1 FUGG as well as the Ministry of Science, Research and the Arts of Baden-Württemberg for bwHPC. The article processing charge was funded by the DFG and the University of Freiburg in the funding program Open Access Publishing.

ACKNOWLEDGMENTS

The authors would like to thank all participants of the study, as well as Robin Burchard for help on the robotic setup, Eric Wolters for evaluating extensions to the highlighting hardware, and Andreas Eitel for providing comments on the initial draft.

SUPPLEMENTARY MATERIAL

The Supplementary Material for this article can be found online at: https://www.frontiersin.org/articles/10.3389/frobt.2020.00038/full#supplementary-material

REFERENCES

Barachant, A., Bonnet, S., Congedo, M., and Jutten, C. (2013). Classification of covariance matrices using a Riemannian-based kernel for BCI applications. *Neurocomputing* 112, 172–178. doi: 10.1016/j.neucom.2012.12.039

Barachant, A., and Congedo, M. (2014). A Plug&Play P300 BCI using information geometry. *arXiv:1409.0107*.

Bartz, D., Höhne, J., and Müller, K.-R. (2014). Multi-target shrinkage. *arXiv: 1412.2041*.

Behncke, J., Schirrmeister, R. T., Burgard, W., and Ball, T. (2018). "The signature of robot action success in EEG signals of a human observer: decoding and visualization using deep convolutional neural networks," in *2018 6th International Conference on Brain-Computer Interface (BCI)* (Gangwon), 1–6. doi: 10.1109/IWW-BCI.2018.8311531

Blankertz, B., Lemm, S., Treder, M., Haufe, S., and Müller, K.-R. (2011). Single-trial analysis and classification of ERP components —A tutorial. *NeuroImage* 56, 814–825. doi: 10.1016/j.neuroimage.2010.06.048

Burget, F., Fiederer, L. D. J., Kuhner, D., Völker, M., Aldinger, J., Schirrmeister, R. T., et al. (2017). "Acting thoughts: towards a mobile robotic service assistant for users with limited communication skills," in *2017 European Conference on Mobile Robots (ECMR)* (Paris), 1–6. doi: 10.1109/ECMR.2017.8098658

Chatrian, G. E., Lettich, E., and Nelson, P. L. (1985). Ten percent electrode system for topographic studies of spontaneous and evoked EEG activities. *Am. J. EEG Technol.* 25, 83–92. doi: 10.1080/00029238.1985.11080163

Chen, X., Wang, Y., Nakanishi, M., Gao, X., Jung, T.-P., and Gao, S. (2015). High-speed spelling with a noninvasive brain–computer interface. *Proc. Natl. Acad. Sci. U.S.A.* 112, E6058–E6067. doi: 10.1073/pnas.1508080112

Citi, L., Poli, R., and Cinel, C. (2010). Documenting, modelling and exploiting P300 amplitude changes due to variable target delays in Donchin's speller. *J. Neural Eng.* 7:056006. doi: 10.1088/1741-2560/7/5/056006

Congedo, M., Barachant, A., and Bhatia, R. (2017). Riemannian geometry for EEG-based brain-computer interfaces; a primer and a review. *Brain Comput. Interf.* 4, 155–174. doi: 10.1080/2326263X.2017.1297192

Foote, T. (2013). "Tf: the transform library, in *2013 IEEE Conference on Technologies for Practical Robot Applications (TePRA)* (Woburn, MA), 1–6. doi: 10.1109/TePRA.2013.6556373

Gramfort, A., Luessi, M., Larson, E., Engemann, D. A., Strohmeier, D., Brodbeck, C., et al. (2013). MEG and EEG data analysis with MNE-Python. *Front. Neurosci.* 7:267. doi: 10.3389/fnins.2013.00267

Gualtieri, M., Kuczynski, J., Shultz, A. M., Ten Pas, A., Platt, R., and Yanco, H. (2017). "Open world assistive grasping using laser selection, in *2017 IEEE International Conference on Robotics and Automation (ICRA)* (Singapore), 4052–4057. doi: 10.1109/ICRA.2017.7989465

Höhne, J., Bartz, D., Hebart, M. N., Müller, K.-R., and Blankertz, B. (2016). Analyzing neuroimaging data with subclasses: a shrinkage approach. *NeuroImage* 124, 740–751. doi: 10.1016/j.neuroimage.2015.09.031

Höhne, J., and Tangermann, M. (2012). "How stimulation speed affects event-related potentials and BCI performance, in *2012 Annual International Conference of the IEEE Engineering in Medicine and Biology Society* (San Diego, CA), 1802–1805. doi: 10.1109/EMBC.2012.6346300

Hübner, D., and Tangermann, M. (2017). "Challenging the assumption that auditory event-related potentials are independent and identically distributed, in *Proceedings of the 7th Graz Brain-Computer Interface Conference 2017* (Graz), 192–197.

Hübner, D., Verhoeven, T., Schmid, K., Müller, K.-R., Tangermann, M., and Kindermans, P.-J. (2017). Learning from label proportions in brain-computer interfaces: online unsupervised learning with guarantees. *PLoS ONE* 12:e0175856. doi: 10.1371/journal.pone.0175856

Iturrate, I., Antelis, J., Kübler, A., and Minguez, J. (2009). A noninvasive brain-actuated wheelchair based on a P300 neurophysiological protocol and automated navigation. *IEEE Trans. Robot.* 25, 614–627. doi: 10.1109/TRO.2009.2020347

Iwane, F., Halvagal, M. S., Iturrate, I., Batzianoulis, I., Chavarriaga, R., Billard, A., et al. (2019). "Inferring subjective preferences on robot trajectories using EEG signals, in *2019 9th International IEEE/EMBS Conference on Neural Engineering (NER)* (San Francisco, CA), 255–258. doi: 10.1109/NER.2019.8717025

Jayaram, V., Alamgir, M., Altun, Y., Schölkopf, B., and Grosse-Wentrup, M. (2016). Transfer learning in brain-computer interfaces. *IEEE Comput. Intell. Mag.* 11, 20–31. doi: 10.1109/MCI.2015.2501545

Kaiser, P., Aksoy, E. E., Grotz, M., and Asfour, T. (2016). "Towards a hierarchy of loco-manipulation affordances, in *2016 IEEE/RSJ International Conference on Intelligent Robots and Systems (IROS)* (Daejeon), 2839–2846. doi: 10.1109/IROS.2016.7759440

Kolkhorst, H., Burgard, W., and Tangermann, M. (2019a). "Learning user preferences for trajectories from brain signals, in *Proceedings of the International Symposium on Robotics Research (ISRR)* (Hanoi).

Kolkhorst, H., Tangermann, M., and Burgard, W. (2018). "Guess what I attend: interface-free object selection using brain signals, in *2018 IEEE/RSJ International Conference on Intelligent Robots and Systems (IROS)* (Madrid), 7111–7116. doi: 10.1109/IROS.2018.8593992

Kolkhorst, H., Veit, J., Burgard, W., and Tangermann, M. (2019b). "Heterogeneity of event-related potentials in a screen-free brain-computer interface, in *Proceedings of the 8th Graz Brain-Computer Interface Conference 2019* (Graz), 228–233. doi: 10.3217/978-3-85125-682-6-42

Kolkhorst, H., Veit, J., Burgard, W., and Tangermann, M. (2020). *Freiburg Screen-Free BCI for Robotic Object Selection: EEG Dataset*. Open Science Framework.

Koppula, H. S., and Saxena, A. (2016). Anticipating human activities using object affordances for reactive robotic response. *IEEE Trans. Patt. Anal. Mach. Intell.* 38, 14–29. doi: 10.1109/TPAMI.2015.2430335

Krawez, M., Caselitz, T., Büscher, D., Van Loock, M., and Burgard, W. (2018). "Building dense reflectance maps of indoor environments using an RGB-D camera, in *2018 IEEE/RSJ International Conference on Intelligent Robots and Systems (IROS)* (Madrid), 3210–3217. doi: 10.1109/IROS.2018.8594107

Lawhern, V. J., Solon, A. J., Waytowich, N. R., Gordon, S. M., Hung, C. P., and Lance, B. J. (2018). EEGNet: a compact convolutional neural network for EEG-based brain–computer interfaces. *J. Neural Eng.* 15:056013. doi: 10.1088/1741-2552/aace8c

Leeb, R., Tonin, L., Rohm, M., Desideri, L., Carlson, T., and Millán, J. d. R. (2015). Towards independence: a BCI telepresence robot for people with severe motor disabilities. *Proc. IEEE* 103, 969–982. doi: 10.1109/JPROC.2015.2419736

Nagel, S., and Spüler, M. (2019). Asynchronous non-invasive high-speed BCI speller with robust non-control state detection. *Sci. Rep.* 9, 1–9. doi: 10.1038/s41598-019-44645-x

Pauwels, K., and Kragic, D. (2015). "SimTrack: a simulation-based framework for scalable real-time object pose detection and tracking, in *2015 IEEE/RSJ International Conference on Intelligent Robots and Systems (IROS)* (Hamburg), 1300–1307. doi: 10.1109/IROS.2015.7353536

Pedregosa, F., Varoquaux, G., Gramfort, A., Michel, V., Thirion, B., Grisel, O., et al. (2011). Scikit-learn: machine learning in python. *J. Mach. Learn. Res.* 12, 2825–2830.

Pennec, X., Fillard, P., and Ayache, N. (2006). A Riemannian framework for tensor computing. *Int. J. Comput. Vis.* 66, 41–66. doi: 10.1007/s11263-005-3222-z

Rivet, B., Souloumiac, A., Attina, V., and Gibert, G. (2009). xDAWN algorithm to enhance evoked potentials: application to brain-computer interface. *IEEE Trans. Biomed. Eng.* 56, 2035–2043. doi: 10.1109/TBME.2009.2012869

Rodrigues, P. L. C., Jutten, C., and Congedo, M. (2019). Riemannian procrustes analysis: transfer learning for brain–computer interfaces. *IEEE Trans. Biomed. Eng.* 66, 2390–2401. doi: 10.1109/TBME.2018.2889705

Salazar-Gomez, A. F., DelPreto, J., Gil, S., Guenther, F. H., and Rus, D. (2017). "Correcting robot mistakes in real time using EEG signals, in *2017 IEEE International Conference on Robotics and Automation (ICRA)* (Singapore), 6570–6577. doi: 10.1109/ICRA.2017.7989777

Schirrmeister, R. T., Springenberg, J. T., Fiederer, L. D. J., Glasstetter, M., Eggensperger, K., Tangermann, M., et al. (2017). Deep learning with convolutional neural networks for EEG decoding and visualization. *Hum. Brain Mapp.* 38, 5391–5420. doi: 10.1109/SPMB.2017.8257015

Schreuder, M., Blankertz, B., and Tangermann, M. (2010). A new auditory multi-class brain-computer interface paradigm: spatial hearing as an informative cue. *PLoS ONE* 5:e9813. doi: 10.1371/journal.pone.0009813

Schreuder, M., Höhne, J., Blankertz, B., Haufe, S., Dickhaus, T., and Michael Tangermann (2013). Optimizing event-related potential based brain–computer interfaces: a systematic evaluation of dynamic stopping methods. *J. Neural Eng.* 10:036025. doi: 10.1088/1741-2560/10/3/036025

Sellers, E. W., and Donchin, E. (2006). A P300-based brain–computer interface: initial tests by ALS patients. *Clin. Neurophysiol.* 117, 538–548. doi: 10.1016/j.clinph.2005.06.027

Shridhar, M., and Hsu, D. (2018). "Interactive visual grounding of referring expressions for human-robot interaction, in *Proceedings of Robotics: Science and Systems* (Pittsburgh, PA). doi: 10.15607/RSS.2018.XIV.028

Tangermann, M., Krauledat, M., Grzeska, K., Sagebaum, M., Blankertz, B., Vidaurre, C., et al. (2009). "Playing Pinball with non-invasive BCI, in *Advances*

in Neural Information Processing Systems 21, eds D. Koller, D. Schuurmans, Y. Bengio, and L. Bottou (Vancouver, BC: Curran Associates, Inc.), 1641–1648.

Thielen, J., van den Broek, P., Farquhar, J., and Desain, P. (2015). Broad-band visually evoked potentials: re(con)volution in brain-computer interfacing. *PLoS ONE* 10:e0133797. doi: 10.1371/journal.pone.0133797

van der Waal, M., Severens, M., Geuze, J., and Desain, P. (2012). Introducing the tactile speller: an ERP-based brain–computer interface for communication. *J. Neural Eng.* 9:045002. doi: 10.1088/1741-2560/9/4/045002

Yair, O., Ben-Chen, M., and Talmon, R. (2019). Parallel transport on the cone manifold of SPD matrices for domain adaptation. *IEEE Trans. Signal Process.* 67, 1797–1811. doi: 10.1109/TSP.2019.2894801

Yger, F., Berar, M., and Lotte, F. (2017). Riemannian approaches in brain-computer interfaces: a review. *IEEE Trans. Neural Syst. Rehabil. Eng.* 25, 1753–1762. doi: 10.1109/TNSRE.2016.2627016

Ying, R., Weisz, J., and Allen, P. K. (2018). "Grasping with your brain: a brain-computer interface for fast grasp selection, in *Robotics Research, Springer Proceedings in Advanced Robotics*, eds A. Bicchi and W. Burgard (Cham: Springer), 325–340. doi: 10.1007/978-3-319-51532-8_20

Zanini, P., Congedo, M., Jutten, C., Said, S., and Berthoumieu, Y. (2018). Transfer learning: a riemannian geometry framework with applications to brain–computer interfaces. *IEEE Trans. Biomed. Eng.* 65, 1107–1116. doi: 10.1109/TBME.2017.2742541

Conflict of Interest: WB is affiliated with the Toyota Research Institute, Los Altos, USA.

The remaining authors declare that the research was conducted in the absence of any commercial or financial relationships that could be construed as a potential conflict of interest.

frontiers in Neuroscience

SYSTEMATIC REVIEW
published: 30 June 2020
doi: 10.3389/fnins.2020.00578

A Systematic Review Establishing the Current State-of-the-Art, the Limitations, and the DESIRED Checklist in Studies of Direct Neural Interfacing With Robotic Gait Devices in Stroke Rehabilitation

Olive Lennon[1], Michele Tonellato[2], Alessandra Del Felice[3,4], Roberto Di Marco[3], Caitriona Fingleton[5], Attila Korik[6], Eleonora Guanziroli[7], Franco Molteni[7], Christoph Guger[8], Rupert Otner[8] and Damien Coyle[6]*

[1] School of Public Health, Physiotherapy and Sports Science, University College Dublin, Dublin, Ireland, [2] Department of Neuroscience, Rehabilitation Unit, University of Padova, Padova, Italy, [3] Department of Neuroscience, NEUROMOVE-Rehab Laboratory, University of Padova, Padova, Italy, [4] Padova Neuroscience Center, University of Padova, Padova, Italy, [5] Department of Physiotherapy, Mater Misericordiae University Hospital, Dublin, Ireland, [6] Intelligent Systems Research Centre, School of Computing, Engineering and Intelligent Systems, Ulster University, Derry, United Kingdom, [7] Villa Beretta Rehabilitation Center, Valduce Hospital, Costa Masnaga, Italy, [8] g.tec Medical Engineering GmbH, Schiedlberg, Austria

OPEN ACCESS

Edited by:
Michela Chiappalone,
Italian Institute of Technology (IIT), Italy

Reviewed by:
Seong-Whan Lee,
Korea University, South Korea
Trieu Phat Luu,
University of Houston, United States

***Correspondence:**
Olive Lennon
olive.lennon@ucd.ie

Specialty section:
This article was submitted to Neuroprosthetics, a section of the journal Frontiers in Neuroscience

Received: 05 December 2019
Accepted: 12 May 2020
Published: 30 June 2020

Citation:
Lennon O, Tonellato M, Del Felice A, Di Marco R, Fingleton C, Korik A, Guanziroli E, Molteni F, Guger C, Otner R and Coyle D (2020) A Systematic Review Establishing the Current State-of-the-Art, the Limitations, and the DESIRED Checklist in Studies of Direct Neural Interfacing With Robotic Gait Devices in Stroke Rehabilitation. Front. Neurosci. 14:578. doi: 10.3389/fnins.2020.00578

Background: Stroke is a disease with a high associated disability burden. Robotic-assisted gait training offers an opportunity for the practice intensity levels associated with good functional walking outcomes in this population. Neural interfacing technology, electroencephalography (EEG), or electromyography (EMG) can offer new strategies for robotic gait re-education after a stroke by promoting more active engagement in movement intent and/or neurophysiological feedback.

Objectives: This study identifies the current state-of-the-art and the limitations in direct neural interfacing with robotic gait devices in stroke rehabilitation.

Methods: A pre-registered systematic review was conducted using standardized search operators that included the presence of stroke and robotic gait training and neural biosignals (EMG and/or EEG) and was not limited by study type.

Results: From a total of 8,899 papers identified, 13 articles were considered for the final selection. Only five of the 13 studies received a strong or moderate quality rating as a clinical study. Three studies recorded EEG activity during robotic gait, two of which used EEG for BCI purposes. While demonstrating utility for decoding kinematic and EMG-related gait data, no EEG study has been identified to close the loop between robot and human. Twelve of the studies recorded EMG activity during or after robotic walking, primarily as an outcome measure. One study used multisource information fusion from EMG, joint angle, and force to modify robotic commands in real time, with higher error rates observed during active movement. A novel study identified used EMG data during robotic gait to derive the optimal, individualized robot-driven step trajectory.

Conclusions: Wide heterogeneity in the reporting and the purpose of neurobiosignal use during robotic gait training after a stroke exists. Neural interfacing with robotic gait after a stroke demonstrates promise as a future field of study. However, as a nascent area, direct neural interfacing with robotic gait after a stroke would benefit from a more standardized protocol for biosignal collection and processing and for robotic deployment. Appropriate reporting for clinical studies of this nature is also required with respect to the study type and the participants' characteristics.

Keywords: stroke rehabilitation, robot-assisted gait trainer, electromyography, electroencephalography, human–machine interface, brain–computer interface

INTRODUCTION

Stroke, a disease with substantial personal and societal consequences, remains the leading cause of acquired disability worldwide. With 13.7 million new cases each year, the associated economic costs of treatment and post-stroke care are significant (Wilkins et al., 2017; Johnson et al., 2019). At 3 months after a stroke, 20% of people remain wheelchair dependent and ∼70% walk with a reduced capacity (Mehrholz et al., 2017). Task-specific training is critical for recovery, and the intensity of practice is strongly associated with improved functional gait outcomes (Kwakkel et al., 2004; Veerbeek et al., 2014).

Providing high intensity restorative exercises for a larger share of the stroke population is part of the Action Plan for Stroke in Europe 2018–2030 (Norrving et al., 2018), yet the delivery of an adequate dosage of gait training for physically dependent patients is challenging in the rehabilitation sector, from manual handling and human resource perspectives. Robotic gait devices, which enable people to walk with electromechanical assistance to achieve a healthy gait trajectory, can potentially overcome some of these practical difficulties (Mehrholz et al., 2017; Cervera et al., 2018) and allow an intensive, high repetition of the gait cycle with reduced therapist involvement (as they no longer need to set the paretic limbs or assist trunk movements) (Sarasola-Sanz et al., 2017). The addition of robotic-assisted gait training (RAGT) to usual rehabilitation has been shown by a systematic review to improve the likelihood of regaining independent walking after a stroke [odds ratio 1.94, 95% confidence interval (CI), 1.39 to 2.71], with a subgroup analysis suggesting that people in the acute phase and non-ambulatory individuals benefit most from the intervention (Mehrholz et al., 2017). Of note is that the improvements in walking velocity and walking capacity did not match the observed improvements in independence in gait.

At present, RAGT alone has not been shown to be superior to equally dosed routine rehabilitation despite the increased intensity of stepping in RAGT (Taveggia et al., 2016; Bruni et al., 2018). When motor function is considered specifically as an outcome, the upper limb robotic devices have proven efficacy in contrast to the lower limb robotic training, where no treatment effect for motor function has been demonstrated (Lin et al., 2019). Current RAGT therapies have focused on providing high-intensity training and repetition but not on patient engagement, motivation, and reward, which are important factors for inducing cortical plasticity (Hogan et al., 2006; Goodman et al., 2014). Limitations in randomized controlled trials (RCTs) in this area to date have been identified (Molteni et al., 2018) and many RAGT protocols were criticized for allowing the trainee to be too passive, with lower metabolic costs, muscle activations, and subject effort reported in comparison to therapist-assisted treadmill training (Cai et al., 2006; Israel et al., 2006; Krishnan et al., 2013). However, rehabilitative robotics, when deployed correctly, have the ability to generate bottom up and top down complex and controlled multisensory stimulation to modify the plasticity of neural connections through the experience of movement (Molteni et al., 2018).

Direct human machine interfaces (HMIs) can translate electrical, magnetic, or metabolic activity at the brain or the muscle level into control signals for external devices (e.g., computers or neuroprosthetic and robotic devices) to replace, restore, or enhance the natural neural output (Wolpaw, 2012; Soekadar et al., 2015). Brain interfacing technology, primarily electroencephalography (EEG)-based brain computer interfaces (BCI,) can offer new strategies for robotic gait re-education after a stroke that can promote more active engagement in movement intent and/or by neurophysiological feedback. In stroke, BCI exploitation has mainly used motor imagery to drive brain activity levels (with no overt motor output) in combination with visual, auditory, or haptic feedback or to control an external device which executes the movement and provides proprioceptive feedback (Prasad et al., 2010; Van Dokkum et al., 2015). Of the nine upper limb studies identified in a recent systematic review of BCI for motor rehabilitation after a stroke, only three used BCI to control a robotic or orthotic device with large to moderate effect sizes noted for improved motor impairment (Cervera et al., 2018) and emerging evidence in upper limb rehabilitation now points to the superiority of BCI robotic training after a stroke to robotic training alone in motor recovery (Varkuti et al., 2013; Ang et al., 2014). No lower limb robotic RCT studies using BCI were reported in this review (Cervera et al., 2018).

Motor intent can also be determined non-invasively by electromyography (EMG) activity and responded to in triggered motion (Hussein et al., 2009) and thus has potential to enhance RAGT. EMG-based robotic movement has emerged as a well-developed field in upper limb rehabilitation in stroke (Ho et al., 2011; Vaca Benitez et al., 2013; Hu et al., 2015), and when used in

robot-assisted rehabilitation has achieved a significantly higher completion rate compared to torque control for the participants with severe to moderate impairment in the upper limb (Paredes et al., 2015). EMG has also been combined with EEG in human–machine interactive force to improve the recognition of movement intent (Mrachacz-Kersting et al., 2012; Jiang et al., 2014; Bhagat et al., 2016).

As reported in a 2018 review of human intent-based control in motor rehabilitation after a stroke, most studies are in the laboratory stage (Li et al., 2018), and a systematic review of RCTs of BCI interfaces after a stroke identified no RAGT studies (Cervera et al., 2018). Therefore, the aim of this systematic review was to establish the current state-of-the-art in EMG and/or EEG neural biosignal deployment during robotic gait training post-stroke as described in the literature (with no limitation by study design applied). Contributing to this review is a panel of relevant stakeholders from the fields of rehabilitation, neurology, biomedical engineering, and BCI engineering who, in providing a summary of available data, comment and make important recommendations to standardize reporting and advance this important and emerging area in robotic-assisted gait rehabilitation in stroke.

The primary question that this review asks is:

what is the current state-of-the-art in neural–exoskeleton interface (non-invasive EEG and/or EMG) during robotic gait training after a stroke?

The secondary review questions asked are the following:

1. What is the profile of the stroke patients in the included studies?
2. What robotic gait devices are deployed?
3. What biosignals are measured in conjunction with the robotic gait devices and what devices (hardware and/or software) are used to capture these biosignals?
4. What protocols are used for recording and processing these biosignals?
5. For what purpose is the acquired biosignal data collected?

As a nascent area, the inclusive approach to study type was taken in this review to allow a true reflection of bioengineering translational research in gait rehabilitation robotics in a clinical population. A compendium of current data collection and signal processing procedures will be developed to allow recommendations for the standardization of future research in this field.

The systematic review was pre-registered with PROSPERO (PROSPERO 2018 CRD42018112252) (Heilinger et al., 2018).

METHODS

Definitions

Prior to conducting the review, several operational definitions were defined by the research team which included an experienced information science researcher and experts in rehabilitation, BCI, and medical engineering. The methodology was based on the Cochrane handbook for systematic reviews of interventions and the PRISMA statement (Preferred Reporting Items for Systematic Reviews and Meta-Analyses) (Higgins and Green, 2011) and used the PICOS acronym to guide the search strategy development. In line with best practice, screening for inclusion at the abstract and the manuscript stages and during data extraction of the included studies was conducted independently by two researchers. Where disagreements arose, they were discussed among the reviewers first and then with an independent third party until a consensus was achieved.

The inclusion criteria for the review population were adults (>18 years) with confirmed diagnosis of stroke and at any stage of stroke recovery. No limitation by stroke etiology, first or recurrent event, or symptom presentation were applied. Adults with other known neurological diseases (e.g., spinal cord injury and multiple sclerosis) were excluded.

The interventions included in the review, broadly termed as "robotic gait training," must comprise exoskeleton or other electromechanically assisted gait devices and be implemented in conjunction with biosignal (EEG and/or EMG) data capture as part of the study. For the purpose of this review, robotic devices could be either end-effector (electromechanically driven footplates simulating the phases of gait) or exoskeleton (robot-driven orthosis) gait devices.

Comparator populations were not a mandatory inclusion criterion, but studies that include a control group or a matched comparator group were considered eligible for inclusion. RCTs, cross-over, or quasi-randomized control studies, case–control studies, cohort studies, cross-sectional studies, case series, and case reports were all eligible for inclusion. Reviews, opinion pieces, editorials, and conference abstracts were excluded. This review was not designed to specifically examine the efficacy of the robotic gait interventions on stroke outcomes; rather, we were interested in the neural biosignals of EEG and or EMG themselves when recorded during robotic gait training after a stroke and how these signals interface with the robotic device.

Information Sources

A systematic search and review of the literature was completed, which was compliant with the PRISMA guidelines (Moher et al., 2010). The following databases were searched from inception up to the 30th of November 2018: PubMed (1949–2018), EMBASE (1947–2018), Web of Science (1945–2018), COMPENDEX (1967–2018), CINAHL (1982–2018), SPORTDiscus (1985–2018), ScienceDirect (1997–2018), and Cochrane Library (1974–2018). No language, publication year, or publication status limits were applied to the database searches. Each database was searched using a comprehensive search strategy which was devised in conjunction with a librarian, including controlled vocabulary terms specific to each database and employing Boolean operators AND and OR. Gray literature was searched for in the following websites: http://bnci-horizon-2020.eu/database/data-sets and OpenGrey. A sample search strategy is provided as part of **Figure 1**.

Study Identification and Selection

The citations identified were subjected to the following review process. Duplicate records were removed. The remaining studies

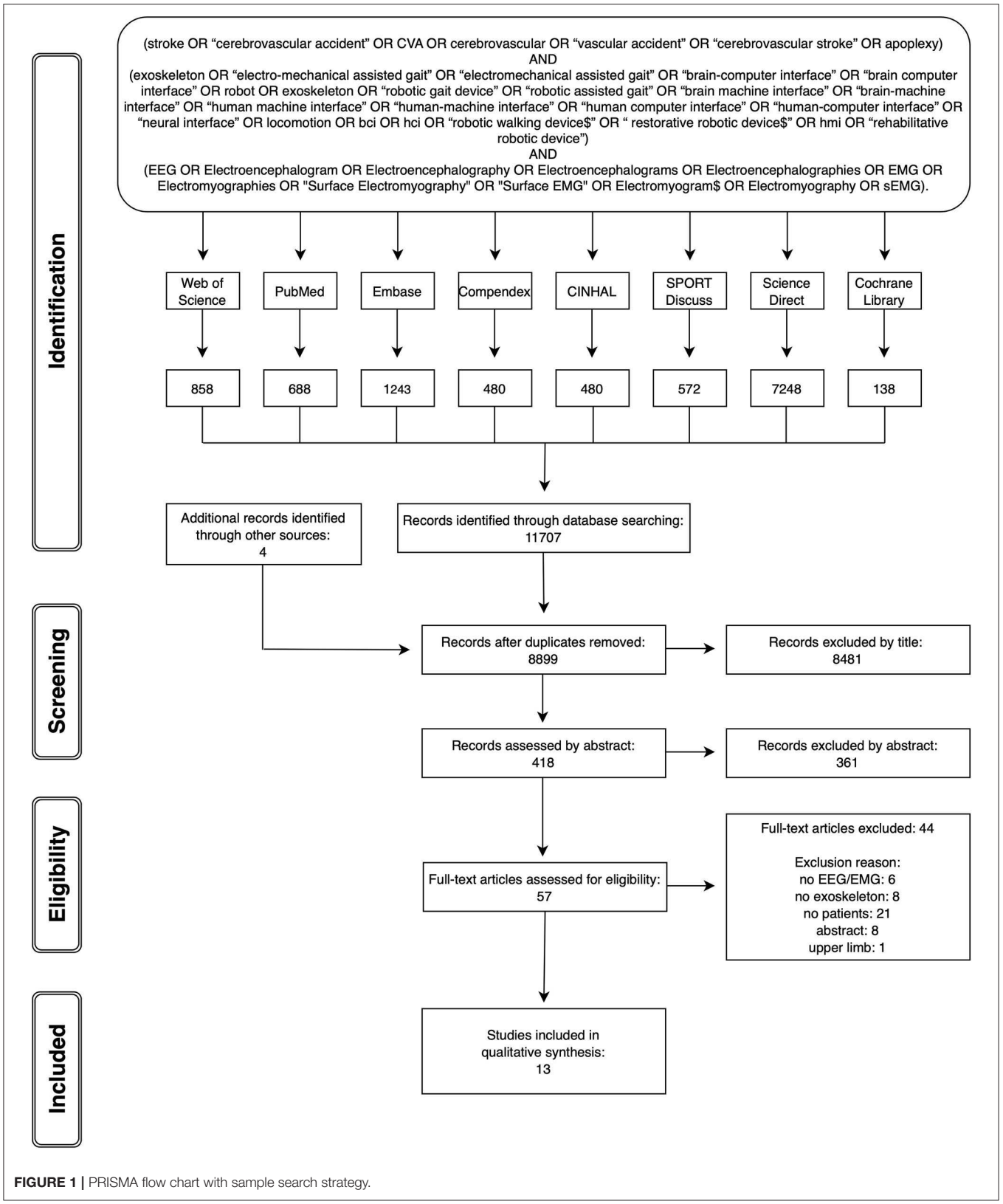

FIGURE 1 | PRISMA flow chart with sample search strategy.

were then reviewed independently by two reviewers against the established eligibility criteria in three stages: screening by title, screening by abstract, and screening by full text. An inclusive approach was taken, whereby if it was not clear whether a study fulfilled the necessary criteria for inclusion, it progressed to the next more in-depth review stage.

Methodological Quality of the Included Studies

The reviewers independently documented the methodological quality of the included studies using the Effective Public Health Practice Public tool (EPHPP) in conjunction with the EPHPP dictionary for standardization. The EPHPP tool has been established as a reliable and valid tool in health research and is suitable to use across a range of differing study methodologies (Thomas et al., 2004, 2008). The disparity in ratings was discussed until a final decision was agreed.

Eight different sections of study quality to be applied as appropriate to the study type were addressed: selection bias, study design, confounders, blinding, data collection methods, withdrawals and dropouts, intervention integrity, and analysis. The tool provides an overall rating of either strong, moderate, or weak quality for each study.

Data Extraction, Synthesis, and Analysis

Data were extracted from the included studies using a pre-agreed, standardized data collection form. The data extracted included (1) the characteristics of stroke study participants (including number, age, stroke type, stroke severity, and ambulatory ability), (2) type of robotic gait devices employed, (3) neural biosignal/s captured, (4) protocol reported for signal capture and processing, and (5) purpose and use of biosignal capture. Discrepancies in extraction, mainly related to the criteria for reporting biosignal processing, were resolved through a group discussion until a consensus was reached.

Narrative and tabular syntheses of data were proposed due to the heterogeneity of the study methodologies included. An overview of the studies meeting the inclusion criteria is initially provided, summarizing across the studies the stroke patient profiles, robotic devices, neural biosignal/s captured during robotic gait training after a stroke, and the purpose of the signal capture.

A summary of current integration of EEG and/or EMG data during robotic walking is presented next, with the current state of the art in closing the BCI/HMI loop in robotic gait training after a stroke being delineated.

The protocols for EEG and EMG signal collection are reported in a tabular format, with a narrative summary identifying the hardware and the software utilized where reported, the number of channels/leads used, and the sites chosen for signal capture.

EEG and EMG signal processing, as employed in the included studies, are again reported in a tabular format, with a summary identifying the frequency of signal capture, filtering processes, and software and algorithms used.

RESULTS

Overall Summary of Studies Identified

The database searches were completed by end of November 2018. **Figure 1** provides the PRISMA flow chart of the studies identified through database searching and through each stage of the review process. From 8,899 articles identified by the search strategy, 13 full papers fitting the inclusion criteria were included.

Tables 1, **2**, which report the EEG and the EMG studies, respectively, detail the characteristics of the stroke participants,

TABLE 1 | Electroencephalography (EEG)-based robotic studies (participants and purpose).

References	Robotic device	Stroke patients	Mobility level	Outcome measures	Purpose of EEG recording	Feedback to robot (Y/N)	Real-time feedback (Y/N)	Adverse events (Y/N)
Calabrò et al. (2018)	EKSO	*N* = 40 H-C 69.0 ± 4.0 yrs RGT 67.0 ± 6.0 yrs OGT Type: I Side: 8L + 12R	FAC < 5 MRC < 4	10 MWT, RMI, TUG, sEMG, CSE, SMI, FPEC	Identify the cortical activations induced by gait training	N	N	Y
Contreras-Vidal et al. (2018)	H2 and continuous-time Kalman decoder	*N* = 6 C 53.5 ± 12.5 yrs Type: 2 I; 2 He; 2 M Side: 2L + 4R	NS	BBS, FGA, 6 MWT, TUG, FM, BI (pre/post)	Decoding gait kinematics	N	N	NS
He et al. (2014)	X1	*N* = 1 US 51 yrs Type: NS Side: 1L	FM-LL 12/34 BBS 38/56 FGA 13/30	EEG decoding accuracies for kinematics and EMG	Feasibility of decoding joint kinematics and muscle activity patterns	N	N	NS

Patient data reported: sample number (N), stroke classified as (A) acute, (SA) subacute, (C) chronic, (US) undefined stroke and (H) hospitalized; age in years (yrs); robot gait training (RGT) and overground gait training (OGT); stroke type classified in (I) ischemic stroke, (He) hemorrhagic, (M) mixed; L, affected side—left; R, affected side—right. Control subject sample (CTRL) is reported, if any. NS: not specified in the manuscript.

Outcomes and mobility: 10 MWT, Ten-Meters Walking Test; RMI, Rivermead Mobility Index; TUG, Timed Up and Go; sEMG, surface electromyography; CSE, Corticospinal Excitability; SMI, Sensory-Motor Integration; FPEC, Fronto-Parietal Effective Connectivity; BBS, Berg Balance Score; FGA, Functional Gait Assessment; 6MWT, Six-Minute Walking Test; FM, Fugl–Meyer assessment; BI, Barthel Index; FAC, Functional Ambulation Classification; MRC, Medical Research Council scale for muscle strength; FM-LL, Fugl–Meyer Lower Limb Scale.

TABLE 2 | Electromyography (EMG)-based robotic studies (participants and purpose).

References	Robotic device	Stroke Patients	Disability level	Outcome measures	Purpose of EMG recording	Feedback to robotic (Y/N)	Real-time feedback (Y/N)	Adverse events (Y/N)
Androwis et al. (2018)	EKSO GT (EXO)	*N* = 5 A (first event) 51.0 ± 17.0 yrs Type: NS Side: 2L + 3R	FIM 26 ± 4	FIM	Test a novel EMG analysis (Burst Duration Similarity Index) and assess the neuromuscular adaptations in lower extremities muscles	N	N	NS
Calabrò et al. (2018)	EKSO (EXO)	*N* = 40 H-C 69.0 ± 4.0 yrs RGT 67.0 ± 6.0 yrs OGT Type: I Side: 8L + 12R RGT 9L + 11R OGT	FAC < 5 MRC < 4	10 MWT, RMI, TUG, sEMG, CSE, SMI, FPEC	Quantify gait parameters and compare mean muscle activity pre/post robotic and standard therapy	N	N	Y
Chisari et al. (2015)	Lokomat (EXO)	*N* = 15 H 62.0 ± 10.0 yrs Type: 10 I, 5 He Side: NS	Ability to walk for a few meters	FMMS, BBS, 10 MWT, TUG, 6 MWT	Strength and motor unit firing rate of vastus medialis	N	N	NS
Coenen et al. (2012)	Lokomat (EXO)	*N* = 10 C 55.0 ± 11.0 yrs CTRL = 10 47 ± 12 yrs Type: 5 I, 5 He Side: 8L + 2R	FAC = 5	sEMG during gait cycle	Compare EMG amplitude in robotic walking, overground walking for stroke patients, and overground walking for control subjects	N	N	NS
Fan and Yin (2013)	Lower extremity exoskeleton with a standing bed frame (EXO, non-commercial)	*N* = 3 H (2 SA, 1 C) 50.7 ± 19.2 yrs CTRL = 3 25.3 ± 1.5 Type: NS Side: 2L + 1R	NS	Exoskeleton forces and angles, joint ROM and active flexion/extension force	To decode movement and predict human motion inattention	Y	Y	NS
Gandolfi et al. (2017)	First mover (EE)	*N* = 2 H-SA 74 yrs CTRL = 10 65.4 ± 6.1 yrs Type: I Side: L	FAC = 0 TCT < 12	sEMG, MI, MRC, AS	Explore the training effects on lower limb function and timing of muscle activation onset and offset	N	N	N
Gandolla et al. (2018)	EKSO GT (EXO)	*N* = 13 (8 A, 5 C) 52 ± 14 yrs Type: 7 I, 6 He Side: 8L + 5R	Tibialis anterior MRC < 4 MAS < 2 at hip, knee, ankle	GM, sEMG during gait cycle	(1) Computational calibration procedure, (2) gait cycle reference	Y	N	NS
He et al. (2014)	X1 (NASA) (EXO)	*N* = 1, 51 yrs CTRL = 2 33.8 ± 0.1 yrs Type: NS Side: L	FM-LL 12/34 BBS 38/56 FGA 13/30	EEG decoding accuracies for kinematics and EMG	Assess muscle activation pattern	N	N	NS
Hesse et al. (2010)	G-EO-Systems (EE)	*N* = 6 SA <75 yrs Type: I Side: 3L + 3R	Independent walker (>20 m, >0.25 m/s) Stair climber (aids/hand rails allowed)	sEMG activation pattern during floor walking and stairs climbing; FAC, RMI, MI, BI	Compare lower limb muscle activation with and without the robot	N	N	NS

(Continued)

TABLE 2 | Continued

References	Robotic device	Stroke Patients	Disability level	Outcome measures	Purpose of EMG recording	Feedback to robotic (Y/N)	Real-time feedback (Y/N)	Adverse events (Y/N)
Ping et al. (2013)	NaTUre-gaits (EXO non-commercial)	*N* = 1 H-C, 73 yrs SCI=2, 32 and 67 yrs CTRL = 4, age NS Type: NS Side: L	Moderate level of assistance to walk	sEMG during gait cycle	Investigate the timing and intensity of activity in the lower limb muscles during the use of the system	N	N	NS
Sloot et al. (2018)	Exosuit (EE)	*N* = 8, age NS Type: NS Side: NS	Walkers (level of assistance: NS)	sEMG, walking speed, energy cost of walking	Maximum EMG values during push-off and swing during walking with and without EE	N	N	NS
Srivastava et al. (2016)	ALEX II (EXO)	*N* = 12 SA-C (6 RGT, 6 BWSTT) RGT: 62.7 ± 12.7 yrs BWSTT: 58.8 ± 9.0 yrs Type: NS Side: 4L + 2R RGT 3L + 3R BWSTT	Walkers (level of assistance: NS)	TUG, 6 MWT, FGA, FM (pre/post)	Compare muscle activation timing during the gait cycle in RGT and BWTSS	Y	N	NS

Robotic devices: EXO, exoskeleton; EE, end-effector. Patient data are reported as: N, sample number; A, classified as acute stroke; SA, classified as subacute stroke; C, classified as chronic stroke; H, hospitalized; SCI, spinal cord injury; RGT, robot gait training; BWSTT, body-weight supported treadmill training; OGT, overground gait training; I, stroke type classified in ischemic stroke; He, stroke type classified in hemorrhagic stroke; M, stroke type classified in mixed; L, affected side—left; R, affected side—right; CTRL, control subject sample is reported, if any; NS, not specified. Outcomes and mobility: FIM, Functional Independence Measure; FAC, Functional Ambulation Classification; MRC, Medical Research Council muscle strength; TCT, Trunk Control Test; MAS, Modified Ashworth Scale; FM-LL, Fugl–Meyer Lower Limb Scale; BBS, Berg Balance Score; FGA, Functional Gait Assessment; 10 MWT, Ten-Meter Walk Test; RMI, Rivermead Mobility Index; TUG, Timed Up and Go; sEMG, surface EMG; CSE, corticospinal excitability; SMI, sensory–motor Integration; FPEC, fronto-parietal effective connectivity; FMMS, Fugl–Meyer Motor Scale; 6 MWT, Six-Minute Walk Test; MI, Motricity Index; AS, Ashworth Scale for spasticity; GM, Gait Motor Index; BI, Barthel Index; FM, Fugl–Meyer assessment.

the robotic gait devices deployed, and the purpose of the neural bio-signal recording.

A total of 96 out of the 122 individuals with stroke who were recruited in the studies received robot-assisted gait training on at least one occasion. Calabrò et al. recruited the largest cohort (40 stroke subjects, 20 of whom underwent robotic training) (Calabrò et al., 2018), whereas others reported a case study (Ping et al., 2013). The stroke participants differed widely across studies in terms of age profile, stroke type, stroke lateralization, and disability levels. Where reported, the ages ranged from 29 to 81 years of age. The laterality of the stroke event was described for 99 of the 122 stroke participants, 46 of whom had a right-sided stroke (with left hemiplegia). Two studies did not report stroke laterality (Chisari et al., 2015; Sloot et al., 2018). Stroke etiology was reported in 92 cases: 72 of which were ischemic in origin, 18 were hemorrhagic, and two were ischemic/hemorrhagic. Six studies did not provide information related to stroke type (Ping et al., 2013; He et al., 2014; Androwis et al., 2018; Sloot et al., 2018). The time from stroke to study participation was reported for 98 patients, with the majority ($N = 57$) recruited in the chronic phase of stroke. Three studies, comprising 13 subjects in total, selected stroke participants during the acute/subacute phase (Hesse et al., 2010; Gandolfi et al., 2017; Androwis et al., 2018). Three studies involved the collection of data from both chronic and acute/subacute phases of stroke ($N = 10$ in acute phase; $N = 15$ in chronic phase) (Fan and Yin, 2013; Srivastava et al., 2016; Gandolla et al., 2018). The stage of stroke recovery was not specified for the remaining 24 participants.

As noted in **Tables 1**, **2**, a variety of methods were employed to describe the walking ability of the participants and, where comparable, the disability levels of the stroke study participants varied. Three authors adopted the Functional Ambulation Classification (FAC) as a standardized scale to describe the dependence levels in walking. Coenen et al. included fully independent walkers (FAC 5) (Coenen et al., 2012), Gandolfi et al. selected people who were unable to walk (FAC 0), (Gandolfi et al., 2017) and Calabrò et al. focused on stroke patients with gait impairment (FAC $\leq$ 4) (Calabrò et al., 2018). Three studies identified the participants as "walkers" but did not specify the level of assistance required, if any (Chisari et al., 2015; Srivastava et al., 2016; Sloot et al., 2018). Other studies described the participants' mean motor subscale score of the Functional Independence Measure (Androwis et al., 2018) [26 ± 4; where 13–38 indicate low scores for motor independence as guided by Itaya et al. (2017)], the Fugl–Meyer Lower Limb Scale (He et al., 2014) [12/34; where a cutoff score of <21 indicates lower mobility levels, as guided by Kwong and Ng (2019)], or strength of the lower limb tibialis anterior muscles of <4 on the MRC scale (Gandolla et al., 2018) or specified the level of assistance required to walk (Hesse et al., 2010; Ping et al., 2013). Two studies did not address the participants' walking status (Fan and Yin, 2013; Contreras-Vidal et al., 2018); however, one of these studies used the 6 MWT as a baseline score.

Exoskeleton devices were the most frequent robotic gait devices deployed in the studies included ($n = 10$ studies). The Lokomat (Lokomat® Hocoma, Switzerland) was used in two studies, EKSO (Ekso bionics®, USA) was used in three

studies (two EKSO GT and one non-specified EKSO); the X1 (NASA, USA), the H2 (Technaid, Spain), the ALEX II (ROAR Laboratory, USA), and NaTUre-gaits (Nanyang Technological University, Singapore) devices were used in one study each. Fan and Yin combined a non-commercial lower extremity exoskeleton robot with a standing bed frame (Fan and Yin, 2013). Three end-effector devices were reported in the included studies [First Mover (Reha Technology AG, Switzerland), G-EO-Systems (Reha Technology AG, Switzerland), and Exosuit (Wyss Institute for Biologically Inspired Engineering, Harvard University, USA)].

Closing the Loop Between Human and Robotic Device

No studies included in this review closed the loop in real time using EEG biosignals during robotic walking after a stroke, indicating that this field has not sufficiently evolved in a patient population such as stroke. One study described a multisensor, real-time movement prediction model that included sEMG of knee flexor and extensor muscles, joint angle, and force to determine the rehabilitation mode and the parameter settings in a bespoke exoskeleton (Fan and Yin, 2013). Errors in movement prediction were evident however during active training, when flexion and extension altered rapidly.

EEG-Based Studies

Three of the thirteen studies included in this review recorded and analyzed EEG activity. As summarized in **Table 1**, two studies used EEG during robotic gait to decode gait kinematics (He et al., 2014; Contreras-Vidal et al., 2018) and muscle activity during walking (He et al., 2014). One study used EEG to determine frontoparietal connectivity as an outcome measure of neuroplasticity following a robotic gait training intervention (Calabrò et al., 2018).

Table 3 summarizes the EEG signal processing methods employed by the researchers. Contreras-Vidal et al. identified neural representation at the brain level for robotic gait using a powered H2 exoskeleton. A wireless, 64-channel, active electrode EEG-based system (BrainAmpDC, Brain Products, Inc., Munich), with continuous-time Kalman decoder operating on delta band, was utilized in five chronic stroke patients to demonstrate the feasibility of an EEG-based BCI-controlled rehabilitative robotic exoskeleton. The classification accuracy for predicting joint angles during gait was noted to improve with multiple training sessions and gait speed (Contreras-Vidal et al., 2018). The pilot study conducted by He et al., using a 10th-order unscented Kalman filter, demonstrated similar moderately high online decoding accuracies for joint kinematics during robotic gait but not for muscle activity patterns during robotic gait training in two healthy participants and one stroke survivor (He et al., 2014) using a multimodal interface comprising EEG [64-channel EEG (actiCap system, Brain Products GmbH, Munich, Germany)], EMG, and motion (goniometers), instrumented in conjunction with the X1 exoskeleton employed during 5-min overground walking sessions of three conditions: no robot, robot off (X1 in passive mode), and robot on (X1 in active mode). The final EEG-based study, an RCT by Calabrò et al. ($N =$ 40 sub-acute and chronic stroke patients), employed 21-channel EEG as a measure of neuroplasticity using frontoparietal effective connectivity (FPEC) but did not interface with the robotic device directly. EEG was recorded using a high-input impedance amplifier (referential input noise $<0.5\ \mu$Vrms at $1 \div 20{,}000$ Hz) of Brain Quick SystemPLUS (Micromed; Mogliano Veneto, Italy), wired to an EEG cap equipped with 21 Ag tin disk electrodes positioned according to the international 10–20 system. An electrooculogram (EOG) was also recorded for blinking artifact detection. EEG and EOG were sampled at 512 Hz, filtered at 0.3–70 Hz, and referenced to linked earlobes. The cortical activations induced by gait training from the EEG recordings were identified by using low-resolution brain electromagnetic tomography (LORETAKEY alpha-software). Structural equation modeling technique (or path analysis) was employed to measure the effective connectivity among the cortical activations induced by gait training. Improved FPEC was observed when robot-assisted gait training was included in the rehabilitation in comparison to conventional rehabilitation alone ($r = 0.601$, $p < 0.001$).

EMG-Based Studies

Table 4 summarizes the EMG measurements from 12 studies included in this review. Only eight of the 12 studies defined the EMG device used: two studies used a Noraxon, two a BTS, one a DataLog, one a Motion Lab, and one a Porti system; one study used a self-made signal acquisition processor. Among these, five were wireless EMG devices.

The majority of the studies collected EMG data to assess neuromuscular adaptations during robotic gait in stroke (Coenen et al., 2012; Ping et al., 2013; Chisari et al., 2015; Srivastava et al., 2016; Androwis et al., 2018; Calabrò et al., 2018; Sloot et al., 2018) or as an outcome measure following robotic training (Hesse et al., 2010; Chisari et al., 2015; Gandolfi et al., 2017). One study employed EMG activity as a calibration tool to identify individualized, optimal robotic parameters based on the gait index score derived from a normalized dataset (Gandolla et al., 2018). Every study used a symmetrical scheme for electrode placement, collecting EMG signals from both stroke-affected and contralateral sides, with the exception of one study (Srivastava et al., 2016) that collected EMG data from the paretic leg only. The number of muscle groups for EMG signal capture varied from only one muscle site (Quadriceps) (Chisari et al., 2015) to up to seven different muscle groups per limb (Hesse et al., 2010; Coenen et al., 2012), with no clear rationale for the muscle groups provided. Three studies referenced the guidelines used to identify optimal electrode placement (SENIAM guidelines) (Chisari et al., 2015; Gandolfi et al., 2017; Gandolla et al., 2018). Eleven out of the 13 studies tested the dorsi-flexors and the plantar-flexors of the ankle joint. Knee joint muscles were assessed by 12 studies. One of these studies recorded rectus femoris only (Chisari et al., 2015), whereas the others registered both flexor and extensor muscle groups. The hip musculature was addressed in three studies (Hesse et al., 2010; Coenen et al., 2012; Srivastava et al., 2016).

Muscle activity and timing of onset were registered and interpreted in relation to the gait cycle in 10 studies (Hesse et al.,

TABLE 3 | Electroencephalography (EEG) signal processing in included studies.

References	Protocol and analysis	Channels	Frequencies	Filtering	Reference	Additional
Calabrò et al. (2018)	High-input impedance amplifier (Brain Quick SystemPLUS, IT) Eyes open recording pre-post rehab session Low-resolution brain electromagnetic tomography to identify cortical activations induced by gait training Structural equation modeling	21 (10–20 config)	512 Hz	BP, 0.3–70 Hz	Referenced to linked earlobes	Electrooculogram
Contreras-Vidal et al. (2018)	Wireless, active electrode EEG (BrainAmpDC, DE) Signals acquired during overground gait session Peripheral channels removed Detrend the remaining channels Down-sample to 100 Hz to match the frequency of H2 EEG and kinematics segmented in walk/stop epochs Principal component analysis applied to EEG data matrix to reduce the dimensionality 10th-order unscented Kalman filter to decode joint kinematics	64	1,000 Hz	Butterworth 4th-order Zero-phase BP, 0.1–3 Hz	FCz	Kinematic data acquired by H2
He et al. (2014)	actiCap system (Brain Products GmbH, DE) Data collected during robotic gait Peripheral channels removed Principal component analysis applied to the EEG data matrix to reduce the dimensionality Common average filter (CAR) 10th-order unscented Kalman filter to predict goniometer and electromyography measurements	64 (10–20 config)	1,000 Hz	BP, 0.01–100 Hz	FCz	EMG Biaxial electrogoniometer Hip and Knee angles measured by the X1

Filter type: BP, band-pass; LP, low-pass; HP, high-pass.

2010; Coenen et al., 2012; Ping et al., 2013; Srivastava et al., 2016; Gandolfi et al., 2017; Androwis et al., 2018; Calabrò et al., 2018; Gandolla et al., 2018; Sloot et al., 2018). A variety of methods were employed, including instrumented gait analysis systems (Androwis et al., 2018), synchronized video analysis (Coenen et al., 2012; Ping et al., 2013), accelerometry (Calabrò et al., 2018), shoe-mounted sensors (Hesse et al., 2010; Gandolfi et al., 2017), or through the monophasic soleus muscle EMG activity and deactivation during gait, where the signal portion between two soleus muscle deactivations corresponds to a step cycle (Gandolla et al., 2018). The detailed protocols, where provided by the authors, are summarized in **Table 5**. Where explicitly reported, all studies set the EMG sampling frequency at or over 1,000 Hz in accordance with the Nyquist sampling principle. This was not specified in four studies (Fan and Yin, 2013; Ping et al., 2013; Gandolla et al., 2018; Sloot et al., 2018). Impedance was checked and kept below 5 kΩ by two studies (Hesse et al., 2010; Gandolfi et al., 2017), while the other studies did not specify impedance checking. The studies applied different signal filtering methods (Butterworth, high/low/band-pass filtering, keeping signals usually between 5/20–300/400/500 Hz). The signals were full-wave-rectified, and root mean square was applied to calculate the EMG amplitude and to provide a global overview of the muscle activity.

Co-registered EMG and EEG Data Collection

Only two papers (He et al., 2014; Calabrò et al., 2018) captured both EEG and EMG data. One study decoded the muscle activation patterns by scalp EEG signals during robotic walking, demonstrating reasonable success at decoding the hip and knee EMG activity in the affected leg of a stroke survivor (He et al., 2014). The authors cited difficulty with the EMG data collection, however, as the exoskeleton device and its attachments, in many cases, were located at the same anatomical sites as the EMG electrodes. The second study reported EMG and EEG as separate measures and was therefore not considered a co-registration of neural signals (Calabrò et al., 2018).

Quality Review

As identified in **Table 5**, many studies were rated as "weak," using the EPHPP guidance tool, primarily due to a potential selection bias during participant recruitment, thereby limiting their representation of the stroke population. Here the majority of studies failed to identify their recruitment strategy. Similarly, the studies received a lower quality rating where the reliability and the validity of the data collection methods were not explicitly reported.

DISCUSSION

This systematic review compiled the current state of the art in the use of neural biosignals during robotic gait training after a stroke. No studies that used EEG signals to close the loop between human and robotic gait device were identified. Two BCI studies that show promise (with adequate training) were identified for the classification of gait in an exoskeleton after a stroke with a view toward a future BCI application (He et al., 2014; Contreras-Vidal et al., 2018). The work presented by Contreras-Vidal (Contreras-Vidal et al., 2018) builds on a previously published

TABLE 4 | Electromyography (EMG) signal processing in included studies.

References	Recording device and processing	Muscles	Hip	Knee	Ankle	Wireless	Frequencies	Filtering	Additional devices
Androwis et al. (2018)	Noraxon (AZ, USA) Amplitude analysis: integrated EMG Timing analysis: Burst Duration Similarity Index	TA, SOL, RF, VL, BF, gastrocnemius	N	Y	Y	Y	2,520 Hz	Butterworth 4th-order Zero-lag BP, 20–300 Hz Notch, 60 Hz	Retroreflective markers
Calabrò et al. (2018)	8-ch BTS (IT) Root mean square for muscle activation	TA, SOL, RF, BF	N	Y	Y	Y	1,000 Hz	BP, 5–300 Hz	Accelerometer
Chisari et al. (2015)	Noraxon, Telemyo 2400T V2 SENIAM guidelines Reference electrode on the patella Frequencies at 50, 75, and 95% of the total power spectral density were estimated Root mean square normalized for the RMS of the maximum voluntary contraction	VM	N	Y	N	Y	3,000 Hz	Zero-lag BP, 20–500 Hz	Isokinetic dynamometer
Coenen et al. (2012)	16-ch Porti (NL) Envelope calculation: rectified EMG, 4th-order LP Butterworth 5 Hz	GM, TA, ST, RF, AL, GLM, GLm	Y	Y	Y	N	1,000 Hz	Butterworth 4th-order, HP, 20 Hz	Video gait analysis
Fan and Yin (2013)	2-ch self-made sEMG acquisition processor	BF and quadriceps	N	Y	N	NS	NS	BP, 10–500 Hz Notch, 50 Hz	Force sensors, angular encoders
Gandolfi et al. (2017)	Device not defined SENIAM guidelines Envelope representation	TA, RF, BF, gastrocnemius	N	Y	Y	NS	1,000 Hz	LP, 480 Hz	Pressure sensor (overshoes)
Gandolla et al. (2018)	FREEEMG (BTS Bioengineering, IT) SENIAM guidelines No processing (activation timing only)	TA, SOL, RF, ST	N	Y	Y	Y	NS	Butterworth 6th-order, HP, 20 Hz	
He et al. (2014)	8-ch DataLOG MWX8 (Biometrics)	TA, VL, BF, gastrocnemius	N	Y	Y	Y	1,000 Hz	BP, 20–460 Hz	Biaxial electrogoniometers, hip and knee angles measured by the X1
Hesse et al. (2010)	Device not defined SENIAM guidelines EMG mean onset and offset points of activation determined by thresholding the envelope	TA, VM, VL, RF, BF, GLm, gastrocnemius	Y	Y	Y	NS	1,000 Hz	1st-order LP, 500 Hz	Overshoe force sensors
Ping et al. (2013)	Device not defined EMG activity was acquired during the robotic gait and referred to the % of the gait cycle. Patients' EMG was confronted with the activity of a healthy control Research focuses on the shape of EMG profile, times of peak, or onset/cessation of myoelectric activity	TA, GM, VL, RF, ST, SM	N	Y	Y	NS	NS	NS	
Sloot et al. (2018)	EMG device not defined Compared maximum EMG values during push-off and swing between with and without robotic device	TA, GM, SOL	N	N	Y	NS	NS	NS	
Srivastava et al. (2016)	16-ch MA-416-003 Motion Lab System (LA) Signal normalization to its peak amplitude Non-negative matrix factorization (dimensionality reduction) to compute muscle modes and understand the effects of gait training on coordination	BF, VL, VM, RF, GLm, SOL, GL, GM, TA, medial hamstrings	Y	Y	Y	N	1,200 Hz	HP, 20 Hz	

Muscle abbreviations: TA, tibialis anterior; GL, gastrocnemius lateralis; GM, gastrocnemius medialis; SOL, soleus; RF, rectus femoris; VL, vastus lateralis; VM, vastus medialis; BF, biceps femoris; ST, semitendinosus; SM, semimembranosus; AL, adductor longus; GLM, gluteus maximus; GLm, gluteus medius (GLm). Filter type: BP, band-pass; LP, low-pass; HP, high-pass.

TABLE 5 | Quality rating of included studies.

References	Selection bias	Study design	Confounders	Blinding	Data collection methods	Withdrawal and dropouts	Total score
Androwis et al. (2018)	Moderate	Moderate	N/A	N/A	Moderate	Moderate	Strong
Calabrò et al. (2018)	Moderate	Strong	Strong	Moderate	Strong	Strong	Strong
Chisari et al. (2015)	Moderate	Moderate	N/A	N/A	Moderate	Weak	Moderate
Coenen et al. (2012)	Moderate	Moderate	Weak	N/A	Weak	Weak	Weak
Contreras-Vidal et al. (2018)	Weak	Moderate	N/A	N/A	Strong	Strong	Moderate
Fan and Yin (2013)	Weak	Weak	Weak	N/A	Weak	Strong	Weak
Gandolfi et al. (2017)	Weak	Moderate	Weak	Moderate	Moderate	Strong	Weak
Gandolla et al. (2018)	Moderate	Weak	N/A	N/A	Strong	N/A	Moderate
He et al. (2014)	Weak	Weak	N/A	N/A	Moderate	N/A	Weak
Hesse et al. (2010)	Weak	Weak	N/A	N/A	Weak	Strong	Weak
Ping et al. (2013)	Weak	Moderate	Weak	N/A	Weak	N/A	Weak
Sloot et al. (2018)	Weak	Moderate	N/A	N/A	Weak	N/A	Weak
Srivastava et al. (2016)	Weak	Strong	Strong	Weak	Strong	Weak	Weak

N/A, not applicable.

framework proposed by this study group (Contreras-Vidal and Grossman, 2013). Otherwise, as with the majority of the EMG studies identified, the EEG signals were used as an outcome measure to evaluate RGT devices in stroke rehabilitation, for example, as an index of fronto-parietal connectivity to quantify neuroplastic changes (Calabrò et al., 2018). A recent systematic review of BCI rehabilitation in stroke supports this finding, where EEG was used to trigger neuromuscular electrical stimulation in the lower limb but not robotic gait devices to date (Cervera et al., 2018).

Specifying a search strategy that must include individuals with stroke in this systematic review yielded very limited EEG data. While this is informative with respect to the current state of the art in this area in stroke rehabilitation, it does not reflect the broader field of EEG-based control for robotic gait devices well. A recent systematic review by Al-Quraishi et al. (2018) comprehensively reported on EEG-based control for upper and lower limb exoskeletons and prostheses. In this review, 14 studies that used EEG-based control for lower limb movement, primarily in healthy subjects and individuals with spinal cord injury, were identified. Among those, nine studies targeted robotic gait-assistive devices (alone or in conjunction with an avatar), three used motor-imagery-only protocols with event-related desynchronization/resynchronization (ERD) (Do et al., 2013; Gordleeva et al., 2017; Lee et al., 2017), four used a movement-based protocol—with the EEG signal analysis undocumented in one (He et al., 2018b), and in the remaining three as ERD (Garcia-Cossio et al., 2015), combined ERD and movement-related cortical potential (MRCP) (López-Larraz et al., 2016), and exogenous steady-state visually evoked potentials with the visual stimuli representing robotic commands (Kwak et al., 2015). Two studies identified used a combination of motor imagery and movement using sensorimotor rhythms and MRCP (Liu et al., 2017) and event-related spectral pertubations (Donati et al., 2016). Notably, in one patient with a spinal cord injury, EEG signals were used to detect gait initiation to trigger the exoskeleton movement (López-Larraz et al., 2016). In another study with healthy individuals, online control of an overground exoskeleton using ERD in sensorimotor networks to train a classifier to identify two different mental states of walking forward intention or turning were demonstrated. In one body-weight-supported exoskeleton system, the user's intention was classified into active and passive walking phases using 62-channel EEG and power spectrum analysis in 8–30 Hz, normalized to the baseline condition to calculate ERD (Garcia-Cossio et al., 2015). The classification accuracies for active and passive walking with baseline were 94 and 93%, respectively, demonstrating the capability of BCI-assisted robotic training. The majority of EEG-based control in lower limb studies ($N = 11$; 79%) included in this cited review (Al-Quraishi et al., 2018) were markedly published from 2015 onwards, indicating a relatively new research area and, in part, explaining the poor penetration in the stroke population identified in this current systematic review. Another review of brain–machine interfaces for controlling lower limb powered robotic systems (He et al., 2018a) identifies that the most common studies in this area are classification-based studies of walk vs. stand tasks in healthy subjects and system performance is not clearly presented in these studies. Several challenges were summarized in this review, including EEG denoising, safety, and responsiveness. Furthermore, it concluded that suitable performance metrics and more clinical trials were required to advance research and development in the field.

One study that investigated closed-loop control between human and robotic gait device involving three stroke survivors was identified in this systematic review (Fan and Yin, 2013). EMG activity levels from knee flexor and extensor muscle groups were measured and a multisystem decoding paradigm, which included EMG in addition to joint angle and force production data, allowed the robotic command to be altered. High error rates in the commands generated during active movement were observed when flexion and extension activity alternated rapidly, limiting application in the clinical setting (Fan and Yin, 2013). EMG methods for motor intent identification have previously been noted to have significant limitations in stroke in that they are

only appropriate for patients who can produce some voluntary movement or high-enough levels of muscle activity and are not suitable for individuals with severe motor impairment, profound muscle fatigue, or abnormally coactivated muscles (Li et al., 2018). Concerns have also been raised that continuous EMG control may indeed reinforce pathological movement rather than encouraging the recovery of normal motion patterns (Krebs et al., 2003).

EMG has been combined with EEG to improve the recognition of movement intent in the upper limb (Bhagat et al., 2016) in the BCI literature. The current review identified two studies that recorded EEG and EMG. However, the two neural biosignals were not used in conjunction in either study to decode movement. One study reported these measures separately (Calabrò et al., 2018), while the other decoded EMG activity in the lower limbs using EEG during robotic walking in one stroke subject (He et al., 2014).

One example was identified in the literature where the best power transfer between subject and robot was achieved through a fine-tuning procedure for robotic parameters based on optimized EMG activity during the gait cycle (Gandolla et al., 2018); in this context, sEMG could prove to be a useful tool to optimize the patient–robot interaction in the clinical setting. However, the current lack of personalization of robotic gait command derived from neural biosignals and the limited ability to tailor robotic training to participant effort and to rehabilitative goals aligned with motor (re)learning principles limit their capacity as truly restorative devices in stroke rehabilitation. Robotic gait devices and the technological advancements enabling their continued development have been the preserve of the field of engineering (Pons, 2010). Translational research that examines deployment of devices in a clinical population must now also draw from expertise in rehabilitation and clinical research. This paper includes input from experts in the field of neurology, rehabilitation, bioengineering, and BCI engineering, discusses shortcomings in the papers identified, and makes recommendations to advance this field of research. A quick reference guide DESIRED (**Table 6**) has been developed by the group to identify a minimum reporting data set as a standard for future studies and the rationale and evidence base guiding these recommendations are described in detail next.

The majority of papers identified reported methodologies related to the devices, biosignals, and/or model development as appropriate to the domain of engineering. As a consequence, when considered as clinical studies in a stroke population and assessed using a broadly applicable quality rating tool (Thomas et al., 2004), the majority of studies were deemed to have a weak methodology. Consistent problems identified across studies related to the selection of stroke subjects and to the reporting of the validity and the reliability of the outcome measures employed. Guidelines with quality control checklists are available across a range of clinical study methodologies, for example, RCTs (Campbell et al., 2012), observational studies (Von Elm et al., 2014), and qualitative methodologies (Booth et al., 2014). When introducing participants with stroke or other neurological pathologies to robotic and/or neural signal-based studies, it is recommended that the authors familiarize themselves with the criteria expected based on the study type to be reported in the paper.

It is interesting to note that none of the papers reviewed provided a rationale for their selection of the stroke participants, and limited details on stroke pathology, stroke laterality, and stroke severity levels were documented. The time from stroke, for example, is something that further warrants attention. After focal damage, there is a brief, approximately 3 months, window of heightened plasticity, the so-called opportunity window which, in combination with training protocols, leads to large gains in motor function (Zeiler and Krakauer, 2013). Emerging evidence now supports smaller, plastic, and non-compensatory recovery in the chronic stages after a stroke also (Mrachacz-Kersting et al., 2015; Carvalho et al., 2018). To compare the neural biosignals and their utility in robotic gait training after a stroke across studies and to allow the results to be interpreted correctly, it is imperative to report this information. No consensus was observed across studies with respect to the gait impairment level of those included in the studies and ranged from those fully and independently mobile to those who are wheelchair dependent, again limiting the conclusions that can be drawn across studies. To stratify the findings from future studies, a minimum data set for participants with stroke is recommended and summarized as: stroke type, laterality, time from stroke to inclusion in the study, and functional ambulatory category (Mehrholz et al., 2007). The impairment of sensation also needs to be taken into account, given that accurate motor control can only be exerted with correct sensory and proprioceptive input. An index of stroke severity would also be a useful addition, for example, the National Institutes of Health Stroke Scale score (Ortiz and Sacco, 2014), as well as the level of cognitive function of the participants, if this is not a stated inclusion/exclusion criterion. To best replicate clinical application, it is advised that only the participants with gait impairment are included in the research.

A review of the brain–machine interface for lower limb systems after a stroke, published in 2015, concluded that additional research and development were required to advance this field (Soekadar et al., 2015). This systematic review now identifies that EEG data use during robotic gait after a stroke remains sub-optimal to closing the loop between person and robot. It is acknowledged that EEG activity during walking is not well-understood in general and discordance exists in the literature on the temporal and the spectral patterns of cortical dynamics during walking (Wagner et al., 2012, 2014; Seeber et al., 2014, 2015; Bradford et al., 2015; Bruijn et al., 2015; Bulea et al., 2015; Storzer et al., 2016; Winslow et al., 2016; Artoni et al., 2017; Luu et al., 2017; Oliveira et al., 2017). A number of research groups (Bradford et al., 2015; Bruijn et al., 2015; Bulea et al., 2015; Winslow et al., 2016; Artoni et al., 2017; Luu et al., 2017; Oliveira et al., 2017) report event-related (de)synchronization (ERD/S) (i.e., an event-related power change) in 8–12 Hz (alpha/mu) and 12–28 Hz (beta) oscillations after the onset of stepping/walking task (Bradford et al., 2015; Bruijn et al., 2015; Bulea et al., 2015; Winslow et al., 2016; Artoni et al., 2017; Luu et al., 2017; Oliveira et al., 2017), while other research groups report ERS at 28–40 Hz (low gamma) during early and mid-swing and ERD toward the end of the swing phase and during double support (Wagner et al.,

TABLE 6 | The DESIRED checklist: minimal reporting dataset for neural biosignals during robotic gait after a stroke.

DESIRED	Minimal requirement	Recommended but not mandatory
Description of study methodology	Adequate description of the clinical study type: e.g., randomized controlled trial; observational study: case study; case series, cross-sectional, pre–post design; mixed methods	Published guideline for study type referenced and checklist completed
Explicit reporting of stroke participant recruitment strategy	Recruitment method stated. Focus of the study on acute/subacute/chronic phases of stroke stated. Number of potential participants approached and number who entered the study described	Participants' location is described, e.g., in-patient acute or rehabilitation center; out-patient rehabilitation center; community dwelling and attending community services or no current rehabilitation provided at the time of recruitment
Stroke participant profile	Stroke pathology, e.g., ischemic or hemorrhagic, stroke side (at brain level); time from stroke to study participation; provide an index of gait impairment, e.g., functional ambulatory category; identify the presence and the type of sensory impairment where relevant	Stroke severity described, e.g., National Institutes of Health Stroke Scale (score included); cognitive level/s described
Intervention described using FITT principles	Frequency, intensity, time, and type of intervention reported	Report who delivered the intervention; the level of skill and training of the interventionist and whether there was fidelity of interventionist
Robotic gait training	Device and manufacturer; exoskeleton vs. end-effector device; over-ground vs. treadmill walking	Robotic mode settings described, e.g., whether step trajectory is fully supported by the robotic device or whether the device allows participant contribution to the step generated
Electroencephalography data capture	At minimum 32-electrode EEG with inclusion of activity from the central pre-motor/motor/sensorimotor and posterior parietal cortical areas to categorize walking from rest and ensuring frequency bands in 8–12 Hz (alpha/mu), 12–28 Hz (beta), and 28–40 Hz (low gamma) are represented in the data collection For motion trajectory prediction, global analysis to identify the most suitable features (potential or band-power time-series, low-delta, mu, or beta frequency band and all cortical areas) currently recommended	State if active electrodes are used and, if so, the planned data filtering. Use of source-resolved EEG dynamics during walking (mobile brain/body imaging) Minimization of artifactual contamination of lateral electrode signals by neck muscle electromyography during walking by blind source separation (typically by independent component analysis or frequency clustering) Potential time-series of the low-delta EEG oscillations or band-power time-series of the mu and beta EEG oscillations may hold the most information for motion trajectory prediction but further supporting research is required
Electromyography data capture	Minimum of two agonist/antagonist paired muscles in the distal and proximal compartment of stroke-affected and contralateral leg. Tibialis anterior, soleus, rectus femoris, and vastus lateralis recommended where stroke impairment and robotic gait device allow clean signal to be collected. Identification of the minimal crosstalk area of the muscle for electrode placement using the guidelines given by Basmajian and Blummenstein, updated by Blanc and Dimanico, with the axis of the electrodes directed parallel to the muscle fibers	Sensor placement checks for single muscles by checking for crosstalk on the other collected traces is recommended where spasticity or muscle shortening is present. Power spectral density computation may be useful when using exoskeleton gait devices to unravel unwanted electrical interference from electrical actuators, battery packs, and cables

2012, 2014; Seeber et al., 2014, 2015; Storzer et al., 2016). The literature does call attention to the importance of the central pre-motor/motor/sensorimotor and posterior parietal cortical areas in neural signal generation during the walking tasks. Thus, for the separation of walking from rest periods, we recommend the above-described cortical areas and the frequency bands are represented in the data collected and processed.

Decoding the 3D motion trajectory of the lower limbs is a more challenging objective (Georgopoulos et al., 2005). In BCI, this method poses an ideal solution for controlling a robotic device as the applied signal processing algorithm reconstructs the track of the intended movement. To date, most joint trajectory decoding studies have focused on reconstructing the movement of the upper limbs (Bradberry et al., 2010) and fingers (Paek et al., 2014) using 0.5–2 Hz slow cortical potentials (SCP) or band-power time-series of mu and beta bands (Korik et al., 2015, 2016, 2018). Motion trajectory prediction has successfully been applied to lower limb kinematics during treadmill walking in healthy individuals by Presacco et al. (2011, 2012) using SCP time-series. Here topographical analysis did not identify a significant pattern of lower limb movement-related cortical areas. Two studies included in this current review identified the utility of the 0.1–3 Hz frequency band for decoding kinematic data (He et al., 2014; Contreras-Vidal et al., 2018) and EMG kinetics during robotic walking after a stroke (He et al., 2014). One of these studies primarily focused on the frontal, temporal, and parietal brain regions (He et al., 2014), while others removed the peripheral channels susceptible to facial/cranial movement-related noise (Contreras-Vidal et al., 2018). Thus, as decoding the motion of lower limbs during walking is a nascent area, we still recommend a global analysis to identify the most suitable features (potential or band-power time-series, low-delta, mu, or beta frequency band and all cortical areas). However, the SCP/mu and beta band-power time-series extracted from the central motor and posterior parietal areas most likely contain maximal information for decoding lower limb movement trajectories.

From the present review, the lack of a standardized EMG recording protocol when applied to people with stroke-related disability in interaction with exoskeletons is evident. This limitation hampers the constitution of shared database repositories and pooling of data. A protocol and reported methodology should include a minimum dataset of muscles, dimensions, and positioning criteria of the surface EMG electrodes, interelectrode distance, techniques to verify the system selectivity, and technical sampling requirements (e.g., amplifier characteristics, electrode diameter, and impedance limits). The guidelines also suggest the inclusion of additional details relating to signal analysis pipelines, such as filtering and signal quality checks (Blanc and Dimanico, 2010; Merletti and Farina, 2016; Benedetti et al., 2017).

Currently, no consensus exists on targeting specific muscle groups during gait analysis in stroke survivors. The surface EMG of agonist and antagonist lower limb muscle activity during gait is emerging as an effective way of defining motor control during spontaneous movement in stroke (Srivastava et al., 2019). A minimum set of agonist and antagonist muscles in the distal and the proximal compartment of the leg needs to be defined to provide comprehensive muscle recruitment patterns and muscle synergies during the gait cycle after a stroke, which could be helpful for future HMI. Additionally, for individuals after a stroke, sEMG data from both legs (stroke affected and non-affected sides) should be collected as motor deficits are not only associated with the stroke-affected side but also of the non-affected side during spontaneous walking (Parvataneni et al., 2007; Bagnato et al., 2009; Tseng and Morton, 2010; Raja et al., 2012). Recent reviews of muscle synergies in post-stroke gait and robotic gait devices support the need for better standardization of muscles chosen for EMG data capture (Molteni et al., 2018; Van Criekinge et al., 2019). Tibialis anterior, soleus, gastrocnemius, and rectus femoris were noted to be most commonly assessed in all muscle synergy studies after a stroke (Van Criekinge et al., 2019). Considering best clinical practice and the need to record agonist and antagonist muscles during gait, a minimum representative muscle set to be targeted in future studies is recommended as bilateral: tibialis anterior, soleus, rectus femoris, and vastus lateralis, where possible. Alternate muscle/s selection may need to be defined by the participant's stroke-related muscle impairment/s or the robotic gait device and its positioning at specific anatomical landmarks for sensor placement, leading to muscle group exclusion.

Only three studies included in this review referred to a guideline document used for the correct positioning of electrodes on muscles. Failure to do this limits the reliable recording of muscle signals and does not address the challenge of avoiding "crosstalk" (diffused signal components coming from co-active or inactive adjacent muscles) (Basmajian, 1983). Correct sensor positioning aims to minimize this phenomenon and allows the researchers to identify a real co-contraction of agonist and antagonist muscle groups, which is common after a stroke. Basmajian and Blummenstein provide instructions to identify the minimal crosstalk area (MCA) for electrode placement on superficial muscles during gait (Basmajian and Blumenstein, 1980; Basmajian, 1983; Campanini et al., 2007; Blanc and Dimanico, 2010). Although the Surface EMG for Non-invasive Assessment of Muscles (SENIAM) guidelines referenced in the included studies are readily available and easy to use (www.seniam.org; Merletti, 2000), the MCA locations defined by Basmajian and Blummenstein, subsequently updated by Blanc and Dimanico (Blanc and Dimanico, 2010), have been proven to be superior to the SENIAM guidelines (Campanini et al., 2007). MCA identification would now be a minimum standard recommendation to follow in this field when studying the EMG timing during gait (Campanini et al., 2007), with the axis of the electrodes directed parallel to the muscle fibers to increase selectivity (Blanc and Dimanico, 2010). Additional quality assurance measures during robotic gait after a stroke, where feasible with the constraints of the device itself, could include sensor placement checks—performed by eliciting contractions of a single muscle and checking for crosstalk on the other collected traces (Benedetti et al., 2017) and strongly recommended where spasticity or muscle shortening may alter placement accuracy—and data check to ascertain the shape of the power spectral density (PSD) of the signal to ensure meaningful content (Merlo and Campanini, 2010), free of movement artifacts. When recording surface EMG in sessions that include the use of exoskeletons, electrical interference on EMG signals coming from electrical actuators, battery packs, and cables is not unexpected, and the PSD computation could prove to be a powerful tool to unravel such unwanted events.

LIMITATIONS

The authors acknowledge that while no language limits were applied when searching across databases, no papers were returned in languages other than English. As such, it is possible that additional manuscripts exist that were not identified through this search strategy. The search also returned studies with heterogeneous use of neural bio-signals, including as an outcome measurement only. While these were included in the review, their purpose was not in line with the primary focus of this review. However, in unifying all studies in this area irrespective of their set purpose, biosignal collection and interpretation in this field could be generalized and commented on constructively.

CONCLUSION

Overall, while there are ever-growing technological advances in robotics, actuators, and sensors, advances in applications to entrain robotic commands with biosignals for gait training in clinical populations such as stroke have been considerably slower. EEG recording in stroke, where the pathology is at the brain level, has been problematic when compared to other neurological pathologies such as spinal cord injury (Castermans et al., 2014), and similarly EMG recording on the stroke-affected side can be problematic (Sarasola-Sanz et al., 2017; Li et al., 2018). Uncertainty still exists in the literature on the best choice of EEG metric (Goh et al., 2018) and in the ability of EMG to respond accurately in real time (Fan and Yin, 2013). This review, summarizing the current state of the art in neural

interface during robotic-assisted gait training after a stroke, identifies a lack of standardization in data collection in this field and provides guidance for study design and reporting future studies. Promising findings for decoding movement during robotic gait after a stroke and potential for EMG, in conjunction with other measurement modes to close the loop, have been elucidated.

DATA AVAILABILITY STATEMENT

All datasets generated for this study are included in the article/supplementary material.

AUTHOR CONTRIBUTIONS

OL, AD, EG, FM, CG, and DC developed the concept for this systematic review. OL, MT, RO, and CF contributed to the development of the search strategy, review of papers, data extraction, and synthesis sections. All the authors had equal involvement in the drafting and the revising of the review article by unique contribution to the intellectual content and consensus among all the authors on the content.

FUNDING

This study has been supported by an EU-funded H2020 Research and Innovation Staff Exchange grant: PRO GAIT grant agreement number 778043. The funders had no role in the study design, data collection and analysis, decision to publish, or preparation of the manuscript.

ACKNOWLEDGMENTS

We would like to thank Alex Heilinger and Diarmuid Stokes for their assistance during the development and the execution of the search strategy.

REFERENCES

Al-Quraishi, M. S., Elamvazuthi, I., Daud, S. A., Parasuraman, S., and Borboni, A. (2018). EEG-based control for upper and lower limb exoskeletons and prostheses: a systematic review. *Sensors* 18:3342. doi: 10.3390/s18103342

Androwis, G. J., Pilkar, R., Ramanujam, A., and Nolan, K. J. (2018). Electromyography assessment during gait in a robotic exoskeleton for acute stroke. *Front. Neurol.* 9:630. doi: 10.3389/fneur.2018.00630

Ang, K. K., Guan, C., Phua, K. S., Wang, C., Zhou, L., Tang, K. Y., et al. (2014). Brain-computer interface-based robotic end effector system for wrist and hand rehabilitation: results of a three-armed randomized controlled trial for chronic stroke. *Front. Neuroeng.* 7:30. doi: 10.3389/fneng.2014.00030

Artoni, F., Fanciullacci, C., Bertolucci, F., Panarese, A., Makeig, S., Micera, S., et al. (2017). Unidirectional brain to muscle connectivity reveals motor cortex control of leg muscles during stereotyped walking. *Neuroimage* 159, 403–416. doi: 10.1016/j.neuroimage.2017.07.013

Bagnato, S., Boccagni, C., Boniforti, F., Trinchera, A., Guercio, G., Letizia, G., et al. (2009). Motor dysfunction of the "non-affected" lower limb: a kinematic comparative study between hemiparetic stroke and total knee prosthesized patients. *Neurol. Sci.* 30, 107–113. doi: 10.1007/s10072-009-0031-0

Basmajian, J. V. (1983). "Electrode placement in electromyographic biofeedback," in *Biofeedback Principles and Practice for clinicians* (Baltimore: Williams & Wilkins), 1–86.

Basmajian, J. V., and Blumenstein, R. (1980). *Electrode Placement in EMG Biofeedback*. Baltimore, MD: Williams and Wilkins.

Benedetti, M. G., Beghi, E., De Tanti, A., Cappozzo, A., Basaglia, N., Cutti, A. G., et al. (2017). SIAMOC position paper on gait analysis in clinical practice: general requirements, methods and appropriateness. Results of an Italian consensus conference. *Gait Posture* 58, 252–260. doi: 10.1016/j.gaitpost.2017.08.003

Bhagat, N. A., Venkatakrishnan, A., Abibullaev, B., Artz, E. J., Yozbatiran, N., Blank, A. A., et al. (2016). Design and optimization of an EEG-based brain machine interface (BMI) to an upper-limb exoskeleton for stroke survivors. *Front. Neurosci.* 10:122. doi: 10.3389/fnins.2016.00122

Blanc, Y., and Dimanico, U. (2010). Electrode placement in Surface electromyography (sEMG)" Minimal Crosstalk Area "(MCA). *Open Rehabil. J.* 3, 110–126. doi: 10.2174/1874943701003010110

Booth, A., Hannes, K., Harden, A., Noyes, J., Harris, J., and Tong, A. (2014). "COREQ (consolidated criteria for reporting qualitative studies)," in *Guidelines for Reporting Health Research: A User's Manual,* eds D. Moher, D. G. Altman, K. F. Schulz, I. Simera, E. Wager (Hoboken, NJ: John Wiley & Sons, Ltd), 214–226.

Bradberry, T. J., Gentili, R. J., and Contreras-Vidal, J. L. (2010). Reconstructing three-dimensional hand movements from noninvasive electroencephalographic signals. *J. Neurosci.* 30, 3432–3437. doi: 10.1523/JNEUROSCI.6107-09.2010

Bradford, J. C., Lukos, J. R., and Ferris, D. P. (2015). Electrocortical activity distinguishes between uphill and level walking in humans. *J. Neurophysiol.* 115, 958–966. doi: 10.1152/jn.00089.2015

Bruijn, S. M., Van Dieën, J. H., and Daffertshofer, A. (2015). Beta activity in the premotor cortex is increased during stabilized as compared to normal walking. *Front. Hum. Neurosci.* 9:593. doi: 10.3389/fnhum.2015.00593

Bruni, M. F., Melegari, C., De Cola, M. C., Bramanti, A., Bramanti, P., and Calabrò R. S. (2018). What does best evidence tell us about robotic gait rehabilitation in stroke patients: a systematic review and meta-analysis. *J. Clin. Neurosci.* 48, 11–17. doi: 10.1016/j.jocn.2017.10.048

Bulea, T. C., Kim, J., Damiano, D. L., Stanley, C. J., and Park, H.-S. (2015). Prefrontal, posterior parietal and sensorimotor network activity underlying speed control during walking. *Front. Hum. Neurosci.* 9:247. doi: 10.3389/fnhum.2015.00247

Cai, L. L., Fong, A. J., Otoshi, C. K., Liang, Y., Burdick, J. W., Roy, R. R., et al. (2006). Implications of assist-as-needed robotic step training after a complete spinal cord injury on intrinsic strategies of motor learning. *J. Neurosci.* 26, 10564–10568. doi: 10.1523/JNEUROSCI.2266-06.2006

Calabrò R. S., Naro, A., Russo, M., Bramanti, P., Carioti, L., Balletta, T., et al. (2018). Shaping neuroplasticity by using powered exoskeletons in patients with stroke: a randomized clinical trial. *J. Neuroeng. Rehabil.* 15:35. doi: 10.1186/s12984-018-0377-8

Campanini, I., Merlo, A., Degola, P., Merletti, R., Vezzosi, G., and Farina, D. (2007). Effect of electrode location on EMG signal envelope in leg muscles during gait. *J. Electromyogr. Kinesiol.* 17, 515–526. doi: 10.1016/j.jelekin.2006.06.001

Campbell, M. K., Piaggio, G., Elbourne, D. R., and Altman, D. G. (2012). Consort 2010 statement: extension to cluster randomised trials. *BMJ* 345:e5661. doi: 10.1136/bmj.e5661

Carvalho, R., Azevedo, E., Marques, P., Dias, N., and Cerqueira, J. J. (2018). Physiotherapy based on problem-solving in upper limb function and neuroplasticity in chronic stroke patients: a case series. *J. Eval. Clin. Pract.* 24, 552–560. doi: 10.1111/jep.12921

Castermans, T., Duvinage, M., Cheron, G., and Dutoit, T. (2014). Towards effective non-invasive brain-computer interfaces dedicated to gait rehabilitation systems. *Brain Sci.* 4, 1–48. doi: 10.3390/brainsci4010001

Cervera, M. A., Soekadar, S. R., Ushiba, J., Millán, J. D., Liu, M., Birbaumer, N., et al. (2018). Brain-computer interfaces for post-stroke motor rehabilitation: a meta-analysis. *Ann. Clin. Transl. Neurol.* 5, 651–663. doi: 10.1002/acn3.544

Chisari, C., Bertolucci, F., Monaco, V., Venturi, M., Simonella, C., Micera, S., et al. (2015). Robot-assisted gait training improves motor performances and modifies Motor Unit firing in poststroke patients. *Eur. J. Phys. Rehabil. Med.* 51, 59–69. Available online at: https://www.minervamedica.it/en/journals/europa-medicophysica/article.php?cod=R33Y2015N01A0059

Coenen, P., van Werven, G., van Nunen, M. P., Van Dieën, J. H., Gerrits, K. H., and Janssen, T. W. (2012). Robot-assisted walking vs overground walking in stroke patients: an evaluation of muscle activity. *J. Rehabil. Med.* 44, 331–337. doi: 10.2340/16501977-0954

Contreras-Vidal, J. L., Bortole, M., Zhu, F., Nathan, K., Venkatakrishnan, A., Francisco, G. E., et al. (2018). Neural decoding of robot-assisted gait during rehabilitation after stroke. *Am. J. Phys. Med. Rehabil.* 97, 541–550. doi: 10.1097/PHM.0000000000000914

Contreras-Vidal, J. L., and Grossman, R. G. (2013). "NeuroRex: a clinical neural interface roadmap for EEG-based brain machine interfaces to a lower body robotic exoskeleton," in *2013 35th Annual International Conference of the IEEE Engineering in Medicine and Biology Society (EMBC)* (Osaka. IEEE).

Do, A. H., Wang, P. T., King, C. E., Chun, S. N., and Nenadic, Z. (2013). Brain-computer interface controlled robotic gait orthosis. *J. Neuroeng. Rehabil.* 10:111. doi: 10.1186/1743-0003-10-111

Donati, A. R., Shokur, S., Morya, E., Campos, D. S., Moioli, R. C., Gitti, C. M., et al. (2016). Long-term training with a brain-machine interface-based gait protocol induces partial neurological recovery in paraplegic patients. *Sci. Rep.* 6:30383. doi: 10.1038/srep30383

Fan, Y., and Yin, Y. (2013). Active and progressive exoskeleton rehabilitation using multisource information fusion from emg and force-position epp. *IEEE Transac. Biomed. Eng.* 60, 3314–3321. doi: 10.1109/TBME.2013.2267741

Gandolfi, M., Geroin, C., Tomelleri, C., Maddalena, I., Kirilova, E. D., Picelli, A., et al. (2017). Feasibility and safety of early lower limb robot-assisted training in sub-acute stroke patients: a pilot study. *Eur. J. Phys. Rehabil. Med.* 53, 870–882. doi: 10.23736/S1973-9087.17.04468-9

Gandolla, M., Guanziroli, E., D'Angelo, A., Cannaviello, G., Molteni, F., and Pedrocchi, A. (2018). Automatic setting procedure for exoskeleton-assisted overground gait: proof of concept on stroke population. *Front. Neurorobot.* 12:10. doi: 10.3389/fnbot.2018.00010

Garcia-Cossio, E., Severens, M., Nienhuis, B., Duysens, J., Desain, P., Keijsers, N., et al. (2015). Decoding sensorimotor rhythms during robotic-assisted treadmill walking for brain computer interface (BCI) applications. *PLoS ONE* 10:137910. doi: 10.1371/journal.pone.0137910

Georgopoulos, A. P., Langheim, F. J., Leuthold, A. C., and Merkle, A. N. (2005). Magnetoencephalographic signals predict movement trajectory in space. *Exp. Brain Res.* 167, 132–135. doi: 10.1007/s00221-005-0028-8

Goh, S. K., Abbass, H. A., Tan, K. C., Al-Mamun, A., Thakor, N., Bezerianos, A., et al. (2018). Spatio–spectral representation learning for electroencephalographic gait-pattern classification. *IEEE Transac. Neural Syst. Rehabil. Eng.* 26, 1858–1867. doi: 10.1109/TNSRE.2018.2864119

Goodman, R. N., Rietschel, J. C., Roy, A., Jung, B. C., Diaz, J., Macko, R. F., et al. (2014). Increased reward in ankle robotics training enhances motor control and cortical efficiency in stroke. *J. Rehabil. Res. Dev.* 51, 213–227, doi: 10.1682/JRRD.2013.02.0050

Gordleeva, S. Y., Lukoyanov, M. V., Mineev, S. A., Khoruzhko, M. A., Mironov, V. I., Kaplan, A. Y., et al. (2017). Exoskeleton control system based on motor-imaginary brain–computer interface. 9, 31–38. doi: 10.17691/stm2017.9.3.04

He, Y., Eguren, D., Azorín, J. M., Grossman, R. G., Luu, T. P., and Contreras-Vidal, J. L. (2018a). Brain–machine interfaces for controlling lower-limb powered robotic systems. *J. Neural Eng.* 15:021004. doi: 10.1088/1741-2552/aaa8c0

He, Y., Luu, T. P., Nathan, K., Nakagome, S., and Contreras-Vidal, J. L. (2018b). A mobile brain-body imaging dataset recorded during treadmill walking with a brain-computer interface. *Sci. Data* 5:180074. doi: 10.1038/sdata.2018.74

He, Y., Nathan, K., Venkatakrishnan, A., Rovekamp, R., Beck, C., Ozdemir, R., et al. (2014). An integrated neuro-robotic interface for stroke rehabilitation using the NASA X1 powered lower limb exoskeleton. *Conf. Proc. IEEE Eng. Med. Biol. Soc.* 2014, 3985–3988. doi: 10.1109/EMBC.2014.6944497

Heilinger, A., Lennon, O., and Ortner, R. (2018). *PROSPERO*. Available online at: http://www.crd.york.ac.uk/PROSPERO/display_record.php?ID=CRD42018112252

Hesse, S., Waldner, A., and Tomelleri, C. (2010). Innovative gait robot for the repetitive practice of floor walking and stair climbing up and down in stroke patients. *J. Neuroeng. Rehabil.* 7:30. doi: 10.1186/1743-0003-7-30

Higgins, J. P., and Green, S. (2011). *Cochrane Handbook for Systematic Reviews of Interventions*, Vol. 4 (Hoboken, NJ: John Wiley and Sons).

Ho, N. S., Tong, K. Y., Hu, X. L., Fung, K. L., Wei, X. J., Rong, W., et al. (2011). An EMG-driven exoskeleton hand robotic training device on chronic stroke subjects: task training system for stroke rehabilitation. *IEEE Int. Conf. Rehabil. Robot*. 2011:5975340. doi: 10.1109/ICORR.2011.5975340

Hogan, N., Krebs, H. I., Rohrer, B., Palazzolo, J. J., Dipietro, L., Fasoli, S. E., et al. (2006). Motions or muscles? Some behavioral factors underlying robotic assistance of motor recovery. *J. Rehabil. Res. Dev.* 43, 605–618. doi: 10.1682/JRRD.2005.06.0103

Hu, X. L., Tong, R. K., Ho, N. S., Xue, J. J., Rong, W., and Li, L. S. (2015). Wrist rehabilitation assisted by an electromyography-driven neuromuscular electrical stimulation robot after stroke. *Neurorehabil. Neural Repair* 29, 767–776. doi: 10.1177/1545968314565510

Hussein, S., Schmidt, H., and Kruger, J. (2009). Adaptive control of an end-effector based electromechanical gait rehabilitation device," in *2009 IEEE International Conference on Rehabilitation Robotics* (Kyoto: IEEE), 366–371.

Israel, J. F., Campbell, D. D., Kahn, J. H., and Hornby, T. G. (2006). Metabolic costs and muscle activity patterns during robotic-and therapist-assisted treadmill walking in individuals with incomplete spinal cord injury. *Phys. Ther.* 86, 1466–1478. doi: 10.2522/ptj.20050266

Itaya, T., Murakami, Y., Ota, A., Nomura, E., Fukushima, T., and Nishigaki, M. (2017). Assessment model to identify patients with stroke with a high possibility of discharge to home: a retrospective cohort study. *Stroke* 48, 2812–2818. doi: 10.1161/STROKEAHA.117.018075

Jiang, N., Mrachacz-Kersting, N., Xu, R., Dremstrup, K., and Farina, D. (2014). "An accurate, versatile, and robust brain switch for neurorehabilitation," in *Brain-Computer Interface Research* (Cham: Springer), 47–61.

Johnson, C. O., Nguyen, M., Roth, G. A., Nichols, E., Alam, T., Abate, D., et al. (2019). Global, regional, and national burden of stroke, 1990–2016: a systematic analysis for the Global Burden of Disease Study 2016. *Lancet Neurol.* 18, 439–458. doi: 10.1016/S1474-4422(19)30034-1

Korik, A., Siddique, N., Sosnik, R., and Coyle, D. (2015). "E3D hand movement velocity reconstruction using power spectral density of EEG signals and neural network," in *2015 37th Annual International Conference of the IEEE Engineering in Medicine and Biology Society (EMBC)* (Milan: IEEE), 8103–8106.

Korik, A., Sosnik, R., Siddique, N., and Coyle, D. (2016). "Imagined 3D hand movement trajectory decoding from sensorimotor EEG rhythms," in *2016 IEEE International Conference on Systems, Man, and Cybernetics (SMC)* (Budapest: IEEE), 4591–4596.

Korik, A., Sosnik, R., Siddique, N., and Coyle, D. (2018). Decoding imagined 3D hand movement trajectories from EEG: evidence to support the use of mu, beta, and low gamma oscillations. *Front. Neurosci.* 12:130. doi: 10.3389/fnins.2018.00130

Krebs, H. I., Palazzolo, J. J., Dipietro, L., Ferraro, M., Krol, J., Rannekleiv, K., et al. (2003). Rehabilitation robotics: performance-based progressive robot-assisted therapy. *Auton. Robots* 15, 7–20. doi: 10.1023/A:1024494031121

Krishnan, C., Kotsapouikis, D., Dhaher, Y. Y., and Rymer, W. Z. (2013). Reducing robotic guidance during robot-assisted gait training improves gait function: a case report on a stroke survivor. *Arch. Phys. Med. Rehabil.* 94, 1202–1206. doi: 10.1016/j.apmr.2012.11.016

Kwak, N.-S., Müller, K.-R., and Lee, S.-W. (2015). A lower limb exoskeleton control system based on steady state visual evoked potentials. *J. Neural Eng.* 12:056009. doi: 10.1088/1741-2560/12/5/056009

Kwakkel, G., van Peppen, R., Wagenaar, R. C., Wood Dauphinee, S., Richards, C., Ashburn, A., et al. (2004). Effects of augmented exercise therapy time after stroke: a meta-analysis. *Stroke* 35, 2529–2539. doi: 10.1161/01.STR.0000143153.76460.7d

Kwong, P. W., and Ng, S. S. (2019). Cutoff score of the lower-extremity motor subscale of fugl-meyer assessment in chronic stroke survivors: a cross-sectional study. *Arch. Phys. Med. Rehabil.* 100, 1782–1787. doi: 10.1016/j.apmr.2019.01.027

Lee, K., Liu, D., Perroud, L., Chavarriaga, R., and Millán, J. R. (2017). A brain-controlled exoskeleton with cascaded event-related desynchronization classifiers. *Rob. Auton. Syst.* 90, 15–23. doi: 10.1016/j.robot.2016.10.005

Li, M., Xu, G., Xie, J., and Chen, C. (2018). A review: motor rehabilitation after stroke with control based on human intent. *Proc. Inst. Mech. Eng. H* 232, 344–360. doi: 10.1177/0954411918755828

Lin, I. H., Tsai, H. T., Wang, C. Y., Hsu, C. Y., Liou, T. H., and Lin, Y. N. (2019). Effectiveness and superiority of rehabilitative treatments in enhancing motor recovery within 6 months poststroke: a systemic review. *Arch. Phys. Med. Rehabil.* 100, 366–378. doi: 10.1016/j.apmr.2018.09.123

Liu, D., Chen, W., Pei, Z., and Wang, J. (2017). A brain-controlled lower-limb exoskeleton for human gait training. *Rev. Sci. Instruments* 88:104302. doi: 10.1063/1.5006461

López-Larraz, E., Trincado-Alonso, F., Rajasekaran, V., Pérez-Nombela, S., Del-Ama, A. J., Aranda, J., et al. (2016). Control of an ambulatory exoskeleton with a brain–machine interface for spinal cord injury gait rehabilitation. *Front. Neurosci.* 10:359. doi: 10.3389/fnins.2016.00359

Luu, T. P., Brantley, J. A., Nakagome, S., Zhu, F., and Contreras-Vidal, J. L. (2017). Electrocortical correlates of human level-ground, slope, and stair walking. *PLoS ONE* 12:e0188500. doi: 10.1371/journal.pone.0188500

Mehrholz, J., Thomas, S., Werner, C., Kugler, J., Pohl, M., and Elsner, B. (2017). Electromechanical-assisted training for walking after stroke. *Cochrane Database Syst. Rev.* 5:CD006185. doi: 10.1002/14651858.CD006185.pub4

Mehrholz, J., Wagner, K., Rutte, K., Meißner, D., and Pohl, M. (2007). Predictive validity and responsiveness of the functional ambulation category in hemiparetic patients after stroke. *Arch. Phys. Med. Rehabil.* 88, 1314–1319. doi: 10.1016/j.apmr.2007.06.764

Merletti, R. (2000). Surface electromyography: the SENIAM project. *Eur. J. Phys. Rehabil. Med.* 36:167.

Merletti, R., and Farina, D. (2016). *Surface Electromyography: Physiology, Engineering, and Applications*. Hoboken, NJ: John Wiley and Sons.

Merlo, A., and Campanini, I. (2010). Technical aspects of surface electromyography for clinicians. *Open Rehabil. J.* 3, 98–109. doi: 10.2174/1874943701003010098

Moher, D., Liberati, A., Tetzlaff, J., and Altman, D. G. (2010). Preferred reporting items for systematic reviews and meta-analyses: the PRISMA statement. *Int. J. Surg.* 8, 336–341. doi: 10.1016/j.ijsu.2010.02.007

Molteni, F., Gasperini, G., Cannaviello, G., and Guanziroli, E. (2018). Exoskeleton and end-effector robots for upper and lower limbs rehabilitation: narrative review. *Phys. Med. Rehabil.* 10, S174–S188. doi: 10.1016/j.pmrj.2018.06.005

Mrachacz-Kersting, N., Jiang, N., Stevenson, A. J., Niazi, I. K., Kostic, V., Pavlovic, A., et al. (2015). Efficient neuroplasticity induction in chronic stroke patients by an associative brain-computer interface. *J. Neurophysiol.* 115, 1410–1421. doi: 10.1152/jn.00918.2015

Mrachacz-Kersting, N., Kristensen, S. R., Niazi, I. K., and Farina, D. (2012). Precise temporal association between cortical potentials evoked by motor imagination and afference induces cortical plasticity. *J. Physiol.* 590, 1669–1682. doi: 10.1113/jphysiol.2011.222851

Norrving, B., Barrick, J., Davalos, A., Dichgans, M., Cordonnier, C., Guekht, A., et al. (2018). Action plan for stroke in Europe 2018–2030. *Eur. Stroke J.* 3, 309–336. doi: 10.1177/2396987318808719

Oliveira, A. S., Schlink, B. R., Hairston, W. D., König, P., and Ferris, D. P. (2017). Restricted vision increases sensorimotor cortex involvement in human walking. *J. Neurophysiol.* 118, 1943–1951. doi: 10.1152/jn.00926.2016

Ortiz, G. A., and Sacco, L. R. (2014). *Wiley Stats Ref: Statistics Reference Online*. National Institutes of Health Stroke Scale (NIHSS).

Paek, A. Y., Agashe, H., and Contreras-Vidal, J. L. (2014). Decoding repetitive finger movements with brain activity acquired via non-invasive electroencephalography. *Front. Neuroeng.* 7:3. doi: 10.3389/fneng.2014.00003

Paredes, L. P., Farina, D., Shin, Y.-I., and Turolla, A. (2015). "Efficacy of torque versus myocontrol for active, robotic-assisted rehabilitation of the shoulder after stroke: an experimental study," in *2015 7th International IEEE/EMBS Conference on Neural Engineering (NER)* (Montpellier: IEEE), 627–630.

Parvataneni, K., Olney, S. J., and Brouwer, B. (2007). Changes in muscle group work associated with changes in gait speed of persons with stroke. *Clin. Biomech.* 22, 813–820. doi: 10.1016/j.clinbiomech.2007.03.006

Ping, W., Low, K., McLaren, J., and des Ouches, P. J. (2013). "Muscle activation of participants while walking on a robotic-assisted locomotion training," *39th Annual Northeast Bioengineering Conference* (IEEE), 19–20.

Pons, J. L. (2010). Rehabilitation exoskeletal robotics. *IEEE Eng. Med. Biol. Mag.* 29, 57–63. doi: 10.1109/MEMB.2010.936548

Prasad, G., Herman, P., Coyle, D., McDonough, S., and Crosbie, J. (2010). Applying a brain-computer interface to support motor imagery practice in people with stroke for upper limb recovery: a feasibility study. *J Neuroeng Rehabil.* 7:60. doi: 10.1186/1743-0003-7-60

Presacco, A., Forrester, L. W., and Contreras-Vidal, J. L. (2012). Decoding intra-limb and inter-limb kinematics during treadmill walking from scalp electroencephalographic (EEG) signals. *IEEE Transac. Neural Syst. Rehabil. Eng.* 20, 212–219. doi: 10.1109/TNSRE.2012.2188304

Presacco, A., Goodman, R., Forrester, L., and Contreras-Vidal, J. L. (2011). Neural decoding of treadmill walking from noninvasive electroencephalographic signals. *J. Neurophysiol.* 106, 1875–1887. doi: 10.1152/jn.00104.2011

Raja, B., Neptune, R. R., and Kautz, S. A. (2012). Coordination of the non-paretic leg during hemiparetic gait: expected and novel compensatory patterns. *Clin. Biomech.* 27, 1023–1030. doi: 10.1016/j.clinbiomech.2012.08.005

Sarasola-Sanz, A., Irastorza-Landa, N., Lopez-Larraz, E., Bibian, C., Helmhold, F., Broetz, D., et al. (2017). "A hybrid brain-machine interface based on EEG and EMG activity for the motor rehabilitation of stroke patients," in *IEEE International Conference on Rehabilitation Robotics,* Vol. 2017 (London), 895–900.

Seeber, M., Scherer, R., Wagner, J., Solis-Escalante, T., and Müller-Putz, G. R. (2014). EEG beta suppression and low gamma modulation are different elements of human upright walking. *Front. Hum. Neurosci.* 8:485. doi: 10.3389/fnhum.2014.00485

Seeber, M., Scherer, R., Wagner, J., Solis-Escalante, T., and Müller-Putz, G. R. (2015). High and low gamma EEG oscillations in central sensorimotor areas are conversely modulated during the human gait cycle. *Neuroimage* 112, 318–326. doi: 10.1016/j.neuroimage.2015.03.045

Sloot, L., Bae, J., Baker, L., O'Donnell, K., Menard, N., Porciuncula, F., et al. (2018). "O 089-A soft robotic exosuit assisting the paretic ankle in patients post-stroke: effect on muscle activation during overground walking," in *Gait Posture.* doi: 10.1016/j.gaitpost.2018.06.124

Soekadar, S. R., Birbaumer, N., Slutzky, M. W., and Cohen, L. G. (2015). Brain–machine interfaces in neurorehabilitation of stroke. *Neurobiol. Dis.* 83, 172–179. doi: 10.1016/j.nbd.2014.11.025

Srivastava, S., Kao, P. C., Reisman, D. S., Scholz, J. P., Agrawal, S. K., and Higginson, J. S. (2016). Robotic assist-as-needed as an alternative to therapist-assisted gait rehabilitation. *Int. J. Phys. Med. Rehabil.* 4:370. doi: 10.4172/2329-9096.1000370

Srivastava, S., Patten, C., and Kautz, S. A. (2019). Altered muscle activation patterns (AMAP): an analytical tool to compare muscle activity patterns of hemiparetic gait with a normative profile. *J. Neuroeng. Rehabil.* 16:21. doi: 10.1186/s12984-019-0487-y

Storzer, L., Butz, M., Hirschmann, J., Abbasi, O., Gratkowski, M., Saupe, D., et al. (2016). Bicycling and walking are associated with different cortical oscillatory dynamics. *Front. Hum. Neurosci.* 10:61. doi: 10.3389/fnhum.2016.00061

Taveggia, G., Borboni, A., Mulé, C., Villafañe, J. H., and Negrini, S. (2016). Conflicting results of robot-assisted versus usual gait training during postacute rehabilitation of stroke patients: a randomized clinical trial. *Int. J. Rehabil. Res.* 39:29. doi: 10.1097/MRR.0000000000000137

Thomas, B., Ciliska, D., Dobbins, M., and Micucci, S. (2004). A process for systematically reviewing the literature: providing the research evidence for public health nursing interventions. *Worldviews Evid. Based Nurs.* 1, 176–184. doi: 10.1111/j.1524-475X.2004.04006.x

Thomas, B., Ciliska, D., Dobbins, M., and Micucci, S. (2008). *Quality Assessment Tool for Quantitative Studies Dictionary*: *The Effective Public Health Practice Project (EPHPP)*. McMaster University.

Tseng, S. C., and Morton, S. M. (2010). Impaired interlimb coordination of voluntary leg movements in poststroke hemiparesis. *J. Neurophysiol.* 104, 248–257. doi: 10.1152/jn.00906.2009

Vaca Benitez, L. M., Tabie, M., Will, N., Schmidt, S., Jordan, M., and Kirchner, E. A. (2013). Exoskeleton technology in rehabilitation: towards an EMG-based orthosis system for upper limb neuromotor rehabilitation. *J. Robotics* 2013:610589. doi: 10.1155/2013/610589

Van Criekinge, T., Vermeulen, J., Wagemans, K., Schröder, J., Embrechts, E., Truijen, S., et al. (2019). Lower limb muscle synergies during walking after stroke: a systematic review. *Disabil. Rehabil.* 1–10. doi: 10.1080/09638288.2019.1578421

Van Dokkum, L., Ward, T., and Laffont, I. (2015). Brain computer interfaces for neurorehabilitation–its current status as a rehabilitation strategy post-stroke. *Ann. Phys. Rehabil. Med.* 58, 3–8. doi: 10.1016/j.rehab.2014.09.016

Varkuti, B., Guan, C., Pan, Y., Phua, K. S., Ang, K. K., Kuah, C. W., et al. (2013). Resting state changes in functional connectivity correlate with movement recovery for BCI and robot-assisted upper-extremity training after stroke. *Neurorehabil. Neural Repair* 27, 53–62. doi: 10.1177/1545968312445910

Veerbeek, J. M., van Wegen, E., van Peppen, R., van der Wees, P. J., Hendriks, E., Rietberg, M., et al. (2014). What is the evidence for physical therapy poststroke? A systematic review and meta-analysis. *PloS ONE* 9:e87987. doi: 10.1371/journal.pone.0087987

Von Elm, E., Altman, D. G., Egger, M., Pocock, S. J., Gøtzsche, P. C., Vandenbroucke, J. P., et al. (2014). The strengthening the reporting of observational studies in epidemiology (STROBE) statement: guidelines for reporting observational studies. *Int. J. Surg.* 12, 1495–1499. doi: 10.1016/j.ijsu.2014.07.013

Wagner, J., Solis-Escalante, T., Grieshofer, P., Neuper, C., Müller-Putz, G., and Scherer, R. (2012). Level of participation in robotic-assisted treadmill walking modulates midline sensorimotor EEG rhythms in able-bodied subjects. *Neuroimage* 63, 1203–1211. doi: 10.1016/j.neuroimage.2012.08.019

Wagner, J., Solis-Escalante, T., Scherer, R., Neuper, C., and Müller-Putz, G. (2014). It's how you get there: walking down a virtual alley activates premotor and parietal areas. *Front. Hum. Neurosci.* 8:93. doi: 10.3389/fnhum.2014.00093

Wilkins, E., Wilson, L., Wickramasinghe, K., Bhatnagar, P., Leal, J., Luengo-Fernandez, R., et al. (2017). *European Cardiovascular Disease* Statistics 2017. University of BATH.

Winslow, A. T., Brantley, J., Zhu, F., Vidal, J. L., and Huang, H. (2016). Corticomuscular coherence variation throughout the gait cycle during overground walking and ramp ascent: a preliminary investigation. *Conf. Proc. IEEE Eng. Med. Biol. Soc.* 2016, 4634–37. doi: 10.1109/EMBC.2016.7591760

Wolpaw. J. R. (2012). "Something new under the sun," in *Brain-Computer Interfaces: Principles and Practice,* eds J. R. Wolpaw, and E. W. Wolpaw (Oxford University Press), 3–14. doi: 10.1093/acprof:oso/9780195388855.003.0001

Zeiler, S. R., and Krakauer, J. W. (2013). The interaction between training and plasticity in the post-stroke brain. *Curr. Opin. Neurol.* 26:609. doi: 10.1097/WCO.0000000000000025

Conflict of Interest: CG and RO are employed at g.tec Medical Engineering GmbH, Austria.

The remaining authors declare that the research was conducted in the absence of any commercial or financial relationships that could be construed as a potential conflict of interest.

frontiers in Robotics and AI

REVIEW
published: 02 October 2020
doi: 10.3389/frobt.2020.00125

Passive Brain-Computer Interfaces for Enhanced Human-Robot Interaction

Maryam Alimardani[1]* *and Kazuo Hiraki*[2]

[1] Department of Cognitive Science and Artificial Intelligence, School of Humanities and Digital Sciences, Tilburg University, Tilburg, Netherlands, [2] Department of General Systems Studies, Graduate School of Arts and Sciences, The University of Tokyo, Tokyo, Japan

Brain-computer interfaces (BCIs) have long been seen as control interfaces that translate changes in brain activity, produced either by means of a volitional modulation or in response to an external stimulation. However, recent trends in the BCI and neurofeedback research highlight passive monitoring of a user's brain activity in order to estimate cognitive load, attention level, perceived errors and emotions. Extraction of such higher order information from brain signals is seen as a gateway for facilitation of interaction between humans and intelligent systems. Particularly in the field of robotics, passive BCIs provide a promising channel for prediction of user's cognitive and affective state for development of a user-adaptive interaction. In this paper, we first illustrate the state of the art in passive BCI technology and then provide examples of BCI employment in human-robot interaction (HRI). We finally discuss the prospects and challenges in integration of passive BCIs in socially demanding HRI settings. This work intends to inform HRI community of the opportunities offered by passive BCI systems for enhancement of human-robot interaction while recognizing potential pitfalls.

Keywords: brain-computer interface (BCI), passive BCIs, human-robot interaction (HRI), cognitive workload estimation, error detection, emotion recognition, EEG, social robots

OPEN ACCESS

Edited by:
Luca Tonin,
University of Padua, Italy

Reviewed by:
Muhammad Jawad Khan,
National University of Sciences and Technology (NUST), Pakistan
Xiaogang Chen,
Institute of Biomedical Engineering (CAMS), China
Matteo Spezialetti,
University of L'Aquila, Italy

***Correspondence:**
Maryam Alimardani
m.alimardani@uvt.nl

Specialty section:
This article was submitted to Computational Intelligence in Robotics, a section of the journal Frontiers in Robotics and AI

Received: *05 March 2020*
Accepted: *05 August 2020*
Published: *02 October 2020*

Citation:
Alimardani M and Hiraki K (2020) Passive Brain-Computer Interfaces for Enhanced Human-Robot Interaction. Front. Robot. AI 7:125. doi: 10.3389/frobt.2020.00125

INTRODUCTION

For generations, the idea of having intelligent machines that can read people's minds and react without direct communication had captured human's imagination. With recent advances in neuroimaging technologies and brain-computer interfaces (BCI), such images are finally turning into reality (Nam et al., 2018). BCIs are the systems that decode brain activity into meaningful commands for machines, thereby bridging the human brain and the outside world. BCIs are primarily developed as a non-muscular communication and control channel for patients suffering from severe motor impairments (Millán et al., 2010; Chaudhary et al., 2015; Lebedev and Nicolelis, 2017; Chen et al., 2019). For instance, a BCI-actuated wheelchair or exoskeleton can assist a patient with ALS or spinal cord injury to regain mobility (Kim et al., 2016; Benabid et al., 2019). Similarly, locked-in patients can be equipped with a BCI system in order to effectively communicate with external world (Sellers et al., 2014; Hong et al., 2018; Birbaumer and Rana, 2019). Stroke patients have also demonstrated effective restoration of motor functions and improvement of life quality after they were trained with a BCI-control task in a neurological rehabilitation session (Soekadar et al., 2015).

However, with the growing popularity of BCIs, new application corners outside of the medical field have emerged for healthy users (Allison et al., 2012; Van Erp et al., 2012; Nam et al., 2018). One

of the mainstream applications is the integration of BCIs with other interactive technologies such as virtual reality (VR) and computer games (Lécuyer et al., 2008; Coogan and He, 2018). Several prototypes have already been developed that enable a user to either navigate through a virtual space or manipulate a digital object only by means of thoughts (Friedman, 2015). The combination of immersive technologies and BCIs entails a two-way benefit for researchers in that the BCI system provides a new form of control channel over the environment, thus changing the user experience, and virtual environments serve as a suitable platform for BCI research as they offer a safe, engaging, and cost-effective tool for the design of BCI experiments and neurofeedback (Allison et al., 2012; Lotte et al., 2012).

In addition to immersive environments, BCIs have also been utilized in combination with physical robots in order to induce a sense of robotic embodiment and remote presence (Alimardani et al., 2013; Beraldo et al., 2018). In these setups, users control a humanoid robotic body and navigate through the physical space by means of their brain activity while they can see through the robot's eyes. Such interactions often lead to a feeling of telepresence and the experience of losing boundary between the real body and the robot's body (Alimardani et al., 2015), paving the way for research in cognitive neuroscience and neural prosthetics (Pazzaglia and Molinari, 2016).

In all the above-mentioned examples, the brain activity features extracted for the BCI classifier are either voluntarily induced by the user (active control) or measured as a response to an external stimulus (reactive control). Such BCI systems that require users to get involved in a cognitive task and provide explicit commands are referred to as active BCIs (Zander and Kothe, 2011; Lightbody et al., 2014). On the other hand, BCIs that are event driven and measure brain responses to a visual, auditory or haptic stimulus are called reactive BCIs (Zander and Kothe, 2011). However, there is a third group of BCIs that drive their outputs from spontaneous brain activity without the need from the user to perform specific mental tasks or receive stimuli. These BCI systems, which normally monitor longer epochs of brain activity for detection of a cognitive state change or emotional arousal, are called passive BCIs (Zander and Kothe, 2011; Aricò et al., 2018). An example of this is a system that monitors a driver's neural dynamics in real-time and alarms him/her in the case of drowsiness detection (Lin C. T. et al., 2010; Khan and Hong, 2015).

Passive BCIs primarily aim at detecting unintentional changes in a user's cognitive state as an input for other adaptive systems (Zander et al., 2010; Aricò et al., 2016). For instance, in the driving example, the output of the BCI system that evaluates driver drowsiness can alternatively be used for administration of the temperature in the car or the volume of the sound system in order to increase alertness of the driver (Liu et al., 2013). Similarly, a BCI that extracts information about a user's ongoing cognitive load and affective states offers numerous applications in the design of adaptive systems and social agents that would adjust their behavior to the user's ongoing mental state, without distracting the user from the main task, thereby enriching the quality of interaction and performance (Szafir and Mutlu, 2012; Alimardani and Hiraki, 2017; Zander et al., 2017; Ehrlich and Cheng, 2018).

In this article, we mainly discuss passive BCIs in the context of human-computer and human-robot interaction. In section BCIs and Cognitive/Affective State Estimation, we first lay out the state of the art in passive BCIs by briefly reviewing existing studies that attempted detection of cognitive and affective state changes from brain responses. We restricted our literature search to studies that adopted electroencephalography (EEG) signals for development of the BCI classifier. Given its mobility, high temporal resolution, and relatively low price, EEG is considered as a feasible non-invasive brain imaging technique that can be deployed into a wide variety of applications including human-robot interaction. In section BCIs and Human-Robot Interaction, we focus on passive BCI-robot studies that used cognitive and affective state measures as a neurofeedback input for a social or mechanical robot, thereby optimizing their response and behavior in a closed-loop interaction. In the last section, we discuss the prospects and challenges that are faced in the employment of passive BCIs in real-world human-robot interaction.

BCIs AND COGNITIVE/AFFECTIVE STATE ESTIMATION

In neuroscientific literature, cognitive state estimation refers to the quantification of neurophysiological processes that underlie attention, working-memory load, perception, reasoning, and decision-making, while affective computing targets assessment of the emotional experience. BCI systems that decode covert information in the brain signals regarding these internal processes can establish an implicit communication channel for an adaptive human-technology interaction, presenting novel applications in the domains of education, entertainment, healthcare, marketing, etc. (Van Erp et al., 2012; Blankertz et al., 2016; Krol and Zander, 2017; Aricò et al., 2018). We identified three main directions for assessment of cognitive and affective states in EEG-based passive BCIs; (1) detection of attention and mental fatigue, (2) detection of errors, and (3) detection of emotions. In the following, we describe the current state of the art in each of these domains, laying out a foundation for future employment of passive BCIs in human-robot interaction.

Detection of Attention and Mental Fatigue

As discussed in the drowsy driver example, monitoring real-time mental workload and vigilance is of particular importance in safety-critical environments (Lin C. T. et al., 2010; Khan and Hong, 2015; Aricò et al., 2017). Non-invasive BCIs that detect drops in attention level and increased mental fatigue can be utilized in a broad range of operational environments and application domains including aviation (Aricò et al., 2016; Hou et al., 2017) and industrial workspaces (Schultze-Kraft et al., 2012) where safety and efficiency are important, as well as educational and healthcare setups where the system can provide feedback from learners to a teacher (Ko et al.,

2017; Spüler et al., 2017), evaluate sustained attention in e-learning platforms (Chen et al., 2017), and execute attention training for clinical patients who suffer from attention deficit hyperactivity disorder (ADHD) (Lim et al., 2019). It is even suggested that detection of attention level can be employed in a hybrid BCI system in which an attention classifier is integrated with other BCI algorithms in order to confirm users' focus on the BCI task and validate the produced response, thereby yielding a more reliable and robust performance (Diez et al., 2015).

Multiple algorithms have already been proposed to quantify the level of alertness and mental workload within EEG brain activity. A large number of these models rely on frequency domain features such as theta, alpha and beta band powers, for estimation of attention level and mental fatigue experienced by the user (Lin C. T. et al., 2010; Roy et al., 2013; Diez et al., 2015; Khan and Hong, 2015; Aricò et al., 2016; Lim et al., 2019). On the other hand, some studies have examined non-linear complexity measures of time series EEG signals such as entropy (Liu et al., 2010; Min et al., 2017; Mu et al., 2017), promoting a fast and less costly method for real-time processing. Although not very common, a few studies have also proposed the usage of event-related potentials (ERP), such as non-target P300, in development of passive classifiers given that such brain responses are affected by both attention and fatigue and thus can provide a measure of target recognition processes (Kirchner et al., 2013; McDaniel et al., 2018).

In addition to spectral and temporal information carried by EEG signals, spatial features such as brain regions from which the signals were collected have been shown important in the detection of different mental state changes (Myrden and Chau, 2017). Although reported results are not always consistent, there is a general consensus on the role of frontal lobe in discrimination of cognitive workload and task difficulty (Zarjam et al., 2015; Dimitrakopoulos et al., 2017), prefrontal and central lobes in detection of fatigue and drowsiness (Min et al., 2017; Ogino and Mitsukura, 2018), and posterior areas (particularly posterior alpha band) in estimation of visuospatial attention (Ko et al., 2017; Myrden and Chau, 2017). It is worth noting that functional connectivity between different brain regions is also suggested in the literature as an index for estimation of engagement and attention (Dimitriadis et al., 2015; Dimitrakopoulos et al., 2017), although due to computational cost it poses limitations on real-time implementation.

Detection of Errors

Failures during technology usage and outputs that deviate from expectation can become a source of dissatisfaction and additional cognitive workload for the user. Unintentional mistakes made by the human or erroneous behavior presented by the system can generate user frustration and aggravate human-system interaction (Zander et al., 2010). Such negative repercussions can be prevented by automatic detection and feedback of errors, as perceived by the user, for online correction or adaptation of system characteristics while the user is still involved in the interaction (Zander et al., 2010; Chavarriaga et al., 2014; Krol and Zander, 2017).

When a user recognizes a mismatch from expectation, an error-related potential (ErrP) is generated in the EEG signals. A passive BCI system that extracts this information in real-time can be used in development of hybrid and adaptive systems that optimize the performance of the user either by removing the erroneous trials (Ferrez and Millán, 2008; Schmidt et al., 2012; Yousefi et al., 2019), or by modifying the classification parameters through online learning of the BCI classifier (Krol and Zander, 2017; Mousavi and de Sa, 2019), or by adjusting the task difficulty level to different individuals in order to improve engagement and motivation (Mattout et al., 2015). For instance, Ferrez and Millán (2008) combined a motor imagery BCI with an error detection algorithm that looked for an ErrP immediately after each trial and filtered out trials that contained an error-related response. Their results displayed a significant improvement of BCI performance in real-time by reducing the classification error rate from 30 to 7%. Similarly, Schmidt et al. (2012) combined online detection of ErrPs with a BCI speller and reported 49% improvement in the mean spelling speed. In a recent report, Dehais et al. (2019) presented a passive BCI classifier for prediction of auditory attentional errors during a real flight condition, proposing future smart cockpits that would adapt to pilots' cognitive needs.

A unique feature of ErrPs is that they would arise in response to any form of discrepancy during interaction/task execution including when the user realizes a self-made error (response ErrP), when s/he is informed about the error through some type of feedback (feedback ErrP), and even when the user senses an error made by a third party (observation ErrP) (Ferrez and Millán, 2005; Gürkök and Nijholt, 2012; Vi et al., 2014). This permits detection and management of errors in any form and at any time during the interaction, promoting closed-loop passive BCIs not only as an efficient and seamless tool for online evaluation of user performance but also as a secondary communication tool in multi-user collaborative environments such as emergency rooms (Vi et al., 2014) where agile and high-risk decision making is required (Poli et al., 2014).

Additionally, recent efforts suggest that different kinds of errors generate different ErrPs, allowing discrimination of error severity and error types (Spüler and Niethammer, 2015; Wirth et al., 2019) based on temporal, spectral, and spatial information in the EEG waveforms. However, the downside of this approach is that, in most cases, the ErrP classifier relies on an event-locked paradigm in which ErrPs can only be extracted within a fixed window from a specified trigger. In real-world applications, the information regarding stimulus time or origin of the error is often unavailable and the latency of user responses may vary across individuals and tasks. Therefore, future integration of such passive BCIs with natural human-agent interactions calls for further developments on self-paced algorithms that make asynchronous error detection possible at any time during the interaction (Lightbody et al., 2014; Spüler and Niethammer, 2015; Yousefi et al., 2019).

Detection of Emotions

With advancement of commercially available wearable sensors, estimation of human emotions from ongoing biosignals has received increased attention in recent years (Al-Nafjan et al.,

2017; Shu et al., 2018; García-Martínez et al., 2019; Dzedzickis et al., 2020). Emotions are particularly important in the design of intelligent and socially interactive systems as they enable the digital agents to generate a well-suited behavior and establish an affective loop with the human partner (Paiva et al., 2014; Ehrlich et al., 2017). Compared to conventional methods of social signal processing and affective computing (such as voice and image processing), biosignals present the advantage of containing spontaneous and less controllable features of emotions. Emotions entail three aspects; physiological arousal, conscious experience of the emotion (subjective feeling) and behavioral expression (Alarcao and Fonseca, 2017). Voice and face recognition technologies can only capture the third aspect, i.e., overt behavioral expression of emotion, whereas brain activity can inform us about the neurophysiological and cognitive processes that generate and lead to such emotional states (Mühl et al., 2014a).

A major challenge in classification of emotions from brain activity is that there is not a unique computational method for extraction and mapping of emotion-related features. There are two theories in the modeling of emotions; discrete model and dimensional model (Kim et al., 2013). The former defines emotions as a set of categorical affective states that represent core emotions such as happiness, sadness, anger, disgust, fear, and surprise (Lin Y. P. et al., 2010; Jenke et al., 2014). The latter maps emotions on either a two-dimensional valence-arousal space (Posner et al., 2005; Atkinson and Campos, 2016) or a three-dimensional valence-arousal-dominance space (Mehrabian, 1996; Reuderink et al., 2013). The discrete model is more popular among BCI developers as it reduces the problem of dimensionality, however it does not consider that the same emotion may manifest on different scales of arousal, valence and dominance. The dimensional model provides continuity as it quantifies emotions on each dimension (valence ranging from positive to negative, arousal ranging from calm to excited and dominance ranging from in-control to submission). Particularly, the 2D model has been previously used in multiple EEG studies (Liberati et al., 2015; Al-Nafjan et al., 2017; Mohammadi et al., 2017), however in these studies, the dimensionality is often simplified again by means of clustering emotions across the valence-arousal coordinates (e.g., fear as negative valence, high arousal or happiness as positive valence, high arousal), which bears the risk of grouping different emotions that share the same valence and arousal levels (e.g., anger and fear) in one cluster (Liberati et al., 2015).

Another challenge in the development of emotional BCIs is the diverse elicitation strategies that exist in the affective computing literature. Multiple types of stimuli including affective pictures, sounds, video fragments and music have been used in the past in order to induce emotional responses (Al-Nafjan et al., 2017). In addition to the lack of consistency among reported results and available EEG datasets, an inherent problem with these forms of stimuli is that there is no evidence whether the induced emotion is a natural affective state or just a reactive response to the stimulus. To counter this issue, some studies have employed a self-induced strategy such as recall of autobiographical emotional memory (Chanel et al., 2009; Iacoviello et al., 2015) or imagination of the emotion by means of verbal narratives (Kothe et al., 2013). This method entails other problems; the self-induced emotions are inevitably weaker than those induced by external stimuli, and users are prone to distraction during the task as it is difficult to maintain mental imageries for a long period (Chanel et al., 2009).

It is worth mentioning that emotions are more than just an affective state for social interaction and adaptive environments; they may also influence other cognitive functions. For instance, frustration can extend negative impacts on attention, decision-making, learning, and response accuracy. Indeed, past research has shown that affective states such as stress, anxiety and frustration can influence BCI performance in estimation of mental workload and attention (Mühl et al., 2014b; Myrden and Chau, 2015; Lotte et al., 2018). Thus, it can be expected that an adaptive multimodal BCI system that identifies users' affective states and regulates tasks accordingly would improve user performance and validity of the system in the long term (Gürkök and Nijholt, 2012).

To sum up, there have been several BCI algorithms proposed for detection of affective state changes from EEG signals (Alarcao and Fonseca, 2017), however, automatic recognition of emotions during ecologically valid tasks and natural interactions remains a challenge, hindering deployment of affective BCIs in other platforms such as human-robot interaction. Future research should attend currently existing issues such as insufficient classification accuracy, inconsistent computational and elicitation techniques, as well as development of BCI models that can extract emotions in an unobtrusive and asynchronous manner over a long period of time.

BCIs AND HUMAN-ROBOT INTERACTION

With more integration of robots into our daily life, the necessity for them to function as social and assistive companions in real-world environments such as schools and healthcare facilities becomes eminent. In addition to human's intentions and control commands, it is crucial for the robots to estimate the emotional states of a human partner in order to be socially responsive, engage longer with users and promote natural HRI (Ficocelli et al., 2015). More importantly, estimation of workload, anxiety and errors is crucial for ergonomic and safe human-robot collaboration in both domestic and industrial spaces (Ajoudani et al., 2018). In this section, we particularly discuss studies that have employed BCIs for passive detection of cognitive and affective states of a human user in order to effectively adapt the behavior of a robot in a closed-loop interaction with the human partner (**Figure 1**).

We restricted our literature search to only non-invasive BCI studies that passively extracted user's cognitive and affective states during interaction with a physical robot, therefore, articles that employed active BCIs for motion control (e.g., motor-imagery based robot operation) or reactive BCIs for intentional selection of behavior for a robotic interface (e.g., robot manipulation triggered by event-related P300 or Steady State Visually Evoked Potential SSVEP) were not included. Another inclusion criterion

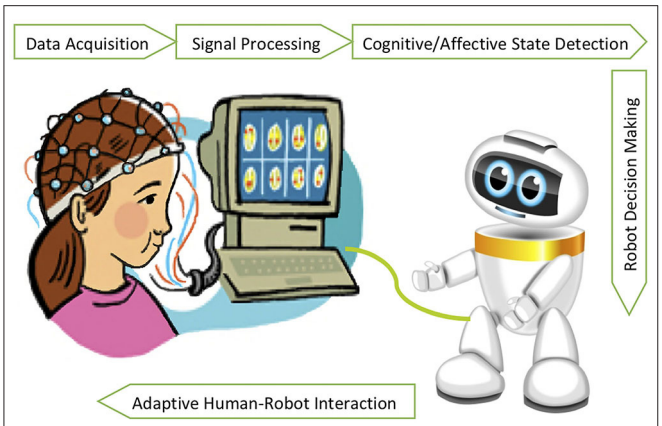

FIGURE 1 | Closed-loop human-robot interaction using passive BCIs.

TABLE 1 | The inclusion and exclusion criteria as used for the selection of BCI-HRI studies in section BCIs and Human-Robot Interaction.

Parameters	Inclusion criteria	Exclusion criteria
Type of BCI	Passive BCIs (hybrid with other BCI types acceptable)	Active or reactive BCIs (e.g., motor imagery, ERP, SSVEP)
Type of signal	EEG (hybrid with other signal types acceptable)	fNIRS, fMRI, MEG
Type of interaction	Interaction with physical robots (e.g., social robots, arm robots)	Interaction with virtual avatars, computer games
Type of analysis	Real-time classification/ feedback to the robot	Offline analysis of brain signals captured during HRI

was usage of AI-powered predictive models together with EEG signals in the study, where a passive BCI classifier was used (or its development was attempted) during real-time interaction with a robot. Neuroscience research in which only brain oscillation patterns associated with robot interaction are reported were either excluded or already reported in section BCIs and Cognitive/Affective State Estimation. Finally, the study should have reported a passive BCI interaction with a physical robot; interactions with virtual or simulated agents were excluded as the definition of a simulated agent is very board and incorporates human-computer interaction and game applications of passive BCIs. The inclusion and exclusion criteria defined for review of BCI-HRI studies in this section are summarized in **Table 1**.

Our search resulted in a total of 10 studies as shown in **Table 2**. In the following, we briefly describe the methodology and outcomes of each listed study.

Szafir and Mutlu (2012) reported an interesting study in which a humanoid robot monitored students' EEG signals during storytelling and gave them attention-evoking immediacy cues (either in verbal or non-verbal form) whenever engagement drops were detected. In doing so, they extracted EEG levels in alpha, beta and theta frequency bands and smoothed them into an engagement signal that would represent attention levels. Every time the attention level went below a pre-defined threshold, the robot displayed immediacy cues such as increased spoken volume, increased eye contact, and head-nodding. Their results showed that participants who experienced interaction with an adaptive BCI-driven robot had a significantly better recall of the story details than those who participated in an interaction with randomly presented immediacy cues. In addition to this, female participants reported a more favorable evaluation of the robot behavior, in terms of improved motivation and rapport, in the BCI condition compared to the random condition. The results of this study highlight the benefits of BCIs in interactive educational setups where real-time detection of user disengagement and attention drop can be compensated by means of an embodied social agent.

Kirchner et al. (2013) employed passive classification of event-related potential P300 in an adaptive human-robot interaction. They reported a brain reading (BR) system that implicitly extracted p300 during teleoperation of an exoskeleton arm whenever an important stimulus was presented to the user. They used the evoked potential amplitude as an indicator of successful stimuli recognition by the user. If the response did not contain P300 or the potential was not strong enough, it implied that the user had missed the important information that was presented and thus the system repeated the stimuli. Authors found a reduced stress level in subjects when BR was embedded in the control interface, recommending their approach as a promising way to improve the functionality of interactive technical systems.

Ehrlich et al. (2014) proposed an EEG-based framework for detection of social cues such as gaze by a humanoid robot as a measure for social engagement. They instructed subjects to either wait for the robot to make eye-contact with them or to intentionally generate brain patterns for the robot to initiate eye-contact with them (influence the robot's behavior). By extracting frequency band powers as discriminating features in an offline analysis, they could find high classification performance between the two conditions. Such predictive model could be implemented in a human-robot interaction in order to enable the robot to estimate its social role and adapt its behavior to the expectations of the human partner.

Iturrate et al. (2015) introduced a reinforcement learning (RL) algorithm that learned optimal motor behavior of a robotic arm based on observation ErrPs carried in the brain signals of a human viewer. The BCI classifier decoded reaching actions as erroneous whenever ErrPs were present. The non-ErrP trials were then employed as an online reward for the RL algorithm. Their approach improved the number of learned actions and control policies compared to random rewards. Authors suggest their algorithm for future application in neuroprosthetics in which implicit input from the patient can optimize the behavior of an artificial limb for goal-oriented movements.

Kim et al. (2017) conducted a study similar to Iturrate et al. (2015) in which they trained a RL algorithm based on the user's ErrPs in a gesture recognition task. They prepared two scenarios; (1) when a simulated arm robot recognized and copied user's gestures, and (2) when a real arm robot recognized and copied user's gestures. In both scenarios, the ErrP classifier used the correct mappings as a reward for the RL algorithm. They

TABLE 2 | List of articles in the literature that used a passive BCI classifier for extraction of user's cognitive and affective state during interaction with a physical robot.

References	EEG feature	BCI classifier output	Adaptive HRI
Szafir and Mutlu (2012)	Spectral band powers	Attention drops in user during storytelling by a robot	The robot provided attention-evoking cues
Kirchner et al. (2013)	Absence of P300	Stimuli recognition during teleoperation of an exoskeleton arm	The robot controller repeated stimuli or changed response window if the user missed the stimuli
Ehrlich et al. (2014)	Spectral band powers	User intention to initiate eye-contact with a robot	None
Iturrate et al. (2015)	Error-related potential	Erroneous motor behavior by an artificial robotic arm in a reaching task	The robot arm controller learned correct and incorrect behavior through reinforcement learning
Kim et al. (2017)	Error-related potential	Wrong mapping between user's gestures and robot's action	The robot updated action-selection strategy and learned gesture meaning through reinforcement learning
Salazar-Gomez et al. (2017)	Error-related potential	Erroneous robot motion in a binary reaching task	The robot switched trajectory based on the observer's EEG response
Ehrlich and Cheng (2018)	Error-related potential	Mismatch in gaze behavior	The robot adapted gaze behavior based on decoded ErrPs
Ehrlich and Cheng (2019)	Error-related potential	Erroneous robot head movement as a response to a directional key press by the user	None
Shao et al. (2019)	Spectral asymmetry	Emotional valence (positive vs. negative) during exercise with a robot coach	The robot provided verbal and non-verbal feedback based on the user's affect and engagement level
Lopes-Dias et al. (2019)	Error-related potential	Erroneous arm robot movement when the robot should have imitated human hand movement.	The robot would give control to human again to correct his/her movement

showed that both simulated and real robots could effectively learn gestures from the human instructor with a high online ErrP detection accuracy (90 and 91%, respectively). However, not surprisingly, the learning curve was different across subjects based on the performance of ErrP classifier. Past studies have shown that ERP-based BCI performance varies across individuals based on psycho-cognitive parameters (Sprague et al., 2016) suggesting that ErrP-based BCIs may require subject-specific calibration and training when integrated within an HRI setting.

Salazar-Gomez et al. (2017) introduced a closed-loop control interface for automatic correction of reaching behavior of a robotic arm. They recorded EEG signals from a human observer while the robot was performing a binary object selection task after a cue presentation. They used ErrP responses as a real-time feedback for the robot to switch trajectory if the selected choice was not compatible with the cue. Despite the sound methodology of this study, authors only reported classification results from four subjects, which makes it difficult to draw firm conclusions. Also, no reports were made regarding user perception of the interaction and attitude toward the robot in open-loop vs. closed-loop HRI. However, an interesting finding in this study was the presence of a secondary ErrP in the closed-loop interaction when the human observed an incorrect interpretation of the feedback by the robot (robot not obeying the human or switching to the wrong trajectory due to misclassification). This suggests the design of new BCI paradigms where secondary and further ErrPs can be incorporated in continuous interactions until an optimal behavior is achieved (Cruz et al., 2018).

Ehrlich and Cheng (2018, 2019) reported two consecutive studies in which they used ErrP signals for detection of mismatch between user's intended gaze and actual robot's gaze (Ehrlich and Cheng, 2018) and user's intended head movement and actual robot's head movement (Ehrlich and Cheng, 2019). In the former study, they used a closed-loop interaction (adaptive behavior by the robot) where the user first guessed the direction of robot gaze from three available choices and then the robot performed a random gaze behavior which was followed by an updated behavior based on the ErrP classifier outcome. Using a learning paradigm for the robot's gaze policy, they showed that a mutual adaptation between the human and robot's behavior emerged, leading to a relatively high classification performance and more efficient interaction. In the latter study (Ehrlich and Cheng, 2019), authors again used a guessing game to compare the observability and decodeability of ErrP responses to two experimental stimuli; an incongruent robot movement vs. an incongruent curser movement. In the first condition, participants guessed the robot head movement from three possible directions (left, right, up) using arrow key-presses, and watched the robot perform a random action. In the second condition, they again guessed a possible direction but watched a curser moving either toward or away from that direction on a computer screen. Although they found a satisfactory classification accuracy (69%) in the HRI scenario, they observed that the classification accuracy for ErrP responses was significantly higher in the cursor scenario (90%), indicating more sensitivity of ErrPs to visually simple cues compared to contextual robot actions.

Shao et al. (2019) used a low-cost EEG (InteraXon Muse 2016) together with heart rate and motion sensors during interaction with a health coach humanoid robot. They extracted EEG frequency band powers in order to classify the emotional valence of the user during exercise with the robot. The robot then presented an online positive or negative feedback (happy,

interested, worried, and sad) based on the user's affect (positive or negative) and engagement level (engaged or not engaged). The participants of their study reported a high acceptance and perceived usability for the robot, however the robot was tested in a non-controlled experiment (no other condition was compared with the above scenario) and the classification results for the affect recognition model was not particularly high (71%), therefore it is possible that the reported results were merely due to the novelty effect caused by the robot presence, and not emotional awareness and adaptive feedback during the interaction.

Finally, Lopes-Dias et al. (2019) attempted asynchronous decoding of ErrPs during online control of an arm robot. Participants had to move their own hand according to a binary stimuli on the screen and using a motion capture system, the robot was expected to copy the same movement in the physical world. In case the hand movement was not detected correctly, an ErrP signal was detected and the robot allowed the user to correct the error. The major finding of this study was the possibility of asynchronous detection of ErrPs using a sliding window during online robot operation. Authors do not discuss their results in the context of human-robot interaction and a possible embodiment effect (Alimardani et al., 2013), however similar to Salazar-Gomez et al. (2017), they observed secondary ErrPs in some participants which confirms the applicability of these later potentials in improvement of robot performance.

Although, this section only focused on EEG-based passive BCIs for the purpose of HRI, it is worth mentioning the potential of other brain imaging techniques such as fNIRS (Canning and Scheutz, 2013) in passive evaluation of user responses during robot interaction, for instance, detection of cognitive workload during multitasking with two robots (Solovey et al., 2012) or detection of affinity and eeriness in robot appearance (Strait and Scheutz, 2014). Additionally, insights can be driven from passive BCI studies with simulated agents and teleoperated robots (Esfahani and Sundararajan, 2011; Cavazza et al., 2015; Aranyi et al., 2016; Zander et al., 2017) to further inform the HRI community of the possible exploitation avenues.

Altogether, passive BCIs show promise in the design of optimal robot behavior by means of indirect communication from the human partner. Our literature review shows that detection of erroneous robot behavior using ErrP signals is the most popular paradigm for integration of passive BCIs in HRI settings. Contrary to our expectation, there were very few studies that employed detection of mental workload or emotions for adaptive social behavior in HRI. This confirms that despite the great effort of AI community in developing several classification models for EEG-based emotion and cognitive state prediction, real-time incorporation of these models in a closed-loop interaction with physical robots are yet not adequately explored. This gap should be addressed by BCI and HRI researchers in the future, thereby creating a synergy between the two domains for promotion of socially intelligent and adaptive robots.

PROSPECTS AND CHALLENGES

As discussed in previous sections, passive BCIs offer a promising means to objectively monitor cognitive and affective states of a technology user either as an offline evaluation metric of the user's performance or as a communication modality for closed-loop adaptive interaction. This puts forward application of passive BCIs in neuroergonomic HRI (Lotte and Roy, 2019) where potential mental overload, attention drops, negative emotions, and human errors can be prevented or managed in an online and unobtrusive manner, thereby increasing the interactivity between the user and the robot and facilitating their collaboration (Krol et al., 2018). Meanwhile, more research is required in the field of HRI to formulate appropriate design principles for context-aware alignment of the robot behavior with human expectations, needs and conventions, once such higher order information from the user is available (Rossi et al., 2017; Sciutti et al., 2018).

Another direction toward future collaboration between passive BCI and HRI research could be development of social robots that assist neurofeedback training for augmented cognition or sustenance of a desirable psychological state (Anzalone et al., 2016; Alimardani and Hiraki, 2017; Alimardani et al., 2018, 2020; Tsiakas et al., 2018; Cinel et al., 2019). One of the main problems with the traditional neurofeedback training paradigms is that the changes in brain features are usually presented to the users through auditory or visual feedback. This lacks engagement with the interface, which makes the training after a short while tedious. Recent works have replaced the old protocol with interactive computer games (Mishra et al., 2016) and immersive virtual environments (Kosunen et al., 2016). However, these applications require steady visual attention toward a computer screen or placement of a head-mounted display over the EEG electrodes that can be intrusive to the user and cause cybersickness. A social robot on the other hand, induces a feeling of co-presence, mind perception, and emotional support (Alimardani and Qurashi, 2019), which can positively influence performance, motivation, and social interaction during a training program (Wiese et al., 2017; Sinnema and Alimardani, 2019; Alimardani et al., 2020). Past research has shown that the physical embodiment of an agent generates a more natural, efficient, and joyful communication during elderly cognitive training (Tapus et al., 2009) as well as a higher learning gain during tutoring interactions (Leyzberg et al., 2012). Therefore, it is expected that a robot-guided cognitive training would extend similar benefits compared to previous non-social environments (Pino et al., 2019).

Although passive BCIs provide substantial opportunity for optimization of performance and interactivity in HRI, their advantages are often mitigated by several limitations with respect to real-world implementation. One of the general challenges in the usage of BCIs in real-world conditions is the high cost and long preparation time that is required for the hardware setup (electrode placement) and software tuning (individualized calibration). Recent development of wireless EEG caps and low-cost commercial headsets has substantially reduced the setup

time for real-world recordings, however they often come at the cost of precision and reliability. Also, there have been attempts in reducing calibration time by means of machine learning techniques and adaptive classifiers that extract common features among all users (Lotte, 2015), known as inter-subject associativity (Saha and Baumert, 2019). On the other hand, deep learning methods have been suggested for automatic learning of representations in the brain activity, thereby reducing the pre-processing and manual feature extraction that is required for BCI classifier training (Nagel and Spüler, 2019; Tanveer et al., 2019). For BCI technology to become mainstream and be employed by non-experts in other research domains, we must reduce the cost of equipment use while improving the quality of recording and precision of algorithms. Hence, further advancement in wearable sensor technology as well as progress in signal processing techniques and computational modeling of brain activity is required for the BCIs to be finally deployed in every-day use.

Another constraint in employing BCIs in real-world scenarios is vulnerability of BCI output to external noise (Minguillon et al., 2017). In most BCI studies, participants are instructed to relax during the recording and avoid unnecessary movements; nevertheless the online performance of these systems is yet far from ideal due to uncontrolled concomitant stimulus in the environment and diverse neurophysiological dynamics across individuals. In the case of passive BCIs, this is an even more severe issue as the user's involvement in another task or integration of the BCI system with other types of technology introduces new artifacts from the environment resulting in undesirable outcome (Zander et al., 2010). Such misclassifications can become particularly critical in the HRI scenarios, as poor performance from the system will produce unwanted behavior from the robot, thereby harming the interaction quality and diminishing the expected effects. A proposed solution for this problem is combination of multiple brain imaging modalities, such as fNIRS and EEG, to develop hybrid BCIs that benefit from both high temporal and high spatial resolution and hence can provide better accuracy and process more commands from the user (Hong and Khan, 2017; Dehais et al., 2018). Similarly, combination of brain signals with other physiological data such as electromyography (EMG) or electrooculography (EOG) can help detect and reduce the effect of noise and increase the number of control commands necessary for multi-task control (Hong and Khan, 2017; Zhang et al., 2019).

In the same vein, care must be taken when collecting data for development of passive BCIs models in complex environments where alternative sources of cognitive and affective stimuli are available. Mappings between target mental states and brain activity should clearly be defined and investigated with careful consideration of confounding factors that might affect neurophysiological variables (Brouwer et al., 2015). For instance, when developing an affective BCI classifier for detection of human emotions during interaction with a robot, the BCI model should be trained and tested in an ecologically valid HRI setting rather than with a set of affective visual stimuli. Such new experimental paradigms may lead to unsuccessful or inconsistent results compared to prior neuroscience studies, however, this should not demotivate researchers from reporting their findings as the BCI field is still in its infancy and the report of negative results is equally valuable for its further progress (Lotte et al., 2020).

Yet, another challenge with respect to integration of passive BCIs in human-robot interaction studies is the high demand for computational resources and data storage, which are indispensible to real-time processing of brain activity as well as real-time configuration of the robot controller. This means that in practice, the two interfaces are often operated on different computers/environments and hence need to communicate with one another through proxy solutions (Müller-Putz et al., 2011). In order to integrate BCIs and robots efficiently, future developments is required to provide cost-effective BCI modules that can be compiled and implemented in multiple environments without requiring extensive programming and adaptation.

Last but not least, we should not lose sight on the emerging ethical issues in real-world employment of passive BCIs such as management of user expectation and sensitive data (Burwell et al., 2017). Obviously, the idea of continuous monitoring and access to someone's thoughts is dreadful, particularly when this information is collected and processed by a humanlike entity such as a robot. Especially, in the case of affective BCIs, there are unique challenges with respect to user autonomy as they entail the risk of manipulation or inducement of affective states without the user's consent (Steinert and Friedrich, 2020). Therefore, it is of high importance to scrutinize the ethical implications of BCI-driven robots and develop educational programs that communicate ethical guidelines to potential users before such technologies are released into the wild.

CONCLUSION

Passive BCI technology holds promise in extracting affective and cognitive states for an optimized human-technology interaction. In this paper, we laid out the current state of the art in passive BCIs and illustrated their implications for real-world applications. We particularly reviewed their possible employment in human-robot interaction with the intention to inform the HRI community of the promises and challenges of passive BCI technology. Future work should continue to advance the synergy between the two domains and further explore the impact and effectiveness of BCI-driven robots during closed-loop interactions with humans.

AUTHOR CONTRIBUTIONS

MA wrote the manuscript with subsequent input from KH. All authors contributed to the article and approved the submitted version.

FUNDING

This research was supported by Grant-in-Aid for JSPS Research Fellow 15F15046, ImPACT Program of Council for Science, Technology and Innovation (Cabinet Office, Government of Japan) and CREST-JST (No. 200800000003).

REFERENCES

Ajoudani, A., Zanchettin, A. M., Ivaldi, S., Albu-Schäffer, A., Kosuge, K., and Khatib, O. (2018). Progress and prospects of the human–robot collaboration. *Auton. Robots* 42, 957–975. doi: 10.1007/s10514-017-9677-2

Alarcao, S. M., and Fonseca, M. J. (2017). Emotions recognition using EEG signals: a survey. *IEEE Trans. Affect. Comput*. 10, 374–393. doi: 10.1109/TAFFC.2017.2714671

Alimardani, M., and Hiraki, K. (2017). "Development of a real-time brain-computer interface for interactive robot therapy: an exploration of EEG and EMG features during hypnosis," in *World Academy of Science, Engineering and Technology, International Journal of Computer, Electrical, Automation, Control and Information Engineering*, Vol. 11, 187–195.

Alimardani, M., Kemmeren, L., Okumura, K., and Hiraki, K. (2020). Robot-assisted mindfulness practice: analysis of neurophysiological responses and affective state change," in *Proceeding of 29th IEEE International Conference on Robot and Human Interactive Communication (Ro-Man 2020)* (Naples).

Alimardani, M., Keshmiri, S., Sumioka, H., and Hiraki, K. (2018). "Classification of EEG signals for a hypnotrack BCI system," in *2018 IEEE/RSJ International Conference on Intelligent Robots and Systems (IROS)* (Madrid: IEEE), 240–245. doi: 10.1109/IROS.2018.8594136

Alimardani, M., Nishio, S., and Ishiguro, H. (2013). Humanlike robot hands controlled by brain activity arouse illusion of ownership in operators. *Sci. Rep.* 3:2396. doi: 10.1038/srep02396

Alimardani, M., Nishio, S., and Ishiguro, H. (2015). "BCI-teleoperated androids; a study of embodiment and its effect on motor imagery learning," in *2015 IEEE 19th International Conference on Intelligent Engineering Systems (INES)* (Bratislava: IEEE), 347–352. doi: 10.1109/INES.2015.7329753

Alimardani, M., and Qurashi, S. (2019). "Mind perception of a sociable humanoid robot: a comparison between elderly and young adults," in *Iberian Robotics Conference* (Cham: Springer), 96–108. doi: 10.1007/978-3-030-36150-1_9

Allison, B. Z., Dunne, S., Leeb, R., Millán, J. D. R., and Nijholt, A. (Eds.). (2012). *Towards Practical Brain-Computer Interfaces: Bridging the Gap From Research to Real-World Applications*. Springer Science and Business Media. doi: 10.1007/978-3-642-29746-5

Al-Nafjan, A., Hosny, M., Al-Ohali, Y., and Al-Wabil, A. (2017). Review and classification of emotion recognition based on EEG brain-computer interface system research: a systematic review. *Appl. Sci.* 7:1239. doi: 10.3390/app7121239

Anzalone, S., Tanet, A., Pallanca, O., Cohen, D., and Chetouani, M. (2016). "A humanoid robot controlled by neurofeedback to reinforce attention in autism spectrum disorder," in *Proceedings of the 3rd Italian Workshop on Artificial Intelligence and Robotics* (Genova).

Aranyi, G., Pecune, F., Charles, F., Pelachaud, C., and Cavazza, M. (2016). Affective interaction with a virtual character through an fNIRS brain-computer interface. *Front. Comput. Neurosci.* 10:70. doi: 10.3389/fncom.2016.00070

Aricò, P., Borghini, G., Di Flumeri, G., Colosimo, A., Bonelli, S., Golfetti, A., et al. (2016). Adaptive automation triggered by EEG-based mental workload index: a passive brain-computer interface application in realistic air traffic control environment. *Front. Hum. Neurosci.* 10:539. doi: 10.3389/fnhum.2016.00539

Aricò, P., Borghini, G., Di Flumeri, G., Sciaraffa, N., and Babiloni, F. (2018). Passive BCI beyond the lab: current trends and future directions. *Physiol. Measur.* 39:08TR02. doi: 10.1088/1361-6579/aad57e

Aricò, P., Borghini, G., Di Flumeri, G., Sciaraffa, N., Colosimo, A., and Babiloni, F. (2017). Passive BCI in operational environments: insights, recent advances, and future trends. *IEEE Trans. Biomed. Eng.* 64, 1431–1436. doi: 10.1109/TBME.2017.2694856

Atkinson, J., and Campos, D. (2016). Improving BCI-based emotion recognition by combining EEG feature selection and kernel classifiers. *Expert Syst. Appl.* 47, 35–41. doi: 10.1016/j.eswa.2015.10.049

Benabid, A. L., Costecalde, T., Eliseyev, A., Charvet, G., Verney, A., Karakas, S., et al. (2019). An exoskeleton controlled by an epidural wireless brain–machine interface in a tetraplegic patient: a proof-of-concept demonstration. *Lancet Neurol.* 18:1112. doi: 10.1016/S1474-4422(19)30321-7

Beraldo, G., Antonello, M., Cimolato, A., Menegatti, E., and Tonin, L. (2018). "Brain-computer interface meets ROS: a robotic approach to mentally drive telepresence robots," in *2018 IEEE International Conference on Robotics and Automation (ICRA)* (Brisbane, QLD: IEEE), 1–6. doi: 10.1109/ICRA.2018.8460578

Birbaumer, N., and Rana, A. (2019). "Brain–computer interfaces for communication in paralysis," in *Casting Light on the Dark Side of Brain Imaging* (Academic Press), 25–29. doi: 10.1016/B978-0-12-816179-1.00003-7

Blankertz, B., Acqualagna, L., Dähne, S., Haufe, S., Schultze-Kraft, M., Sturm, I., et al. (2016). The Berlin brain-computer interface: progress beyond communication and control. *Front. Neurosci.* 10:530. doi: 10.3389/fnins.2016.00530

Brouwer, A. M., Zander, T. O., Van Erp, J. B., Korteling, J. E., and Bronkhorst, A. W. (2015). Using neurophysiological signals that reflect cognitive or affective state: six recommendations to avoid common pitfalls. *Front. Neurosci.* 9:136. doi: 10.3389/fnins.2015.00136

Burwell, S., Sample, M., and Racine, E. (2017). Ethical aspects of brain computer interfaces: a scoping review. *BMC Med. Ethics* 18:60. doi: 10.1186/s12910-017-0220-y

Canning, C., and Scheutz, M. (2013). Functional near-infrared spectroscopy in human-robot interaction. *J. Hum. Robot Interact.* 2, 62–84. doi: 10.5898/JHRI.2.3.Canning

Cavazza, M., Charles, F., Gilroy, S. W., Porteous, J., Aranyi, G., Cordry, J., et al. (2015). Virtual agents in brain-computer interfaces. *Int. J. Virtual Real.* 15, 48–60. doi: 10.20870/IJVR.2015.15.1.2868

Chanel, G., Kierkels, J. J., Soleymani, M., and Pun, T. (2009). Short-term emotion assessment in a recall paradigm. *Int. J. Hum. Comput. Stud.* 67, 607–627. doi: 10.1016/j.ijhcs.2009.03.005

Chaudhary, U., Birbaumer, N., and Curado, M. R. (2015). Brain-machine interface (BMI) in paralysis. *Ann. Phys. Rehabil. Med.* 58, 9–13. doi: 10.1016/j.rehab.2014.11.002

Chavarriaga, R., Sobolewski, A., and Millán, J. D. R. (2014). Errare machinale est: the use of error-related potentials in brain-machine interfaces. *Front. Neurosci.* 8:208. doi: 10.3389/fnins.2014.00208

Chen, C. M., Wang, J. Y., and Yu, C. M. (2017). Assessing the attention levels of students by using a novel attention aware system based on brainwave signals. *Br. J. Educ. Technol.* 48, 348–369. doi: 10.1111/bjet.12359

Chen, X., Zhao, B., Wang, Y., and Gao, X. (2019). Combination of high-frequency SSVEP-based BCI and computer vision for controlling a robotic arm. *J. Neural Eng.* 16:026012. doi: 10.1088/1741-2552/aaf594

Cinel, C., Valeriani, D., and Poli, R. (2019). Neurotechnologies for human cognitive augmentation: current state of the art and future prospects. *Front. Hum. Neurosci.* 13:13. doi: 10.3389/fnhum.2019.00013

Coogan, C. G., and He, B. (2018). Brain-computer interface control in a virtual reality environment and applications for the internet of things. *IEEE Access* 6, 10840–10849. doi: 10.1109/ACCESS.2018.2809453

Cruz, A., Pires, G., and Nunes, U. J. (2018). Double ErrP detection for automatic error correction in an ERP-based BCI speller. *IEEE Trans. Neural Syst. Rehabilit. Eng.* 26, 26–36. doi: 10.1109/TNSRE.2017.2755018

Dehais, F., Dupres, A., Di Flumeri, G., Verdiere, K., Borghini, G., Babiloni, F., et al. (2018). "Monitoring pilot's cognitive fatigue with engagement features in simulated and actual flight conditions using an hybrid fNIRS-EEG passive BCI," in *2018 IEEE International Conference on Systems, Man, and Cybernetics (SMC)* (Miyazaki: IEEE), 544–549. doi: 10.1109/SMC.2018.00102

Dehais, F., Rida, I., Roy, R. N., Iversen, J., Mullen, T., and Callan, D. (2019). "A pBCI to predict attentional error before it happens in real flight conditions," in *2019 IEEE International Conference on Systems, Man and Cybernetics (SMC)* (Bari: IEEE), 4155–4160. doi: 10.1109/SMC.2019.8914010

Diez, P. F., Correa, A. G., Orosco, L., Laciar, E., and Mut, V. (2015). Attention-level transitory response: a novel hybrid BCI approach. *J. Neural Eng.* 12:056007. doi: 10.1088/1741-2560/12/5/056007

Dimitrakopoulos, G. N., Kakkos, I., Dai, Z., Lim, J., deSouza, J. J., Bezerianos, A., et al. (2017). Task-independent mental workload classification based upon common multiband EEG cortical connectivity. *IEEE Trans. Neural Syst. Rehabilit. Eng.* 25, 1940–1949. doi: 10.1109/TNSRE.2017.2701002

Dimitriadis, S. I., Sun, Y. U., Kwok, K., Laskaris, N. A., Thakor, N., and Bezerianos, A. (2015). Cognitive workload assessment based on the tensorial treatment of EEG estimates of cross-frequency phase interactions. *Ann. Biomed. Eng.* 43, 977–989. doi: 10.1007/s10439-014-1143-0

Dzedzickis, A., Kaklauskas, A., and Bucinskas, V. (2020). Human emotion recognition: review of sensors and methods. *Sensors* 20:592. doi: 10.3390/s20030592

Ehrlich, S., Guan, C., and Cheng, G. (2017). "A closed-loop brain-computer music interface for continuous affective interaction," in *2017 International Conference on Orange Technologies (ICOT)* (Singapore: IEEE), 176–179. doi: 10.1109/ICOT.2017.8336116

Ehrlich, S., Wykowska, A., Ramirez-Amaro, K., and Cheng, G. (2014). "When to engage in interaction—And how? EEG-based enhancement of robot's ability to sense social signals in HRI," in *2014 14th IEEE-RAS International Conference on Humanoid Robots (Humanoids)* (Madrid: IEEE), 1104–1109. doi: 10.1109/HUMANOIDS.2014.7041506

Ehrlich, S. K., and Cheng, G. (2018). Human-agent co-adaptation using error-related potentials. *J. Neural Eng.* 15:066014. doi: 10.1088/1741-2552/aae069

Ehrlich, S. K., and Cheng, G. (2019). A feasibility study for validating robot actions using eeg-based error-related potentials. *Int. J. Soc. Robot.* 11, 271–283. doi: 10.1007/s12369-018-0501-8

Esfahani, E. T., and Sundararajan, V. (2011). Using brain–computer interfaces to detect human satisfaction in human–robot interaction. *Int. J. Hum. Robot.* 8, 87–101. doi: 10.1142/S0219843611002356

Ferrez, P. W., and Millán, J. D. R. (2005). "You are wrong!—automatic detection of interaction errors from brain waves," in *Proceedings of the 19th International Joint Conference on Artificial Intelligence (No. EPFL-CONF-83269)* (Edinburgh).

Ferrez, P. W., and Millán, J. D. R. (2008). "Simultaneous real-time detection of motor imagery and error-related potentials for improved BCI accuracy," in *Proceedings of the 4th International Brain-Computer Interface Workshop and Training Course (No. CNBI-CONF-2008-004)* (Graz), 197–202.

Ficocelli, M., Terao, J., and Nejat, G. (2015). Promoting interactions between humans and robots using robotic emotional behavior. *IEEE Trans. Cybern.* 46, 2911–2923. doi: 10.1109/TCYB.2015.2492999

Friedman, D. (2015). "Brain-computer interfacing and virtual reality," in *Handbook of Digital Games and Entertainment Technologies*, eds R. Nakatsu, M. Rauterberg, and P. Ciancarini (Singapore: Springer), 1–22. doi: 10.1007/978-981-4560-52-8_2-1

García-Martínez, B., Martinez-Rodrigo, A., Alcaraz, R., and Fernández-Caballero, A. (2019). "A review on nonlinear methods using electroencephalographic recordings for emotion recognition," in *IEEE Transactions on Affective Computing*. doi: 10.1109/TAFFC.2018.2890636

Gürkök, H., and Nijholt, A. (2012). Brain–computer interfaces for multimodal interaction: a survey and principles. *Int. J. Hum. Comput. Interact.* 28, 292–307. doi: 10.1080/10447318.2011.582022

Hong, K. S., and Khan, M. J. (2017). Hybrid brain–computer interface techniques for improved classification accuracy and increased number of commands: a review. *Front. Neurorobot.* 11:35. doi: 10.3389/fnbot.2017.00035

Hong, K. S., Khan, M. J., and Hong, M. J. (2018). Feature extraction and classification methods for hybrid fNIRS-EEG brain-computer interfaces. *Front. Hum. Neurosci.* 12:246. doi: 10.3389/fnhum.2018.00246

Hou, X., Trapsilawati, F., Liu, Y., Sourina, O., Chen, C. H., Mueller-Wittig, W., et al. (2017). "EEG-based human factors evaluation of conflict resolution aid and tactile user interface in future Air Traffic Control systems," in *Advances in Human Aspects of Transportation* (Cham: Springer), 885–897. doi: 10.1007/978-3-319-41682-3_73

Iacoviello, D., Petracca, A., Spezialetti, M., and Placidi, G. (2015). A real-time classification algorithm for EEG-based BCI driven by self-induced emotions. *Comput. Methods Programs Biomed.* 122, 293–303. doi: 10.1016/j.cmpb.2015.08.011

Iturrate, I., Chavarriaga, R., Montesano, L., Minguez, J., and Millán, J. D. R. (2015). Teaching brain-machine interfaces as an alternative paradigm to neuroprosthetics control. *Sci. Rep.* 5:13893. doi: 10.1038/srep13893

Jenke, R., Peer, A., and Buss, M. (2014). Feature extraction and selection for emotion recognition from EEG. *IEEE Trans. Affect. Comput.* 5, 327–339. doi: 10.1109/TAFFC.2014.2339834

Khan, M. J., and Hong, K. S. (2015). Passive BCI based on drowsiness detection: an fNIRS study. *Biomed. Opt. Express* 6, 4063–4078. doi: 10.1364/BOE.6.004063

Kim, K. T., Suk, H. I., and Lee, S. W. (2016). Commanding a brain-controlled wheelchair using steady-state somatosensory evoked potentials. *IEEE Trans. Neural Syst. Rehabilit. Eng.* 26, 654–665. doi: 10.1109/TNSRE.2016.2597854

Kim, M. K., Kim, M., Oh, E., and Kim, S. P. (2013). A review on the computational methods for emotional state estimation from the human EEG. *Comput. Math. Methods Med.* 2013:573734. doi: 10.1155/2013/573734

Kim, S. K., Kirchner, E. A., Stefes, A., and Kirchner, F. (2017). Intrinsic interactive reinforcement learning–Using error-related potentials for real world human-robot interaction. *Sci. Rep.* 7:17562. doi: 10.1038/s41598-017-17682-7

Kirchner, E. A., Kim, S. K., Straube, S., Seeland, A., Wöhrle, H., Krell, M. M., et al. (2013). On the applicability of brain reading for predictive human-machine interfaces in robotics. *PLoS ONE* 8:e81732. doi: 10.1371/journal.pone.0081732

Ko, L. W., Komarov, O., Hairston, W. D., Jung, T. P., and Lin, C. T. (2017). Sustained attention in real classroom settings: An EEG study. *Front. Hum. Neurosci.* 11:388. doi: 10.3389/fnhum.2017.00388

Kosunen, I., Salminen, M., Järvelä, S., Ruonala, A., Ravaja, N., and Jacucci, G. (2016). "RelaWorld: neuroadaptive and immersive virtual reality meditation system," in *Proceedings of the 21st International Conference on Intelligent User Interfaces* (Sonoma), 208–217. doi: 10.1145/2856767.2856796

Kothe, C. A., Makeig, S., and Onton, J. A. (2013). "Emotion recognition from EEG during self-paced emotional imagery," in *2013 Humaine Association Conference on Affective Computing and Intelligent Interaction (ACII)* (Geneva: IEEE), 855–858. doi: 10.1109/ACII.2013.160

Krol, L. R., Andreessen, L. M., Zander, T. O., Nam, C. S., Nijholt, A., and Lotte, F. (2018). "Passive brain-computer interfaces: a perspective on increased interactivity," in *Brain-Computer Interfaces Handbook: Technological and Theoretical Advances*, eds F. Lotte, A. Nijholt, and C. S. Nam (Oxford: Taylor & Francis Group), 69–86. doi: 10.1201/9781351231954-3

Krol, L. R., and Zander, T. O. (2017). "Passive BCI-based neuroadaptive systems," in *Proceedings of the 7th Graz Brain-Computer Interface Conference 2017* (Graz: GBCIC). doi: 10.3217/978-3-85125-533-1-46

Lebedev, M. A., and Nicolelis, M. A. (2017). Brain-machine interfaces: from basic science to neuroprostheses and neurorehabilitation. *Physiol. Rev.* 97, 767–837. doi: 10.1152/physrev.00027.2016

Lécuyer, A., Lotte, F., Reilly, R. B., Leeb, R., Hirose, M., and Slater, M. (2008). Brain-computer interfaces, virtual reality, and videogames. *Computer* 41, 66–72. doi: 10.1109/MC.2008.410

Leyzberg, D., Spaulding, S., Toneva, M., and Scassellati, B. (2012). "The physical presence of a robot tutor increases cognitive learning gains," in *Proceedings of the Annual Meeting of the Cognitive Science Society, Vol. 34* (Sapporo).

Liberati, G., Federici, S., and Pasqualotto, E. (2015). Extracting neurophysiological signals reflecting users' emotional and affective responses to BCI use: a systematic literature review. *NeuroRehabilitation* 37, 341–358. doi: 10.3233/NRE-151266

Lightbody, G., Galway, L., and McCullagh, P. (2014). "The brain computer interface: barriers to becoming pervasive," in *Pervasive Health* (London: Springer), 101–129. doi: 10.1007/978-1-4471-6413-5_5

Lim, C. G., Poh, X. W. W., Fung, S. S. D., Guan, C., Bautista, D., Cheung, Y. B., et al. (2019). A randomized controlled trial of a brain-computer interface based attention training program for ADHD. *PLoS ONE* 14:e0216225. doi: 10.1371/journal.pone.0216225

Lin, C. T., Chang, C. J., Lin, B. S., Hung, S. H., Chao, C. F., and Wang, I. J. (2010). A real-time wireless brain–computer interface system for drowsiness detection. *IEEE Trans. Biomed. Circuits Syst.* 4, 214–222. doi: 10.1109/TBCAS.2010.2046415

Lin, Y. P., Wang, C. H., Jung, T. P., Wu, T. L., Jeng, S. K., Duann, J. R., et al. (2010). EEG-based emotion recognition in music listening. *IEEE Trans. Biomed. Eng.* 57, 1798–1806. doi: 10.1109/TBME.2010.2048568

Liu, J., Zhang, C., and Zheng, C. (2010). EEG-based estimation of mental fatigue by using KPCA–HMM and complexity parameters. *Biomed. Signal Process. Control* 5, 124–130. doi: 10.1016/j.bspc.2010.01.001

Liu, N. H., Chiang, C. Y., and Hsu, H. M. (2013). Improving driver alertness through music selection using a mobile EEG to detect brainwaves. *Sensors* 13, 8199–8221. doi: 10.3390/s130708199

Lopes-Dias, C., Sburlea, A. I., and Müller-Putz, G. R. (2019). Online asynchronous decoding of error-related potentials during the continuous control of a robot. *Sci. Rep.* 9:17596. doi: 10.1038/s41598-019-54109-x

Lotte, F. (2015). Signal processing approaches to minimize or suppress calibration time in oscillatory activity-based brain–computer interfaces. *Proc. IEEE* 103, 871–890. doi: 10.1109/JPROC.2015.2404941

Lotte, F., Faller, J., Guger, C., Renard, Y., Pfurtscheller, G., Lécuyer, A., et al. (2012). "Combining BCI with virtual reality: towards new applications and improved BCI," in *Towards Practical Brain-Computer Interfaces* (Berlin; Heidelberg: Springer), 197–220. doi: 10.1007/978-3-642-29746-5_10

Lotte, F., Jeunet, C., Chavarriaga, R., Bougrain, L., Thompson, D. E., Scherer, R., et al. (2020). Turning negative into positives! Exploiting 'negative'results in Brain–Machine Interface (BMI) research. *Brain Comput. Interfaces* 6, 178–189. doi: 10.1080/2326263X.2019.1697143

Lotte, F., Jeunet, C., Mladenović, J., N'Kaoua, B., and Pillette, L. (2018). "A BCI challenge for the signal processing community: considering the user in the loop," in *Signal Processing and Machine Learning for Brain-Machine Interfaces* (IET), 1–33.

Lotte, F., and Roy, R. N. (2019). "Brain–computer interface contributions to neuroergonomics," in *Neuroergonomics* (Academic Press), 43–48. doi: 10.1016/B978-0-12-811926-6.00007-5

Mattout, J., Perrin, M., Bertrand, O., and Maby, E. (2015). Improving BCI performance through co-adaptation: applications to the P300-speller. *Ann. Phys. Rehabil. Med.* 58, 23–28. doi: 10.1016/j.rehab.2014.10.006

McDaniel, J. R., Gordon, S. M., Solon, A. J., and Lawhern, V. J. (2018). "Analyzing p300 distractors for target reconstruction," in *2018 40th Annual International Conference of the IEEE Engineering in Medicine and Biology Society* (Honolulu: EMBC) (IEEE), 2543–2546. doi: 10.1109/EMBC.2018.8512854

Mehrabian, A. (1996). Pleasure-arousal-dominance: a general framework for describing and measuring individual differences in temperament. *Curr. Psychol.* 14, 261–292. doi: 10.1007/BF02686918

Millán, J. D. R., Rupp, R., Mueller-Putz, G., Murray-Smith, R., Giugliemma, C., Tangermann, M., et al. (2010). Combining brain–computer interfaces and assistive technologies: state-of-the-art and challenges. *Front. Neurosci.* 4:161. doi: 10.3389/fnins.2010.00161

Min, J., Wang, P., and Hu, J. (2017). Driver fatigue detection through multiple entropy fusion analysis in an EEG-based system. *PLoS ONE* 12:e0188756. doi: 10.1371/journal.pone.0188756

Minguillon, J., Lopez-Gordo, M. A., and Pelayo, F. (2017). Trends in EEG-BCI for daily-life: Requirements for artifact removal. *Biomed. Signal Process. Control* 31, 407–418. doi: 10.1016/j.bspc.2016.09.005

Mishra, J., Anguera, J. A., and Gazzaley, A. (2016). Video games for neuro-cognitive optimization. *Neuron* 90, 214–218. doi: 10.1016/j.neuron.2016.04.010

Mohammadi, Z., Frounchi, J., and Amiri, M. (2017). Wavelet-based emotion recognition system using EEG signal. *Neural Comput. Appl.* 28, 1985–1990. doi: 10.1007/s00521-015-2149-8

Mousavi, M., and de Sa, V. R. (2019). Spatio-temporal analysis of error-related brain activity in active and passive brain–computer interfaces. *Brain Comput. Interfaces* 6, 118–127. doi: 10.1080/2326263X.2019.1671040

Mu, Z., Hu, J., and Min, J. (2017). Driver fatigue detection system using electroencephalography signals based on combined entropy features. *Appl. Sci.* 7:150. doi: 10.3390/app7020150

Mühl, C., Allison, B., Nijholt, A., and Chanel, G. (2014a). A survey of affective brain computer interfaces: principles, state-of-the-art, and challenges. *Brain Comput. Interfaces* 1, 66–84. doi: 10.1080/2326263X.2014.912881

Mühl, C., Jeunet, C., and Lotte, F. (2014b). EEG-based workload estimation across affective contexts. *Front. Neurosci.* 8:114. doi: 10.3389/fnins.2014.00114

Müller-Putz, G. R., Breitwieser, C., Cincotti, F., Leeb, R., Schreuder, M., Leotta, F., et al. (2011). Tools for brain-computer interaction: a general concept for a hybrid BCI. *Front. Neuroinform.* 5:30. doi: 10.3389/fninf.2011.00030

Myrden, A., and Chau, T. (2015). Effects of user mental state on EEG-BCI performance. *Front. Hum. Neurosci.* 9:308. doi: 10.3389/fnhum.2015.00308

Myrden, A., and Chau, T. (2017). A passive EEG-BCI for single-trial detection of changes in mental state. *IEEE Trans. Neural Syst. Rehabilit. Eng.* 25, 345–356. doi: 10.1109/TNSRE.2016.2641956

Nagel, S., and Spüler, M. (2019). World's fastest brain-computer interface: Combining EEG2Code with deep learning. *PLoS ONE* 14:e0221909. doi: 10.1371/journal.pone.0221909

Nam, C. S., Nijholt, A., and Lotte, F. (Eds.). (2018). *Brain–Computer Interfaces Handbook: Technological and Theoretical Advances*. CRC Press. doi: 10.1201/9781351231954

Ogino, M., and Mitsukura, Y. (2018). Portable drowsiness detection through use of a prefrontal single-channel electroencephalogram. *Sensors* 18:4477. doi: 10.3390/s18124477

Paiva, A., Leite, I., and Ribeiro, T. (2014). "Emotion modeling for social robots," in *The Oxford Handbook of Affective Computing*, eds R. Calvo, S. D'Mello, J. Gratch, and A. Kappas 296–308. doi: 10.1093/oxfordhb/9780199942237.001.0001

Pazzaglia, M., and Molinari, M. (2016). The embodiment of assistive devices—from wheelchair to exoskeleton. *Phys. Life Rev.* 16, 163–175. doi: 10.1016/j.plrev.2015.11.006

Pino, O., Palestra, G., Trevino, R., and De Carolis, B. (2019). The humanoid robot nao as trainer in a memory program for elderly people with mild cognitive impairment. *Int. J. Soc. Robot.* 12, 21–33. doi: 10.1007/s12369-019-00533-y

Poli, R., Valeriani, D., and Cinel, C. (2014). Collaborative brain-computer interface for aiding decision-making. *PLoS ONE* 9:e102693. doi: 10.1371/journal.pone.0102693

Posner, J., Russell, J. A., and Peterson, B. S. (2005). The circumplex model of affect: an integrative approach to affective neuroscience, cognitive development, and psychopathology. *Dev. Psychopathol.* 17, 715–734. doi: 10.1017/S0954579405050340

Reuderink, B., Mühl, C., and Poel, M. (2013). Valence, arousal and dominance in the EEG during game play. *Int. J. Auton. Adapt. Commun. Syst.* 6, 45–62. doi: 10.1504/IJAACS.2013.050691

Rossi, S., Ferland, F., and Tapus, A. (2017). User profiling and behavioral adaptation for HRI: a survey. *Pattern Recognit. Lett.* 99, 3–12. doi: 10.1016/j.patrec.2017.06.002

Roy, R. N., Bonnet, S., Charbonnier, S., and Campagne, A. (2013). "Mental fatigue and working memory load estimation: interaction and implications for EEG-based passive BCI," in *Engineering in Medicine and Biology Society (EMBC), 2013 35th Annual International Conference of the IEEE* (Osaka: IEEE), 6607–6610. doi: 10.1109/EMBC.2013.6611070

Saha, S., and Baumert, M. (2019). Intra-and inter-subject variability in EEG-based sensorimotor brain computer interface: a review. *Front. Comput. Neurosci.* 13:87. doi: 10.3389/fncom.2019.00087

Salazar-Gomez, A. F., DelPreto, J., Gil, S., Guenther, F. H., and Rus, D. (2017). "Correcting robot mistakes in real time using eeg signals," in *2017 IEEE International Conference on Robotics and Automation (ICRA)* (Singapore: IEEE), 6570–6577. doi: 10.1109/ICRA.2017.7989777

Schmidt, N. M., Blankertz, B., and Treder, M. S. (2012). Online detection of error-related potentials boosts the performance of mental typewriters. *BMC Neurosci.* 13:19. doi: 10.1186/1471-2202-13-19

Schultze-Kraft, M., Gugler, M., Curio, G., and Blankertz, B. (2012). "Towards an online detection of workload in industrial work environments," in *34th Annual International Conference of the IEEE EMBS* (San Diego, CA), 4792–4795.

Sciutti, A., Mara, M., Tagliasco, V., and Sandini, G. (2018). Humanizing human-robot interaction: on the importance of mutual understanding. *IEEE Technol. Soc. Magaz.* 37, 22–29. doi: 10.1109/MTS.2018.2795095

Sellers, E. W., Ryan, D. B., and Hauser, C. K. (2014). Noninvasive brain-computer interface enables communication after brainstem stroke. *Sci. Transl. Med.* 6:257re7. doi: 10.1126/scitranslmed.3007801

Shao, M., Alves, S. F. D. R., Ismail, O., Zhang, X., Nejat, G., and Benhabib, B. (2019). "You are doing great! Only one rep left: an affect-aware social robot for exercising," in *2019 IEEE International Conference on Systems, Man and Cybernetics (SMC)* (IEEE), 3811–3817. doi: 10.1109/SMC.2019.8914198

Shu, L., Xie, J., Yang, M., Li, Z., Li, Z., Liao, D., et al. (2018). A review of emotion recognition using physiological signals. *Sensors* 18:2074. doi: 10.3390/s18072074

Sinnema, L., and Alimardani, M. (2019). "The attitude of elderly and young adults towards a humanoid robot as a facilitator for social interaction," in *International Conference on Social Robotics* (Cham: Springer), 24–33. doi: 10.1007/978-3-030-35888-4_3

Soekadar, S. R., Birbaumer, N., Slutzky, M. W., and Cohen, L. G. (2015). Brain–machine interfaces in neurorehabilitation of stroke. *Neurobiol. Dis.* 83, 172–179. doi: 10.1016/j.nbd.2014.11.025

Solovey, E., Schermerhorn, P., Scheutz, M., Sassaroli, A., Fantini, S., and Jacob, R. (2012). "Brainput: enhancing interactive systems with streaming fnirs brain input," in *Proceedings of the SIGCHI Conference on Human Factors in Computing Systems* (ACM), 2193–2202. doi: 10.1145/2207676.2208372

Sprague, S. A., McBee, M. T., and Sellers, E. W. (2016). The effects of working memory on brain–computer interface performance. *Clin. Neurophysiol.* 127, 1331–1341. doi: 10.1016/j.clinph.2015.10.038

Spüler, M., Krumpe, T., Walter, C., Scharinger, C., Rosenstiel, W., and Gerjets, P. (2017). "Brain-computer interfaces for educational applications," in *Informational Environments* (Cham: Springer), 177–201. doi: 10.1007/978-3-319-64274-1_8

Spüler, M., and Niethammer, C. (2015). Error-related potentials during continuous feedback: using EEG to detect errors of different type and severity. *Front. Hum. Neurosci.* 9:155. doi: 10.3389/fnhum.2015.00155

Steinert, S., and Friedrich, O. (2020). Wired emotions: ethical issues of affective brain–computer interfaces. *Sci. Eng. Ethics* 26, 351–367. doi: 10.1007/s11948-019-00087-2

Strait, M., and Scheutz, M. (2014). Using near infrared spectroscopy to index temporal changes in affect in realistic human-robot interactions. *PhyCS* 14, 385–392. doi: 10.5220/0004902203850392

Szafir, D., and Mutlu, B. (2012). "Pay attention!: designing adaptive agents that monitor and improve user engagement," in *Proceedings of the SIGCHI Conference on Human Factors in Computing Systems* (Austin: ACM), 11–20. doi: 10.1145/2207676.2207679

Tanveer, M. A., Khan, M. J., Qureshi, M. J., Naseer, N., and Hong, K. S. (2019). Enhanced drowsiness detection using deep learning: an fNIRS study. *IEEE Access* 7, 137920–137929. doi: 10.1109/ACCESS.2019.2942838

Tapus, A., Tapus, C., and Mataric, M. (2009). "The role of physical embodiment of a therapist robot for individuals with cognitive impairments," in *RO-MAN 2009-The 18th IEEE International Symposium on Robot and Human Interactive Communication* (Toyama: IEEE), 103–107. doi: 10.1109/ROMAN.2009.5326211

Tsiakas, K., Abujelala, M., and Makedon, F. (2018). Task engagement as personalization feedback for socially-assistive robots and cognitive training. *Technologies* 6:49. doi: 10.3390/technologies6020049

Van Erp, J., Lotte, F., and Tangermann, M. (2012). Brain-computer interfaces: beyond medical applications. *Computer* 45, 26–34. doi: 10.1109/MC.2012.107

Vi, C. T., Jamil, I., Coyle, D., and Subramanian, S. (2014). "Error related negativity in observing interactive tasks," In *Proceedings of the SIGCHI Conference on Human Factors in Computing Systems* (Toronto, ON: ACM), 3787–3796.

Wiese, E., Metta, G., and Wykowska, A. (2017). Robots as intentional agents: using neuroscientific methods to make robots appear more social. *Front. Psychol.* 8:1663. doi: 10.3389/fpsyg.2017.01663

Wirth, C., Dockree, P. M., Harty, S., Lacey, E., and Arvaneh, M. (2019). Towards error categorisation in BCI: single-trial EEG classification between different errors. *J. Neural Eng.* 17:016008. doi: 10.1088/1741-2552/ab53fe

Yousefi, R., Sereshkeh, A. R., and Chau, T. (2019). Development of a robust asynchronous brain-switch using ErrP-based error correction. *J. Neural Eng.* 16:066042. doi: 10.1088/1741-2552/ab4943

Zander, T. O., and Kothe, C. (2011). Towards passive brain–computer interfaces: applying brain–computer interface technology to human–machine systems in general. *J. Neural Eng.* 8:025005. doi: 10.1088/1741-2560/8/2/025005

Zander, T. O., Kothe, C., Jatzev, S., and Gaertner, M. (2010). "Enhancing human-computer interaction with input from active and passive brain-computer interfaces," in *Brain-Computer Interfaces* (London: Springer), 181–199. doi: 10.1007/978-1-84996-272-8_11

Zander, T. O., Shetty, K., Lorenz, R., Leff, D. R., Krol, L. R., Darzi, A. W., et al. (2017). Automated task load detection with electroencephalography: towards passive brain–computer interfacing in robotic surgery. *J. Med. Robot. Res.* 2:1750003. doi: 10.1142/S2424905X17500039

Zarjam, P., Epps, J., and Lovell, N. H. (2015). Beyond subjective self-rating: EEG signal classification of cognitive workload. *IEEE Trans. Auton. Ment. Dev.* 7, 301–310. doi: 10.1109/TAMD.2015.2441960

Zhang, J., Wang, B., Zhang, C., Xiao, Y., and Wang, M. Y. (2019). An EEG/EMG/EOG-based multimodal human-machine interface to real-time control of a soft robot hand. *Front. Neurorobot.* 13:7. doi: 10.3389/fnbot.2019.00007

Conflict of Interest: The authors declare that the research was conducted in the absence of any commercial or financial relationships that could be construed as a potential conflict of interest.

frontiers in Robotics and AI

ORIGINAL RESEARCH
published: 15 October 2020
doi: 10.3389/frobt.2020.558531

Errors in Human-Robot Interactions and Their Effects on Robot Learning

Su Kyoung Kim[1]*, *Elsa Andrea Kirchner*[1,2], *Lukas Schloßmüller*[2] and *Frank Kirchner*[1,2]

[1] Robotics Innovation Center, German Research Center for Artificial Intelligence (DFKI GmbH), Bremen, Germany, [2] Research Group Robotics, University of Bremen, Bremen, Germany

During human-robot interaction, errors will occur. Hence, understanding the effects of interaction errors and especially the effect of prior knowledge on robot learning performance is relevant to develop appropriate approaches for learning under natural interaction conditions, since future robots will continue to learn based on what they have already learned. In this study, we investigated interaction errors that occurred under two learning conditions, i.e., in the case that the robot learned without prior knowledge (cold-start learning) and in the case that the robot had prior knowledge (warm-start learning). In our human-robot interaction scenario, the robot learns to assign the correct action to a current human intention (gesture). Gestures were not predefined but the robot had to learn their meaning. We used a contextual-bandit approach to maximize the expected payoff by updating (a) the current human intention (gesture) and (b) the current human intrinsic feedback after each action selection of the robot. As an intrinsic evaluation of the robot behavior we used the error-related potential (ErrP) in the human electroencephalogram as reinforcement signal. Either gesture errors (human intentions) can be misinterpreted by incorrectly captured gestures or errors in the ErrP classification (human feedback) can occur. We investigated these two types of interaction errors and their effects on the learning process. Our results show that learning and its online adaptation was successful under both learning conditions (except for one subject in cold-start learning). Furthermore, warm-start learning achieved faster convergence, while cold-start learning was less affected by online changes in the current context.

Keywords: human-robot interaction (HRI), error-related potentials (ErrPs), reinforcement learning, robotics, long-term learning, learning with prior knowledge

OPEN ACCESS

Edited by:
Luca Tonin,
University of Padua, Italy

Reviewed by:
Fumiaki Iwane,
École Polytechnique Fédérale de Lausanne, Switzerland
Pedro Neto,
University of Coimbra, Portugal

***Correspondence:**
Su Kyoung Kim
su-kyoung.kim@dfki.de

Specialty section:
This article was submitted to Computational Intelligence in Robotics, a section of the journal Frontiers in Robotics and AI

Received: *02 May 2020*
Accepted: *19 August 2020*
Published: *15 October 2020*

Citation:
Kim SK, Kirchner EA, Schloßmüller L and Kirchner F (2020) Errors in Human-Robot Interactions and Their Effects on Robot Learning. Front. Robot. AI 7:558531. doi: 10.3389/frobt.2020.558531

1. INTRODUCTION

The "human-in-the-loop" approach, e.g., through human feedback, is an interesting approach to learning in robots. Previous studies have used both explicit and implicit human feedback for robot learning, such as active learning of rewards through the use of human ratings (Daniel et al., 2014) or online generation of rewards through the use of EEG-based human feedback (Iturrate et al., 2015; Kim et al., 2017). The most commonly used EEG components are error-related potentials (ErrPs), which are evoked by the perception of unusual human or robot actions (Falkenstein et al., 2000; Parra et al., 2003; van Schie et al., 2004; Iturrate et al., 2010, 2015; Kim and Kirchner, 2013, 2016; Chavarriaga et al., 2014; Kim et al., 2017, 2020; Salazar-Gomez et al., 2017; Ehrlich and Cheng, 2018, 2019b). Single-trial detections of event-related potentials (ERPs) are possible by using machine learning techniques and signal processing

methods (Müller et al., 2004; Lotte et al., 2018), which has been demonstrated in various application areas (review, Zhang et al., 2018). In robot learning, single-trial detections are required for online generation of EEG-based human feedback for each robot's actions. One issue in single-trial EEG detections is to hardly achieve 100% classification accuracy (Kirchner et al., 2013). Another issue is a high subject variability between ErrP classification performance, which is well-known in brain-computer interfaces (BCIs) (Blankertz et al., 2009; Vidaurre and Blankertz, 2010; Ahn and Jun, 2015; Jeunet et al., 2015; Morioka et al., 2015; Ma et al., 2019) and brain imaging (Seghier and Price, 2018; Betzel et al., 2019). A relevant question when using EEG-based human feedback in robot learning is the unknown influence of human-robot interaction on the generation of EEG-based human feedback. Indeed, it has not been systematically investigated how human-robot interactions influence the online generation of EEG-based human feedback in general and especially when several interaction components play together in human-robot interaction or cooperation.

The future cooperation with robots requires an intensive investigation of interaction concepts and learning approaches in robot systems with regard to their applicability in poorly controlled environments, in case of faulty or changing human behavior and when using several interaction options. This is important because it is difficult and very strenuous or even impossible for humans to repeatedly behave identically as a robot can. A good example is the interaction with gestures. There are individual differences even in the choice of gestures, not to mention the fine to great differences in the execution of exactly the same gesture by two different people. Depending on the situation in which a person finds himself, the gestures are also performed differently. The execution of gestures also typically changes over time and depending on the frequency of execution. Often, a person spontaneously thinks of another gesture and executes a different gesture. People can cope well with these changes in the behavior of the human interaction partner. Robots or artificial learning processes have much more problems with this.

A conceivable application is that a robot performs pick-and-place tasks together with a human interaction partner. The task is to sort objects differently depending on current situations determined by human behavior (e.g., human gesture). The robot therefore has no completely fixed predefined task procedure, but does know for example which places are feasible for the robot or the human to reach. On the other hand, the human changes the desired places of objects (selection of the reachable places) depending on current situation or task efficiency. For example, the robot picks up objects and place them in locations that correspond to the current human gesture. After the action selection, the robot receives human feedback on the correctness of action selection (e.g., the robot selects a correct position for placing objects or not) and updates an action strategy based on human feedback. In this way, the robot learns an action that corresponds to the current situation determined by human gesture and also adapts an action strategy depending on online changes of human intention. Two interaction errors can occur here: (a) human gestures, which can be easily changed over time or which can vary between different interaction partners (different people), can be misinterpreted by the robot and (b) human implicit feedback in the form of EEG that can be incorrectly decoded, since a decoder is not perfectly trained. Such online learning and adaptation based on human feedback can be beneficial in unknown situations or unknown environments, e.g., space explorations. In this case, the robot has only a little predefined knowledge about task solution before explorations and can extend knowledge directly by learning from human feedback. Further, it can also be relevant in more pre-defined scenarios, i.e., assembly in production line, to adapt to individual preferences.

In order to develop new interaction concepts and learning procedures that can better deal with such changes in human behavior, we first have to investigate which influence which mistakes have on learning in the robot and which influence misbehavior of the robot has on feedback from humans. In this paper we want to use the example of implicit learning of gesture-action pairs from intrinsic human feedback based on brain activity to investigate the effect of errors in the recognition of EEG signals and gestures on interactive learning.

We investigate interaction errors under two conditions. First, the robot learns with prior knowledge and second, without prior knowledge. Although almost all studies on robot learning assume that the robot has no previous knowledge, this is actually a completely unrealistic situation especially for humans. Humans, like many other animals, almost always learn on the basis of previous knowledge. With our study we want to show that there are differences in the effects of interaction errors depending on whether learning takes place with or without previous knowledge.

1.1. Concept of Human-Robot Interaction (HRI)

In our human-robot interaction scenario, the robot learns actions that are best assigned to the *current* human intentions. Our concept of human-robot interaction (HRI) is illustrated in **Figure 1**. The subject interacts with the robot by selecting a specific gesture that expresses the human intention. The robot observes the current gesture and chooses an action based on the policy from previous trials. The subject observes the chosen action of the robot and evaluates it intrinsically. This intrinsic evaluation is reflected in certain EEG activities, which are a neuronal correlate of the implicit intrinsic evaluation of the correctness of the action of the robot. The robot learns a policy based on human feedback and updates the policy after every other interaction with the subject where further experience is gained. Finally, the robot learns correct mappings between gestures and actions (i.e., correct gesture-action pairs), which is updated in real time by human's online feedback.

The learning algorithm used in our HRI concept is based on a contextual bandit approach (e.g., Li et al., 2010). The contextual bandit approach is well-suited for our HRI scenario, since a robot learns to choose actions which are best assigned with the given context (human's current gestures). The contextual bandit approach is a variant of reinforcement learning, in which only one action is chosen per episode (details, see section 2.2).

Our HRI contains two interfaces between human and robot: (a) gesture interface that encodes human's intents in form of

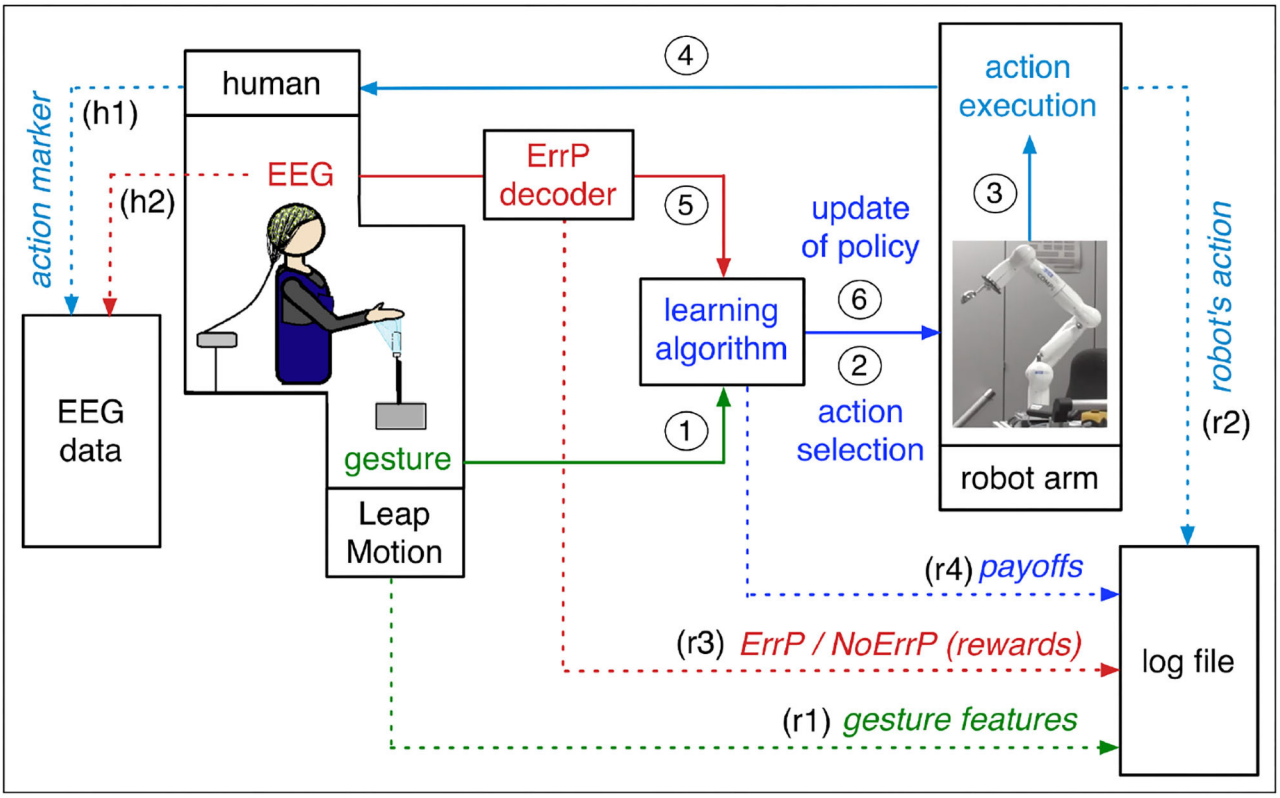

FIGURE 1 | The concept of our approach. Continuous lines represent the information flow of the learning process, and dotted lines represent the logs of the learning process and markers of the EEG data. Solid lines: The subject communicates with the robot in the form of gestures and gesture features are sent to the learning algorithm as human intention (1). Based on gesture features, the learning algorithm selects an action (2). The robot executes the chosen action (3). The subject observes the executed actions of the robot (4). The test person gives an intrinsic feedback on the robot's choice of action in the form of an EEG. The ErrP is evoked, for example, when the action performed by the robot does not match the current human gesture. The output of ErrP decoder (binary classification: ErrP or No ErrP) is sent to the learning algorithm as rewards (5). The learning algorithm updates the policy based on human feedback (6). Dotted lines: Feature vectors of human gesture are written in the log file (r1). Executed actions of the robot are written in the log file (r2) and in the EEG as action markers (h1). EEG signals are continually recorded and saved as EEG data (h2). The outputs of ErrP decoder (rewards) are written in the log file (r3). Payoffs of each gesture-action pair are written in the log file (r4). Details, see sections 1.1 and 2.2.

gestures and (b) EEG interface that decodes human's intrinsic feedbacks on robot's actions in form of EEGs. Both interfaces provide inputs to the learning algorithm that triggers actions in the robotic system (robot arm) that are best assigned with the given gestures. Hence, learning performance depends on the quality of inputs that are provided by both interfaces. In our HRI scenario, misinterpretations of human intention (human gesture) and human feedback (human evaluation) affect learning performance. In other words, an incorrect coding of human intention and an incorrect decoding of human feedback has an impact on the learning performance of the robot.

1.2. HRI Errors: Gesture Errors and ErrP Misclassifications

In our previous study (Kim et al., 2017) we investigated the effect of ErrP classification performance on robot learning performance, since the results of the ErrP classification are directly used as a reward in the learning algorithm. Thus, we focused on the analysis on ErrP-classification performance. In our HRI scenario, however, the robot receives not only implicit human feedback but also human gestures as explicit input for the interaction. Thus, the robot has two kinds of inputs for interactions with human: (a) human gestures in form of gesture features and (b) human feedback in form of ErrPs, which are neural correlates of human's implicit evaluation on robot's actions. Both types of input can be incorrect in real applications for different reasons.

Gesture errors can be generated when human gestures are not correctly recorded for several reasons. First, hand positions of the subjects are often out of range of sensors (infrared cameras) due to changes of body posture of the subjects. In most cases, the subjects are not aware of such large variances of their own hand positions. Second, in a few cases, we have also a general hardware problem. The gesture recording system called Leap Motion does not accurately enough catch hand gestures due to the limited range of infrared cameras. The accuracy of gesture capture depends on how the subject's hands enter the camera's sensors. Third, some subjects change their gesture

TABLE 1 | (A) Four gesture types; **(B)** Errors in human-robot interaction (HRI) and their effects on learning performance.

Gesture type	Feature vector	Recorded feature vectors
(A)		
Left	[−1 0 0 0]	[−0.85 0.11 0.15 0.21]
Right	[1 0 0 0]	[0.91 0.22 0.32 0.19]
Upward	[0 1 0 0]	[0.14 −0.84 0.15 0.93]
Forward	[0 −1 0 1]	[0.11 0.81 0.11 0.23]

		Online robot learning					Offline analysis			
		(a)	(b)	(c)	(d)	(e)	(f)	(g)	(h)	(i)
Case	**Perception**	**Human gesture**	**Recorded gesture**	**Robot action**	**ErrP detection**	**Rewards**	**Gesture error**	**ErrP error**	**ErrP classification**	**Impact on learning**
(B)										
1	Human robot	Left	Left	Left	No ErrP	1	No	No	TN	Positive
2	Human robot	Left	Left	Left	ErrP	−0.25	No	Yes	FP	Negative
3	Human robot	Left	Left	Right	No ErrP	1	No	Yes	FN	Negative
4	Human robot	Left	Left	Right	ErrP	−0.25	No	No	TP	Positive
5	Human robot	Left	Right	Left	No ErrP	1	Yes	No Yes	TN FN	Negative
6	Human robot	Left	Right	Left	ErrP	−0.25	Yes	Yes No	FP TP	Positive
7	Human robot	Left	Right	Right	No ErrP	1	Yes	Yes No	FN TN	Positive
8	Human robot	Left	Right	Right	ErrP	−0.25	Yes	No Yes	TP FP	Negative

The recorded feature vectors are presented as example. ErrP error stands for ErrP error classification. The positive class stands for faulty action of the robot. Only the cases in which the test subjects perform the gesture to move the robot to the left *are described as examples.*

patterns during the experiments. For example, at the beginning of the experiment, these subjects made gestures to move the robot to the *right* with their hands open, but in the middle of the experiment they closed their hands before finishing the whole gesture. In this case, an additional gesture feature (e.g., closed hand) was added [1, 0, 0, 1], which is used for the gesture *forward* [0, −1, 0, 1]. Again, the subjects are not aware of their own changes of gesture pattern. An overview of the gesture vector depending on the gesture type is shown in **Table 1A**. All types of gesture errors provide wrong gesture features to the robot and thus the robot perceives gesture features that are not coherent with gestures that the subjects intended to perform. Therefore, in our data analysis gesture errors are defined as gesture incoherence between human and robot, i.e., incoherence between gestures performed (by humans) and perceived (by robots). Note that maximum values of feature vectors (second column of **Table 1A**) cannot be reached by actually performed human gestures. We observed individual differences in gesture features within the same gesture type (inter-subject variability) and differences in gesture characteristics between repeatedly executed identical gesture types within the same test subjects (inter-gesture variability).

Human feedback (reward) can also be wrong for various reasons. We consider incorrect decoding of human implicit feedback (ErrP) as the most common reason for incorrect human feedback. In general, the accuracy of the trained ErrP decoder is seldom achieved with 100%. Hence, ErrP misclassifications, i.e., both false positives (FP) and false negatives (FN) were counted as erroneous human feedback in our data analysis. Erroneous human feedback can in a few cases also be generated by gesture errors, although there are no ErrP misclassifications (details in section 2.1). Erroneous human feedback can also be caused if the test subjects miss the robot's actions due to lack of attention. In this case, ErrP detections are incorrect and thus erroneous feedbacks are sent to the robot. However, we have found that such errors are indeed rare, since the task (observing the actions of the robot) was actually very simple. This was also shown by the oral feedback of the test persons to our questions, how often they approximately missed the actions of the robot. For this reason, we excluded this type of error from our data analysis.

Both ErrP misclassifications and gesture errors can occur together and influence each other. The interaction of both types of errors can lead to erroneous feedback to the robot, which affects robot learning. The interaction between ErrP misclassifications and gesture errors and their effects on robot learning is reported in detail in section 2.1.

2. METHODS

2.1. Expected Effects of HRI Errors on Learning Performance

Figure 2A shows a schematic overview of the effects of ErrP classifications on the learning process of the robot, where there are no gesture errors (no faulty recording of gestures). ErrPs are used as implicit evaluation of robot's action choice: when ErrPs are detected, negative feedbacks are given to the robot, whereas positive feedbacks are given to the robot when ErrPs are not detected (solid red lines, in **Figure 2A**). There are two cases for robot learning, when ErrP detections are correct: (a) a positive feedback (No ErrP) is given to a correct gesture-action pair (a1 in **Figure 2A**) and (b) a negative feedback (ErrP) is given to a wrong gesture-action pair (b2 in **Figure 2A**). In both cases, the robot learns correct gesture-action pairs (case 5 and 8 in **Figure 2A** and **Table 1B**). However, when ErrP detections are wrong, erroneous feedbacks are given to the robot: (a) a negative feedback (ErrP) is given to a correct gesture-action pair (a2 in **Figure 2A**) and (b) a positive feedback (No ErrP) is given to a wrong gesture action-pair (b1 in **Figure 2A**). In both cases, the robot learns wrong gesture-action pairs (case 6 and 7 in **Figure 2A** and **Table 1B**). Hence, ErrP misclassifications can generate erroneous feedback that negatively affect the learning process in two ways: (a) ErrPs are detected although robot's actions are correct, i.e., false positive (FP) and (b) ErrPs are not detected although robot's actions are wrong, i.e., false negative (FN), where positive class stands for erroneous actions.

Figure 2B shows a schematic overview of the negative effects of gesture errors on the robot's learning performance, where ErrP detections are correct *per se*. Gesture errors can have a direct or indirect effect on the robot's learning performance, but their impact on the learning process is not straightforward, since gesture errors affect ErrP error classifications that further influence the learning process. This means that the effects of gesture errors on the learning process cannot be easily interpreted. When gestures are incorrectly recorded, the performed gestures of human are not coherent with the recorded gestures (green dotted line in **Figure 2B**). Hence, the robot perceives gesture features that are incoherent with the subject's performed gestures and decides an action based on the perceived gestures. On the other hand, human feedbacks are generated based on the performed gestures of human. In fact, the test subjects always compare their executed gestures (not the recorded gestures) and the robot's action choices (H-a and H-b in **Figure 2B**). They are not aware of incorrectly recorded gestures, because the test subjects perceive almost no false recordings of their own gestures when interacting with the robot online. Therefore, human feedback to the robot (No ErrP/ErrP) is generated based on the gestures performed by the human, while the robot receives characteristics of the recorded gestures. That means, online-reward generations (ErrP detections) are based on human perception, whereas action choices of the robot are based on robot perception. In the end, erroneous recordings of gestures lead to the generation of incorrect feedback: (a) ErrP with correct gesture-action pairs (Ra in **Figure 2B**) and (b) No ErrP on an incorrect gesture-action pair (Rb in **Figure 2B**), although the ErrP detections are correct in themselves, i.e., there are no ErrP misclassifications (Ha and Hb in **Figure 2B**).

For schematic overviews, we visualized the effect of ErrP classifications (rewards) without gesture errors (**Figure 2A**) or the effect of gesture errors without ErrP misclassifications (**Figure 2B**). However, ErrP misclassifications and gesture errors can occur together and interact.

Table 1B shows all theoretically possible cases of input errors (gesture errors/ErrP misclassifications) and their combinations in our HRI scenario. In **Table 1B** only the cases are exemplarily described in which the subjects perform the gesture to move the robot to *left*.

When there are no gesture errors (case 1, 2, 3, 4 in **Table 1B**), ErrP-classification performances are same for both human perception and robot perception (**Table 1B**-h). When gesture errors are observed (case 5, 6, 7, 8 in **Table 1B**), ErrP-classification performances are different between human perception and robot perception (**Table 1B**-h). Gesture errors have a negative effect on the robot's learning process if they occur without ErrP error classifications (case 5 and 8 in **Table 1B**), because the robot learns gesture-action pairs based on the recorded gestures and not on the executed human gestures and receives erroneous feedback from the test persons (case 5: No ErrPs on *right-left* pairs; case 8: ErrPs on *right-right* pairs). However, when gesture errors and ErrP misclassifications occur together, learning performances of the robot are positively affected, since gesture errors cancel out ErrP misclassifications (case 6 and 7 in **Table 1B**) and the robot receives correct feedbacks from the subjects (case 6: ErrP on *right-left* pairs; case 7: No ErrP on *right-right* pairs).

In summary, misinterpretations of human intention (gesture errors) and human feedback (ErrP error classifications) can separately influence the learning process as follows: Learning process can be negatively affected by (a) ErrP misclassifications without gesture errors (case 2 and 3 in **Table 1B**) or (b) gesture errors without ErrP misclassifications (case 5 and 8 in **Table 1B**). However, in a few cases, there is an interaction between gesture errors and ErrP misclassifications, which positively affects the learning process, since gesture errors cancel out ErrP misclassifications (case 6 and 7 in **Table 1B**). Finally, the absence of both error types (correct gesture recordings and correct ErrP detections) has a positive impact on the learning process (case 1 and 4 in **Table 1B**).

2.2. Learning Algorithm

In our HRI scenario, a robot learns to choose actions which are best assigned with the given context (human's current gestures), in which robot's actions have single-state episodes and the

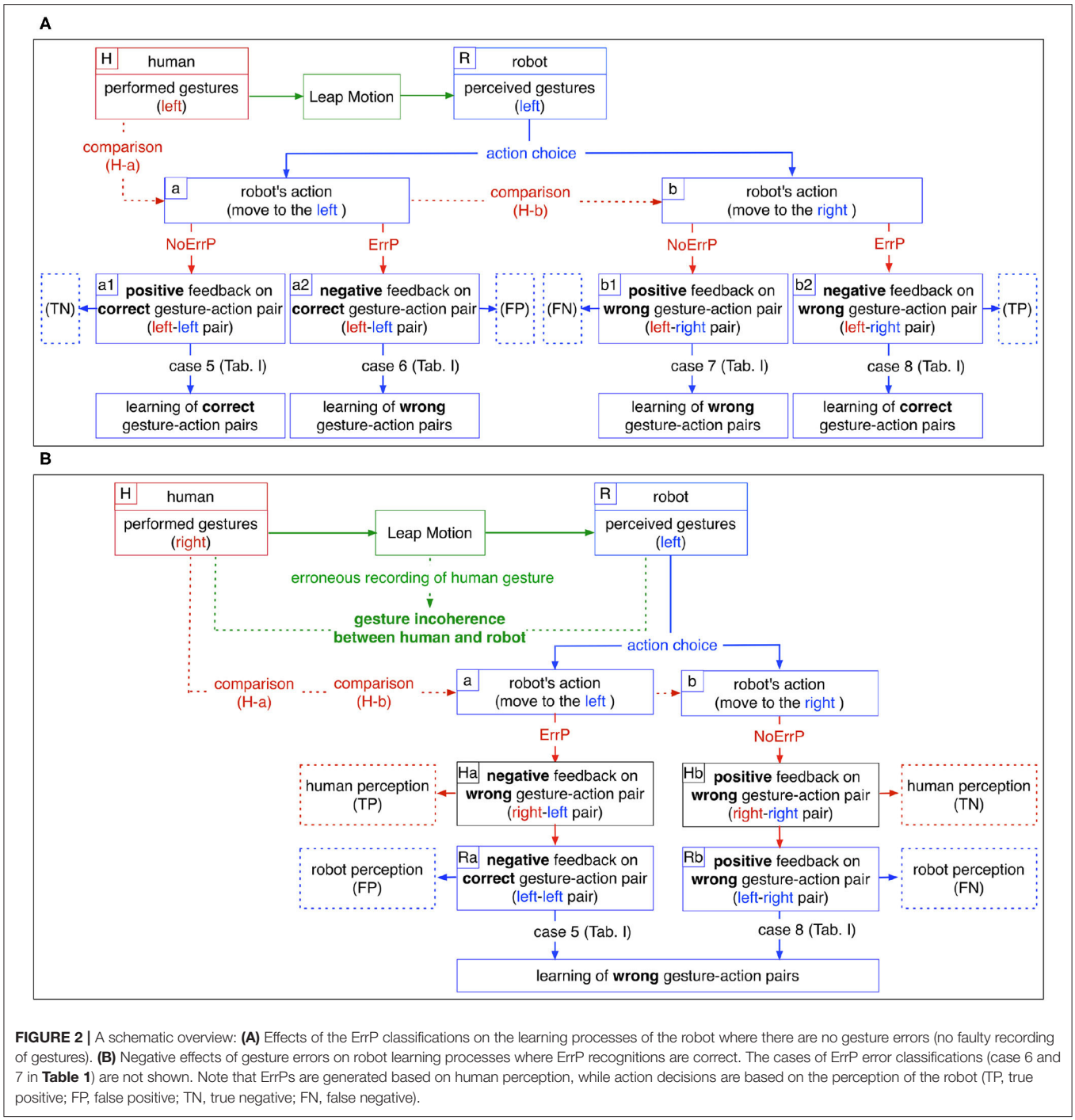

FIGURE 2 | A schematic overview: **(A)** Effects of the ErrP classifications on the learning processes of the robot where there are no gesture errors (no faulty recording of gestures). **(B)** Negative effects of gesture errors on robot learning processes where ErrP recognitions are correct. The cases of ErrP error classifications (case 6 and 7 in **Table 1**) are not shown. Note that ErrPs are generated based on human perception, while action decisions are based on the perception of the robot (TP, true positive; FP, false positive; TN, true negative; FN, false negative).

context is independent of each other. Thus, the contextual bandit approach is well-suited for our HRI scenario. Among state-of-the art contextual bandits approaches, we chose LinUCB (Li et al., 2010) as learning algorithm (see Algorithm 1). In principle, LinTS (Agrawal and Goyal, 2013) is also suitable for our HRI scenario. Although both algorithms are interchangeable, empirical evaluation of both algorithms led to different learning performances depending on application scenarios (Chapelle and Li, 2011). Further, other state-of-art algorithms regarding multi-arm bandits can also be implemented for contextual bandits settings (Cortes, 2018). However, LinUCB (Li et al., 2010) is a popular approach that has been evaluated in numerous scenarios and proved as a fast and effective approach in contextual bandit settings [e.g., HybridLinUCB (Li et al., 2010), GOB.Lin (Cesa-Bianchi et al., 2013), CLUB (Gentile et al., 2014), CoLin (Wu et al., 2016)].

Contextual bandits (Langford and Zhang, 2008) have single-state episodes, since they obtain only one immediate reward per episode. This is similar to *k*-armed bandits (Auer et al., 2002) that is the simplest form of reinforcement learning. However, contextual bandits use the information about the state of the environment (cf. *k*-armed bandits) and thus make decision dependent on the state of the environment (context). That means, the policy of context (state)-action pair is updated per episode (trial) and the context is independent of each other. Accordingly, the context is different for each episode (trial). For example, in our HRI scenario, the subject performs different types of gesture (left, right, forward, upward) for each episode, e.g., *left gesture* ($x_{1,1}$) for the first episode, *right gesture* ($x_{2,2}$) for the second episode, *left gesture* ($x_{3,1}$) for the third episode, *forward gesture* ($x_{4,3}$) for the fourth episode, etc. **Figure 3** shows a schematic visualization of LinUCB (Li et al., 2010) in a given context in a specific episode as an example.

In LinUCB (Li et al., 2010), it is assumed that the predicted payoff (the expected payoff) of an arm a is linear in its d-dimensional feature $x_{t,a}$ with some unknown coefficient vector θ_a^*: $E[r_{t,a}|x_{t,a}] = x_{t,a}^T\theta_a^*$. Note that the model is called disjoint, since the parameters are not shared among different arms. Ridge regression is applied to the training data (D_a, c_a) in order to estimate the coefficients θ_a^* (details, see below). The algorithm observes feature vector x_t and selects an action a_t based on *the predicted payoffs* of all actions. After action selection, the algorithm receives *the current payoff* r_{t,a_t} and updates the policy with the new observation ($x_{t,a_t}, a_t, r_{t,a_t}$). The step-by-step description follows below (see Algorithm 1).

The exploration parameter α is determined before the learning was used as input (line 0). For each time, e.g., for each trial (line 1), the algorithm observes all features (line 2). When the action has not been observed before (line 4), one $d \times d$ identity matrix (I_d) and one zero vector of length d ($0_{d\times 1}$) are instantiated (line 5, line 6), where d is the number of features. The coefficient $\hat{\theta}_a$ is estimated by applying ridge regression to the training data (D_a, c_a), where D_a is a $m \times d$ design matrix and c_a is the vector of length m (where m is the number of observations): $\hat{\theta}_a = (D_a^T D_a + I_d)^{-1} D_a^T c_a$. In the Algorithm 1, $D_a^T D_a + I_d$ is rewritten as A_a and $D_a^T c_a$ is rewritten as b_a (line 8). Accordingly, $\hat{\theta}_a$ can be rewritten as $A_a^{-1} b_a$. Payoffs $P_{t,a}$ are estimated as the sum of ridge regression for the current feature $x_{t,a}$ (i.e., the expected payoff: $\hat{\theta}_a\ x_{t,a}$) and the standard deviation of the expected payoff ($\sqrt{x_{t,a}^T\ A_a^{-1}\ x_{t,a}}$), where the standard deviation is multiplied by the parameter α that determines the degree of exploration (line 9). The algorithm chooses the action with the highest expected payoff ($arg\ max_{a\in\mathscr{A}_t} P_{t,a}$) and observes the received *current* payoff r_t on the chosen action (line 11). Finally, the training data (D_a, c_a) is updated in action space A_{a_t} and context space b_{a_t} (line 12 and line 13), which is fitted by applying ridge regression to estimate $\hat{\theta}_a$ for the next trial. Therefore, the expected payoff is linear in its d-dimensional feature $x_{t,a}$ with some unknown coefficient vector θ_a^*: $E[r_{t,a}|x_{t,a}] = x_{t,a}^T\theta_a^*$. Payoffs $p_{t,a}$ are affected by two parameters: the expected payoff (exploitation) and the standard deviation of the expected payoff (exploration). The optimum of action strategy is obtained by balancing exploration and exploitation.

Algorithm 1 LinUCB (Li et al., 2010)

0: Inputs: $\alpha \in \mathbb{R}_+$
1: **for** $t = 1, 2, 3, \ldots, T$ **do**
2: Observe features of all arms $a \in \mathscr{A}_t$: $x_{t,a} \in \mathbb{R}^d$
3: **for all** $a \in \mathscr{A}_t$ **do**
4: **if** a is new **then**
5: $A_a \leftarrow I_d$ (d-dimensional identity matrix)
6: $b_a \leftarrow 0_{d\times 1}$ (d-dimensional zero vector)
7: **end if**
8: $\hat{\theta}_a \leftarrow A_a^{-1}\ b_a$
8: $P_{t,a} \leftarrow \hat{\theta}_a^T\ x_{t,a} + \alpha\sqrt{x_{t,a}^T\ A_a^{-1}\ x_{t,a}}$
10: **end for**
11: Choose arm $a_t = arg\ max_{a\in\mathscr{A}_t} P_{t,a}$ with ties broken arbitrarily and observe a real valued payoff r_t
12: $A_{a_t} \leftarrow A_{a_t} + x_{t,a_t}\ x_{t,a_t}^T$
13: $b_{a_t} \leftarrow b_{a_t} + r_t\ x_{t,a_t}$
14: **end for**

In our HRI scenario, the algorithm learns to select robot's actions a_t that are best assigned with the current context x_t, i.e., the current human intention in form of gesture feature recorded by the Leap Motion. The current payoff, i.e., the immediate reward is the ErrP-classification output (ErrP or No ErrP), which is given to the action chosen by the LinUCB algorithm, i.e., the executed action of the robot. As mentioned earlier, action selection was made conditional on human gesture (left, right, forward, upward). We call actions together with gesture features "gesture-action pairs" (i.e., context-action pairs). The LinUCB algorithm learns a correct mapping between human gesture features and actions of the robot, i.e., a correct gesture-action pair. In fact, the robot should learn which action is correctly executed. Hence, our HRI scenario is designed that the predictions of correct mappings (No ErrP) are highly rewarded [1] than the predictions of wrong mappings (ErrP) that are minimally punished [−0.25]. To this end, we used two windows for the same action in online ErrP detection and the predictions of correct mappings (No ErrP) were sent to the learning algorithm, only when No ErrP was predicted from both time windows (**Table 2**). As a result, the rewards for predicted correct mapping (TN, FN) were weighted more strongly than predicted wrong mapping (FP, TN). Note that the reward values of [−0.25, 1] were empirically determined. Further, the exploration parameter α was also empirically determined [$\alpha = 1$].

One of the key elements of our approach is to adapt the previous learned policy when changing the current human intention (i.e., when changing the semantics of gestures). Thus, human gesture was not predefined, i.e., no initial semantics of gestures was given to the robot. Rather, the robot learned the current meaning of human gesture, which can be changed online. That means, there were no fixed labels (no fixed semantics of gestures) to train a model. For this reason, we did not train

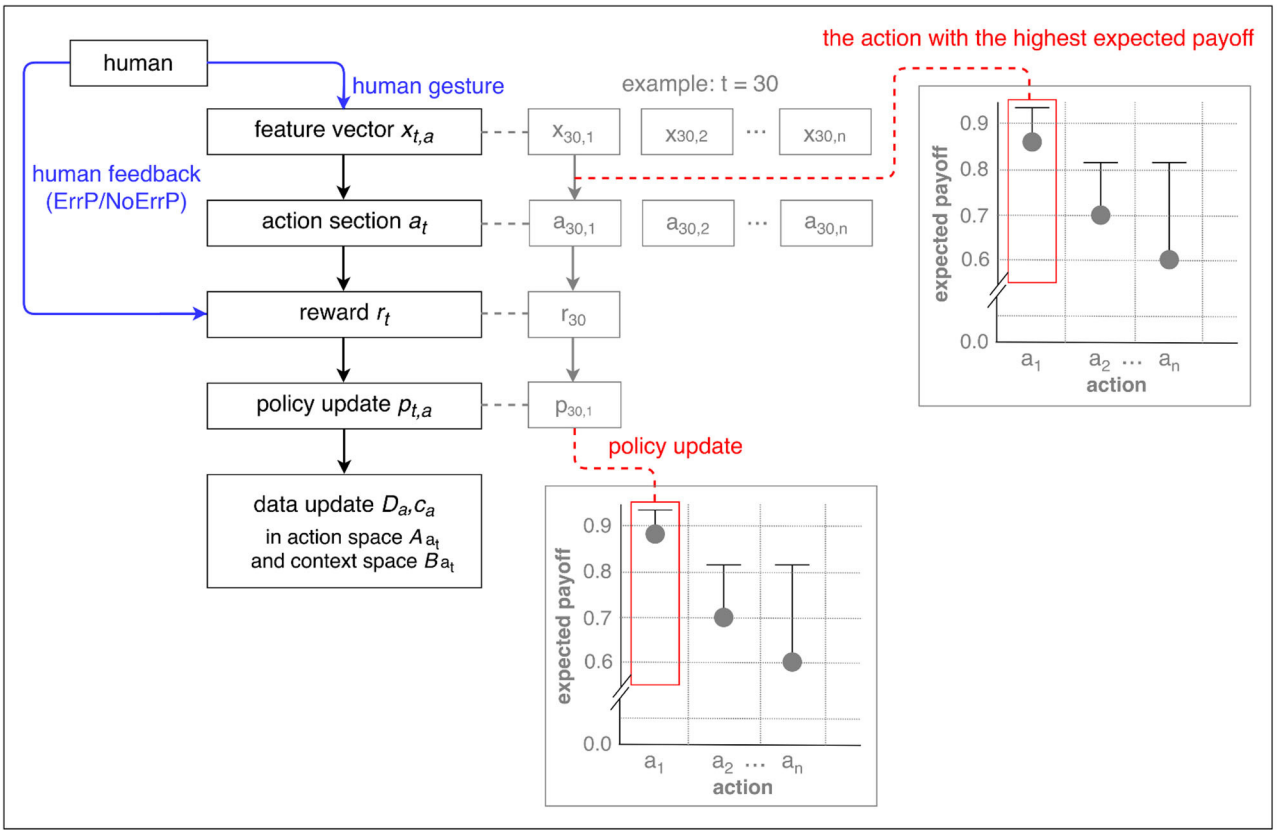

FIGURE 3 | A schematic visualization of LinUCB (Li et al., 2010). Action selection and policy update were depicted in the given context x_1 for the 30th trial (episode) as an example. In accordance with our HRI scenario, the subjects performed the *left gesture* ($x_{30,1}$) among other gesture types ($x_{30,2}$, $x_{30,3}$, $x_{30,4}$) in the current episode (in the 30th episode). In this example, a correct action x_1 (left action of the robot) is chosen in the given context x_1 (left gesture). The policy [i.e., the expected payoff that is equivalent to the upper confidence bound (UCB)] is updated for the chosen action, i.e., x_1-a_1 pair.

TABLE 2 | Use of ErrP detection as a reward in the learning algorithm.

(A) Actual label	Correct		Correct		Wrong		Wrong	
(B1) Prediction (1st window)	No ErrP	No ErrP	ErrP	ErrP	No ErrP	No ErrP	ErrP	ErrP
(B2) Prediction (2nd window)	No ErrP	ErrP	No ErrP	ErrP	No ErrP	ErrP	No ErrP	ErrP
(C) Predicted label	No ErrP (correct)		ErrP (wrong)		No ErrP (correct)		ErrP (wrong)	
(D) Rewards	1		−0.25		1		−0.25	
(E) ErrP evaluation	TN		FP		FN		TP	

Actual labels are obtained by comparing between gesture labels and action labels (gesture-action pairs). The outputs of ErrP decoder, i.e., predictions (B1 and B2) are obtained by two windows with the same robot actions (same gesture-action pair). A decision was made from two windows, and this is used as predicted labels (C) for the confusion matrix. Rewards (D) are sent to the learning algorithm (online learning). The evaluation of the ErrP classifications (ErrP detections) is based on the confusion matrix.

a classifier to distinguish different types of *predefined* gestures. Instead, the robot received gesture feature vectors recorded by the Leap Motion instead of classified gestures. Accordingly, no *classified* gestures were sent to the robot. The chosen algorithm called LinUCB enables to learn gesture-action pairs without prior knowledge of gesture meaning.

In fact, we observed a variation of gesture feature vectors between trials within the same subject (details, see section 1.2), but this did not prevent robust learning of gesture-action pairs. Learning remains robust due to the updates of context space per trial: The current context, i.e., gesture feature vector ($x_{t,a}$) was added to the context space ($b_{a,t}$) together with the corresponding current payoff ($r_{t,a}$) for each trial. This update of the context space allows for robust learning despite of variations of gesture feature vectors between trials (e.g., [−0.9, 0.15, 0.29, 0.37], [−0.8, 0.27, 0.41, 0.05], [−0.95, 0.29, 0.11, 0.88], etc.) for the *left* gesture type (default value [−1, 0, 0, 0]). In this way, gesture feature vectors were adapted per trial within a subject.

The main scope of this study was to analyze erroneous inputs and their impacts on learning performance. The data analysis

was based on the log files that were generated for each online experiment. Note that learning was completed for each online experiment (i.e., each online dataset). The following outputs were logged online per trial within an online experiment:

- Updates of action space A_a and context space b_a (line 5 and 6 in Algorithm 1)
- Gesture feature vector for the current trial $x_{t,a}$ (line 1 in Algorithm 1, **Figure 1**-r1)
- The action with the highest expected payoff for the current trial a_t (line 11 in Algorithm 1, **Figure 1**-r2)
- The current payoff, i.e., the immediate reward r_t for the current trial (line 11 in Algorithm 1, **Figure 1**-r3)
- The expected payoffs $P_{t,a}$ (line 9 in Algorithm 1, **Figure 1**-r4)

Gesture feature vectors were logged automatically while online learning (**Figure 1**-r1). That means, gesture feature vectors recorded by Leap Motion was logged online. However, human gestures, i.e., gestures performed by human could not be logged online. Thus, we filmed human gestures and robot's actions during online experiments. After experiments, we investigated which gesture feature vectors were perceived by the robot. To this end, we reconstructed gestures per trial based on the logged gesture feature vectors in the log file. Such reconstruction was done only for offline data analysis. We used the following decision criteria for reconstruction of gestures: (a) $m = 1$, if $m > 0.5$ (b) $m = -1$, if $m < -0.5$ (c) $m = 0$, if $-0.5 < m < 0.5$, where m is each component of vector. The gesture feature vector consists of four components (details, see section 2.3.4). In this way, we obtained filmed gestures and reconstructed gestures. Finally, gesture errors were estimated by comparing filmed human gestures (e.g., *left* gesture) and the reconstructed gesture based on recorded gesture vectors [e.g., −0.8, 0.1, 0.2, 0.1]. Further, filmed gestures were used to determine the correctness of gesture-action pairs and to find a true label to generate a confusion matrix for human's perspective, whereas the reconstructed gestures were used as a true label to generate a confusion matrix for robot's perspective (details, see section 2.4).

2.3. Scenario and Dataset

We used the data that was recorded in the previous study for investigation on flexible adaptation of learning strategy using EEG-based reinforcement signals in real-world robotic applications (Kim et al., 2020). In the previous study (Kim et al., 2020), data was recorded from eight subjects (2 females, 6 males, age: 27.5 ± 6.61, right-handed, normal or corrected-to normal vision). The experiments were carried out in accordance with the approved guidelines. Experimental protocols were approved by the ethics committee of the University of Bremen. Written informed consent was obtained from all participants that volunteered to perform the experiments.

In our HRI scenario (Kim et al., 2017), the subjects perform gestures (left, right, forwards) and observe the robot's actions as response to the human gestures (Details, see section 1.1 and **Figure 1**). In the extend HRI scenario (Kim et al., 2020), the subjects add a new gesture (upwards) after about 30 trials, while the robot still learns the mapping between human gestures and its own actions. That means, the subjects determine the meaning of the gesture (human intent) and select one of gestures. The robots learns to select an action that is best assigned to the current human intents (current gesture) based on human implicit feedback in form of EEG. The goal of the previous study was to investigate whether the robot can flexibly adapt the learning strategy in real time, when the user changes the *current* intentions (in form of EEG). For example, the subjects changed their control strategy e.g., by adding a new context (gesture) to the previous used gestures. Our results showed that the robot could adapt the previously learned policy depending on online changes of the user's intention (Kim et al., 2020). This investigation was validated under two learning conditions: (a) learning algorithm was trained with a few samples (1 or 2 gesture-action pairs) before online learning (pretraining) and (b) learning algorithm was not trained before online learning (no-pretraining).

2.3.1. Scenario Description

In the previous study (Kim et al., 2020), we collected data in two different scenarios: (a) observation scenario and (b) interaction scenario. In the *observation* scenario, the subjects observed the robot's action. Here, the subjects were not required to interact with the robot, e.g., by performing gestures, since human gestures and robot's action choice were already preprogrammed. A hand gesture was displayed to the subjects as a word (left, right, forward, or upward) on the monitor, which is located on the left side of the robot. Then, a feature vector of the displayed gesture (**Table 1A**, second column) was sent to the pseudo-learning algorithm, where action selections were preprogrammed. Gesture-action pairs are preprogrammed with the class ratio of 8:1 (correct/wrong actions). The observation scenario was designed to train a ErrP classifier in order to detect ErrPs online in the interaction scenario. In the observation scenario, the subjects did not perform gestures and the robot did not learn any action selection strategy. In this way, we could reduce the recording time for training data for ErrP decoder. We trained a classifier for each subject to distinguish ErrP and No ErrP, which was later used to detect ErrPs in the *interaction* scenario. Such classifier transfer was successfully evaluated in our previous studies (Kim and Kirchner, 2013, 2016; Kim et al., 2017).

In the *interaction* scenario, the subjects performed one of four gesture types (left, right, forward, and upward). As mentioned before, we used the Leap Motion to record human gestures. Gesture feature vectors recorded by Leap Motion were sent to the LinUCB algorithm. Then, the algorithm selected an action and sent this action selection to the robot. The subject observed the action choice of the robot and at the same time the implicit evaluation of the chosen action of the robot was measured by using the EEG and the so called ErrP was detected online per action choice.

Implicit human evaluations (ErrP/No ErrP) were sent to the LinUCB algorithm as rewards.

2.3.2. Datasets for Training of ErrP Decoder (Observation Scenario)

For training a classifier (ErrP decoder), we recorded data in the *observation* scenario, in which the subjects observe the

robot's actions without performing a gesture to reduce the recording time of EEG data. The subjects were instructed to observe the gesture that was displayed as a word (left, right, forward, or upward) on the monitor. After the display of the gesture disappeared on the monitor, the robot started to move the arm. The subjects were instructed to observe the actions of the robot. Six datasets were recorded from each subject. Each dataset consists of 80 correct actions of the robot and 10 wrong actions of the robot (90 instances in total). Gesture-action pairs are preprogrammed with the class ratio of 8:1 (correct/wrong actions). We had a uniform number of training dataset, i.e., all participants had the same number of training dataset (six datasets).

2.3.3. Online Datasets During Robot Learning (Interaction Scenario)

In the online application (i.e., online EEG-based RL learning), the subjects performed gestures to communicate with the robot. To this end, we used the *interaction* scenario. The subjects were instructed to freely perform one of three gestures (left, right, forward, see **Table 1B**) and add the fourth gesture (upward, see **Table 1B**), when they heard a short tone that was given to the subjects after 30 trials. Before the start of the online experiments in the interaction scenario, all subjects had a short practice set to train the correct use of Leap Motion.

The robot chooses an action as response of the current human intention (human gesture) and receives an immediate reward in form of ErrP-classification output [ErrP/No ErrP]. The robot updates the policy based on human feedback (details, see section 2.2).

2.3.3.1. Learning condition

Two learning conditions were investigated in online learning: warm-start learning (pre-training) and cold-start learning (no pre-training). In warm-start learning, a few trials (# of trial $n < 4$) were pre-trained, i.e., a few gesture-action pairs were trained with the perfect human feedback (i.e., the perfect ErrP-classifications). That means, the perfect human feedback was given to the action choice of the robot that was preprogrammed. Hence, we expected less erroneous actions of the robot (i.e., less mapping errors) in the beginning of learning phase for warm-start learning compared to cold-start learning. Note that the three kinds of gestures (left, right, forward) were pre-trained, but not the fourth gesture (upward) that was added during learning process online. In cold-start learning, we did not pre-train any gesture-action pairs. For all subjects, we started with the warm-start learning condition before the cold-start learning conditions to prevent the frustration of subjects, which can be caused by a large number of erroneous actions of the robot in cold-start learning. We did not alternate both learning conditions within subjects.

2.3.3.2. Number of trials in both learning conditions

In warm-start learning, we used the same number of trials for all subjects (90 trials). In cold-start learning, we used the same number of trials for all subjects (90 trials) except for one subject (60 trials, 90 trials, 120 trials for each online dataset). In fact, we investigated a different number of trials to find the appropriate number of trials. We aimed to find when the learning curve is stabilized (no mapping errors). To this end, we started with 120 trials and reduced the number of trials (90 trials, 60 trials). We did this evaluation on the first subject. In total, three datasets with 120 trials were recorded from the first subject. We reduced gradually the time to give a short tone for adding a new gesture. In the first dataset, the short tone was given to the subject after 60 trials (**Figure 7**). In the second dataset, the short tone was given to the subject after 50 trials (**Figure 5**). In the third dataset, the short tone was given to the subject after 40 trials. Finally, we decided to give a short tone for adding a new gesture after 30 trials. Based on this analysis, 60 trials were already enough for convergence in this subject. However, we are aware of subject variability in ErrP-classification performance and that for some subjects more trials might be needed. Moreover, we also did not intend to record on different days due to changes of electrode positions. Actually, the duration of the dataset with 120 trials was 32 min. This would have been too long for one session in total. Hence, we determined 90 trials for online dataset in both learning conditions. That means, there was no difference in the number of trials between warm-start learning and cold-start learning. Note that the first two datasets with 120 trials were excluded for statistical analysis (inference statistics). However, we included them for descriptive analysis and visualization for three reasons: (a) descriptive visualization of the learning curve in different number of trials (90 trials vs. 120 trials; **Figures 5A,B** vs. **Figures 5C,D**), (b) descriptive visualization of gesture errors (i.e., incoherence between human's perspective and robot's perspective, see **Figure 7**, **Table 5**), and (c) descriptive visualization of a few number of gesture errors (**Figure 5**, **Table 6**) and a large number of gesture errors (**Figure 7**, **Table 5**).

2.3.3.3. Number of online datasets in both learning conditions

In warm-start learning, we recorded three online datasets for four subjects and two online datasets for four subjects. In total, we recorded 20 datasets in warm-start learning. In cold-start learning, two online datasets were recorded for five subjects and three online sets were recorded for two subjects. For one subject, we recorded only one online dataset. This participant was very tired after recording the online dataset. Thus, we did not record further online datasets, since this participant could not concentrate on the task. In total, we recorded 17 datasets in cold-start learning. It is worth noting that the number of online datasets has no impact on the learning performance of the robot or ErrP-classification performance, since the learning process is completed within an online dataset (online experiment) and thus the learning of online datasets is independent of each other. It is thus enough to record only one online dataset (online experiment) per subject. However, we recorded more than one online dataset to obtain more data for this evaluation, in case that a participant allowed us to record more than one online dataset. The number of online datasets for each subject and each learning condition was reported in **Supplementary Table 1**. As shown in **Supplementary Table 1**, there was no high difference between learning conditions within subjects. Note that the different

number of datasets between learning conditions were taken into consideration in inference statistics.

2.3.4. EEG Recording, Gesture Recording, and Robot Arm

For both scenarios (interaction/observation), EEG were continuously recorded using the with 64-channel actiCap system (Brain Products GmbH, Munich, Germany), sampled at 5 kHz, amplified by two 32 channel Brain Amp DC amplifiers (Brain Products GmbH, Munich, Germany), and filtered with a low cut-off of 0.1 Hz and high cut-off of 1 kHz. Impedance was kept below 5 kΩ. The EEG channels were placed according to an extended standard 10–20 system.

For recording of human gesture, we used the Leap Motion system (Leap Motion Inc., San Francisco, USA). The Leap Motions uses a stereo image generated by using two monochromatic infrared cameras. The positions of hand and finger bones can be detected in x, y, and z coordinates relative to the sensor. We used the x, y, z components of the palm normal vector and a value from 0 to 1, which describes how far the hand is opened or closed. (flat hand [0], fist [1]). We recorded ten samples with the length of 100 ms per gesture and averaged them. Gesture feature vectors were used as inputs (human intention) for the LinUCB algorithm. Four types of gestures were used in the experiments: left, right, forward, and upward (see **Table 1A**). Gesture features recorded by LeapMotion were logged online (**Figure 1**-r1, details, see section 2.2). Additionally, we filmed online experiments to record gestures performed by human. In this way we received both gestures performed by humans (*gestures*) and gestures perceived by the robot (*gestures*).

The LinUCB algorithm selects actions, which were sent to a six degree of freedom (6-DOF) robotic arm called COMPI (Bargsten and Ferandez, 2015), which was developed at our institute (RIC, DFKI, Germany). We implemented six predefined actions (left, right, forward, upward, and back to start) in joint space, which were triggered from the LinUCB algorithm.

2.4. Data Analysis

For analysis of EEG data, we used a Python-based framework for preprocessing and classification (Krell et al., 2013). The EEG signal was segmented into epochs from −0.1 to 1 s after the start of the robot's action for each action type (correct/wrong trial). All epochs were normalized to zero mean for each channel, decimated to 50 Hz, and band pass filtered (0.5–10 Hz). We used the xDAWN spatial filter (Rivet et al., 2009) for feature extraction and 8 pseudo channels were obtained after spatial filtering. Two windows were used for the same robot's action and thus features were extracted from two windows (8 pseudo channels): [−0.1–0.6 s, 0–0.7 s] and normalized over all trials. A total of 280 features (8 pseudo channels × 35 data points = 280 for each sliding window) were used to train a classifier. A linear support vector machine (SVM) (Chang and Lin, 2011) was used for classification.

In this study, we performed two main analyses: (a) learning performance of the robot (mapping errors) and (b) ErrP-classification performance (rewards for learning algorithm). For evaluation of learning performance of the robot, we evaluate the correctness of gesture-action pairs by comparing between human gestures and robot's actions. For evaluation of ErrP-classification performance, we generated a confusion matrix based on the outputs of ErrP decoder (predicted label) with the correctness of gesture-action pairs (actual label).

For example, when gestures performed by human and actions of the robot are identical (e.g., gesture: *left*; action: *left*), robot's actions are correct, i.e., gesture-action pairs (*left-left* pairs) are correct. When ErrPs are detected on *correct* gesture-action pairs (e.g., *left-left* pairs), predictions of the ErrP decoder are wrong (FP). Otherwise, predictions of the ErrP decoder are correct (TP). In contrast, if ErrPs are not detected on *wrong* gesture-action pairs (e.g., *left-right* pairs), ErrP classifications are wrong (FN). Otherwise, predictions of the ErrP decoder are correct (TN). Note that the positive class stands for a wrong action of the robot.

Hence, evaluations of robot's performance and ErrP-classification performance are straightforward, when gestures performed by human and gestures recorded by LeapMotion are identical (i.e., there occur no gesture errors). In this case, the logs of learning process (**Figure 1**-dotted lines) are enough for evaluation of robot's learning performance and ErrP-classification performance. For example, we can evaluate the correctness of robot's actions by comparing gesture features (**Figure 1**-r1) with executed actions (**Figure 1**-r2). We can also evaluate ErrP-classification performance by comparing the output of ErrP decoder (**Figure 1**-r3) with gesture (**Figure 1**-r1)-action (**Figure 1**-r2) pair.

However, there were incoherences between gestures perceived by the robot (recorded gestures) and gestures performed by human, which result in two different perspectives (**Table 1B** and **Figure 2B**). Such incoherences between human perception and robot perception can affect the robot's learning performance, since ErrPs are elicited by (*performed*) gesture-action pairs, whereas the learning algorithm updates the current strategy based on (*perceived*) gesture-action pairs (details, see section 1.2). For this reason, data was analyzed in both perspectives (human/robot). For human's perspective, the correctness of robot's actions was calculated by comparing *filmed gestures* with robot's actions, where we filmed human's action while performing gestures. For robot's perspective, the correctness of robot's actions was calculated by comparing *reconstructed gestures* with robot's actions, where we reconstructed gestures based on gesture features recorded by Leap Motion. Therefore the ErrP classification performance was also different between the human and the robot perspective, because the correctness of the robot actions (actual marking) was different between both perspectives (**Table 1B**).

Finally, four steps of data analysis were performed. First, we evaluated learning performance of the robot (mapping errors) and learning progress of the robot in the whole learning phase. Further, we evaluated the changes of learning progress after changing the current human intention. To this end, we divided the whole learning phase in three learning phases according to the time point of when a new gesture (changes of human intents) was added. In this way, we determined three learning phases: (a)

beginning phase (start-1/3), (b) phase after adding a new gesture (1/3-2/3), and (c) final phase (2/3-end). Second, we evaluated ErrP-classification performance in the whole learning progress. Third we analyzed the effect of ErrP-classification performance on learning performance by comparing the pattern of learning progress in mapping errors and the pattern of learning progress in ErrP-classification performance. Fourth, we computed gesture errors by calculating incongruence between robot's perception and humans' perception to analyze the effect of gesture errors on learning performance of the robot. Finally, we analyzed the interaction effect of gesture errors and ErrP misclassifications on learning performance of the robot. All analyses were performed under both learning conditions (warm-start learning and cold-start learning) as well as under both perspectives (human's perspective and robot's perspective).

2.5. Statistical Analysis

We investigated the effect of interaction errors (ErrP misclassification, gesture errors) on robot's learning performance (mapping errors) in both learning conditions (cold-start learning, warm-start learning), both perspectives (human's perspective, robot's perspective), and three learning phases (beginning phase, phase after adding a new gesture, final phase). To this end, three factors were designed in statistics: learning condition (two levels: cold-start learning, warm-start learning), perspective (two levels: human's perspective, robot's perspective), and learning phase (three levels: beginning phase, phase after adding a new gesture, final phase).

For statistical analysis, we performed six investigations to find out (a) effects of learning condition, learning phase, and perspective on learning performance of the robot (mapping errors), (b) effects of learning condition, learning phase, and perspective on ErrP misclassifications (FN ∪ FP), (c) effects of learning condition, learning phase, and perspective on TP, (d) effects of learning condition, learning phase, and perspective on FN, (e) effects of learning condition, learning phase, and perspective on TN, and (f) effects of learning condition, learning phase, and perspective on FP (see **Figures 4B**, **6B,D,F,H**; for a descriptive analysis of both robot's learning performance and ErrP-classification performance, see **Table 3**).

To this end, a three-way repeated measures ANOVA was performed with learning condition (2 levels: warm-start learning, cold-start learning) as between-subjects factor and perspective (2 levels: human's perspective, robot's perspective) and learning phase (3 levels: beginning phase, phase after adding a new gesture, final phase) as within-subjects factors. Note that the sample size was unequal for learning condition, since one subject performed only one online experiment (online dataset) in the cold-start learning condition. For this reason, the independent variable *learning condition* was considered as between-subjects factor in the three-way repeated measures ANOVA. Dependent variables were robot's learning performance (mapping errors), ErrP-classification performance, e.g., misclassifications (FN ∪ FP), FN, FP, TN, and FP. For each dependent variable, we separately performed the three-way repeated measures ANOVA. Greenhouse Geisser correction was applied if necessary. Three *post-hoc* analyses were performed, i.e., pairwise comparisons were performed at each factor to compare (1) both learning conditions for each perspective (human's perspective vs. robot's perspective), (2) both perspectives for each learning condition (warm-start learning vs. cold-start learning), and (3) three learning phases for each learning condition and each perspective (beginning phase vs. phase after adding a new gesture vs. final phase). Bonferroni correction was performed for pairwise comparisons.

Further, we compared both learning conditions and both perspectives for all trials to analyze effects of learning condition and perspective on mapping errors and ErrP-classification performance in the whole learning phase (see **Figures 4A**, **6A,C,E,G**, a descriptive visualization of the whole learning phase as an example, see **Figure 5**). To this end, the results were pooled from three learning phases for each learning condition and each perspective. This is equivalent to a two-way repeated measures ANOVA with learning condition (2 levels: warm-start learning, cold-start learning) as between-subjects factor and perspective (2 levels: human's perspective, robot's perspective) as within-subjects factor. Two *post-hoc* analyses were performed, i.e., pairwise comparisons were performed at each factor to compare (1) both learning conditions for each perspective (human's perspective vs. robot's perspective) and (2) both perspectives for each learning condition (warm-start learning vs. cold-start learning). Bonferroni correction was performed for pairwise comparisons.

Finally, we performed three investigations to find out (a) relationship between robot's learning performance

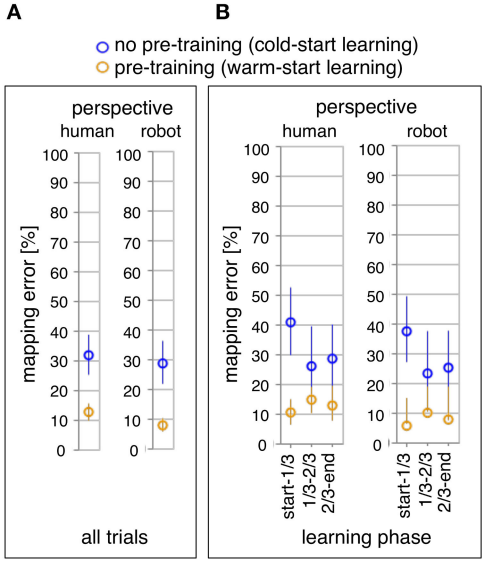

FIGURE 4 | Online learning performance of the robot: the average of mapping errors across all datasets for the whole learning phase **(A)** and the three learning phases **(B)**. Mapping errors are presented for both perspectives: the human and the robot perspective. For each perspective, both learning conditions are compared: pre-training (yellow) vs. no pre-training (blue).

TABLE 3 | The mean ErrP-classification performance across all subjects and the standard error of the mean for both learning conditions and both perspectives.

	Human's perspective		Robot's perspective	
	Cold-start learning	**Warm-start learning**	**Cold-start learning**	**Warm-start learning**
Mapping error	31.75 ± 5.79	12.61 ± 1.85	28.26 ± 6.11	7.84 ± 1.35
Gesture error	5.70 ± 1.65	5.88 ± 1.24	5.70 ± 1.65	5.88 ± 1.24
ErrP misclassifications	23.12 ± 4.56	12.81 ± 1.66	23.89 ± 4.54	13.13 ± 1.80
FN	15.33 ± 4.72	3.96 ± 0.73	14.14 ± 4.85	1.73 ± 0.41
FP	7.79 ± 1.82	8.85 ± 1.36	9.74 ± 2.06	11.40 ± 1.60
TP	16.42 ± 2.26	8.66 ± 1.43	14.46 ± 2.22	6.11 ± 1.10
TN	60.45 ± 5.76	78.53 ± 2.75	61.65 ± 5.92	80.76 ± 2.63
FNR (1-TPR)	37.26 ± 5.34	28.80 ± 4.42	34.90 ± 5.71	19.20 ± 3.93
FPR (1-TNR)	13.57 ± 3.28	10.52 ± 1.67	15.45 ± 3.23	12.72 ± 1.88

FNR = FN/(FN+TP), FPR = FP/(FP+TN), ErrP misclassification = FN ∪ FP.

(mapping errors) and ErrP-classification performance (see **Table 4A**; a descriptive visualization, see **Figure 8A** and **Supplementary Figure 1**), (b) relationship between robot's learning performance (mapping errors) and gesture errors (see **Table 4B**; a descriptive visualization, see **Figure 8B**), and (c) relationship between gesture errors and ErrP-classification performance (see **Table 4C**; a descriptive visualization, see **Figure 8C** and **Supplementary Figure 2**). To this end, we calculated correlation coefficients for each investigation (a,b,c). Concerning ErrP-classification performance, we performed a correlation analysis separately for ErrP misclassifications (FN ∪ FP), TP, TN, FP, and FN (see **Tables 4A,C**). All correlation analyses were performed separately for each learning condition (warm-start learning, cold-start learning) and each perspective (human's perspective, robot's perspective). Correlation coefficients and significances were reported for each correlation analysis (see **Table 4**).

3. RESULTS

Table 3 shows the overall results of descriptive analysis: the number of mapping errors (robot's learning performance), gesture errors, and ErrP misclassifications including false positive (FP) and false negative (FN) for both perspectives and both learning conditions. In addition, false positive rate (FPR) and false negative rate (FNR) were reported for both perspectives and both learning conditions. As mentioned earlier, the number of trials varied between subjects in online test sets. Thus, we calculated the number of mapping errors, gesture errors, and ErrP misclassifications in % (details, see section 2.3).

3.1. Learning Performance of the Robot

In our HRI scenario, the robot learns the mapping between human gestures and robot's actions, i.e., correct gesture-action pairs. Hence, the number of errors in the mapping between human gestures and robot's actions (i.e., mapping errors) was used as performance measure. **Table 3** shows the number of mapping errors for both learning conditions and both perspectives.

Figure 4A shows the comparison of the total number of mapping errors (i.e., in the whole learning phase) between both learning conditions for each perspective. The number of mapping errors was significantly decreased in the warm-start learning condition (pre-training) compared to the cold-start learning condition (no pre-training) in both perspectives [$F_{1,35} = 12.29, p < 0.002$, *human perspective:* $p < 0.003$, *robot perspective:* $p < 0.002$]. For both learning conditions, the number of mapping errors was reduced in robot's perspective compared to human's perspective for both learning conditions [$F_{1,35} = 25.98, p < 0.001$, *cold-start learning:* $p < 0.011$, *warm-start learning:* $p < 0.001$].

Figure 4B shows the comparison of three different learning phases in both learning conditions. We divided the whole learning phase in three learning phases according to the time point of when a new gesture (changes of human intents) was added. Different patterns of the learning process were observed between both learning conditions. The number of mapping errors was not significantly varied between learning phases in warm-start learning, whereas a significant reduction of mapping errors was observed between learning phases in cold-start learning [$F_{2,70} = 3.63, p < 0.033$]. This pattern was shown for both perspectives. In warm-start learning, the number of mapping errors was slightly (but not significantly) increased in the second learning phase (after adding a new gesture) and slightly (but not significantly) reduced in the third learning phase. [*human's perspective: start-1/3 vs. 1/3-2/3:* $p = 0.51$, *1/3-2/3 vs. 2/3-end:* $p = 1.0$, *start-1/3 vs. 2/3-end:* $p = 1.0$; *robot's perspective: start-1/3 vs. 1/3-2/3:* $p = 0.41$, *1/3-2/3 vs. 2/3-end:* $p = 1.0$, *start-1/3 vs. 2/3-end:* $p = 1.0$]. In cold-start learning, the number of mapping errors was significantly reduced in the second learning phase (after adding a new gesture) and slightly (but not significantly) increased in the third learning phase [*human's perspective: start-1/3 vs. 1/3-2/3:* $p < 0.001$, *1/3-2/3 vs. 2/3-end:* $p = 1.0$, *start-1/3 vs. 2/3-end:* $p < 0.01$; *robot's perspective: start-1/3 vs. 1/3-2/3:* $p < 0.001$, *1/3-2/3 vs. 2/3-end:* $p = 1.0$, *start-1/3 vs. 2/3-end:p* < 0.006]. Further, the

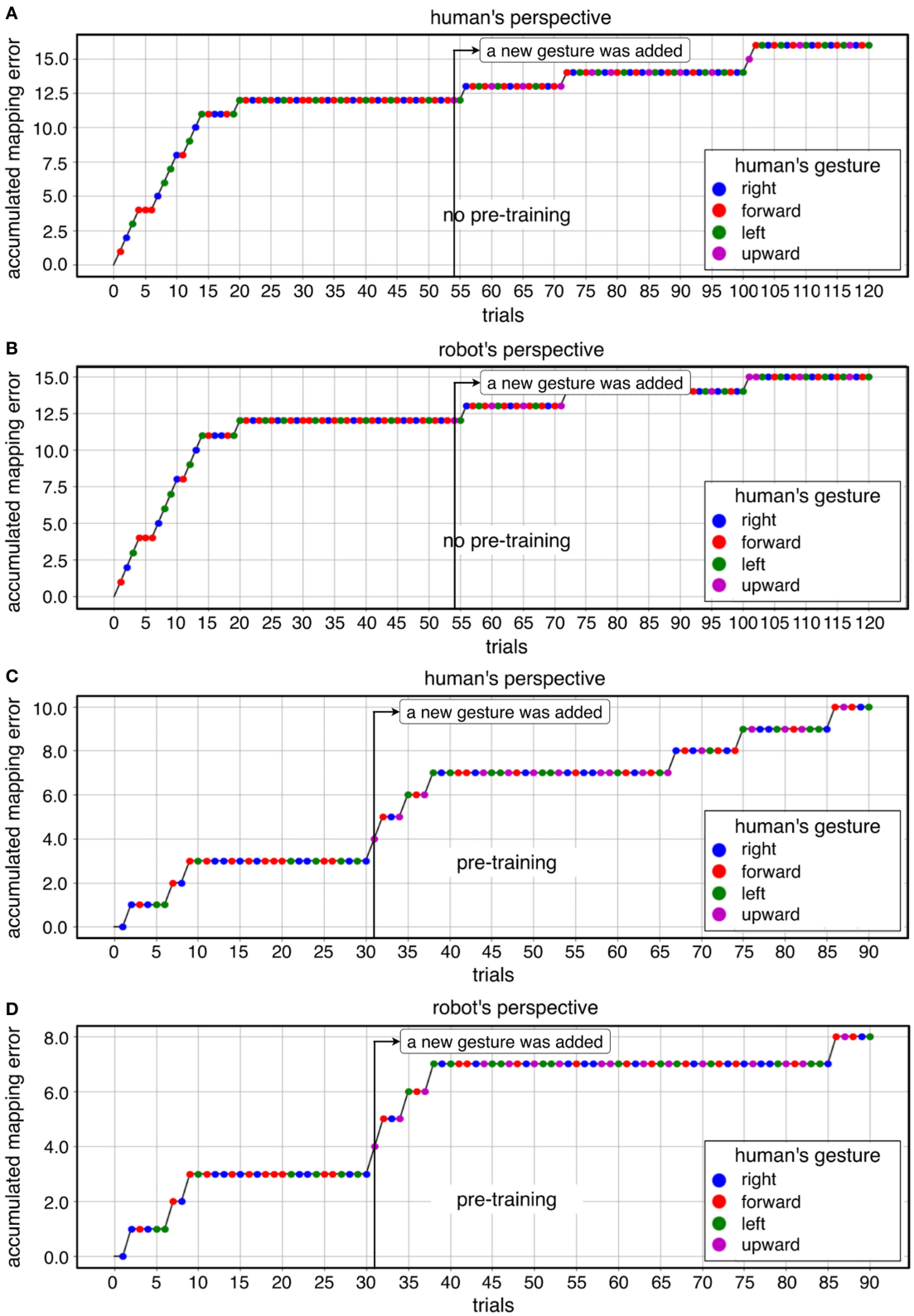

FIGURE 5 | A descriptive visualization of learning progress for both learning conditions in both perspective: **(A)** cold-start learning (no pre-training) for human's perspective, **(B)** cold-start learning (no pre-training) for robot's perspective, **(C)** warm-start learning (pre-training) for human's perspective, **(D)** warm-start learning (pre-training) for robot's perspective.

TABLE 4 | Correlation analysis.

	Human's perspective		Robot's perspective	
	Cold-start learning	**Warm-start learning**	**Cold-start learning**	**Warm-start learning**
(A) Correlation between robot's learning performance and ErrP-classification performance				
ErrP misclassification	0.892**	0.684**	0.888**	0.680**
FN	0.927**	0.715**	0.944**	0.705**
FP	−0.172	0.453*	−0.262	0.584**
TN	−0.950**	−0.897**	−0.942**	−0.869**
TP	0.622**	0.934**	0.693**	0.965**
FNR (1-TPR)	0.707**	0.209	0.745**	0.228
FPR (1-TNR)	0.486*	0.577**	0.395	0.660**
(B) Correlation between robot's learning performance and gesture errors				
Gesture errors	−0.089	0.803**	−0.274	0.503*
(C) Correlation between ErrP-classification performance and gesture errors				
ErrP misclassification	−0.221	0.488*	−0.090	0.573**
FN	−0.190	0.604**	−0.248	0.356
FP	−0.036	0.272*	0.385	0.533*
TN	0.101	−0.676**	0.150	−0.595**
TP	0.169	0.735**	0.214	0.485*
FNR (1-TPR)	0.075	0.208	0.001	0.037
FPR (1-TNR)	0.153	0.388	0.103	0.595**

*(A) Correlation between the robot's learning performance (mapping errors) and the ErrP-classification performance for both learning conditions and both perspectives. (B) Correlation between the robot's learning performance (mapping errors) and gesture errors for both learning conditions and both perspectives. (C) Correlation between the ErrP-classification performance and gesture errors for both learning conditions and both perspectives. Note that ** stands for significant level of $p < 0.01$ (2-sided) and * stands for significant level of $p < 0.05$ (2-sided). TPR = 1-FNR; TNR = 1-FPR. ErrP misclassification: FP ∪ FN.*

number of mapping errors was significantly reduced for warm-start learning compared to cold-start learning in the first learning phase for both perspectives [*warm-start learning vs. cold-start learning:* $p < 0.001$ *for both perspectives*]. However, there was no significant difference between both learning conditions in the second learning phase [*warm-start learning vs. cold-start learning:* $p = 0.079$ *for human's perspective;* $p = 0.051$ *for robot's perspective*]. In the final learning phase, the number of mapping errors was again reduced for warm-start learning compared to cold-start learning [*warm-start learning vs. cold-start learning:* $p < 0.022$ *for human's perspective;* $p < 0.010$ *for robot's perspective*].

Figure 5 shows a descriptive visualization of the learning progress of the whole learning phase as an example, which was separately visualized in both learning conditions and both perspectives. In the beginning of the learning phase, we observed a high increase of mapping errors in cold-start learning compared to warm-start learning. Accordingly, the learning curve in cold start learning slowly stabilized compared to warm start learning before a new gesture was added. This learning pattern was shown for both perspectives. However, once the learning curve had stabilized, adding a new gesture to cold start learning had less impact on learning than warm-start learning. In contrast, the number of mapping errors has been increased immediately after adding a new gesture for warm-start learning (**Figures 5C,D** after 30 trials). After the learning curve had stabilized, there was some variation in both learning conditions. In the late learning phase (2/3-end) fluctuations were observed, which were caused by FP especially during warm start learning. In warm-start learning, FP occurred more frequently in the late learning phase compared to cold-start learning. This was consistent with the correlation analysis, according to which FP showed a significant correlation with mapping errors for the learning condition *warm start*, but not for the learning condition *cold start* (**Table 4A**, details, see section 3.3). Note that the class ratio was different depending on datasets as shown in **Figures 5C,D**, since the number of correct and wrong actions depends on the online learning performance of the robot.

In summary, it can be observed that the total number of mapping errors of the robot during warm-start learning has been reduced compared to cold-start learning in both perspectives. After adding a new gesture, the number of mapping errors in warm-start learning was slightly increased, while the number of mapping errors in cold-start learning was reduced after adding a new gesture. In warm start learning, an earlier stabilization of the robot's learning progress was observed than in cold-start learning at the beginning of the learning phases. That means, the learning curve was stabilized quickly in warm-start learning compared to cold-start learning. In other words, the algorithm is converged in warm-start learning before adding a new gesture, whereas the convergence was not reached in cold-start learning before adding a new gesture. However, the difference in mapping errors between the two learning conditions disappeared in the second learning phase (after adding a new gesture), because a slight increase in mapping errors in warm start learning and a significant reduction in mapping errors in cold start learning

canceled out the effect of warm start learning on the robot's learning performance in the second learning phase. In fact, there were less fluctuations of learning progress for cold-start learning condition across all subjects after adding a new gesture compared to warm-start learning. Note that individual differences were more clearly observed for cold-start learning compared to warm-start learning (see **Figure 8**, details, see section 3.3).

3.2. ErrP-Classification Performance in the Whole Learning Phase

In our HRI scenario, the results of classifiers trained to recognize ErrPs were used as a reward in our learning algorithm. To measure the ErrP classification performance, a confusion matrix was calculated and the number of FN, FP, TP, and TN was used as performance metric.

Table 3 shows the number of FN, FP, TP, and TN. The number of FN was significantly reduced in warm-start learning compared to cold-start learning. However, the number of FP was slightly (but not statistically) increased for warm-start learning compared to cold-start learning. Hence, the number of FN was higher for FN than FP, whereas the number of FN was lower compared to FP in warm-start learning.

Figure 6 shows the comparison of ErrP-classification performance (FN, FP, TP, TN) between both learning conditions and both perspectives for all trials (**Figures 6A,C,E,G**). We found differences between both learning conditions in ErrP-detection performances. The number of ErrP misclassifications (FN ∪ FP) was reduced for warm-start learning compared to cold-start learning under both perspectives [$F_{1,35} = 5.36, p < 0.029$, *human perspective:* $p < 0.031$, *robot perspective:* $p < 0.027$]. Especially, the number of FN was substantially reduced in warm-start learning compared to cold-start learning under both perspectives [$F_{1,35} = 7.21, p < 0.012$, *human perspective:* $p < 0.015$, *robot perspective:* $p < 0.01$]. However, the number of FP was not significantly differed between both learning conditions. [$F_{1,35} = 0.034, p < 0.569$, *human perspective:* $p = 0.64$, *robot perspective:* $p = 0.53$]. The number of TN was increased for warm-start learning compared to cold-start learning [$F_{1,35} = 9.29, p < 0.005$, *human perspective:* $p < 0.006$, *robot perspective:* $p < 0.005$]. In contrast, the number of TP was increased for cold-start learning compared to warm-start learning [$F_{1,35} = 11.10, p < 0.003$, *human perspective:* $p < 0.006$, *robot perspective:* $p < 0.002$]. The FNR was reduced for warm-start learning compared to cold-start learning in robot's perspective, but not in human's perspective [$F_{1,35} = 3.81, p = 0.059$, *human perspective:* $p = 0.227$, *robot perspective:* $p < 0.027$]. The FPR was not significantly reduced for warm-start learning compared to cold-start learning under both perspectives [$F_{(1,35)} = 0.67, p = 0.420$, *human perspective:* $p = 0.391$, *robot perspective:* $p = 0.461$].

We also found differences between both perspectives in ErrP-detection performances. Under both learning conditions, the number of aberrations in the robot perspective was reduced compared to the human perspective. [$F_{1,35} = 25.98, p < 0.001$, *cold-start learning:* $p < 0.010$, *warm-start learning:* $p < 0.001$]. The number of FN was reduced under the robot perspective compared to the human perspective for warm start learning, but not for cold start learning [$F_{1,35} = 16.89, p < 0.002$, *cold-start learning:* $p = 0.06$, *warm-start learning:* $p < 0.001$]. In contrast, the number of FP was increased under the robot perspective compared to the human perspective under both learning conditions [$F_{1,35} = 16.30, p < 0.001$ *cold-start learning:* $p < 0.023$, *warm-start learning:* $p < 0.003$]. Altogether, the number of ErrP misclassifications (FN ∪ FP) was not differed between both perspectives [$F_{1,35} = 0.82, p = 0.372$, *cold-start learning:* $p = 0.39$, *warm-start learning:* $p = 0.69$]. The number of TNs was increased from the robot perspective compared to the human perspective for warm start learning, but not for cold start learning [$F_{1,35} = 16.92, p < 0.001$, *cold-start learning:* $p = 0.058$, *warm-start learning:* $p < 0.001$]. However, the number of TP from the robot perspective was reduced compared to the human perspective for both learning conditions [$F_{1,35} = 16.30, p < 0.001$, *cold-start learning:* $p < 0.02$, *warm-start learning:* $p < 0.002$]. FNR was reduced from the robot perspective compared to the human perspective in warm start learning, but not in cold start learning [$F_{1,35} = 4.34, p < 0.046$, *cold-start learning:* $p = 0.058$, *warm-start learning:* $p < 0.02$]. The FPR was increased from the robot perspective compared to the human perspective for both learning conditions [$F_{1,35} = 12.90, p < 0.002$, *cold-start learning:* $p < 0.032$, *warm-start learning:* $p < 0.008$]. Note that we have not found any interaction between the three factors (learning condition, learning phase, perspective). Hence, the results of pairwise comparisons between levels of factors could be well-interpreted.

In summary, it can be said that the ErrP classification performance was influenced by the learning conditions. Especially wrong classifications of incorrect robot actions (FN) and correct classifications of correct robot actions (TN) were strongly influenced by the learning conditions. Correct classifications of erroneous actions (TP) were also influenced by the learning condition, but this effect was not higher than TN or FN.

3.3. Effect of ErrP-Classification Performance on Learning Performance

Figure 6 shows ErrP-classification performance (FN, FP, TP, TN) in the three learning phases (**Figures 6B,D,F,H**). As expected, we found that the pattern of TP and FN (i.e., correct or incorrect classifications of *erroneous actions* of the robot) was coherent with the pattern of *erroneous actions* of the robot (i.e., mapping errors) (**Figure 4B** vs. **Figure 6F**; **Figure 4B** vs. **Figure 6B**). However, the pattern of TN (i.e., correct classifications of *correct actions* of the robot) was reversed compared to the pattern of mapping errors (**Figure 4B** vs. **Figure 6H**).

3.3.1. Correct Classifications of Erroneous Actions of the Robot (TP)

Figure 6F shows the number of TP for the three learning phases and both learning conditions. As expected, the pattern of correct classifications of *erroneous actions* of the robot matched with the pattern of *erroneous actions* of the robot (mapping errors). In warm-start learning, the number of TP was slightly (but not significant) increased in the second learning phase and slightly

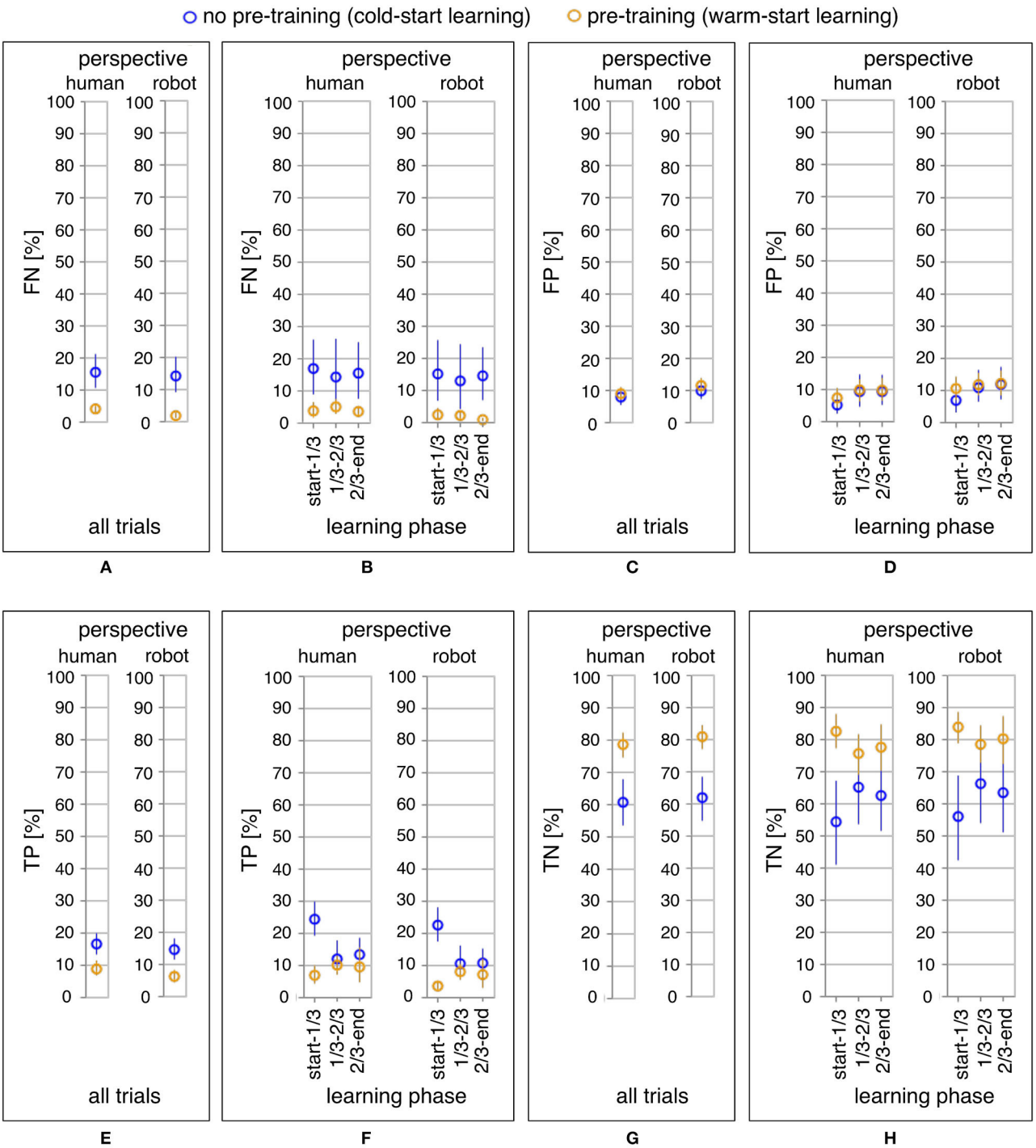

FIGURE 6 | ErrP-classification performance (FN, FP, TP, TN): the average of FN across all datasets, the average of FP across all datasets, the average of TP across all datasets, the average of TN across all datasets for the whole learning phase **(A,C,E,G)** and the three learning phases **(B,D,F,H)** in both perspectives. For each perspective, both learning conditions are compared: pre-training (yellow) vs. no pre-training (blue).

(but not significant) reduced in the third learning phase [*human's perspective: start-1/3 vs. 1/3-2/3:* $p = 0.532$, *1/3-2/3 vs. 2/3-end:* $p = 1.0$, *start-1/3 vs. 2/3-end:* $p = 1.0$; *robot's perspective: start-1/3 vs. 1/3-2/3:* $p = 0.155$, *1/3-2/3 vs. 2/3-end:* $p = 0.556$, *start-1/3 vs. 2/3-end:* $p = 1.0$]. In cold-start learning, the number of TP was significantly reduced in the second learning phase and

slightly (but not significantly) increased in the third learning phase [*human's perspective: start-1/3 vs. 1/3-2/3:* $p < 0.001$, *1/3-2/3 vs. 2/3-end:* $p = 1.0$, *start-1/3 vs. 2/3-end:* $p < 0.004$; *robot's perspective: start-1/3 vs. 1/3-2/3:* $p < 0.001$, *1/3-2/3 vs. 2/3-end:* $p = 1.0$, *start-1/3 vs. 2/3-end:* $p < 0.006$]. The same pattern was observed in the learning performance of the robot, i.e., mapping errors (**Figure 4B** vs. **Figure 6F**). Furthermore, the number of TPs for warm start learning was reduced compared to cold start learning only for the beginning of the learning phase for both perspectives [*start-1/3: warm-start learning vs. cold-start learning:* $p < 0.001$ *in both perspectives*]. After adding a new gesture, there was no significant difference between both learning conditions [*1/3-2/3: warm-start learning vs. cold-start learning;* $p = 0.534$ *in human's perspective,* $p = 0.417$ *in robot's perspective; 2/3-end: warm-start learning vs. cold-start learning:* $p = 0.334$ *in human's perspective,* $p = 0.305$ *in robot's perspective*]. In cold-start learning, differences between the two perspectives only became evident for the final learning phase [*human's perspective vs. robot's perspective:* $p = 0.153$ *for start-1/3;* $p = 0.178$ *for 1/3-2/3;* $p < 0.012$ *for 2/3-end*]. In warm-start learning, differences between both perspectives were found in all learning phases [*human's perspective vs. robot's perspective:* $p < 0.007$ *for start-1/3;* $p < 0.010$ *for 1/3-2/3;* $p < 0.013$ *for 2/3-end*].

3.3.2. Correct Classifications of Correct Actions of the Robot (TN)

Figure 6H shows the number of TN for three learning phases and both learning conditions. As expected, we observed that the pattern of learning phases in TN was inverse to the pattern of learning phases in mapping errors (**Figure 4B** vs. **Figure 6H**). In warm-start learning, the number of TN was slightly (but not significant) reduced in the second learning phase and slightly (but not significant) increased in the third learning phase for both perspectives [*human's perspective: start-1/3 vs. 1/3-2/3:* $p = 0.102$, *1/3-2/3 vs. 2/3-end:* $p = 0.712$, *start-1/3 vs. 2/3-end:* $p = 1.0$; *robot's perspective: start-1/3 vs. 1/3-2/3:* $p = 1.0$, *1/3-2/3 vs. 2/3-end:* $p = 0.251$, *start-1/3 vs. 2/3-end:* $p = 1.0$]. In contrast, in cold-start learning, the number of TN was significantly increased in the second learning phase and slightly (but not significantly) reduced in the third learning phase for both perspectives [*human's perspective: start-1/3 vs. 1/3-2/3:* $p < 0.001$, *1/3-2/3 vs. 2/3-end:* $p = 1.0$, *start-1/3 vs. 2/3-end:* $p < 0.001$; *robot's perspective: start-1/3 vs. 1/3-2/3:* $p < 0.012$, *1/3-2/3 vs. 2/3-end:* $p = 1.0$, *start-1/3 vs. 2/3-end:p* $= 0.321$]. In particular, the number of TN for warm start learning was increased compared to cold start learning. This was only shown for the initial phase and the end of the learning phase from both perspectives [*start-1/3:* $p < 0.001$ *in both perspectives; 1/3-2/3:* $p = 0.116$ *in human's perspective,* $p = 0.072$ *in robot's perspective; 2/3-end:* $p < 0.039$ *in human's perspective,* $p < 0.022$ *in robot's perspective*]. Further, we found differences between both perspectives in the second and final learning phase for warm-start learning and only in the beginning of learning phase in cold-start learning [*warm-start learning:* $p = 0.055$ *for start-1/3;* $p < 0.002$ *for 1/3-2/3;* $p < 0.007$ *for 2/3-end; cold-start learning:* $p < 0.033$ *for start-1/3;* $p = 0.190$ *for 1/3-2/3;* $p = 0.371$ *for 2/3-end*].

3.3.3. Incorrect Classifications of Correct Actions of the Robot (FP)

Figure 6D shows the number of FP for the three learning phases under both learning conditions. We observed no difference between learning phases and between learning conditions. We found no significant difference between three learning phases in both perspective [*(a) human's perspective: warm-start learning: start-1/3 vs. 1/3-2/3:* $p = 0.168$, *1/3-2/3 vs. 2/3-end:* $p = 0.216$, *start-1/3 vs. 2/3-end:* $p = 1.0$, *cold-start learning: start-1/3 vs. 1/3-2/3:* $p = 0.084$; *1/3-2/3 vs. 2/3-end:* $p = 0.313$; *start-1/3 vs. 2/3-end:* $p = 1.0$; *(b) robot's perspective: warm-start learning: start-1/3 vs. 1/3-2/3:* $p = 1.0$, *1/3-2/3 vs. 2/3-end:* $p = 1.0$, *start-1/3 vs. 2/3-end:* $p = 1.0$, *cold-start learning: start-1/3 vs. 1/3-2/3:* $p = 0.438$, *1/3-2/3 vs. 2/3-end:* $p = 0.917$, *start-1/3 vs. 2/3-end:* $p = 0.438$]. Further, we found no differences between both learning conditions for both perspectives [*human's perspective: warm-start learning vs. cold-start learning:* $p = 0.323$ *for start-1/3,* $p = 0.867$ *for 1/3-2/3,* $p = 0.891$ *for 2/3-end; robot's perspective: warm-start learning vs. cold-start learning:* $p = 0.323$ *for start-1/3,* $p = 0.867$ *for 1/3-2/3,* $p = 0.891$ *for 2/3-end*]. Further, we found significant differences between both perspectives for all learning phases in warm-start learning [*human's perspective vs. robot's perspective:* $p < 0.008$ *for start-1/3;* $p < 0.014$ *for 1/3-2/3:* $p < 0.011$ *for 2/3-end*]. In cold-start learning, differences between both perspectives were shown only for the final learning phase [*human's perspective vs. robot's perspective:* $p = 0.164$ *for start-1/3;* $p = 0.067$ *for 1/3-2/3:* $p < 0.015$ *for 2/3-end*].

3.3.4. Incorrect Classifications of Erroneous Actions of the Robot (FN)

Figure 6B shows the number of FN for the three learning phases under both learning conditions. Only in cold-start learning, the pattern of FN was coherent with the pattern of mapping errors. We found no significant difference between three learning phases for both perspectives [*(a) human's perspective: warm-start learning: start-1/3 vs. 1/3-2/3:* $p = 0.964$, *1/3-2/3 vs. 2/3-end,* $p = 1.0$; *start-1/3 vs. 2/3-end:* $p = 1.0$; *cold-start learning: start-1/3 vs. 1/3-2/3:* $p = 0.835$, *1/3-2/3 vs. 2/3-end:* $p = 1.0$, *start-1/3 vs. 2/3-end:* $p = 1.0$; *(b) robot's perspective: warm-start learning: start-1/3 vs. 1/3-2/3:* $p = 1.0$, *1/3-2/3 vs. 2/3-end:* $p = 1.0$, *start-1/3 vs. 2/3-end:* $p = 1.0$; *cold-start learning: start-1/3 vs. 1/3-2/3:* $p = 1.0$, *1/3-2/3 vs. 2/3-end:* $p = 1.0$, *start-1/3 vs. 2/3-end:* $p = 1.0$]. Further, the number of FN was reduced for warm-start learning compared to cold-start learning for the first and the final learning phase, but not for the second learning phase. This pattern was shown for both perspectives [*human's perspective: warm-start learning vs. cold-start learning:* $p < 0.011$ *for start-1/3,* $p = 0.051$ *for 1/3-2/3,* $p < 0.002$ *for 2/3-end; robot's perspective: warm-start learning vs. cold-start learning:* $p < 0.008$ *for start-1/3,* $p = 0.085$ *for 1/3-2/3,* $p = 0.009$ *for 2/3-end*]. Further, we found significant differences between both perspectives for the second and the final learning phase, but not for the first learning phase in warm-start learning [*human's perspective vs. robot's perspective:* $p = 0.060$ *for start-1/3,* $p < 0.002$ *for 1/3-2/3,* $p < 0.007$ *for 2/3-end*]. The reversed pattern was shown in cold-start learning [*human's perspective vs. robot's perspective:*

$p < 0.025$ *for start-1/3,* $p = 0.135$ *for 1/3-2/3,* $p = 0.371$ *for 2/3-end*].

3.3.5. Correlation Between ErrP-Classification Performance and Mapping Errors

Table 4A shows the correlation between learning performance of the robot (mapping errors) and ErrP-classification performance for each learning condition and each perspective, in which correlations of mapping errors were separately calculated with ErrP misclassifications (FP∪FN),TP, TN, FP, and FN (details for statistical analysis, see section 2.5). Note that ** stands for significant level of $p < 0.01$ (2-sided) and * stands for significant level of $p < 0.05$ (2-sided). **Figure 8A** shows a descriptive visualization of robot's learning performance and ErrP misclassification (more details, see **Supplementary Figure 1**, which shows a descriptive visualization of each correlation shown in **Table 4A**). An individual dot represents the result of mapping errors corresponding to ErrP misclassifications (FP ∪ FN), TP, TN, FP, and FN in each dataset, where different colors (yellow, blue) represent different learning conditions (warm-start learning, cold-start learning).

As expected, we observed a high correlation between learning performance of the robot and ErrP-classification performance under both learning conditions (see **Table 4A**). However, a higher correlation was observed for cold-start learning compared to warm-start learning. This pattern was more obviously shown in FN and TN. FN strongly correlated with learning performance in the cold-start learning condition compared to the warm-start learning condition [*cold-start learning vs. warm-start learning:* $r = 0.927$ *vs.* $r = 0.715$ *for human's perspective; cold-start learning vs. warm-start learning:* $r = 0.944$ *vs.* $r = 0.705$ *for robot's perspective*]. Note that we obtained a single correlation coefficient for each correlation analysis. Hence, the comparison between learning conditions was descriptively reported. The same pattern was shown for TN [*cold-start learning vs. warm-start learning:* $r = -0.950$ *vs.* $r = -0.897$ *for human's perspective; cold-start learning vs. warm-start learning:* $r = -0.942$ *vs.* $r = -0.869$ *for robot's perspective*]. In contrast, the reversed pattern was shown for TP, i.e., a higher correlation was observed for the warm-start learning compared to cold-start learning [*cold-start learning vs. warm-start learning:* $r = 0.622$ *vs.* $r = 0.934$ *for human's perspective; cold-start learning vs. warm-start learning:* $r = 0.693$ *vs.* $r = 0.965$ *for robot's perspective*]. For FP, there was no correlation for cold-start learning [*human's perspective:* $r = -0.172$, *robot's perspective:* $r = -0.262$].

Further, a descriptive analysis showed that a higher difference between datasets in robot's learning performance was observed in cold-start learning compared to warm-start learning. As shown in **Figure 8A**, all datasets of warms-start learning were placed in the dark green boxes, whereas 5 datasets of cold-start learning were placed in the light green boxes. The same pattern was shown in ErrP-detection performance (**Figure 8A**), which was a plausible reason for a high correlation between robot's learning performance and ErrP-detection performance (**Table 4A**). Note again that an individual dot represents the result of mapping errors corresponding to ErrP misclassifications (FP ∪ FN), TP, TN, FP, and FN in each dataset and different colors (yellow, blue) represent different learning conditions (warms-start learning and cold-start learning).

In summary, FN had a stronger impact on cold-start learning compared to warm-start learning, whereas FP had a stronger effect on warm-start learning compared to cold-start learning. In other words, the learning performance of the robot was impaired more during cold start learning than during warm start learning if incorrect robot actions were not detected, i.e., ErrPs were not detected if the actions of the robot were wrong. Further, FN had an effect on learning performance for both learning conditions, whereas FP had an impact on learning performance for warm-start learning, but not for cold-start learning. Consistent with a higher number of mapping errors, the number of TP was higher in cold-start learning than in warm-start learning.

3.4. Effect of Gesture Errors on Learning Performance

As mentioned earlier, we considered wrong recordings of human gestures as gesture errors, which lead to incoherences between performed and perceived gestures, i.e., incoherences between gestures performed by the subjects and gestures recorded by LeapMotion. The subjects perceived their own performed gesture and the robot perceived the gesture features recorded by LeapMotion. Therefore we analyzed the learning performance of robots and the ErrP classification performance depending on the two perspectives (robot perspective/ human perspective).

Figure 7 shows differences in learning progress between both perspectives that are caused by gesture errors. Gestures that were performed by the subjects are depicted in **Figure 7A**, whereas gestures that were recorded by the Leap Motion and perceived by the robot are depicted in **Figure 7B**. As shown in **Figure 7**, gestures were differently colored depending on perspective, e.g., *upward* (violet point) for human's perspective and *forward* (red point) for robot's perspective on the same action of the robot in the trial 69 (**Figure 7A** vs. **Figure 7B**, see **Table 5D**). When there were no gesture errors, wrong actions of the robot (mapping errors) were the same for both perspectives (see trial 1, 2, 4, 7, 9, 14 in **Figure 7**). When gesture errors occurred, the effect of gesture errors was not clear, which required a further analysis (details, see **Table 5**).

Table 5 shows four cases where we observed the interaction effects of gesture errors on learning performance (the correctness of robot actions, i.e., mapping errors) with ErrP recognition performance: (A) No occurrence of gesture errors and correct actions of the robot for both perspectives, (B) No occurrence of gesture errors and wrong actions of the robot for both perspectives, (C) Occurrence of gesture errors and correct robot actions from the robot's perspective, but incorrect robot actions from the human perspective, and (D) Occurrence of gesture errors and wrong actions of the robot from both perspectives. Note that the trials that are visualized

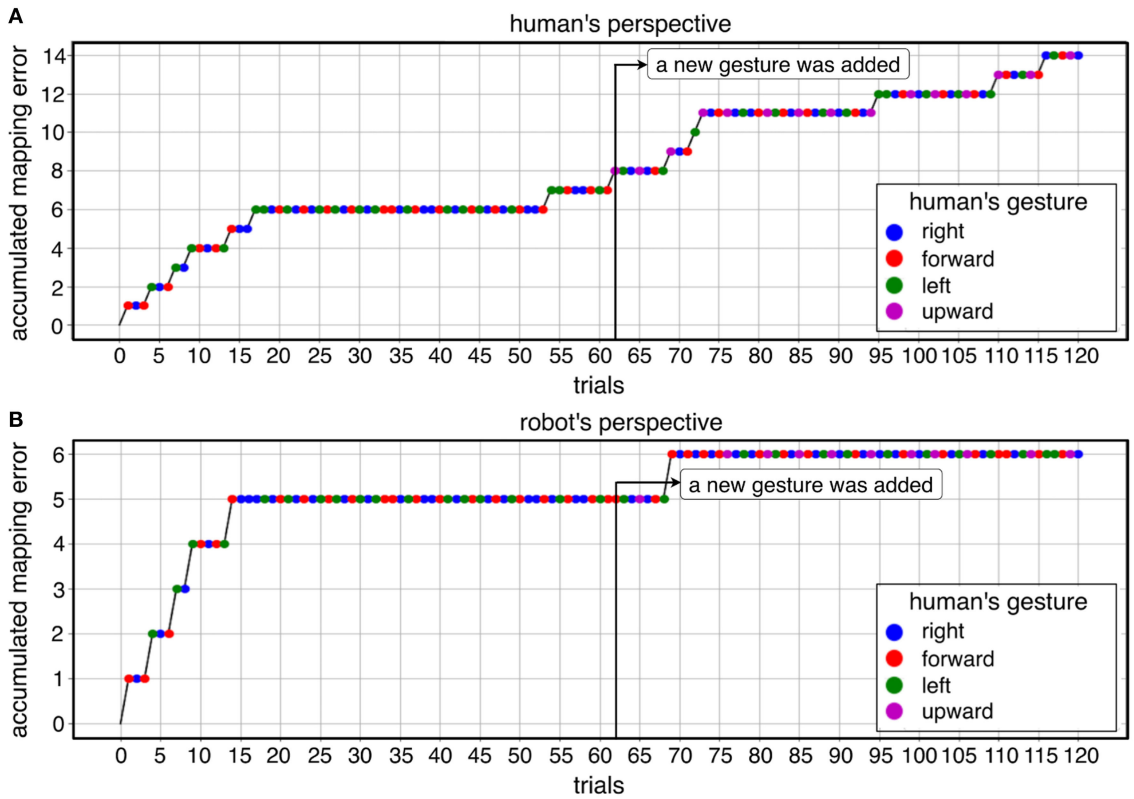

FIGURE 7 | A descriptive analysis of differences in learning progress between both perspectives (**A** and **B**) that are caused by gesture errors. A descriptive visualization of learning progress of both perspectives is shown in the cold-start learning condition (no pre-training) as an example of one subject. The first five mapping errors (trial 1, 2, 4, 7, 9, 14) and the mapping errors in the trial 69 are the same for both perspectives. Other mapping errors (trial 17, 54, 62, 72, 73, 95, 110, 116) are shown for the human's perspective, but not for robot's perspective. Such different perceptions between human and robot due to gesture errors and their impacts on learning progress are analyzed in consideration of interaction with ErrP-detection performance and summarized in **Table 5** (details, see text).

in **Figure 7** are equivalent to the trials that are shown in **Table 5**.

3.4.1. Correct Actions of the Robot Without Gesture Errors (Table 5A)

When there were no gesture errors and the robot's actions were also correct, ErrP-detection performance had a direct impact on the learning process (**Table 5A**). In other words, the learning performance was affected only by ErrP-classification performance. Correct classifications, i.e., detections of *ErrPs* on wrong gesture-action pairs (TP) and detections of *No ErrPs* on correct gesture-action pairs (TN) had a positive impact on the learning process.

3.4.2. Wrong Actions of the Robot Without Gesture Errors (Table 5B)

If the robot's actions were wrong even though there were no gesture errors, the learning performance was also only affected by the ErrP recognition performance (**Table 5B**). Correct classifications, i.e., detections of *ErrPs* on wrong gesture-action pairs (TP) and detections of *No ErrPs* on correct gesture-action pairs (TN) had a positive impact on the learning process. In contrast, wrong classifications, i.e., detections of *No ErrPs* on wrong gesture-action pairs (FN) and detections of *ErrPs* on correct gesture-action pairs (FP) had a negative effect on the learning process.

3.4.3. Correct Actions of the Robot With Gesture Errors (Table 5C)

If the robot's actions were correct, although gesture errors occurred, we observed two different effects: (1) Gesture errors had a negative effect on the learning performance, when ErrP detection was correct from the human's perspective (trial 54, 62, 73, 95, 110, 116 in **Table 5C**) and (2) Negative effects of gesture errors were canceled out, when ErrP detection were wrong from the human's perspective (trial 17, 72 in **Table 5C**). For example, when ErrPs were detected on wrong gesture-action pairs from the human's perspective (e.g., *left-right* pair in trial 54 in **Table 5C**), ErrP classifications were correct (TP). In contrast, when the robot perceived correct gesture-action pairs on the same actions of the robot (e.g., *right-right* pair in trial 54 in **Table 5C**), ErrP classifications were wrong from the robot's perspective (FP), which led to negative impacts on the learning progress. However, such negative effects of gesture errors on learning performance were canceled out, when ErrP detections were wrong from the human's perspective.

TABLE 5 | Different perceptions between humans and robots due to gesture errors (9 gesture errors in total in this example, see cases C and D).

Case	Trial	Human gesture	Recorded gesture	Robot's action	ErrP detection	Human CL	Robot CL
A	5	Right	Right	Right	No ErrP	TN	TN
	6	Forward	Forward	Forward	No ErrP	TN	TN
	8	Right	Right	Right	No ErrP	TN	TN
	9	Left	Left	Forward	ErrP	TP	TP
	10	Forward	Forward	Forward	No ErrP	TN	TN
	11	Right	Right	Right	No ErrP	TN	TN
	12	Forward	Forward	Forward	No ErrP	TN	TN
	13	Left	Left	Forward	ErrP	TP	TP
	15	Right	Right	Right	No ErrP	TN	TN
	16	Right	Right	Right	No ErrP	TN	TN
B	1	Forward	Forward	Right	ErrP	TP	TP
	2	Right	Right	Right	No ErrP	TN	TN
	3	Forward	Forward	Forward	No ErrP	TN	TN
	4	Left	Left	Forward	No ErrP	FN	FN
	7	Left	Left	Forward	No ErrP	FN	FN
	14	Forward	Forward	Left	ErrP	TP	TP
C	17	Left	Right	Right	No ErrP	FN	TN
	54	Left	Right	Right	ErrP	TP	FP
	62	Upward	Forward	Forward	ErrP	TP	FP
	72	Left	Right	Right	No ErrP	FN	TN
	73	Upward	Forward	Forward	ErrP	TP	FP
	95	Left	Right	Right	ErrP	TP	FP
	110	Upward	Forward	Forward	ErrP	TP	FP
	116	Right	Left	Left	ErrP	TP	FP
D	69	Upward	Forward	Right	ErrP	TP	TP

*The learning progress of this example is shown in **Figure 7**. Four cases of interaction between gesture errors and ErrP recognition performance and their effects on learning progress were observed: (A) No occurrence of gesture errors and correct actions of the robot from both perspectives, (B) No occurrence of gesture errors and wrong actions of the robot from both perspectives, (C) occurrence of gesture errors and correct actions of the robot from the robot's perspective, but not from the human's perspective, and (D) occurrence of gesture errors and wrong actions of the robot from both perspectives. CL: classification performance. robot CL: ErrP-detection performance from the robot's perspective. human CL: ErrP-detection performance from the human's perspective. Note that the robot's perception (robot CL) affects learning progress and the elicitation of ErrPs is based on the human's perception (matching between human gesture and robot's action). Note that not all trials are described in this example.*

TABLE 6 | Different perceptions between human and robot due to gesture errors (one gesture error in total in this example, see case D).

Case	Trial	Human gesture	Recorded gesture	Robot's action	ErrP detection	Human CL	Robot CL
A	5	Forward	Forward	Forward	No ErrP	TN	TN
	6	Forward	Forward	Forward	No ErrP	TN	TN
	9	Left	Left	Left	No ErrP	TN	TN
	11	Forward	Forward	Forward	No ErrP	TN	TN
	15	Forward	Forward	Forward	No ErrP	TN	TN
	16	Right	Right	Right	Right	TN	TN
	17	Right	Right	Right	Right	TN	TN
	18	Forward	Forward	Forward	Forward	TN	TN
	19	Left	Left	Left	Left	TN	TN
B	1	Forward	Forward	Left	ErrP	TP	TP
	2	Right	Right	Left	ErrP	TP	TP
	3	Left	Left	Right	No ErrP	FN	FN
	4	Forward	Forward	Right	ErrP	TP	TP
	7	Right	Right	Forward	ErrP	TP	TP
	8	Left	Left	Right	ErrP	TP	TP
	10	Right	Right	Left	ErrP	TP	TP
	12	Left	Left	Forward	ErrP	TP	TP
	13	Right	Right	Left	ErrP	TP	TP
	14	Left	Left	Forward	ErrP	TP	TP
	20	Left	Left	Forward	ErrP	TP	TP
	56	Right	Right	Upward	ErrP	TP	TP
	72	Forward	Forward	Left	ErrP	TP	TP
	102	Forward	Forward	Upward	ErrP	TP	TP
C	–	–	–	–	–	–	–
D	101	Upward	Forward	Right	ErrP	TP	TP

*Learning progress of this example is shown in **Figures 5A,B**. Four cases of the interaction between gesture errors and their impacts on learning progress were observed: (A) No occurrence of gesture errors and correct actions of the robot from both perspectives, (B) No occurrence of gesture errors and wrong actions of the robot from both perspectives, (C) occurrence of gesture errors and correct actions of the robot from the robot's perspective, but not from the human's perspective, and (D) occurrence of gesture errors and wrong actions of the robot from both perspectives. CL: classification performance. robot CL: ErrP-detection performance from the robot's perspective. human CL: ErrP-detection performance from the human's perspective. Note that the robot's perception (robot CL) affects learning progress and the elicitation of ErrPs is based on the human's perception (matching between human gesture and robot's action). Note that not all trials are described in this example.*

For example, ErrP classifications (detections of *No ErrP*) were wrong on gesture-action pairs (*left-right* pairs) from the human's perspective, whereas ErrP classifications (detections of *No ErrP*) were correct on gesture-action pairs (*right-right* pairs) from the robot's perspective (see trial 17, 72 in **Table 5C**). In this case, gesture errors had a positive effect on learning performance because the ErrPs recognition was incorrect from the human perspective.

3.4.4. Wrong Actions of the Robot With Gesture Errors (Table 5D)

When gesture errors occurred and the robot's actions were wrong, the learning performance was affected only by ErrP-detection performance. In this case, gesture-action pairs were wrong from both perspectives (see trial 69 in **Table 5D**): *upward-right* pair for human's perspective and *forward-right* pair for robot's perspective. Hence, ErrP classifications (detections of *ErrPs*) were correct (TP) and learning performance was not negatively affected.

In general, the number of gesture errors varied between subjects and sets. We visualized two examples for different numbers of gesture errors: 9 gesture errors (**Figures 7A,B**, and **Table 5**) vs. one gesture error (**Figures 5A,B**, and **Table 6**).

3.4.5. Correlation Between Gesture Errors and Mapping Errors and Correlation Between Gesture Errors and ErrP-Classification Performance

Table 4B shows the correlation between gesture errors and mapping errors for both learning conditions and both perspectives and its descriptive visualization is shown in

Figure 8B (more details, see **Supplementary Figure 2**). We found a correlation between gesture errors and the robot's learning performance for warm-start learning but not for cold-start learning [*cold-start learning vs. warm-start learning:* $r = 0.803$ *vs.* $r = -0.089$ *for human's perspective; cold-start learning vs. warm-start learning:* $r = 0.503$ *vs.* $r = -0.274$ *for robot's perspective*]. Furthermore, the reason why the correlation between gesture and mapping errors was only shown for warm start learning can be explained by further correlation analysis. **Table 4C** shows the correlation between ErrP-detection performance and gesture errors for both learning conditions and both perspectives and its descriptive visualization is shown in **Figure 8C** (more details, see **Supplementary Figure 2**). For both perspectives, we found a correlation between ErrP misclassifications and gesture errors for warm-start learning, but not for cold-start learning [*cold-start learning vs. warm-start learning:* $r = -0.221$ *vs.* $r = 0.488$ *for human's perspective; cold-start learning vs. warm-start learning:* $r = -0.090$ *vs.* $r = 0.573$ *for robot's perspective*]. Both correlation analyses (**Tables 4B,C**) showed that gesture errors had an impact on learning performance (mapping errors), only when gesture errors correlate with ErrP misclassifications (**Table 4B** vs. **Table 4C**, **Figure 8B** vs. **Figure 8C**).

In summary, it can be said that gesture errors affected the learning performance of the robot in other ways. Due to gesture errors, an incorrect feedback (human evaluation) was sent to the robot, although the human evaluation itself was correct. However, such negative effects of gesture errors on robot learning performance disappeared if the ErrP classification was incorrect. Furthermore, we could find out afterwards that gesture errors had no effect on the robot's learning performance if the robot action selection was wrong and the ErrP classification was correct.

3.5. Summary of Results

We showed that the robot learned actions that were best assigned to human gestures based on EEG-based reinforcement signals. In the proposed HRI scenario, human gestures were not predefined, i.e., no initial semantics of gestures was given to the robot. Rather, the robot learned the current meaning of human gesture (i.e., the meaning of human gesture that can be changed online). To this end, we used a contextual bandit approach that maximizes the expected payoff by updating the current human intention (human gesture) and the current human feedback (ErrP) after each action selection of the robot.

Robot learning and its online adaptation were successful for both warm-start learning and cold-start learning. Only for one subject robot learning was not successful in cold-start learning due to a very low detection performance of ErrPs used for human's intrinsic feedback (rewards). Further, cold-start learning required more data to reach a stabilization of the learning curve compared to warm-start learning *before* adding a new context (e.g., before adding a new gesture). However, cold-start learning was less affected by changes of the current context (e.g., *after* adding a new gesture) compared to warm-start learning, which indicates that cold-start learning was stable for updating of the learned strategy once learning reached convergence.

Online detection of ErrPs used for rewards in the used learning algorithm was successful for both learning conditions except for one subject who showed a very low performance of ErrP detections in cold-start learning. Our assumption that the ErrP-classification performance affects robot's learning performance was supported by a high correlation between robot's learning performance and ErrP-detection performance in both learning condition (**Table 4A**). Further, a descriptive analysis showed a higher variability between datasets in cold-start learning compared to warm-start learning, which can be shown in **Figure 8**. For example, five datasets of cold-start learning were placed in the light green boxes, whereas all datasets of warms-start learning were placed in the dark green boxes (**Figure 8**). However, correlation coefficients were computed for each learning condition and the comparison between both learning conditions (inference statistics) was not possible, since there was only one coefficient value for each learning condition.

Gesture errors that were not detected online but analyzed offline had no direct impact on robot's learning performance. Rather, gesture errors affected robot's learning performance only when gesture errors interacted with ErrP-detection performance. Especially, we observed a correlation between gesture errors and ErrP-detection performance in warm-start learning (**Table 4C**), which led to a correlation between robot's learning performance and gesture errors in warm-start learning (**Table 4B**). In contrast, we observed no correlation between gesture errors and ErrP-detection performance in cold-start learning (**Table 4C**), which resulted in *no* correlation between robot's learning performance and gesture errors in cold-start learning (**Table 4B**).

4. DISCUSSION

In this paper, we analyzed errors that occur in HRI and their impacts on online learning performance of the robot. Our results indicate that a little prior knowledge facilitates learning progress and allows a faster stabilization of the learning curve compared to learning without prior knowledge. Warm-start learning was advantaged, since a few trials (i.e., gesture-action pairs) were pre-trained with the perfect human feedback (correct detections of ErrP/No ErrP). Further, the reason for the faster learning can be explained by the higher ErrP classification performance, i.e., the significant reduction of ErrP misclassifications in warm-start learning compared to cold-start learning. Especially the role of the FN, i.e., the absence of robot mistakes (mapping error), seems to be very important for learning performance both for learning with prior knowledge and for learning without prior knowledge. In contrast, false alarm (FP) seems to have a small overall effect on the robot's learning performance with a greater effect on warm-start learning compared to cold-start learning. This is supported by correlations between FN and mapping errors in both learning conditions and correlations between FP and mapping errors shown for warm-start learning but not for cold-start learning (**Table 4A**, **Supplementary Figure 1**). The reason why FN had a higher influence on the learning performance of the robot compared to FP can be explained by the use of different weights of rewards depending on the

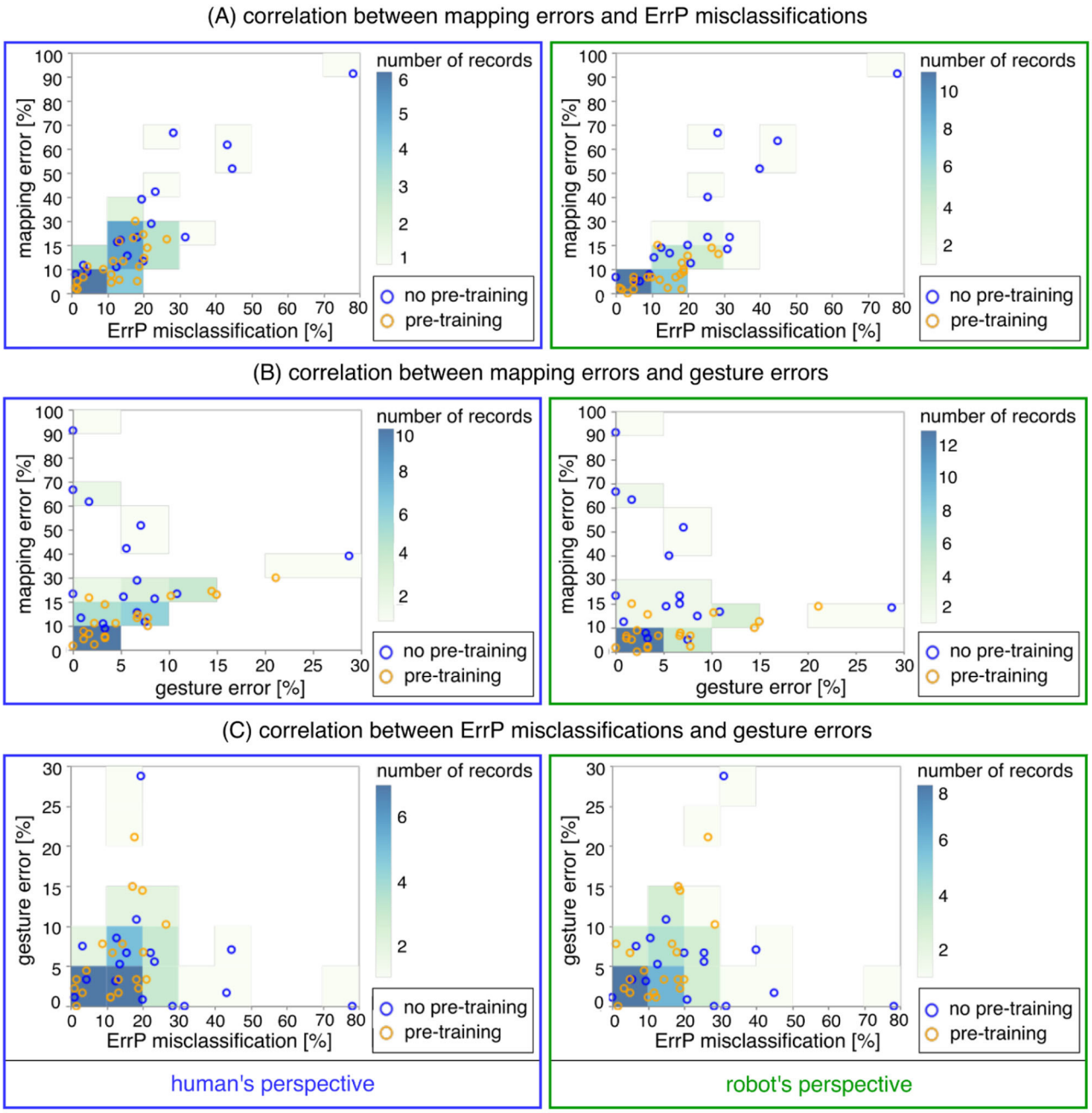

FIGURE 8 | A descriptive visualization of correlation analysis: **(A)** correlation between mapping errors and ErrP misclassifications, **(B)** correlation between mapping errors and gesture errors, and **(C)** correlation between ErrP misclassifications and gesture errors. A statistical analysis of three types of correlation **(A–C)** is reported in **Table 4**. For each perspective, the comparison between both learning conditions is depicted in different colors: pre-training (yellow) vs. no pre-training (blue). Each dot represents each dataset (details, see text). A descriptive visualization of further correlation analyses are depicted in **Supplementary Figures 1**, **2**.

results of ErrP classifications (**Table 2**): our HRI scenario was designed that the predictions of correct mappings (No ErrP) were highly rewarded compared to the predictions of wrong mappings (ErrP), since a *correct* gesture-action pair should be learned by the UCB algorithm. Further, our results suggest that not only ErrP misclassifications (FN, FP) but also correct classifications of ErrPs/No ErrPs (TP, TN) can have an impact on learning performance of the robot under both learning conditions. This is supported by the findings of negative correlations of TN with mapping errors and positive correlations of TP with mapping error (**Table 4A**, **Supplementary Figure 1**). Further, the faster stabilization of the learning curve in warm-start learning seems to cause the lower number of TPs (correct detections of erroneous actions of the robot) in warm-start learning compared to cold-start learning, although the number of TNs (correct detections of correct action of the robot) in

warm-start learning was higher compared to cold-start learning. Another possible reason why the ErrP classification performance was higher for warm-start learning compared to cold-start learning is that the subjects started always with warm-start learning before cold-start learning and thus the subjects could be more tired in cold-start learning compared to warm-start learning. The effect of tiredness on ErrP expression is relevant for continuous interaction and learning and will be investigated in future.

Our results indicate that learning without prior knowledge requires more trials to stabilize the learning curve compared to warm-start learning. This can be shown in the learning curve descriptively (e.g., **Figure 5**). However, cold-start learning was less affected by changes of the current context (e.g., *after* adding a new gesture) compared to warm-start learning, once learning reached convergence. This was shown by the result that the mean number of incorrect robot actions over all subjects was even statistically reduced during cold-start learning, although a new gesture was added to online learning (**Figure 4**). The reason why the number of erroneous actions of the robot was increased after adding a new gesture in warm-start learning in contrast to cold-start learning can be explained in the following way. For both learning conditions (warm-start learning/cold-start learning), the new gesture (*upwards*) was not chosen before and thus had a high variance, i.e., a high upper confidence interval (UCI), which leads to a high expected payoff, i.e., a high upper confidence bound (UCB) accordingly. In cold-start learning, the expected payoff of the previous learned gesture-action pairs (*left*, *right*, *forward*) could not be higher compared to the expected payoff of the new gesture (*upwards*) before adding the new gesture. Thus, for example, when the subject adds a new gesture, the probability that the new gesture is chosen could be high due to a high expected payoff caused by a high variance. That means, the transition to the learning of the new gesture could be very smoothy due to a high UCB caused by a high UCI. Thus, the algorithm could explore in a natural way. In contrast, the expected payoff of previous learned gesture-action pairs (*left*, *right*, *forward*) could be substantially higher compared to a new gesture-action pair (*upwards*) in warm-start learning. Hence, the algorithm could have no soft transition to the learning of the new gesture-action pair in warm-start learning. In fact, the expected payoff of three gesture-action pairs (*left*, *right*, *forward*) could be already high, since the UCB algorithm could reach very quickly convergence due to pre-training before adding the new gesture. For this reason, the transition to the learning of a new gesture-action pair could not be smoothly in warm-start learning, which could lead to the increased number of erroneous actions of the robot in warm-start learning immediately after adding a new gesture (**Figure 4**).

Our assumption that ErrP-classification performance used as rewards affects learning performance of the robot was confirmed by a high correlation between ErrP-classification performance and robot's learning performance in both learning conditions. However, gesture errors had an impact on robot' learning performance, only when gesture errors correlated with ErrP-classification performance. This indicates that gesture errors have an indirect effect on learning performance of the robot, whereas ErrP-classification performance has a direct impact on robot's learning performance.

Different effects of ErrP-classification performance on robot's learning performance between both learning conditions, e.g., the lower number of learning performance of the robot (mapping error) and the lower number of ErrP misclassifications in warm-start learning compared to cold-start learning cannot be explained by our investigation. One could possibly explain it by assuming the following: a subject might eventually have recognized a systematic repetition of wrong assignments of human gesture and robot's action, e.g., *left-right* pairs, the human can expect the upcoming action of the robot (e.g., *right* action) after performing a specific gesture type (*left* gesture) *before* observing the robot's action. We assume that such an expectation of the human would affect the online detection of ErrPs. We further assume that such situations would occur more often in cold-start learning compared to warm-start learning. The chosen algorithm is capable of correcting the wrongly learned gesture-action pairs (relearning). We assumed that more experiences (i.e., more data) are required for relearning (correction of wrong assignments) compared to learning in the initial state (blank state). However, this is a vague interpretation. Thus, the relearning pattern between both learning condition can be investigated in the future to analyze different effects of ErrP-classification performance on learning performance of the robot between both learning conditions.

Further, the descriptive analysis of learning progress in individual datasets (i.e., descriptive visualization of 74 datasets) shows that most subjects showed a stabilization of learning curve after 30 trials (i.e., after adding a new gesture). However, in cold-start learning some subjects seem to require considerably more trials to stabilize the learning curve. This indicates that the time point of adding a new context (gesture) was not optimal for some subjects in cold-start learning. Note that we did not depict all 74 visualizations of learning progress (learning curve) in this paper (just two datasets as examples). We analyzed learning progress by performing inferential statistical analysis, i.e., by statistically comparing mean differences over all subjects between three learning phases (**Figure 4**), since learning progress of individual datasets can be visualized only descriptively. Note that we visualized 74 learning curves from 74 datasets for each perspective (human's perspective/robot's perspective): 20 datasets $\times$ 2 perspectives $=$ 40 datasets; 17 datasets $\times$ 2 perspectives $=$ 34 datasets). On the other hand, an outlier can be easily interpreted without explicitly performing an inference statistics as shown in **Figure 8** (light green box in the top right side of the visualization). Note that **Figure 8** descriptively shows variability between individual datasets in ErrP-classification performance and learning performance of the robot (mapping errors). This outlier (one dataset of one subject) had an extremely low learning performance of the robot and also an extremely low ErrP-classification performance (especially a high number of FN). Actually it is reasonable to understand that the robot could hardly learn correct actions if the ErrP decoder constantly failed to recognize ErrPs. Future investigations should focus on the relationship (correlation) between ErrP-classification

performance and learning progress of the robot *per learning phase*, where the determination of learning phase is also a relevant issue for investigations of interaction errors on robot's learning progress.

In general, the number of attempts plays a critical role in reinforcement learning and the agent updates the policy based on rewards that are predefined before learning begins. In HRI, on the other hand, the rewards (human feedback) are generated during online learning and can therefore be influenced by interactions with the robot, i.e., the online learning performance of the robot (e.g., changes in online learning performance during interaction with humans). Therefore, not only the number of attempts but also interaction effects of online learning performance on the generation of human feedback can have an influence on the robot's learning performance (mapping error). Assuming that only the number of trials has an influence on the learning performance of the robot, our results suggest that for some subjects in cold start learning more than 90 trials might be necessary. In practice, it is not always possible to record more than 90 trials from subjects, and recording large numbers of trials is not realistic for some subjects and many applications. One limits oneself to recording a sufficient number of human examples within a reasonable period of time. Indeed, research is needed into the interaction effects between the generation of human feedback and the online learning performance of the robot. It is known that the number of trials (episodes) has an influence on the learning performance of the robot. However, we do not know if increasing the number of trials has a clear effect on the robot's learning performance if there is a human-robot interaction and this interaction influences the generation of EEG-based human feedback. For example, we do not know whether the learning curve stabilizes with the increase in the number of trials (more than 90 tests) for a subject considered an outlier. In our study we did not investigate the effects of the online learning performance of robots on the generation of human feedback, which is very challenging to investigate. As shown in our investigations, the generation of human feedback can also be influenced by other interaction components in HRI (e.g., human gestures). Hence, it is not straightforward to explain subject variability in online learning performance of the robot. In this paper we analyzed the interaction effects of two different interaction components (human feedback and human gesture) on the robot's online learning performance. The question of the interaction effects between the generation of human feedback and the robot's online learning performance, i.e., the effects of the robot's online learning performance on the generation of human feedback, can be investigated in the future.

In most EEG-based BCIs the robot actions were directly corrected binary based on ErrP detections [e.g., *left* (wrong) → *right* (correct) or *right* (wrong) → *left* (correct)] (Salazar-Gomez et al., 2017) or the control policy of robots were learned and optimized based on online ErrP detections (Iturrate et al., 2015; Kim et al., 2017). In a recent study, ErrPs were used for co-adaptation of human and robot (Ehrlich and Cheng, 2018) and for modeling of co-adaptation of human and robot (Ehrlich and Cheng, 2019a). In most studies there was only one interaction component (human feedback, i.e., ErrP) (Iturrate et al., 2015). In our study we have two interaction components (human feedback and human gestures) that can separately or jointly influence the online performance of robots. In this paper, we investigated individual effects of two interaction components on the learning performance of a robot and interaction effects of two interaction components on the learning performance of the robot. Even if learning in a robot is possible without prior knowledge and despite errors in the interpretation of gestures or the detection of ErrP, our results show that it is quite useful to use prior knowledge. They also show that learning with prior knowledge regarding the subjects variability is more stable, which should be investigated more systematically in the future. In general, we could show that errors in both interaction components have less impact on the general learning behavior if previous knowledge is used, whereas false positive results have a greater effect. However, false negative results, i.e., not recognizing mistakes, should be considered more critical. We were able to explain our results partly by the way the learning algorithm used works. However, there are still open questions. For example, the influence of humans is a factor that is difficult to model, but has a great influence on the results. In the future, therefore, the effects of interactions with the robot (changes in the robot's online learning performance) on the online generation of EEG-based human feedback should be analyzed to study the variability of the robot's learning performance depending on the interacting human. Furthermore, our results indicate that both warm start learning (fast convergence) and cold start learning (more exploration) have advantages. For example, it would be possible to give specific prior knowledge (warm start learning) when a change of state is not strongly expected, or to let the agent do natural exploration (cold start learning) to enable the robot to adapt more quickly to likely state changes.

DATA AVAILABILITY STATEMENT

The datasets presented in this article are not readily available because there is no permission to transfer the data to third parties. Requests to access the datasets should be directed to su-kyoung.kim@dfki.de.

ETHICS STATEMENT

The studies involving human participants were reviewed and approved by the ethics committee of the University of Bremen, Universität Bremen, Rechtsstelle—Referat 06 Bibliothekstraße 1, 28359, Bremen. The patients/participants provided their written informed consent to participate in this study.

AUTHOR CONTRIBUTIONS

SK, EK, and FK developed the proposed human-robot interaction (HRI) concept and the HRI scenarios for evaluation of the proposed concept. SK recorded the data and performed data analysis, generated the results including all figures and all tables and performed statistical evaluations, and wrote the methods and results and most parts of introduction and discussion. LS also analyzed the data. EK gave the critical feedback on all parts of sections and wrote introduction and discussion. FK gave the

critical feedback on overall works. SK, EK, LS, and FK discussed the results together and wrote the overall manuscript. All authors contributed to the article and approved the submitted version.

FUNDING

This work was funded by the Federal Ministry of Economics and Energy (BMWi), Project Management Agency German Aerospace Center (DLR). Funding reference number: FKZ 50RA1701 and FKZ 50RA1703.

SUPPLEMENTARY MATERIAL

The Supplementary Material for this article can be found online at: https://www.frontiersin.org/articles/10.3389/frobt.2020.558531/full#supplementary-material

REFERENCES

Agrawal, S., and Goyal, N. (2013). "Thompson sampling for contextual bandits with linear payoffs," in *International Conference on Machine Learning (ICML)* (Atlanta, GA), 127–135.

Ahn, M., and Jun, S. C. (2015). Performance variation in motor imagery brain-computer interface: a brief review. *J. Neurosci. Methods* 243, 103–110. doi: 10.1016/j.jneumeth.2015.01.033

Auer, P., Cesa-Bianchi, N., and Fischer, P. (2002). Finite-time analysis of the multiarmed bandit problem. *Mach. Learn.* 47, 235–256. doi: 10.1023/A:1013689704352

Bargsten, V., and Ferandez, J. D. G. (2015). "COMPI: development of a 6-DOF compliant robot arm for human-robot cooperation," in *Proceedings of the 8th International Workshop on Human-Friendly Robotics (HFR)* (Munich).

Betzel, R. F., Bertolero, M. A., Gordon, E. M., Gratton, C., Dosenbach, N. U., and Bassett, D. S. (2019). The community structure of functional brain networks exhibits scale-specific patterns of inter- and intra-subject variability. *Neuroimage* 202:115990. doi: 10.1016/j.neuroimage.2019.07.003

Blankertz, B., Sanelli, C., Halder, S., Hammer, E., Kübler, A., Müller, K.-R., et al. (2009). Predicting BCI performance to study BCI illiteracy. *BMC Neurosci.* 10:P84. doi: 10.1186/1471-2202-10-S1-P84

Cesa-Bianchi, N., Gentile, C., and Zappella, G. (2013). "A gang of bandits," in *Advances in Neural Information Processing Systems (NIPS)*, eds C. J. C. Burges, L. Bottou, M. Welling, Z. Ghahramani, and K. Q. Weinberger (Lake Tahoe, CA: NIPS Proceedings), 737–745.

Chang, C.-C., and Lin, C.-J. (2011). LIBSVM: A library for support vector machines. *ACM Trans. Intell. Syst. Techno.* 27, 1–27. doi: 10.1145/1961189.1961199

Chapelle, O., and Li, L. (2011). "An empirical evaluation of thompson sampling," in *Advances in Neural Information Processing Systems*, eds G. J. Shawe-Taylor, R. S. Zemel, P. L. Bartlett, F. Pereira, and K. Q. Weinberger (NIPS Proceedings), 2249–2257.

Chavarriaga, R., Sobolewski, A., and Millán, J. D. R. (2014). Errare machinale est: the use of error-related potentials in brain-machine interfaces. *Front. Neurosci.* 8:208. doi: 10.3389/fnins.2014.00208

Cortes, D. (2018). Adapting multi-armed bandits policies to contextual bandits scenarios. *arXiv[preprint].arXiv:1811.04383.*

Daniel, C., Viering, M., Metz, J., Kroemer, O., and Peters, J. (2014). "Active reward learning," in *Proceedings of Robotics: Science and Systems* (Berkeley, CA). doi: 10.15607/RSS.2014.X.031

Ehrlich, S. K., and Cheng, G. (2018). Human-agent co-adaptation using error-related potentials. *J. Neural Eng.* 15:066014. doi: 10.1088/1741-2552/aae069

Ehrlich, S. K., and Cheng, G. (2019a). "A computational model of human decision making and learning for assessment of co-adaptation in neuro-adaptive human-robot interaction," in *2019 IEEE International Conference on Systems, Man and Cybernetics (SMC)* (Bari: IEEE), 264–271. doi: 10.1109/SMC.2019.8913872

Ehrlich, S. K., and Cheng, G. (2019b). A feasibility study for validating robot actions using EEG-based error-related potentials. *Int. J. Soc. Robot.* 11, 271–283. doi: 10.1007/s12369-018-0501-8

Falkenstein, M., Hoormann, J., Christ, S., and Hohnsbein, J. (2000). ERP components on reaction errors and their functional significance: a tutorial. *Biol. Psychol.* 51, 87–107. doi: 10.1016/S0301-0511(99)00031-9

Gentile, C., Li, S., and Zappella, G. (2014). "Online clustering of bandits," in *International Conference on Machine Learning (ICML)*, 757–765.

Iturrate, I., Chavarriaga, R., Montesano, L., Minguez, J., and Millán, J. D. R. (2015). Teaching brain-machine interfaces as an alternative paradigm to neuroprosthetics control. *Sci. Rep* (Anchorage, AK). 5:13893. doi: 10.1038/srep13893

Iturrate, I., Montesano, L., and Minguez, J. (2010). "Robot reinforcement learning using EEG-based reward signals," in *IEEE International Conference of on robotics and automation (ICRA)* (Anchorage), 4181–4184. doi: 10.1109/ROBOT.2010.5509734

Jeunet, C., NKaoua, B., Subramanian, S., Hachet, M., and Lotte, F. (2015). Predicting mental imagery-based BCI performance from personality, cognitive profile and neurophysiological patterns. *PLoS ONE* 10:e0143962. doi: 10.1371/journal.pone.0143962

Kim, S. K., and Kirchner, E. A. (2013). "Classifier transferability in the detection of error related potentials from observation to interaction," in *Proceedings of the IEEE International Conference on Systems, Man, and Cybernetics (SMC)* (Manchester), 3360–3365. doi: 10.1109/SMC.2013.573

Kim, S. K., and Kirchner, E. A. (2016). Handling few training data: classifier transfer between different types of error-related potentials. *IEEE Trans. Neural Syst. Rehabil. Eng.* 24, 320–332. doi: 10.1109/TNSRE.2015.2507868

Kim, S. K., Kirchner, E. A., and Kirchner, F. (2020). "Flexible online adaptation of learning strategy using EEG-based reinforcement signals in real-world robotic applications," in *Proceedings of the IEEE International Conference on Robotics and Automation (ICRA)* (Paris).

Kim, S. K., Kirchner, E. A., Stefes, A., and Kirchner, F. (2017). Intrinsic interactive reinforcement learning–using error-related potentials for real world human-robot interaction. *Sci. Rep.* 7:17562. doi: 10.1038/s41598-017-17682-7

Kirchner, E. A., Kim, S. K., Straube, S., Seeland, A., Wöhrle, H., Krell, M. M., et al. (2013). On the applicability of brain reading for predictive human-machine interfaces in robotics. *PLoS ONE* 8:e81732. doi: 10.1371/journal.pone.0081732

Krell, M. M., Straube, S., Seeland, A., Wöhrle, H., Teiwes, J., Metzen, J. H., et al. (2013). pySPACE–a signal processing and classification environment in Python. *Front. Neuroinform.* 7:40. doi: 10.3389/fninf.2013.00040

Langford, J., and Zhang, T. (2008). "The epoch-greedy algorithm for multi-armed bandits with side information," in *Advances in Neural Information Processing Systems 20*, eds J. C. Platt, D. Koller, Y. Singer, and S. T. Roweis (Vancouver: NIPS Proceedings), 817–824.

Li, L., Chu, W., Langford, J., and Schapire, R. E. (2010). "A contextual-bandit approach to personalized news article recommendation," in *Proceedings of the 19th International Conference on World Wide Web* (Raleigh, NC), 661–670. doi: 10.1145/1772690.1772758

Lotte, F., Bougrain, L., Cichocki, A., Clerc, M., Congedo, M., Rakotomamonjy, A., et al. (2018). A review of classification algorithms for EEG-based brain-computer interfaces: a 10 year update. *J. Neural Eng.* 15:031005. doi: 10.1088/1741-2552/aab2f2

Ma, B.-Q., Li, H., Zheng, W.-L., and Lu, B.-L. (2019). "Reducing the subject variability of EEG signals with adversarial domain generalization," in *International Conference on Neural Information Processing* (Vancouver), 30–42. doi: 10.1007/978-3-030-36708-4_3

Morioka, H., Kanemura, A., Hirayama, J., Shikauchi, M., Ogawa, T., Ikeda, S., et al. (2015). Learning a common dictionary for subject-transfer decoding with resting calibration. *Neuroimage* 111, 167–178. doi: 10.1016/j.neuroimage.2015.02.015

Müller, K.-R., Krauledat, M., Dornhege, G., Curio, G., and Blankertz, B. (2004). Machine learning techniques for brain-computer interfaces. *Biomed. Eng.* 49, 11–21. doi: 10.1007/978-3-540-73345-4_80

Parra, L., Spence, C., Gerson, A., and Sajda, P. (2003). Response error correction–a demonstration of improved human-machine performance using real-time EEG monitoring. *IEEE Trans. Neural Syst. Rehabil. Eng.* 11, 173–177. doi: 10.1109/TNSRE.2003.814446

Rivet, B., Souloumiac, A., Attina, V., and Gibert, G. (2009). xDAWN algorithm to enhance evoked potentials: application to brain-computer interface. *IEEE Trans. Biomed. Eng.* 56, 2035–2043. doi: 10.1109/TBME.2009.2012869

Salazar-Gomez, A. F., DelPreto, J., Gil, S., Guenther, F. H., and Rus, D. (2017). "Correcting robot mistakes in real time using EEG signal," in *Proceedings of IEEE International Conference on Robotics and Automation (ICRA)*. doi: 10.1109/ICRA.2017.7989777

Seghier, M. L., and Price, C. J. (2018). Interpreting and utilising intersubject variability in brain function. *Trends Cogn. Sci.* 22, 517–530. doi: 10.1016/j.tics.2018.03.003

van Schie, H. T., Mars, R. B., Coles, M. G. H., and Bekkering, H. (2004). Modulation of activity in medial frontal and motor cortices during error observation. *Nat. Neurosci.* 7, 549–554. doi: 10.1038/nn1239

Vidaurre, C., and Blankertz, B. (2010). Towards a cure for BCI illiteracy. *Brain Topogr.* 23, 194–198. doi: 10.1007/s10548-009-0121-6

Wu, Q., Wang, H., Gu, Q., and Wang, H. (2016). "Contextual bandits in a collaborative environment," in *Proceedings of the 39th International ACM SIGIR conference on Research and Development in Information Retrieval* (Pisa), 529–538. doi: 10.1145/2911451.2911528

Zhang, W., Tan, C., Sun, F., Wu, H., and Zhang, B. (2018). A review of EEG-based brain-computer interface systems design. *Brain Science Advances* 4, 156–167. Available online at: https://journals.sagepub.com/doi/full/10.26599/BSA.2018.9050010

Conflict of Interest: The authors declare that the research was conducted in the absence of any commercial or financial relationships that could be construed as a potential conflict of interest.

frontiers in Neuroscience

ORIGINAL RESEARCH
published: 16 October 2020
doi: 10.3389/fnins.2020.509364

Decoding Kinematic Information From Primary Motor Cortex Ensemble Activities Using a Deep Canonical Correlation Analysis

Min-Ki Kim[1], Jeong-Woo Sohn[2] and Sung-Phil Kim[1]**

[1] Department of Biomedical Engineering, Ulsan National Institute of Science and Technology, Ulsan, South Korea,
[2] Department of Medical Science, College of Medicine, Catholic Kwandong University, Gangneung, South Korea

The control of arm movements through intracortical brain–machine interfaces (BMIs) mainly relies on the activities of the primary motor cortex (M1) neurons and mathematical models that decode their activities. Recent research on decoding process attempts to not only improve the performance but also simultaneously understand neural and behavioral relationships. In this study, we propose an efficient decoding algorithm using a deep canonical correlation analysis (DCCA), which maximizes correlations between canonical variables with the non-linear approximation of mappings from neuronal to canonical variables via deep learning. We investigate the effectiveness of using DCCA for finding a relationship between M1 activities and kinematic information when non-human primates performed a reaching task with one arm. Then, we examine whether using neural activity representations from DCCA improves the decoding performance through linear and non-linear decoders: a linear Kalman filter (LKF) and a long short-term memory in recurrent neural networks (LSTM-RNN). We found that neural representations of M1 activities estimated by DCCA resulted in more accurate decoding of velocity than those estimated by linear canonical correlation analysis, principal component analysis, factor analysis, and linear dynamical system. Decoding with DCCA yielded better performance than decoding the original FRs using LSTM-RNN (6.6 and 16.0% improvement on average for each velocity and position, respectively; Wilcoxon rank sum test, $p < 0.05$). Thus, DCCA can identify the kinematics-related canonical variables of M1 activities, thus improving the decoding performance. Our results may help advance the design of decoding models for intracortical BMIs.

Keywords: primary motor cortex (M1), decoding algorithm, Kalman filter, long short-term memory recurrent neural network, intracortical brain–machine interface, deep canonical correlation analysis

OPEN ACCESS

Edited by:
Damien Coyle,
Ulster University, United Kingdom

Reviewed by:
Joseph Thachil Francis,
University of Houston, United States
Karunesh Ganguly,
University of California,
San Francisco, United States

****Correspondence:***
Jeong-Woo Sohn
jsohn@ish.ac.kr
Sung-Phil Kim
spkim@unist.ac.kr

Specialty section:
This article was submitted to Neuroprosthetics, a section of the journal Frontiers in Neuroscience

Received: *01 November 2019*
Accepted: *22 September 2020*
Published: *16 October 2020*

Citation:
Kim M-K, Sohn J-W and Kim S-P (2020) Decoding Kinematic Information From Primary Motor Cortex Ensemble Activities Using a Deep Canonical Correlation Analysis. Front. Neurosci. 14:509364. doi: 10.3389/fnins.2020.509364

INTRODUCTION

The primary motor cortex (M1) is robustly linked to the kinematic parameters of the upper limbs (Humphrey, 1972; Humphrey and Corrie, 1978; Georgopoulos et al., 1982, 1986; Sergio et al., 2005; Schwartz, 2007; Aggarwal et al., 2008; Vargas-Irwin et al., 2010). This concept provides a basis for decoding information in an intracortical brain–machine interface (BMI), which often harnesses

M1 activities to infer continuous movement parameters in order to enable the neural control of external effectors. Intracortical BMIs have largely relied on functional relationships between M1 activities and kinematics (Moran and Schwartz, 1999b; Paninski et al., 2003; Wu et al., 2004; Shanechi et al., 2016; Vaskov et al., 2018). For instance, a number of BMIs have been developed based on a finding that a population vector constructed from the firing activities of a neuronal ensemble can predict the kinematic variables of arm movements, such as direction, speed, position, and velocity (Georgopoulos et al., 1986, 1988; Flament and Hore, 1988; Schwartz et al., 1988; Moran and Schwartz, 1999b; Paninski et al., 2003; Wang et al., 2007). In addition to the population vector, neural representations capturing the shared variability in the population's neural activity have been demonstrated to be effective in predicting behavioral covariates (Yu et al., 2009; Shenoy et al., 2013; Cunningham and Yu, 2014; Kao et al., 2015). These neural representations can be acquired through unsupervised learning techniques such as principal components analysis (PCA) (Ames et al., 2014; Kaufman et al., 2014), factor analysis (FA) (Yu et al., 2009), and a linear dynamical system (LDS) based latent-state estimation (Kao et al., 2015) and are known to allow a decoder to guarantee stable outputs (Yu et al., 2009; Kao et al., 2013). Such neural representations of neural population activity could help enhance decoding kinematic variables. Decoding models for intracortical BMIs are broadly categorized into two categories. The first category is a generative method that operates based on the generation of neuronal firing activities from kinematic states described by encoding models. The second category is a direct method that operates based on a direct input–output function approximation from neuronal firing activities to kinematic variables (Chapin et al., 1999; Sussillo et al., 2012; Dethier et al., 2013; Ahmadi et al., 2019).

Generative decoding methods designed for BMIs include a population vector algorithm (Georgopoulos et al., 1986; Schwartz and Moran, 2000; Van Hemmen and Schwartz, 2008), a Kalman filter (KF) (Wu et al., 2004, 2006; Gilja et al., 2012; Golub et al., 2014), a point process-based adaptive filter (Wang et al., 2009; Shanechi et al., 2014), and a particle filter (Gao et al., 2001), to name a few. These methods infer kinematic information from observed neuronal activities via encoding models. The performance of generative decoding methods thus substantially depends on the assumptions and appropriateness of encoding models. Furthermore, direct decoding methods designed for BMIs include the Wiener filter (Chapin et al., 1999; Serruya et al., 2002; Fagg et al., 2009; Chhatbar and Francis, 2013; Willett et al., 2013), support vector regression (Kim et al., 2006; Xu et al., 2011), and artificial neural networks (ANNs) (Wessberg et al., 2000; Sanchez et al., 2003). Particularly, ANNs can serve as a direct approximator of a non-linear functional relationship between M1 activities and kinematic variables. Various types of ANNs have been suggested to decode M1 activities, including time-delay neural networks (Kim et al., 2003; Wang et al., 2005), recurrent neural network (RNN) (Sussillo et al., 2012), and echo-state network (Rao et al., 2005). Furthermore, owing to recent breakthroughs in deep learning, using deep neural networks (DNNs) for decoding M1 activities has become plausible (Sussillo et al., 2012; Ahmadi et al., 2019). For instance, a long short-term memory RNN (LSTM-RNN), one of the non-linear models harnessing temporal information in past neural activities, outperformed other decoding models for BMIs (Ahmadi et al., 2019). Despite their high performance, the intricate architectures of DNNs often require a much larger training data to achieve a successful decoding process. Furthermore, recent efforts to record a larger number of neuronal activities (e.g., >1,000 units) demand effective representational spaces of neuronal ensemble activities, which will also reduce the burden of training DNNs (Marblestone et al., 2013).

Considering the advantage of DNNs as a universal non-linear approximator, in the present study, we propose a novel approach for decoding M1 activities to estimate limb kinematics by exploring a joint representational space between M1 activities and kinematics. In this joint space, the representation variables of a neuronal ensemble and kinematic parameters are created in a way to maximize coupling between neuronal and kinematic representation variables. Among the many ways of doing so, we leveraged methods, such as a canonical correlation analysis (CCA), to maximize correlations between these variables. As one of the multivariate statistical methods, CCA maximizes correlations between joint (canonical) variables. A conventional linear canonical correlation analysis (LCCA) builds a linear mapping between a neuronal ensemble and canonical variables (Hotelling, 1936; Anderson, 1984; Friman et al., 2007). However, more informative neuronal canonical variables can be extracted from neuronal ensemble activities by using a non-linear method. A recently developed deep canonical correlation analysis (DCCA) allows us to examine this possibility by approximating a non-linear mapping from neuronal ensemble activities to canonical variables with a DNN (Andrew et al., 2013). Previous non-invasive brain–computer interface (BCI) studies showed the effectiveness of DCCA as a means of feature extraction from electroencephalogram associated with various covariates of interest, such as eye movements and visual stimulus frequencies (Vu et al., 2016; Qiu et al., 2018; Liu et al., 2019). For example, Vu et al. successfully improved the performance of the steady-state visual evoked potential-based BCI using DCCA-based feature extraction (Vu et al., 2016). Although DCCA suffers from the same difficulty in interpreting neural activities as DNNs, canonical variables estimated by DCCA may effectively represent kinematics-related neuronal ensemble activities. Consequently, decoding these canonical variables may achieve a similar or superior performance to decoding original firing rates (FRs) while keeping a decoding model concise.

Based on this hypothesis, the present study aims to investigate how hand velocity information is represented in canonical variables found by LCCA or DCCA and to compare those representations with other neural representations (PCA, FA, and LDS) extracted from naïve ensemble FRs ($Z_{E\text{-}FR}$). Moreover, we aim to investigate the performance of decoding hand velocity information from the five types of neuronal representations (E-FR, PCA, FA, LCCA, and DCCA) using one of the two types of decoders, i.e., LKF and LSTM-RNN. Additionally, we examine whether DCCA yields better velocity decoding performance compared to a neural dynamical filter (NDF), which is a linear

mapping model to predict kinematic variables from LDS-based latent states (Kao et al., 2015). In this study, we apply various decoding methods to the data of M1 firing activity and hand movements in two non-human primates that performed a 2D reaching task with one arm.

MATERIALS AND METHODS

Datasets

The two datasets used in this study are available on a neuroscience data depository, called the Collaborative Research in Computational Neuroscience (Flint et al., 2012; Lawlor et al., 2018; Perich et al., 2018). Each dataset includes the cortical firing activity and hand movement recordings, which were acquired from a non-human primate performing an arm reaching task on 2D spaces with one arm (see **Figure 1A**). The dataset CRT (center-out reaching task) of Flint et al. includes M1 activities for monkeys to perform a center-out reaching task to acquire eight different targets that were placed at 45° intervals around a circle with their home placed on the center (Flint et al., 2012). The dataset SRT (sequential reaching task) of Lawlor et al. (2018) includes M1 and dorsal premotor cortical activities during a sequential reaching task, where a series of targets were randomly displayed on 2D spaces (Lawlor et al., 2018; Perich et al., 2018). All cortical activities were extracellularly recorded by a 128-channel acquisition system (Cerebus, Blackrock Microsystems, Inc., Salt Lake City, UT, United States) through 96-channel silicon microelectrode arrays chronically implanted in the arm area of M1.

In this study, we analyzed only M1 activities to develop and test decoders. The spike trains of each neuron were binned with a non-overlapping window of 50 ms to maximize the mutual information between neural FRs and kinematics (Paninski et al., 2003; Suminski et al., 2010). FRs were estimated by spike counts within the bin divided by its size (i.e., 50 ms). We also square-root-transformed the FRs in each bin to make them more normally distributed for linear decoding models (Schwartz and Moran, 1999). Then, we performed a Gaussian kernel smoothing process to reduce temporal noise of individual unit activities, where the kernel standard deviation (SD) was determined according to Yu et al. (2009) (SD = 80 ms in the dataset CRT, SD = 140 ms in the dataset SRT). An instantaneous hand position was converted into the velocity and its absolute value (speed). This kinematic combination (velocity and speed) is shown to be appropriate predictors for establishing tuning models (Rasmussen et al., 2017). Using the velocity and speed, we calculated the goodness of fit (r^2) of a linear tuning model for each neuron, which was designed based on the cosine tuning model (Moran and Schwartz, 1999a), expressed by: $\mathrm{z}(t) = \beta_0 + \beta_1 \mathrm{v}(t) + \beta_2 \mathrm{v}(t) + \epsilon(t)$ where $\mathrm{z}(t)$ is FRs, β_0, β_1, and β_2 are model coefficients, and $\mathrm{v}(t)$ and $\mathrm{v}(t)$ denote a vector of velocity and its norm (speed) at time t, respectively. Then, we selected the neurons with $r^2 > 0.01$, where the threshold of r^2 (>0.01) was empirically determined. A total of 155 and 63 neurons passed these criteria in the datasets CRT and SRT, respectively. The datasets CRT and SRT included 175 and 496 successful trials, respectively, in which animals successfully acquired the targets during the tasks. To build and validate decoders, the first 75% of the trials were used for training and the remaining 25% of the trials were used for testing: the training and testing sets of the dataset CRT contained 131 and 44 trials, respectively, and those of the dataset SRT contained 372 and 124 trials, respectively. Every parameter estimation of the models built in this study (see below) was performed using the training set only.

Neural Representation Extraction via Supervised Learning Methods

Linear Canonical Correlation Analysis

Canonical correlation analysis is one of the multivariate statistical methods that extracts joint canonical variables from random vectors z and x. In this study, z and x correspond to the FRs $[z_1, z_2, \ldots, z_M]^{\mathrm{T}} \in \mathbb{R}^{m\times 1}$ from m neurons and the hand kinematics $[x_1, x_2, x_3]^{\mathrm{T}} \in \mathbb{R}^{3\times 1}$, where x_1 and x_2 denote the velocity of the x- and y-coordinates, respectively, and x_3 denotes the speed. An LCCA seeks linear mappings from z and x to canonical variables by maximizing correlations between canonical variables (Hotelling, 1936; Anderson, 1984; Friman et al., 2007). The canonical coefficients $\{\boldsymbol{\alpha}, \boldsymbol{\beta}\}$ on these linear mappings are defined as

$$\left\{\boldsymbol{\alpha}^*, \boldsymbol{\beta}^*\right\} = \underset{\alpha^*,\beta^*}{\operatorname{argmax}}\, \rho\left(\boldsymbol{\alpha}^{\mathrm{T}}\mathbf{z}, \boldsymbol{\beta}^{\mathrm{T}}\mathbf{x}\right) \tag{1}$$

$$= \underset{\alpha^*,\beta^*}{\operatorname{argmax}}\, \frac{\boldsymbol{\alpha}^{\mathrm{T}}\Sigma_{ZX}\boldsymbol{\beta}}{\sqrt{\boldsymbol{\alpha}^{\mathrm{T}}\Sigma_{Z}\boldsymbol{\alpha}\cdot\boldsymbol{\beta}^{\mathrm{T}}\Sigma_{\mathrm{X}}\boldsymbol{\beta}}} \tag{2}$$

where $\rho(\cdot)$ denotes a function of the correlation between canonical variables. Σ_Z and Σ_X are the covariance matrices of centralized data $\bar{\mathbf{z}}$ and $\bar{\mathbf{x}}$, respectively, and Σ_{ZX} is the sample cross-covariance matrix. To make the canonical coefficients scale-free, the denominator is constrained to have unit variance, such that

$$\left\{\boldsymbol{\alpha}^*, \boldsymbol{\beta}^*\right\} = \underset{\boldsymbol{\alpha}^{\mathrm{T}}\Sigma_Z\boldsymbol{\alpha}=\boldsymbol{\beta}^{\mathrm{T}}\Sigma_X\boldsymbol{\beta}=1}{\operatorname{argmax}}\, \boldsymbol{\alpha}^{\mathrm{T}}\Sigma_{ZX}\boldsymbol{\beta} \tag{3}$$

The singular value decomposition is used to derive $\boldsymbol{\alpha}^*$ and $\boldsymbol{\beta}^*$. Using these variables, the canonical variables of z and x can be estimated by

$$\hat{u}_Z = \boldsymbol{\alpha}^{*\mathrm{T}}\bar{\mathbf{z}} \tag{4}$$

$$\hat{u}_X = \boldsymbol{\beta}^{*\mathrm{T}}\bar{\mathbf{x}} \tag{5}$$

By using the eigenvectors corresponding to the largest eigenvalues, we repeatedly computed a pair of canonical variables, $\{\hat{u}_Z, \hat{u}_X\}$, until the number of pairs equals m or 3. For convenience, we call the linear neural ($\hat{u}_Z$) and kinematic ($\hat{u}_X$) canonical variables $\mathrm{Z_{LCV}}$ and $\mathrm{X_{LCV}}$, respectively.

Deep Canonical Correlation Analysis

A DCCA is one of the advanced CCA methods based on DNNs. DCCA finds non-linear mappings from z and x to canonical

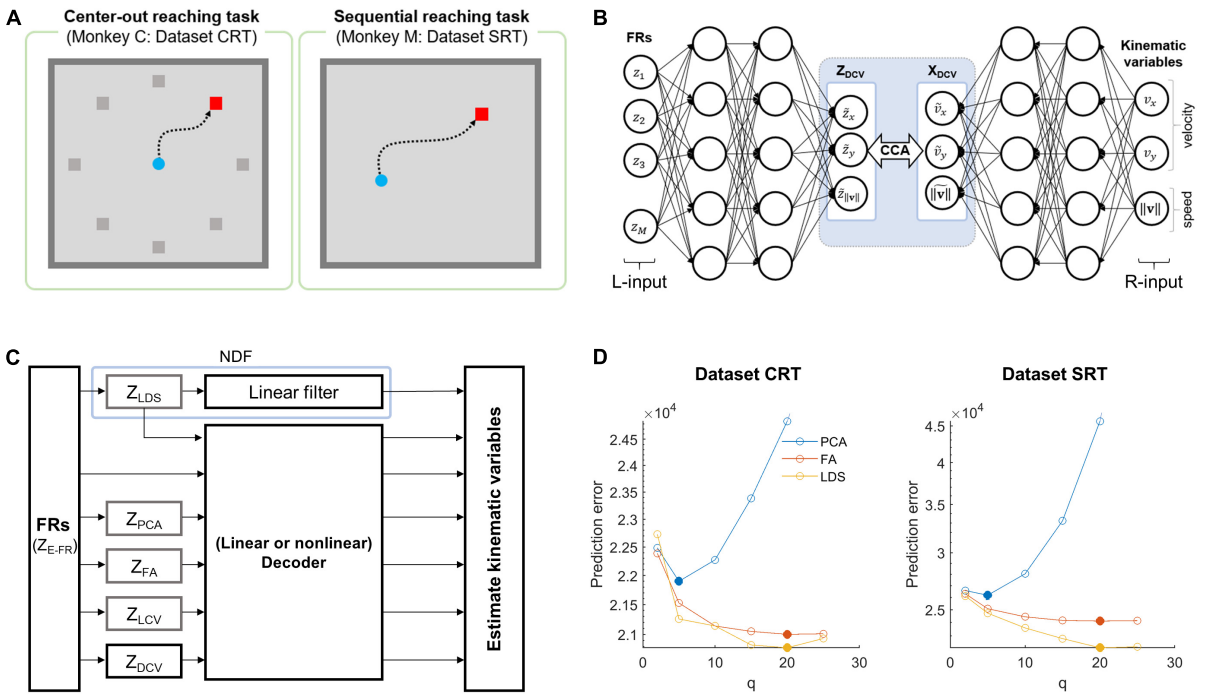

FIGURE 1 | Simulation overview for assessing the effects of DCCA on two decoders. **(A)** Behavioral tasks for each dataset. The left panel denotes a center-out reaching task which the monkey C performed, and the right panel is a sequential reaching task which the monkey M performed. **(B)** The schematic diagram depicts the DCCA between firing rates and kinematic variables. The left inputs (L-input) of the networks indicate the naïve firing rates and the right inputs (R-input) of the networks denote the kinematic variables: *x*- and *y*-velocity, and speed. A dotted-line box between the networks denotes a canonical correlation analysis (CCA) between the left-canonical variables (Z_{DCV}) and the right-canonical variables (X_{DCV}). **(C)** The block diagram depicts a simulation paradigm for a comparative study of decoding. **(D)** Prediction errors for the state dimensionalities (*q*) of each dataset. The filled circle denotes proper dimensionality corresponding to the minimum prediction error for each dimensionality reduction method (Yu et al., 2009). Each color code denotes the dimensionality reduction method.

variables through stacked non-linear transformation layers, as shown in **Figure 1B** (Andrew et al., 2013). The non-linear mappings $f_z^l(z)$ and $f_x^l(x)$ are defined as

$$f_z^l(\mathbf{z}) = \sigma\left(W_l^{(Z)}\mathbf{u}_{l-1}^{(Z)} + \mathbf{b}_l^{(Z)}\right) \in \mathbb{R}^{m\times 1} \quad (6)$$

$$f_x^l(\mathbf{x}) = \sigma\left(W_l^{(X)}\mathbf{u}_{l-1}^{(X)} + \mathbf{b}_l^{(X)}\right) \in \mathbb{R}^{3\times 1} \quad (7)$$

where $W_l^{(\cdot)}$ denotes a matrix of weights at the *l-th* layer, $\mathbf{u}_{l-1}^{(\cdot)}$ is the output vector from the $(l-1)$-*th* layer, $\mathbf{b}_l^{(\cdot)}$ is a vector of biases at the *l-th* layer, and $\sigma(\cdot)$ is a non-linear function. A parameter set $\boldsymbol{\theta}$, which includes W and $\mathbf{b}$, is estimated by maximizing correlations between functional outputs as follows:

$$\arg\max_{\boldsymbol{\theta}_Z^*,\boldsymbol{\theta}_X^*} \rho\left(f_Z(\mathbf{z},\boldsymbol{\theta}_Z), f_X(\mathbf{x},\boldsymbol{\theta}_X)\right) \quad (8)$$

To seek $\boldsymbol{\theta}_Z^*$ and $\boldsymbol{\theta}_X^*$, the backpropagation algorithm is used to optimize parameters W and $\mathbf{b}$ based on the gradient of $\rho(\cdot)$. The parameters in each layer are initialized in advance through a pretraining process using a denoising autoencoder (Vincent et al., 2008). The deep neural canonical variables can be computed as $\hat{o}_Z = f_Z(\mathbf{z},\boldsymbol{\theta}_Z)$, and the deep kinematic canonical variables can be computed as $\hat{o}_X = f_X(\mathbf{x},\boldsymbol{\theta}_X)$. In that case, we call the deep neural ($\hat{o}_Z$) and kinematic ($\hat{o}_X$) canonical variables Z_{DCV} and X_{DCV}, respectively.

In addition to $\boldsymbol{\theta}$, we also need to optimize the hyperparameters of DNNs, for which we employed the Bayesian optimization method (Ahmadi et al., 2019). To optimize the hyperparameters, we empirically preset the range for each parameter: the number of nodes in a layer $\in \{2^4, 2^5, \ldots, 2^{10}\}$, the number of layers $\in \{1, 2, \ldots, 4\}$, an encoder and decoder batch size $\in \{2^5, 2^6, \ldots, 2^8\}$, a learning rate $\in \{1e{-}5, 1e{-}4, \ldots, 1e{-}2\}$, a regularization parameter for each view $\in \{1e{-}6, \ldots, 1e{-}1\}$, a weight decay parameter (or an L_2 regularization parameter) $\in \{1e{-}6, \ldots, 1e{-}1\}$, and a trade-off parameter $\in \{1e{-}6, \ldots, 1e{-}1\}$. While other parameters determine the learning and architecture of a general DNN, the trade-off parameter is used for regularizing correlations with a quadratic penalty, uniquely associated with DCCA. The Bayesian optimization is iteratively performed 1,000 times to select reliable parameters. **Table 1** shows the optimized hyperparameters obtained in this study for each dataset using the publicly available MATLAB toolbox for the DCCA (Wang et al., 2015).

Neural Representation Extraction via Unsupervised Learning Methods

For the purpose of comparison, we also extracted low-dimensional representations of neural population firing activity using several methods, including PCA, FA, and LDS, which

TABLE 1 | Optimized hyperparameters for DCCA with respect to each dataset.

	Hyperparameters	CRT	SRT
Function of *Z*	# nodes (*z*)	1024	256
	# layers (*z*)	2	2
	RCOV (*z*)	0.04	0.08
Function of *X*	# nodes (*x*)	1024	64
	# layers (*x*)	3	3
	RCOV (*x*)	0.04	0.04
Common	Batch size (encoder, autoencoder)	256/256	128/128
	Batch size (decoder, autoencoder)	64/64	512/512
	L_2 regularization	6.8e−04	3.7e−04
	η	0.01	0.01
	λ	0.01	0.02

Hidden layer activator is fixed as a sigmoid function.
η, learning rate; λ, trade-off parameter; RCOV, regularization parameter for the total layers.

are widely used in intracortical BMIs. Below we describe each method briefly.

Principal Component Analysis

We applied principal component analysis (PCA) to the FR data of all neuronal units. A Gaussian kernel smoothing process was used as preprocessing for FRs before applying PCA to avoid a case where neurons with highly fluctuating firing rates influenced decoding (Yu et al., 2009). Then, we extracted principal components (PCs) of FR using PCA from the training data. Note that PCA was performed on a single trial basis rather than trial-averaged data in order to focus on covariance between neuronal units in single trials. To determine the number of PCs that would be included in the set of neural representations, we followed the procedure proposed by Yu et al. (2009). Briefly, using the eigenvectors obtained from the training set, we extracted all PCs (i.e., as many as neuronal units) for the testing set, which were then sorted according to the magnitude of corresponding eigenvalues in a descending way. Afterward, we selected the first 5 PCs and reconstructed FRs from them. The mean absolute error between true FRs and reconstructed FRs was calculated. We kept adding the next 5 PCs, reconstructing FRs and calculating error in the same way as above. As a result, the minimum reconstruction error was achieved with the first 5 PCs for both datasets of CRT and SRT (**Figure 1D**), which constituted neural representations by PCA, denoted as Z_{PCA}. Note that the smoothing process was applied again to the final set of PCs before decoding.

Factor Analysis

A factor analysis (FA) allows us to find low-dimensional latent factors to elucidate shared variability among the population activities (Santhanam et al., 2009). Again, we performed the smoothing to FRs before applying FA. To estimate latent factors from FRs, we adopted the FA method proposed by Yu et al., which adjusted FA for neural data (Yu et al., 2009; Kao et al., 2015). Then, in a similar way to PCA, we determined the number of factors included in a set of neural representations using the reconstruction error of the testing set. We found the minimum error with 20 factors for both CRT and SRT datasets, which were further used as the set of neural representations by FA, denoted as Z_{FA}.

Linear Dynamical System for M1 States

Observed neuronal population activity can be interpreted as a noisy observation of low-dimensional and dynamical neural states (Shenoy et al., 2013; Kao et al., 2015). Using the LDS-based neural state estimation approach proposed by Kao et al. (2015), we estimated dynamic neural latent states from the population activity. We determined the dimensionality of neural states using the procedure above based on reconstruction error. We set the dimensionality to 20 for both CRT and SRT datasets, with which the minimum reconstruction error was achieved. A vector of these neural state was used as neural representations by LDS, denoted as Z_{LDS}. Note that we used a linear filter [formally called a neural dynamical filter (NDF)] instead of Kalman filter when decoding Z_{LDS} because Z_{LDS} already represented latent dynamics of neural activity such that state estimation of Kalman filter might not be suitable for it.

Neural Representation Analysis

We first examined Pearson correlations between canonical variables; $\rho(\hat{u}_Z, \hat{u}_X)$ or $\rho(\hat{o}_Z, \hat{o}_Z)$. Both canonical variables of neural FRs ($\hat{u}_Z$ or $\hat{o}_Z$) are supposed to adequately represent kinematic information because they are highly correlated with the canonical variables of kinematic parameters ($\hat{u}_X$ or $\hat{o}_X$), provided that the linear or non-linear mappings of LCCA or DCCA are appropriately built. To validate this assumption, we performed a tuning analysis of not only the neural canonical variables but also other neural representations using a linear regression model, in which the tuning quality of each neural representation with respect to velocity and speed was analyzed. The temporal linear regression model of a single neural representation (z) to the kinematic parameters (x) was given as $\mathbf{z}(t) = \boldsymbol{\beta}_0 + \boldsymbol{\beta}\mathbf{x}(t) + \boldsymbol{\epsilon}(t)$ where $\boldsymbol{\beta}_0$ and $\boldsymbol{\beta}$ denote coefficients and $\boldsymbol{\epsilon}(t)$ is the error term at time t (Schwartz and Moran, 1999, 2000; Paninski et al., 2003; Rasmussen et al., 2017). The tuning quality of a neural representation was assessed by the goodness-of-fit (r^2) of the tuning model. In addition to this, we also computed the decoding performance using each neural representation in the training data with a linear Kalman filter. The decoding performance was measured by the mean absolute error between actual and decoded velocity from the training data. Finally, we assessed the predictive performance of each of the five neural representations above during training using both the goodness-of-fit of the tuning model and the training error.

Decoding Algorithms

Kalman Filter

A linear Kalman filter (LKF) is one of the popular generative decoding methods based on the linear dynamical system (Wu et al., 2006). LKF follows a first-order Markov rule, such that a state vector (velocity and speed) $^{x}_{t}$ at time t evolves from x_{t-1} at time $t-1$. In this study, the state vector corresponds to the

kinematic parameter vector. The system model, which describes the state transition, and the observation model, which describes the generation of observation o_t from x_t, are given by

$$\mathbf{x}_t = A\mathbf{x}_{t-1} + Q_{t-1} \quad (9)$$

$$\mathbf{o}_t = H\mathbf{x}_t + V_t \quad (10)$$

where A denotes the system model parameter matrix, H is the observation model parameter matrix, and Q and V are the process and observation noise following a Gaussian distribution, respectively. The neural observation vector $\mathbf{o}_t$ can be either the $Z_{E\text{-}FR}$ vector ($\mathbf{z}_t$) or the vector of the other neural representations. To predict $\mathbf{x}_t$, we initialized $\mathbf{x}_0 = \mathbf{0}$ at the beginning of every trial

TABLE 2 | Optimized hyperparameters with respect to the representation pairs for LSTM-RNN (CRT/SRT dataset).

	$Z_{E\text{-}FR}$	Z_{PCA}	Z_{FA}	Z_{LDS}	Z_{LCV}	Z_{DCV}
No. nodes	35/40	15/64	15/64	15/15	15/64	35/64
Mini-batch size	128/16	16/256	16/32	128/64	128/32	128/32
RCOV	0.01/0.01	0.05/1e−03	0.02/0.09	0.08/0.09	0.1/0.1	0.1/0.1
η	6e−03/1e−04	0.01/1e−04	0.01/1e−04	1e−04/1e−04	0.01/1e−04	1e−03/1e−04

η, *learning rate; RCOV, regularization parameter; no. hidden layers {1}, gradient decay factor {0.95}, squared gradient decay factor {0.95}, and activation function {logistic sigmoid} are fixed.*

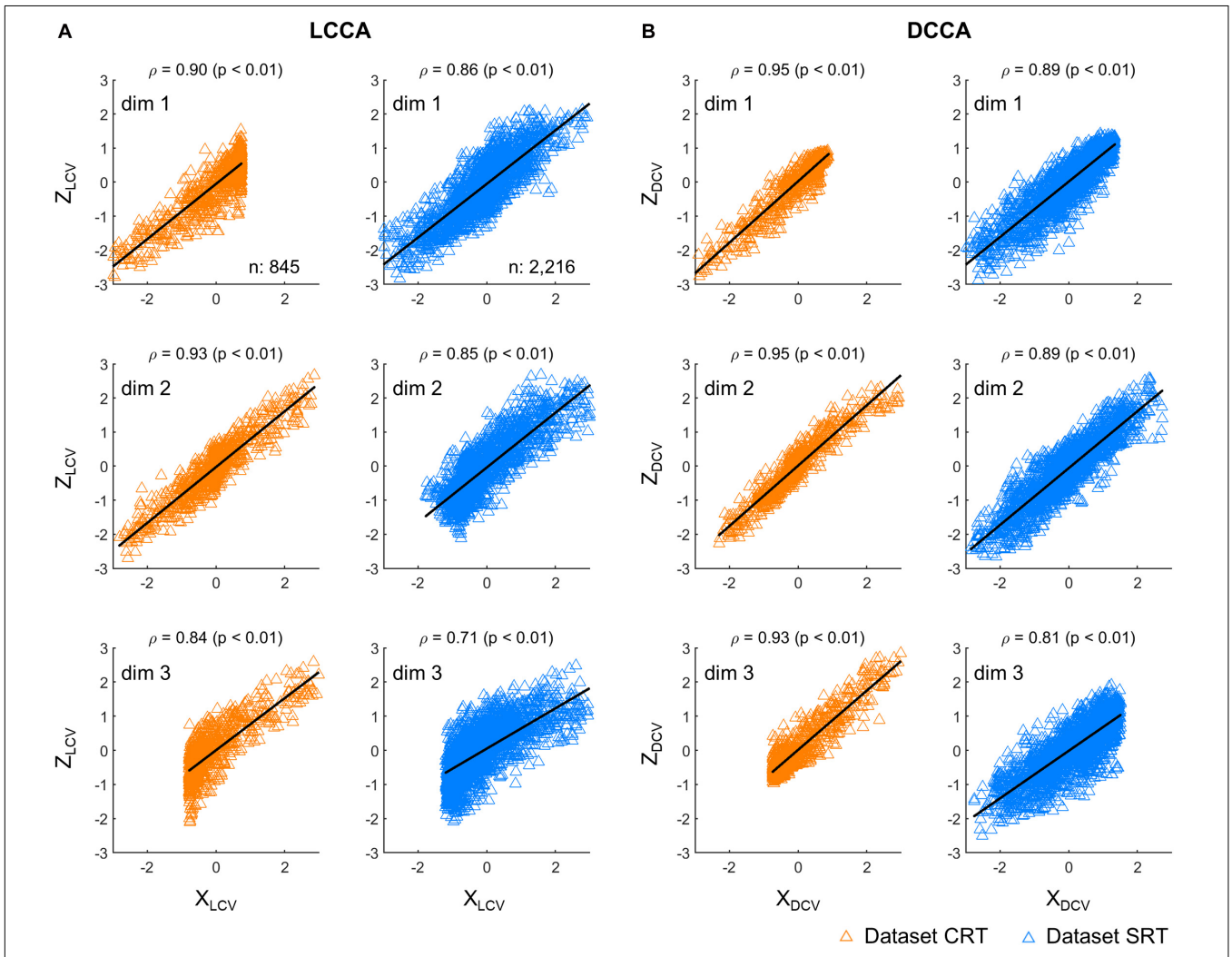

FIGURE 2 | Correlations between canonical variables. **(A)** Correlations between canonical variables extracted by LCCA (Z_{LCV} and X_{LCV}). **(B)** Correlations between canonical variables extracted by DCCA (Z_{DCV} and X_{DCV}). The upward-pointing triangles denote the samples per time step of the canonical variables. ρ denotes the Pearson's correlation coefficient and *p* indicates to exist a significant linear regression relationship between *X* and *Z*. Each row corresponds to each dimensionality of the canonical variables. The orange triangles denote the dataset CRT and the blue triangles represent the dataset SRT.

after converging the Kalman gain to its steady state in advance (Dethier et al., 2013).

Long Short-Term Memory in Recurrent Neural Networks

An LSTM-RNN based on an RNN architecture has been well suited in predicting kinematics from neuronal activities (Ahmadi et al., 2019). The components of LSTM-RNN are enumerated as follows: c is a memory cell, $\mathbf{f}$ is a forget gate, and $\mathbf{i}$ and $\mathbf{o}$ are input and output gates, which correspond to $\mathbb{R}^l$, where l denotes the number of hidden units. LSTM-RNN operates by regulating the information flow with these gates via the cell. Given W as a matrix of weights with respect to the recurrent connection or input/output, $\mathbf{h}$ as a vector of the hidden layer, and $\mathbf{b}$ as a vector of biases, each gate can be calculated by

$$\mathbf{f}_t = \sigma_{sigmoid}(W_{f,z}\mathbf{y}_t + W_{f,l}\mathbf{h}_{t-1} + \mathbf{b}_f) \quad (11)$$

$$\mathbf{i}_t = \sigma_{sigmoid}(W_{i,z}\mathbf{y}_t + W_{i,l}\mathbf{h}_{t-1} + \mathbf{b}_i) \quad (12)$$

$$\mathbf{o}_t = \sigma_{sigmoid}(W_{o,z}\mathbf{y}_t + W_{o,l}\mathbf{h}_{t-1} + \mathbf{b}_o) \quad (13)$$

where the input vector $\mathbf{y}$ is either the $Z_{E\text{-}FR}$ vector ($\mathbf{z}_t$) or the vector of the other neural representations at time t and $\sigma_{sigmoid}(\cdot)$ denotes the sigmoidal activation function. The subscripts indicate the corresponding gates and their recurrent connection. The information flow of the cell memory can be updated by

$$\mathbf{c}_u = \sigma_{tanh}(W_{c,z}\mathbf{z}_t + W_{c,l}\mathbf{h}_{t-1} + \mathbf{b}_c) \quad (14)$$

$$\mathbf{c}_t = f_t \otimes \mathbf{c}_{t-1} + \mathbf{i}_t \otimes \mathbf{c}_u \quad (15)$$

$$\mathbf{h}_t = \mathbf{o}_t \otimes \sigma_{tanh}(\mathbf{c}_t) \quad (16)$$

where $\sigma_{tanh}(\cdot)$ denotes the hyperbolic tangent function and $\otimes$ denotes the element-wise product. To train LSTM-RNN, we utilized the Adam optimizer built-in MATLAB deep learning toolbox. The hyperparameters of LSTM-RNN were optimized by the Bayesian optimizer in the same way as DCCA. The Bayesian optimizer performed an objective function evaluation 500 times. In our analysis, we set the gradient decay factor as 0.95 and the squared gradient decay factor as 0.99. Then, the training batches were shuffled at every epoch for the training efficiency. **Table 2** shows the optimized hyperparameters for LSTM-RNN.

Decoding Performance Evaluation

To evaluate the effects of CCA on decoding, we composed three representations of neuronal activities: $Z_{E\text{-}FR}$, Z_{PCA}, Z_{FA}, Z_{LDS}, Z_{LCV}, and Z_{DCV} (see **Figure 1C**). In this study, we performed decoding to predict the hand velocity X_{VEL} from each neural representation using LKF and LSTM-RNN.

For the evaluation of the decoding performance, we measured the decoding error by the Euclidean distance between the actual and predicted kinematic parameters. The decoding error was measured for the hand velocity v and hand position p, which were reconstructed from the cumulated velocity for each trial. The decoding error of the i-th trial was calculated as

$$\mathbf{e}_i = \frac{1}{n}\sum_{t=1}^{n} e(t) \quad (17)$$

where $e(t)$ is an absolute instantaneous error, $e(t) = |\mathbf{v}(t) - \hat{\mathbf{v}}(t)|$ or $e(t) = |\mathbf{p}(t) - \hat{\mathbf{p}}(t)|$ at time t, and n is the number of samples in the i-th trial. To compare the decoding performance between the neural representations ($Z_{E\text{-}FR}$, Z_{PCA}, Z_{FA}, Z_{LDS}, Z_{LCV}, and Z_{DCV}), we applied the Friedman test to evaluate the effects of decoder inputs in accordance with the types of decoders (LKF and LSTM-RNN). For the Friedman test, the dependent variables consist of a decoding error, and the factors include the decoder input and decoder type. We also performed a *post hoc* statistical analysis using the Bonferroni correction ($p < 0.05$).

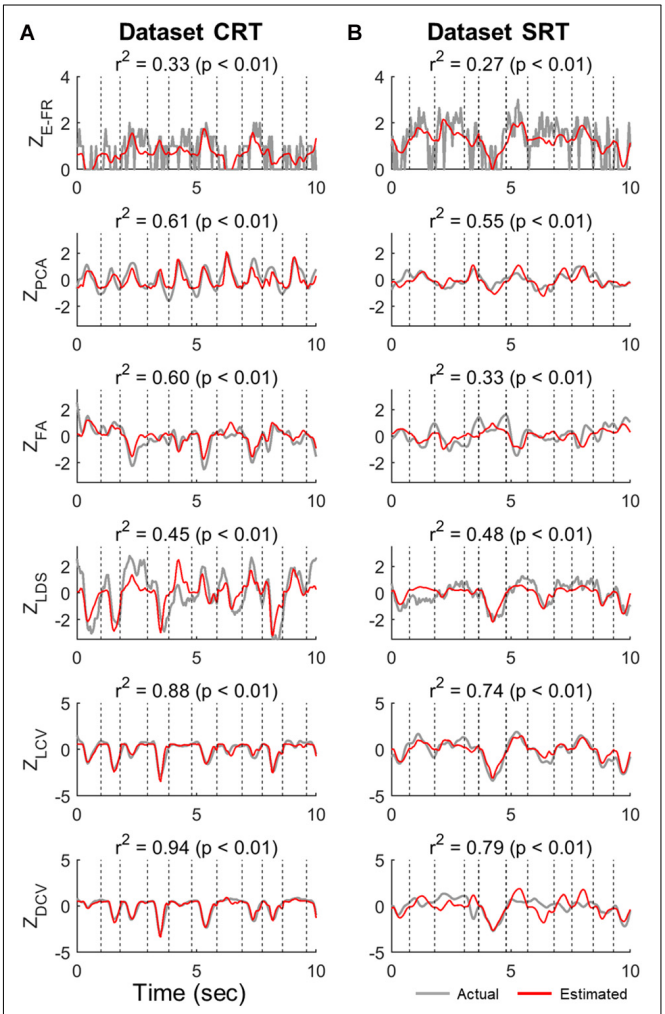

FIGURE 3 | Estimation of neural representations by linear velocity tuning models (testing data). Single traces of the actual neural representations over time in each trial of the test data (gray lines) are superimposed by the corresponding estimates by the linear velocity tuning model (red lines). Here, we present the representative traces of neural representations that were most accurately estimated by the linear velocity tuning models yielding the highest r^2, where r^2 denotes the goodness-of-fit of the linear velocity tuning model. The top row indicates the estimation of $Z_{E\text{-}FR}$ in each dataset (CRT and SRT). From the second to fourth rows are the estimations of Z_{PCA}, Z_{FA}, and Z_{LDS} in each dataset. The bottom two rows denote the estimation of Z_{LCV} and Z_{DCV}. Column **(A)** and **(B)** correspond to dataset CRT and SRT, respectively.

RESULTS

First, we investigated correlations between the neural and kinematic canonical variables. **Figure 2** depicts correlations between the canonical variables, each extracted from firing rates (Z) and kinematics (X), respectively. The canonical variables were obtained from the testing set either by using LCCA or DCCA. Correlations were calculated between the corresponding pairs of neural and kinematic canonical variables, where a total of three pairs were determined by the number of kinematic parameters. DCCA resulted in higher correlations than LCCA for every dataset: the correlation coefficients for the dataset CRT ranged from 0.93 to 0.95 using DCCA and from 0.84 to 0.90 using LCCA ($p < 0.01$, Wilcoxon rank sum test), and those for the dataset SRT ranged from 0.81 to 0.89 using DCCA and from 0.71 to 0.86 using LCCA ($p < 0.01$, Wilcoxon rank sum test).

Next, we examined the tuning of neuronal FRs and neural representations ($Z_{E\text{-}FR}$, Z_{PCA}, Z_{FA}, Z_{LDS}, Z_{LCV}, and Z_{DCV}) concerning kinematic parameters (X_{VEL}) using the testing set. The quality of tuning was measured by the r^2 of the linear regression model with X_{VEL} as the regressors (see Section "Neural Representation Analysis").

Figure 3 shows the examples of the actual values of $Z_{E\text{-}FR}$, Z_{LCV}, and Z_{DCV} and the estimated values by the linear velocity tuning model. For $Z_{E\text{-}FR}$, we selected the neuron whose FRs was most accurately estimated by the model (i.e., the highest value of r^2). Among the neural representations analyzed here, the linear model tracked the variation of Z_{DCV} most accurately yielding the highest r^2 (Friedman test, Bonferroni correction, $p < 0.05$). Notably, the linear model can estimate even time-invariant parts of Z_{DCV} (see the bottom row of **Figure 3**), which often spanned over multiple trials, even though X_{VEL} varied during these periods.

Figures 4A,B depict the distributions of r^2 for $Z_{E\text{-}FR}$, Z_{LCV}, and Z_{DCV} in the datasets CRT and SRT, respectively. The mean values of r^2 for Z_{DCV} (0.93 in the dataset CRT and 0.74 in the

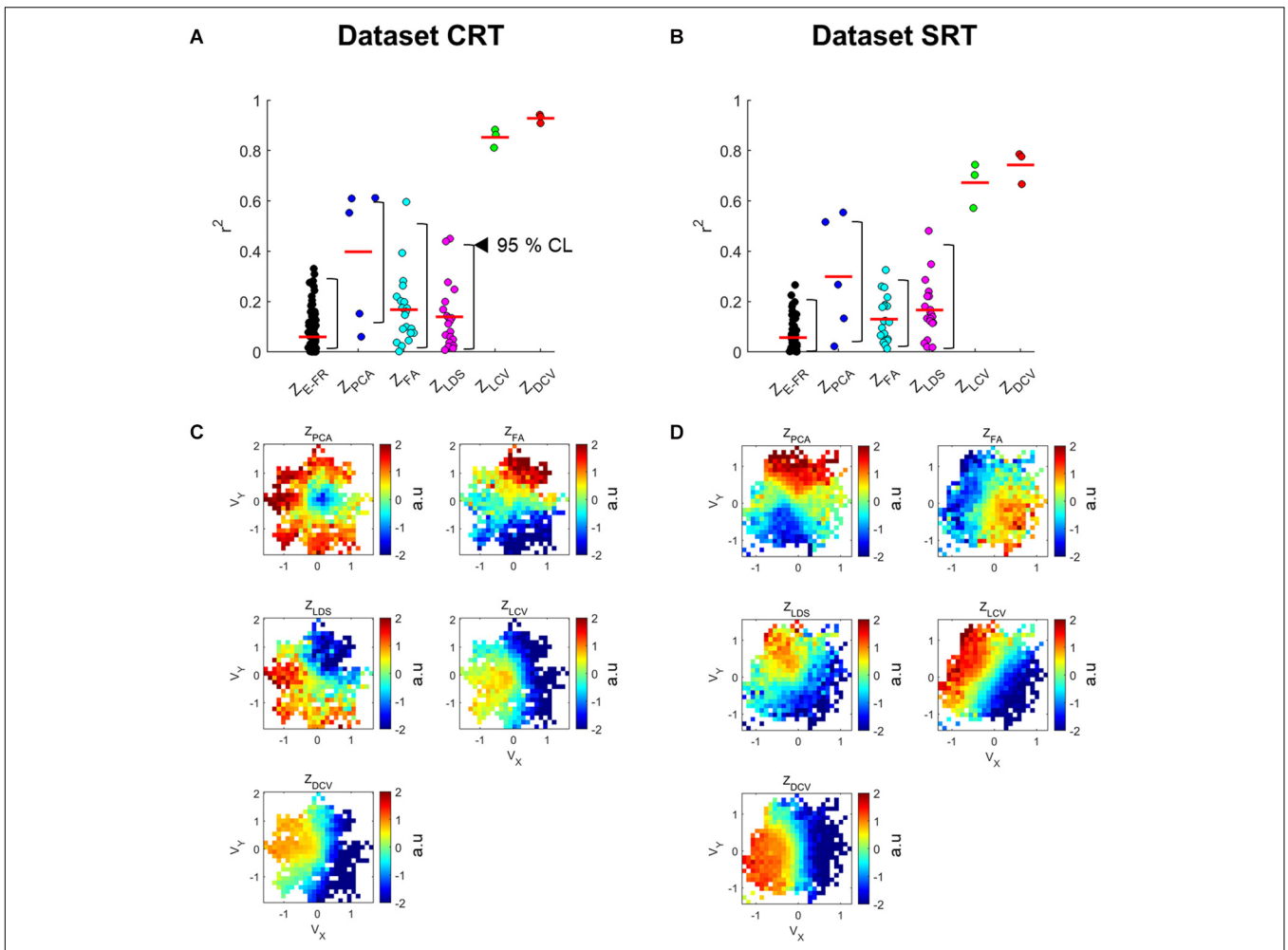

FIGURE 4 | Velocity tuning properties of neuronal canonical variables estimated by the neural representations. **(A,B)** The points denote the linear velocity tuning quality (r^2) for all dimensions of the input variables ($Z_{E\text{-}FR}$, Z_{PCA}, Z_{FA}, Z_{LDS}, Z_{LCV}, and Z_{DCV}). The red horizontal line denotes the averaged r^2 of all dimensions. Black left-pointing pointer denotes a 95% confidence level of each neural representation's r^2. **(C,D)** Each panel depicts the topographical map of the input variable to the kinematic variables, such as velocity (v). In this case, each panel corresponds to the best-tuned dimensionality showing high r^2.

dataset SRT) and Z_{LCV} (0.85 in the dataset CRT and 0.67 in the dataset SRT) were considerably higher than those for Z_{PCA} (0.40 in the dataset CRT and 0.30 in the dataset SRT), Z_{FA} (0.17 in the dataset CRT and 0.13 in the dataset SRT), and Z_{LDS} (0.14 in the dataset CRT and 0.17 in the dataset SRT) (Friedman test, multiple comparison with Bonferroni correction, $p < 0.05$). Moreover, the neural canonical variables found by DCCA (Z_{DCV}) was more tuned to velocity than those by LCCA (Z_{LCV}) (Wilcoxon rank sum test: $p = 0.02$ in the dataset CRT, $p = 0.04$ in the dataset SRT). Moreover, the neural canonical variables found by DCCA (Z_{DCV}) was more tuned to velocity than those by LCCA (Z_{LCV}). **Figures 4C,D** depict the topographical maps of the neural canonical variables showing high r^2 in the 2D velocity space. Although Z_{LCV} and Z_{DCV} were created to maximize correlations with the canonical variables of kinematics, not kinematics *per se*, they showed tuning with the actual velocity.

We then examined both the training error and average r^2 of each neural representation, as shown in **Figure 5**. It reveals that Z_{DCV} yielded not only the highest r^2 but also the lowest training error (0.09 in the dataset CRT, 0.12 in the dataset SRT). Although we also observed relatively low training error using neural representations of FA and LDS, the average r^2 of them were not high compared to those of CCA.

The decoding performance was evaluated for each combination of neural representations and decoders (see **Figure 1**). **Figure 6** depicts the true and decoded velocity trajectories for each combination. The results show that decoding Z_{DCV} produced the most accurate prediction of velocity (Friedman test with Bonferroni correction, $p < 0.05$. See **Tables 3**, **4**). **Figure 7** depicts the true and reconstructed position trajectories in the dataset CRT. When decoding $Z_{E\text{-}FR}$ and Z_{LCV}, LSTM-RNN reconstructed the hand position more accurately than LKF. However, when decoding Z_{DCV}, there was no apparent difference between the decoders. Z_{DCV} also led to the smallest variance of the reconstructed trajectories [variance, $Z_{E\text{-}FR}$: x-pos = 0.83, y-pos = 0.82; Z_{PCA}: x-pos = 1.00, y-pos = 1.01; Z_{FA}: x-pos = 0.83, y-pos = 0.80; Z_{LDS} (NDF): x-pos = 0.71, y-pos = 0.74; Z_{LCV}: x-pos = 0.74, y-pos = 0.80; Z_{DCV}: x-pos = 0.61, y-pos = 0.62 when using LKF, whereas $Z_{E\text{-}FR}$: x-pos = 0.87, y-pos = 0.77; Z_{PCA}: x-pos = 0.75, y-pos = 0.79; Z_{FA}: x-pos = 0.70, y-pos = 0.65; Z_{LDS}: x-pos = 0.78, y-pos = 0.77; Z_{LCV}: x-pos = 0.60, y-pos = 0.60; Z_{DCV}: x-pos = 0.53, y-pos = 0.53 when using LSTM-RNN in the dataset CRT]. Decoding Z_{DCV} yielded the best performance of reconstructing the hand position using either LKF or LSTM-RNN (Friedman test, multiple comparison with Bonferroni correction, $p < 0.05$. See **Tables 3**, **4**). The standard deviations (STDs) of the actual velocity and position in the dataset CRT are $X = 0.24$ and $Y = 0.26$ for velocity and $X = 1.82$, and $Y = 1.76$ for position, and those in the dataset SRT are $X = 0.21$ and $Y = 0.20$ for velocity and $X = 1.66$ and $Y = 1.52$ for position. For LKF, the decoding error is less than the STDs of the X- and Y-axes of the actual velocity by 5.7 and 4.2% on overage, respectively. Moreover, the decoding error is less than the STDs of the actual position by 72.1 and 69.1%. For LSTM-RNN, the decoding error is less than the STDs of the actual velocity by 5.7 and 4.6%, and the decoding error is less than those of the actual position by 72.3 and 70.0%.

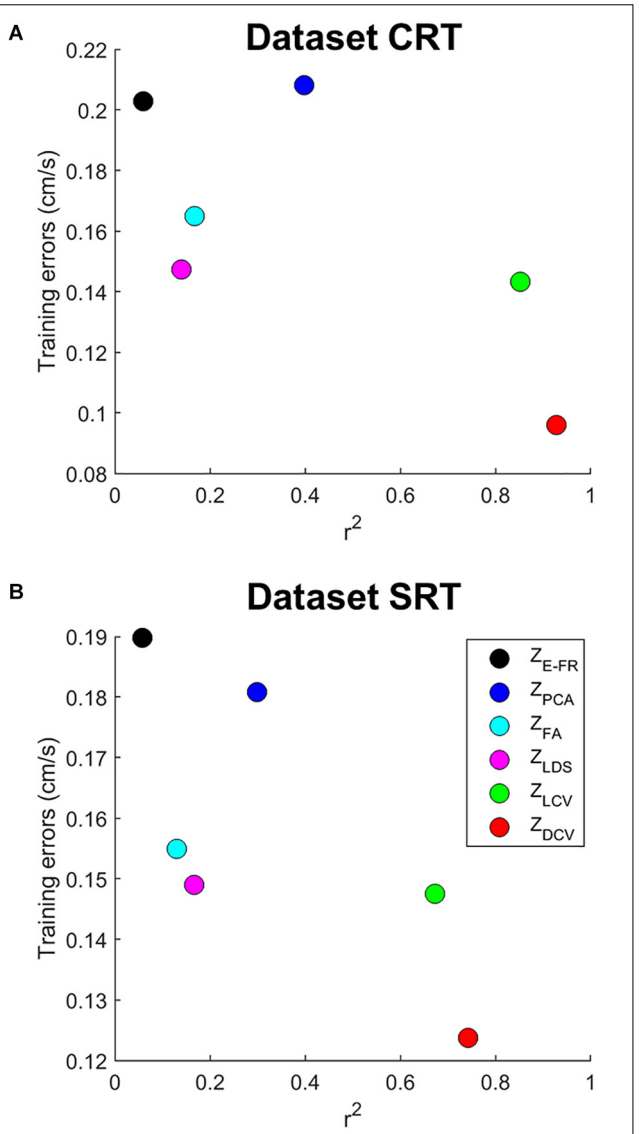

FIGURE 5 | The relationship between training error and average r^2 of velocity-tuning for each dimensionality of the neural representations. Each colored circle corresponds to the mean of r^2 and training error for a neural representation ($Z_{E\text{-}FR}$, Z_{PCA}, Z_{FA}, Z_{LDS}, Z_{LCV}, and Z_{DCV}). The **(A)** top and **(B)** bottom panel correspond to the datasets CRT and SRT.

Figure 8A depicts the comparison of the decoding error for the hand velocity across different neural representations and decoders. For the dataset CRT, the one-way Friedman test revealed the main effect of neural representation (Z_{FR}, Z_{PCA}, Z_{FA}, Z_{LDS}, Z_{LCV}, and Z_{DCV}) on the decoding error when using LKF ($\chi^2 = 166.6$, $p < 0.01$) or when using LSTM-RNN ($\chi^2 = 128.1$, $p < 0.01$). When using LKF, a *post hoc* multiple comparison test with Bonferroni correction showed lower decoding error with Z_{DCV} than other neural representations ($ps < 0.01$) except for Z_{LDS} ($p = 0.25$). When using LSTM-RNN, it also showed lower decoding error with Z_{DCV} than other neural representations ($ps < 0.01$). For the dataset SRT, the Friedman

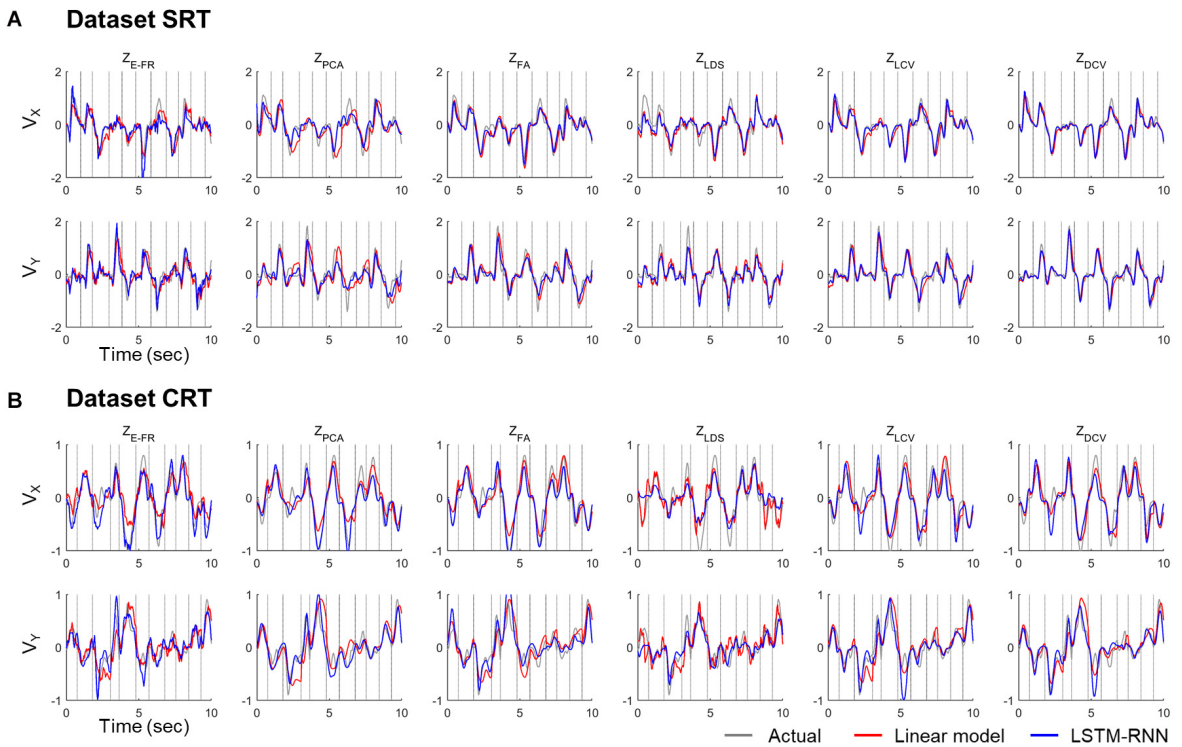

FIGURE 6 | Decoded velocity trajectory from each pair of the variables (testing data). Each column denotes the decoded (*X*- and *Y*-axis) velocity trajectories according to the predictors: $Z_{E\text{-}FR}$, Z_{PCA}, Z_{FA}, Z_{LDS}, Z_{LCV}, and Z_{DCV}. The solid gray lines denote the actual velocity, and the solid red and blue lines depict the outputs of linear model and LSTM-RNN, respectively. For linear model, LKF was used for $Z_{E\text{-}FR}$, Z_{PCA}, Z_{FA}, Z_{LCV}, and Z_{DCV}, whereas NDF (linear filter) was used for Z_{LDS}. The vertical gray lines denote boundary between trial intervals for the reaching. The top **(A)** and bottom **(B)** panel correspond to the datasets CRT and SRT.

TABLE 3 | Correlation coefficients of the decoded velocity (datasets CRT and SRT).

LKF	$Z_{E\text{-}FR}$	Z_{PCA}	Z_{FA}	Z_{LDS}*	Z_{LCV}	Z_{DCV}
CRT						
X	0.64 ± 0.25	0.38 ± 0.30	0.72 ± 0.27	0.82 ± 0.21	0.73 ± 0.28	0.77 ± 0.33
Y	0.69 ± 0.18	0.62 ± 0.26	0.71 ± 0.20	0.84 ± 0.13	0.75 ± 0.18	0.84 ± 0.18
SRT						
X	0.58 ± 0.29	0.60 ± 0.40	0.66 ± 0.31	0.76 ± 0.24	0.66 ± 0.31	0.71 ± 0.31
Y	0.54 ± 0.29	0.51 ± 0.35	0.62 ± 0.31	0.59 ± 0.28	0.62 ± 0.32	0.64 ± 0.32
LSTM-RNN	$Z_{E\text{-}FR}$	Z_{PCA}	Z_{FA}	Z_{LDS}	Z_{LCV}	Z_{DCV}
CRT						
X	0.74 ± 0.26	0.70 ± 0.29	0.80 ± 0.20	0.82 ± 0.25	0.79 ± 0.32	0.80 ± 0.33
Y	0.81 ± 0.16	0.76 ± 0.22	0.83 ± 0.14	0.87 ± 0.14	0.87 ± 0.15	0.91 ± 0.11
SRT						
X	0.72 ± 0.31	0.74 ± 0.35	0.79 ± 0.27	0.78 ± 0.31	0.78 ± 0.28	0.79 ± 0.27
Y	0.69 ± 0.28	0.72 ± 0.31	0.73 ± 0.29	0.69 ± 0.36	0.75 ± 0.26	0.75 ± 0.28

Decoding error of Z_{LDS} corresponds to that of the NDF.*

test revealed the main effect of neural representation on the decoding error when using LKF (χ^2 = 75.8, $p < 0.01$) or when using LSTM-RNN (χ^2 = 25.7, $p < 0.01$). When using LKF, the *post hoc* test showed lower decoding error with Z_{DCV} than other neural representations ($ps < 0.01$) except for Z_{LDS} ($p \cong 1$). When using LSTM-RNN, it showed lower decoding error with Z_{DCV} than $Z_{E\text{-}FR}$ ($p < 0.01$) only, while showing no difference between Z_{DCV} and other representations ($ps > 0.05$).

Figure 8B depicts the comparison of the error between true and reconstructed hand positions. For the dataset CRT, the Friedman test revealed the main effect of neural representation on the position error when using LKF (χ^2 = 71.9, $p < 0.01$) or when using LSTM-RNN (χ^2 = 80.7, $p < 0.01$). When using

TABLE 4 | Velocity and position decoding errors (datasets CRT/SRT).

LKF	$Z_{E\text{-}FR}$	Z_{PCA}	Z_{FA}	Z_{LDS}*	Z_{LCV}	Z_{DCV}
Velocity (cm/s)						
CRT	0.21 ± 0.04	0.28 ± 0.07	0.21 ± 0.04	0.16 ± 0.05	0.19 ± 0.04	0.13 ± 0.03
SRT	0.16 ± 0.05	0.17 ± 0.05	0.16 ± 0.04	0.15 ± 0.04	0.16 ± 0.05	0.15 ± 0.05
Position (cm)						
CRT	0.97 ± 0.36	1.20 ± 0.44	0.99 ± 0.34	0.91 ± 0.55	0.87 ± 0.32	0.57 ± 0.24
SRT	0.95 ± 0.60	1.01 ± 0.53	0.94 ± 0.43	0.90 ± 0.53	0.93 ± 0.48	0.83 ± 0.45
LSTM-RNN	$Z_{E\text{-}FR}$	Z_{PCA}	Z_{FA}	Z_{LDS}	Z_{LCV}	Z_{DCV}
Velocity (cm/s)						
CRT	0.18 ± 0.05	0.19 ± 0.05	0.16 ± 0.04	0.14 ± 0.05	0.13 ± 0.03	0.10 ± 0.02
SRT	0.14 ± 0.04	0.13 ± 0.04	0.12 ± 0.04	0.14 ± 0.06	0.12 ± 0.04	0.12 ± 0.05
Position (cm)						
CRT	1.15 ± 0.53	1.07 ± 0.43	0.92 ± 0.34	0.93 ± 0.50	0.65 ± 0.32	0.51 ± 0.22
SRT	0.86 ± 0.48	0.88 ± 0.52	0.78 ± 0.41	1.01 ± 0.60	0.82 ± 0.46	0.79 ± 0.46

Decoding error of Z_{LDS} corresponds to that of the NDF.*

LKF, the *post hoc* test showed lower error with Z_{DCV} than neural representations (ps < 0.01). When using LSTM-RNN, it showed lower error with Z_{DCV} than other neural representations except for Z_{LCV} ($p = 0.53$). For the dataset SRT, the Friedman test revealed the main effect of the neural representation on the position error when using LKF ($\chi^2 = 33.1$, $p < 0.01$) or when using LSTM-RNN ($\chi^2 = 13.6$, $p < 0.01$). When using LKF, the *post hoc* test showed lower error with Z_{DCV} than other neural representations except for Z_{LDS} ($p = 0.06$). When using LSTM-RNN, it showed lower error with Z_{DCV} than Z_{LDS} ($p < 0.01$), whereas there was no difference between Z_{DCV} and others.

Moreover, we evaluated the possible interaction effects of neural representations and decoder types using a two-way Friedman test (**Figure 9**). For the dataset CRT, the two-way Friedman test revealed the main effects of decoder [$\chi^2(1) = 116.9$, $p < 0.01$] and neural representation [$\chi^2(2) = 261.9$, $p < 0.01$] on the velocity decoding error (**Figure 9A**). The *post hoc* test with Bonferroni correction showed lower error using LSTM-RNN than using LKF for all neural representations ($p < 0.01$). For all decoders, the decoding error of velocity with Z_{DCV} was smaller than any other neural representations (ps < 0.01). For the dataset SRT, the two-way Friedman test revealed the main effect of decoder [$\chi^2(1) = 175.4$, $p < 0.01$] and neural representation [$\chi^2(2) = 59.0$, $p < 0.01$]. The *post hoc* test showed lower error using LSTM-RNN than using LKF ($p < 0.01$). For all decoders, the decoding error of velocity with Z_{DCV} was smaller than $Z_{E\text{-}FR}$ and Z_{PCA} (ps < 0.01).

Figure 9B depicts the same two-way statistical analysis on the error between true and reconstructed hand positions. For the dataset CRT, the two-way Friedman test revealed the main effects of decoder [$\chi^2(1) = 4.4$, $p < 0.05$] and neural representation [$\chi^2(2) = 143.1$, $p < 0.01$] on the position error. The *post hoc* test showed no difference between decoders ($p = 0.3$). For all decoders, the position error with Z_{DCV} was smaller than any other neural representations (ps < 0.01). For the dataset SRT, it showed the main effects of decoder [$\chi^2(1) = 14.3$, $p < 0.01$] and neural representation [$\chi^2(2) = 28.2$, $p < 0.01$]. The *post hoc* test showed no difference between decoders ($p = 0.1$). For all decoders, the position error with Z_{DCV} was smaller than any other neural representations (ps < 0.05).

DISCUSSION

In this study, we proposed a method to identify low-dimensional representations of M1 neuronal FR activities using canonical correlation analyses. Furthermore, we applied those canonical variables to the decoding models to predict the arm movements of non-human primates and compared the effect of the neural representations in terms of decoding performance. As expected, we confirmed that the canonical variables found by DCCA were well tuned to the hand velocity. Decoding arm movement information using canonical variables estimated by DCCA resulted in a superior performance to either cases using LCCA-estimated canonical variables or using the other neural representations regardless of the decoder type, i.e., LKF or LSTM-RNN. In particular, the performance of LKF was significantly more improved using DCCA than decoding FRs using LSTM-RNN. These findings suggest that we can design a simple linear decoder (LKF) with DCCA while achieving performance as good as using relatively complex DNNs.

The improvement of decoding M1 activities using LCCA or DCCA may be partly because canonical variables found by them showed superior tuning to velocity over the other neural representations, including individual neuronal FRs (**Figure 3**). Therefore, the LKF, drawing heavily on the quality of observation models, can benefit from the extracted canonical variables even when LCCA greatly reduced the number of neural variables. Particularly, DCCA-estimated neural canonical variables showed better tuning indices (r^2) than LCCA-estimated neural canonical variables, which subsequently led to a better decoding performance of DCCA. Meanwhile, training error that directly reflects the learning quality of the decoding model revealed superior over the other neural representations along

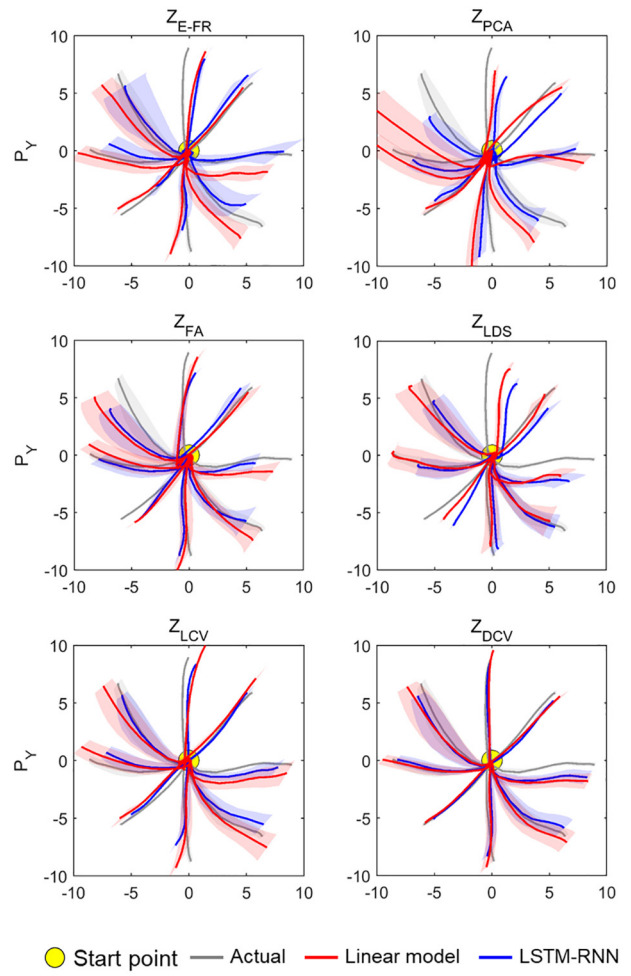

FIGURE 7 | Reconstructed position trajectory in the dataset CRT (testing data). Each panel denotes the reconstructed position trajectories according to the predictors: $Z_{E\text{-}FR}$, Z_{PCA}, Z_{FA}, Z_{LDS}, Z_{LCV}, and Z_{DCV}. Solid gray lines denote the true position trajectories, red lines denote the position trajectories reconstructed from the output of linear model, and blue lines denote the position trajectories from the output of LSTM-RNN. For linear model, LKF was used for $Z_{E\text{-}FR}$, Z_{PCA}, Z_{FA}, Z_{LCV}, and Z_{DCV}, whereas NDF (linear filter) was used for Z_{LDS}. The filled yellow circle denotes the home position (0, 0) from which non-human primates started to move their hands. Solid lines denote the averaged position trajectories across the trials, and shaded lines denote the standard errors across 44 trials with respect to each direction.

with r^2. This finding indicates that non-linear projections may be more suitable to extract joint canonical variables between high-dimensional neural activities and low-dimensional kinematic parameters. However, DCCA cannot provide direct links between canonical variables and individual neurons, which LCCA can do.

Besides better characteristics of the canonical variables, there could be another reason why DCCA improved decoding using LKF while the other neural representations did not. PCA is known to have difficulty distinguishing between changes in the underlying neural state, which becomes limitations to decoding kinematic information from noisy firing activity (Yu et al., 2009). Although FA also is a useful frame to extract independent and shared variability across neurons, it follows the assumption that the noise variance of an individual neuron is fixed over time (Yu et al., 2009). Above all, since these approaches (including LDS) aim to extract the latent states of population activity without kinematic information, it is difficult to extract elaborate components related to complex movement. This could be a reasonable reason why DCCA yielded a better performance on decoding models than the neural representations via unsupervised learning methods.

As for decoding methods, a DNN, represented by LSTM-RNN here, efficiently decoded neuronal population firing patterns because it can effectively process neuronal temporal dynamics through memory cells in a relatively concise network architecture. Furthermore, a state-space model, such as LKF, shows an advantage of representing temporal dynamics of kinematics in its system model, but its first-order linear system model may not be sufficient to elucidate the kinematic dynamics of arm movements. In addition, a direct decoding model, such as LSTM-RNN, can be free from any statistical assumption on data, which is often necessary in a generative model, such as LKF. Our results showing the superior performance of LSTM-RNN over LKF are in line with those of previous reports (e.g., Ahmadi et al., 2019).

In addition to direct mapping to velocity through the decoders, a more straightforward linear mapping could be taken into account; for example, we can simply reconstruct velocity from the canonical kinematic representations (X_{LCV} or X_{DCV}), which were estimated from the corresponding neural representations (Z_{LCV} or Z_{DCV}). To test whether how this simple mapping worked, we attempted to reconstruct velocity only through LCCA and DCCA without explicit decoders as follows. First, we estimated X_{LCV} (or X_{DCV}) from Z_{LCV} (or Z_{DCV}) by linear regression such as

$$X_k = \alpha_0 + \alpha_1 Z_k + e \tag{18}$$

where X_k and Z_k represent the k-th canonical variable, respectively, e represents residual error and α_0 and α_1 are canonical coefficients. Second, we reconstructed velocity from the estimated X_{LCV} (or X_{DCV}) during testing. For LCCA, the reconstruction of velocity was straightforward simply by inverting linear mapping between X_{LCV} and velocity. For DCCA, velocity was reconstructed by the inverse of activation function (here, a logit function) and the linear model between the layers, which was expressed as:

$$-\log\left(\left(\beta_{l,l-1} X W_l^{-1} - 1\right)^{-1}\right) \tag{19}$$

where $\beta_{l,l-1}$ represents coefficients between the outputs of layer l and $l-1$, and W_l is a matrix of the weight in l-th layer. We observed that the reconstructed velocity with this procedure exhibited lower performance than directly decoding Z (Z_{LCV} or Z_{DCV}) into velocity using LKF by 9.9% on average (11.4% for LCCA, and 8.3% for DCCA). Apparently, this analysis verified that direct reconstruction of velocity through mappings built by CCA was poorer than those from the proposed decoding

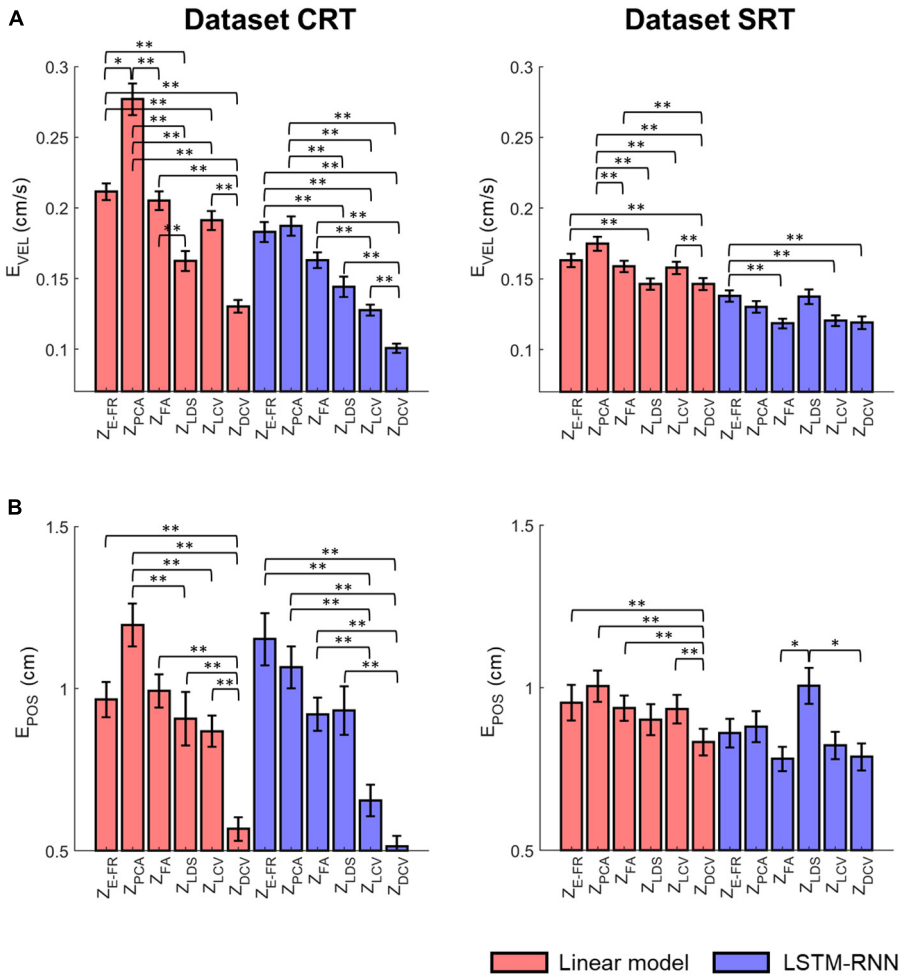

FIGURE 8 | Comparison of the decoding error for the velocity between the neural representations for each decoder. The mean error of decoding the hand velocity **(A)** and reconstructing the hand position **(B)** from decoded velocity [from six different neural representations (i.e., $Z_{E\text{-}FR}$, Z_{PCA}, Z_{FA}, Z_{LDS}, Z_{LCV}, and Z_{DCV})] (see the text for the descriptions of neural representations) using decoders [linear model (orange), and LSTM-RNN (purple)]. For linear model, LKF was used for $Z_{E\text{-}FR}$, Z_{PCA}, Z_{FA}, Z_{LCV}, and Z_{DCV}, whereas NDF (linear filter) was used for Z_{LDS}. The vertical lines indicate the standard error, and the asterisks denote the significantly different relationship [$^{*}p < 0.05$, $^{**}p < 0.01$, Friedman test with the multiple comparisons (with Bonferroni correction)]. The left and right columns correspond to the dataset CRT and SRT, respectively.

methods to predict velocity from neural representations using LKF or LSTM-RNN.

We can expect that the dimensionality of neuronal populations will increase further as the neurotechnology of large-scale neuronal recordings advances in the near future. Such a development will raise an issue of how efficiently we should design a decoder for intracortical BMIs. Our results suggest that DCCA, along with other dimensionality reduction techniques, can provide advantages to construct a compact but informative feature space for effective decoding. Unlike unsupervised dimensionality reduction techniques without kinematic information, DCCA can find a low-dimensional space to maximize correlations with target kinematic parameters, increasing a chance to improve predicting kinematic parameters such as velocity from neural activities. It has been well known that decoding velocity information of a prosthetic device from neural activity can be useful for BMIs in clinical environments (Kim et al., 2008; Wodlinger et al., 2015). Therefore, we suggest that our proposal method can be preferred if one considers the efficiency and performance of BMIs.

Although this study shows the feasibility of the improvement of decoding for BMIs using the proposed method, we have not validated it in an online BMI control paradigm, which should be conducted in future work. When applying the current decoding method to online BMIs in humans with tetraplegia, where the kinematic information of limbs is not available, we should consider how to extract kinematics of a target prosthetic device. To address this issue, many previous human BMI studies employed a training paradigm in which participants imagined limb movements following the instructed motion of an object shown on the screen. Then, a decoding algorithm could be built by associating M1 activities elicited during movement

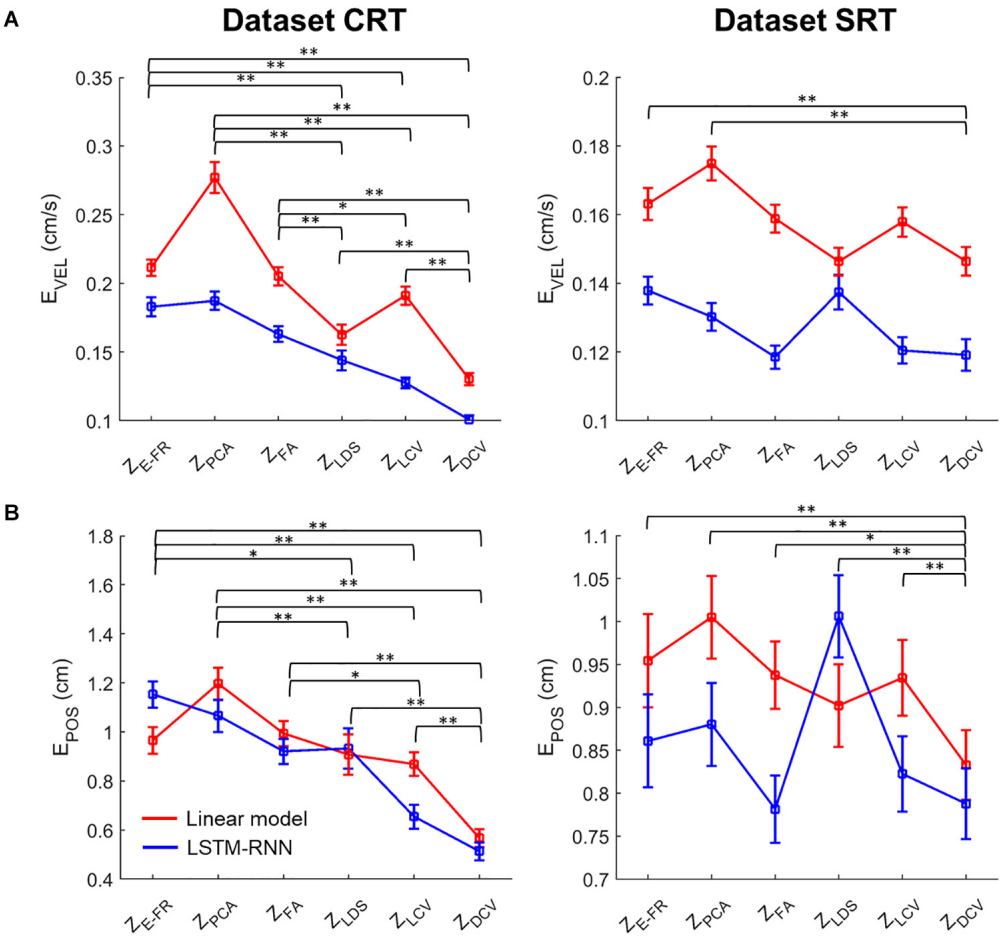

FIGURE 9 | Comparison of the decoding error for the velocity and reconstructed position between neural representations for all decoders. The mean error (open squares) of decoding the hand **(A)** velocity and **(B)** position from the six different neural representations (i.e., $Z_{E\text{-}FR}$, Z_{PCA}, Z_{FA}, Z_{LDS}, Z_{LCV}, and Z_{DCV}) (see the text for descriptions of neural representations) using decoders [linear model (red), and LSTM-RNN (blue)]. For linear model, LKF was used for $Z_{E\text{-}FR}$, Z_{PCA}, Z_{FA}, Z_{LCV}, and Z_{DCV}, whereas NDF (linear filter) was used for Z_{LDS}. The vertical lines indicate the standard error, and the asterisks denote the significantly different relationship [$^{*}p < 0.05$, $^{**}p < 0.01$, a two-way Friedman test with the multiple comparisons (with Bonferroni correction)]. The left and right columns correspond to the dataset CRT and SRT, respectively.

imagination with the kinematics of the object (Hochberg et al., 2006; Kim et al., 2008; Aflalo et al., 2015; Jarosiewicz et al., 2015; Wodlinger et al., 2015). Although there could exist a substantial gap between the true kinematics and the output of the decoding algorithm initially built in this way, the BMI performance could be further increased by repeatedly updating the same decoding algorithm through "closed-loop" training. Importantly, most decoding algorithms used in human BMIs have been initially developed in the preliminary non-human primate studies. Therefore, we believe that our decoding algorithm based on deep CCA in non-human primates can benefit human BMIs in a similar fashion.

DATA AVAILABILITY STATEMENT

Publicly available datasets were analyzed in this study. This data can be found here: http://crcns.org/data-sets/movements/dream and http://crcns.org/data-sets/motor-cortex/pmd-1/about-pmd-1.

AUTHOR CONTRIBUTIONS

M-KK and S-PK conceived the research. M-KK conducted the analysis and wrote the manuscript. J-WS and S-PK provided edited the manuscript. All authors contributed to the article and approved the submitted version.

FUNDING

This research was supported by the Brain Research Program through the National Research Foundation of Korea (NRF) funded by the Ministry of Science and ICT (2016M3C7A1904988).

REFERENCES

Aflalo, T., Kellis, S., Klaes, C., Lee, B., Shi, Y., Pejsa, K., et al. (2015). Decoding motor imagery from the posterior parietal cortex of a tetraplegic human. *Science* 348, 906–910. doi: 10.1126/science.aaa5417

Aggarwal, V., Acharya, S., Tenore, F., Shin, H. C., Etienne-Cummings, R., Schieber, M. H., et al. (2008). Asynchronous decoding of dexterous finger movements using M1 neurons. *IEEE Trans. Neural. Syst. Rehabil. Eng.* 16, 3–14. doi: 10.1109/TNSRE.2007.916289

Ahmadi, N., Constandinou, T. G., and Bouganis, C.-S. (2019). "Decoding Hand Kinematics from Local Field Potentials Using Long Short-Term Memory (LSTM) Network," in *2019 9th International IEEE/EMBS Conference on Neural Engineering (NER)* (San Francisco, CA: Cornell University), 415–419. doi: 10.1109/NER.2019.8717045

Ames, K. C., Ryu, S. I., and Shenoy, K. V. (2014). Neural dynamics of reaching following incorrect or absent motor preparation. *Neuron* 81, 438–451. doi: 10.1016/j.neuron.2013.11.003

Anderson, T. W. (1984). *An Introduction to Multivariate Statistical Analysis*, 2nd Edn. New Jersey: John Wiley and Sons.

Andrew, G., Aroral, R., Bilmes, J., and Livescu, K. (2013). "Deep Canonical Correlation Analysis," in *Proceedings of the 30th International Conference on Machine Learning* (Atlanta: University of Washington), 1247–1255.

Chapin, J. K., Moxon, K. A., Markowitz, R. S., and Nicolelis, M. A. L. (1999). Real-time control of a robot arm using simultaneously recorded neurons in the motor cortex. *Nat. Neurosci.* 2, 664–670. doi: 10.1038/10223

Chhatbar, P. Y., and Francis, J. T. (2013). Towards a Naturalistic Brain-Machine Interface: Hybrid Torque and Position Control Allows Generalization to Novel Dynamics. *PLoS One.* 8:e52286. doi: 10.1371/journal.pone.0052286

Cunningham, J. P., and Yu, B. M. (2014). Dimensionality reduction for large-scale neural recordings. *Nat. Neurosci.* 17, 1500–1509. doi: 10.1038/nn.3776

Dethier, J., Nuyujukian, P., Ryu, S. I., Shenoy, K. V., and Boahen, K. (2013). Design and validation of a real-time spiking-neural-network decoder for brain-machine interfaces. *J. Neural. Eng.* 10:036008. doi: 10.1088/1741-2560/10/3/036008

Fagg, A. H., Ojakangas, G. W., Miller, L. E., and Hatsopoulos, N. G. (2009). Kinetic trajectory decoding using motor cortical ensembles. *IEEE Trans. Neural. Syst. Rehabil. Eng.* 17, 487–496. doi: 10.1109/TNSRE.2009.2029313

Flament, D., and Hore, J. (1988). Relations of motor cortex neural discharge to kinematics of passive and active elbow movements in the monkey. *J. Neurophysiol.* 60, 1268–1284. doi: 10.1152/jn.1988.60.4.1268

Flint, R. D., Lindberg, E. W., Jordan, L. R., Miller, L. E., and Slutzky, M. W. (2012). Accurate decoding of reaching movements from field potentials in the absence of spikes. *J. Neural. Eng.* 9, 46006. doi: 10.1088/1741-2560/9/4/046006

Friman, O., Borga, M., Lundberg, P., and Knutsson, H. (2007). "Canonical Correlation Analysis: in Applied Multivariate Statistical Analysis," in *Applied Multivariate Statistical Analysis* (Berlin: Springer), 321–330. doi: 10.1007/978-3-540-72244-1_14

Gao, Y., Black, M. J., Bienenstock, E., Shoham, S., and Donoghue, J. P. (2001). "Probabilistic Inference of Hand Motion from Neural Activity in Motor Cortex," in *Proceedings of the 14th International Conference on Neural Information Processing Systems: Natural and Synthetic* (Canada: MIT Press), 213–220. doi: 10.7551/mitpress/1120.003.0032

Georgopoulos, A. P., Kalaska, J. F., Caminiti, R., and Massey, J. T. (1982). On the relations between the direction of two-dimensional arm movements and cell discharge in primate motor cortex. *J. Neurosci.* 2, 1527–1537. doi: 10.1523/jneurosci.02-11-01527.1982

Georgopoulos, A. P., Kettner, R. E., and Schwartz, A. B. (1988). Primate motor cortex and free arm movements to visual targets in three-dimensional space. *II. Coding of the direction of movement by a neuronal population. J. Neurosci.* 8, 2928–2937. doi: 10.1523/jneurosci.08-08-02928.1988

Georgopoulos, A. P., Schwartz, A. B., and Kettner, R. E. (1986). Neuronal Population Coding of Movement Direction. *Science* 233, 1416–1419. doi: 10.1126/science.3749885

Gilja, V., Nuyujukian, P., Chestek, C. A., Cunningham, J. P., Yu, B. M., Fan, J. M., et al. (2012). A high-performance neural prosthesis enabled by control algorithm design. *Nat. Neurosci.* 15, 1752–1757. doi: 10.1038/nn.3265

Golub, M. D., Yu, B. M., Schwartz, A. B., and Chase, S. M. (2014). Motor cortical control of movement speed with implications for brain-machine interface control. *J. Neurophysiol.* 112, 411–429. doi: 10.1152/jn.00391.2013

Hochberg, L. R., Serruya, M. D., Friehs, G. M., Mukand, J. A., Saleh, M., Caplan, A. H., et al. (2006). Neuronal ensemble control of prosthetic devices by a human with tetraplegia. *Nature* 442, 164–171. doi: 10.1038/nature04970

Hotelling, H. (1936). Relations between two sets of variates. *Biometrika* 28, 321–377. doi: 10.2307/2333955

Humphrey, D. R. (1972). Relating motor cortex spike trains to measures of motor performance. *Brain Res.* 40, 7–18. doi: 10.1016/0006-8993(72)900999 0096

Humphrey, D. R., and Corrie, W. S. (1978). Properties of pyramidal tract neuron system within a functionally defined subregion of primate motor cortex. *J. Neurophysiol.* 41, 216–243. doi: 10.1152/jn.1978.41.1.216

Jarosiewicz, B., Sarma, A. A., Bacher, D., Masse, N. Y., Simeral, J. D., Sorice, B., et al. (2015). Virtual typing by people with tetraplegia using a self-calibrating intracortical brain-computer interface. *Sci. Transl. Med.* 7:313ra179. doi: 10.1126/scitranslmed.aac7328

Kao, J. C., Nuyujukian, P., Ryu, S. I., Churchland, M. M., Cunningham, J. P., and Shenoy, K. V. (2015). Single-trial dynamics of motor cortex and their applications to brain-machine interfaces. *Nat. Commun.* 6, 1–12. doi: 10.1038/ncomms8759

Kao, J. C., Nuyujukian, P., Stavisky, S., Ryu, S. I., Ganguli, S., and Shenoy, K. V. (2013). Investigating the role of firing-rate normalization and dimensionality reduction in brain-machine interface robustness. *Proc. Annu. Int. Conf. IEEE Engin. Med. Biol. Soc.* 2013, 293–298. doi: 10.1109/EMBC.2013.6609495

Kaufman, M. T., Churchland, M. M., Ryu, S. I., and Shenoy, K. V. (2014). Cortical activity in the null space: Permitting preparation without movement. *Nat. Neurosci.* 17, 440–448. doi: 10.1038/nn.3643

Kim, K. H., Kim, S. S., and Kim, S. J. (2006). Superiority of nonlinear mapping in decoding multiple single-unit neuronal spike trains: A simulation study. *J. Neurosci. Methods* 150, 202–211. doi: 10.1016/j.jneumeth.2005.06.015

Kim, S. P., Sanchez, J. C., Erdogmus, D., Rao, Y. N., Wessberg, J., Principe, J. C., et al. (2003). Divide-and-conquer approach for brain machine interfaces: Nonlinear mixture of competitive linear models. *Neural. Networks* 16, 865–871. doi: 10.1016/S0893-6080(03)00108104

Kim, S. P., Simeral, J. D., Hochberg, L. R., Donoghue, J. P., and Black, M. J. (2008). Neural control of computer cursor velocity by decoding motor cortical spiking activity in humans with tetraplegia. *J. Neural. Eng.* 5, 455–476. doi: 10.1088/1741-2560/5/4/010

Lawlor, P. N., Perich, M. G., Miller, L. E., and Kording, K. P. (2018). Linear-nonlinear-time-warp-poisson models of neural activity. *J. Comput. Neurosci.* 45, 173–191. doi: 10.1007/s10827-018-0696696

Liu, W., Qiu, J.-L., Zheng, W.-L., and Lu, B.-L. (2019). *Multimodal emotion recognition using deep canonical correlation analysis*. arXiv Preprint arXiv:1908.05349.

Marblestone, A. H., Zamft, B. M., Maguire, Y. G., Shapiro, M. G., Cybulski, T. R., Glaser, J. I., et al. (2013). Physical principles for scalable neural recording. *Front. Comput. Neurosci.* 7, 1–34. doi: 10.3389/fncom.2013.00137

Moran, D. W., and Schwartz, A. B. (1999a). Motor cortical activity during drawing movements: Population representation during spiral tracing. *J. Neurophysiol.* 82, 2693–2704. doi: 10.1152/jn.1999.82.5.2693

Moran, D. W., and Schwartz, A. B. (1999b). Motor cortical representation of speed and direction during reaching. *J. Neurophysiol.* 82, 2676–2692. doi: 10.1152/jn.1999.82.5.2676

Paninski, L., Fellows, M. R., Hatsopoulos, N. G., and Donoghue, J. P. (2003). Spatiotemporal Tuning of Motor Cortical Neurons for Hand Position and Velocity. *J. Neurophysiol.* 91, 515–532. doi: 10.1152/jn.00587.2002

Perich, M. G., Lawlor, P. N., Kording, K. P., and Miller, L. E. (2018). *Extracellular neural recordings from macaque primary and dorsal premotor motor cortex during a sequential reaching task*. Available online at: crcns.org.http://dx.10.6080/K0FT8J72 (accessed May, 2019).

Qiu, J. L., Liu, W., and Lu, B. L. (2018). "Multi-view emotion recognition using deep canonical correlation analysis," in *25th International Conference, ICONIP 2018*. (Berlin: Springer).

Rao, Y. N., Kim, S. P., Sanchez, J. C., Erdogmus, D., Principe, J. C., Carmena, J. M., et al. (2005). "Learning mappings in brain machine interfaces with echo state networks. in Proceedings. (ICASSP '05)," in *IEEE International Conference on Acoustics, Speech, and Signal Processing* (New Jersey: IEEE), 233–236. doi: 10.1109/ICASSP.2005.1416283

Rasmussen, R. G., Schwartz, A., and Chase, S. M. (2017). Dynamic range adaptation in primary motor cortical populations. *Elife* 6:e21409. doi: 10.7554/eLife.21409

Sanchez, J. C., Erdogmus, D., Rao, Y., Principe, J. C., Nicolelis, M., and Wessberg, J. (2003). "Learning the contributions of the motor, premotor, and posterior parietal cortices for hand trajectory reconstruction in a brain machine interface," in *First International IEEE EMBS Conference on Neural Engineering, 2003. Conference Proceedings* (New Jersey: IEEE), 59–62. doi: 10.1109/CNE.2003.1196755

Santhanam, G., Yu, B. M., Gilja, V., Ryu, S. I., Afshar, A., Sahani, M., et al. (2009). Factor-analysis methods for higher-performance neural prostheses. *J. Neurophysiol.* 102, 1315–1330. doi: 10.1152/jn.00097.2009

Schwartz, A. B. (2007). Useful signals from motor cortex. *J. Physiol.* 579, 581–601. doi: 10.1113/jphysiol.2006.126698

Schwartz, A. B., Kettner, R. E., and Georgopoulos, A. P. (1988). Primate motor cortex and free arm movements to visual targets in three- dimensional space. *I. Relations between single cell discharge and direction of movement*. *J. Neurosci.* 8, 2913–2927. doi: 10.1523/JNEUROSCI.08-08-02913.1988

Schwartz, A. B., and Moran, D. W. (1999). Motor cortical representation of speed and direction during reaching. *J. Neurophysiol.* 82, 2676–2692. doi: 10.1152/jn.1999.82.5.2676

Schwartz, A. B., and Moran, D. W. (2000). Arm trajectory and representation of movement processing in motor cortical activity. *Eur. J. Neurosci.* 12, 1851–1856. doi: 10.1046/j.1460-9568.2000.00097.x

Sergio, L. E., Hamel-Pâquet, C., and Kalaska, J. F. (2005). Motor cortex neural correlates of output kinematics and kinetics during isometric-force and arm-reaching tasks. *J. Neurophysiol.* 94, 2353–2378. doi: 10.1152/jn.00989.2004

Serruya, M. D., Hatsopoulos, N. G., Paninski, L., and Donoghue, M. R. F. J. P. (2002). Instant neural control of a movement signal. *Nature* 416, 141–142. doi: 10.1038/416141a

Shanechi, M. M., Orsborn, A., Moorman, H., Gowda, S., and Carmena, J. M. (2014). "High-performance brain-machine interface enabled by an adaptive optimal feedback-controlled point process decoder," in *2014 36th Annual International Conference of the IEEE Engineering in Medicine and Biology Society* (New Jersey: IEEE), 6493–6496. doi: 10.1109/EMBC.2014.6945115

Shanechi, M. M., Orsborn, A. L., and Carmena, J. M. (2016). Robust Brain-Machine Interface Design Using Optimal Feedback Control Modeling and Adaptive Point Process Filtering. *PLoS Comput. Biol.* 12:e1004730. doi: 10.1371/journal.pcbi.1004730

Shenoy, K. V., Sahani, M., and Churchland, M. M. (2013). Cortical control of arm movements: A dynamical systems perspective. *Annu. Rev. Neurosci.* 36, 337–359. doi: 10.1146/annurev-neuro-062111150509

Suminski, A. J., Tkach, D. C., Fagg, A. H., and Hatsopoulos, N. G. (2010). Incorporating feedback from multiple sensory modalities enhances brain-machine interface control. *J. Neurosci.* 30, 16777–16787. doi: 10.1038/mp.2011.182

Sussillo, D., Nuyujukian, P., Fan, J. M., Kao, J. C., Stavisky, S. D., Ryu, S., et al. (2012). A recurrent neural network for closed-loop intracortical brain-machine interface decoders. *J. Neural. Eng.* 9, 026027. doi: 10.1088/1741-2560/9/2/026027

Van Hemmen, J. L., and Schwartz, A. B. (2008). Population vector code: a geometric universal as actuator. *Biol. Cybern.* 98, 509–518. doi: 10.1007/s00422-008-0215213

Vargas-Irwin, C. E., Shakhnarovich, G., Yadollahpour, P., Mislow, J. M. K., Black, M. J., and Donoghue, J. P. (2010). Decoding complete reach and grasp actions from local primary motor cortex populations. *J. Neurosci.* 30, 9659–9669. doi: 10.1523/JNEUROSCI.5443-09.2010

Vaskov, A. K., Irwin, Z. T., Nason, S. R., Vu, P. P., Nu, C. S., Bullard, A. J., et al. (2018). Cortical Decoding of Individual Finger Group Motions Using ReFIT Kalman Filter. *Front. Neurosci.* 12:751. doi: 10.3389/fnins.2018.00751

Vincent, P., Larochelle, H., Bengio, Y., and Manzagol, P.-A. (2008). "Extracting and composing robust features with denoising autoencoders," in *Proceeding ICML '08 Proceedings of the 25th international conference on Machine learning* (New York: ACM Press), 1096–1103. doi: 10.1145/1390156.1390294

Vu, H., Koo, B., and Choi, S. (2016). "Frequency detection for SSVEP-based BCI using deep canonical correlation analysis," in *2016 IEEE International Conference on Systems, Man, and Cybernetics* (Tokyo: SMC), 001983–001987.

Wang, W., Arora, R., Livescu, K., and Bilmes, J. (2015). *MATLAB package for Deep Canonically Correlated Autoencoders (DCCAE)*. Available online at: https://ttic.uchicago.edu/$\sim$wwang5/dccae.html. (accessed January 2019).

Wang, W., Chan, S. S., Heldman, D. A., and Moran, D. W. (2007). Motor Cortical Representation of Position and Velocity During Reaching. *J. Neurophysiol.* 97, 4258–4270. doi: 10.1152/jn.01180.2006

Wang, Y., Kim, S. P., and Principe, J. C. (2005). "Comparison of TDNN training algorithms in brain machine interfaces," in *Proceedings. 2005 IEEE International Joint Conference on Neural Networks* (New Jersey: IEEE), 2459–2462. doi: 10.1109/IJCNN.2005.1556288

Wang, Y., Paiva, A. R. C., Príncipe, J. C., and Sanchez, J. C. (2009). Sequential Monte Carlo Point-Process Estimation of Kinematics from Neural Spiking Activity for Brain-Machine Interfaces. *Neural. Comput.* 21, 2894–2930. doi: 10.1162/neco.2009.01-08699

Wessberg, J., Stambaugh, C. R., Kralik, J. D., Beck, P. D., Laubach, M., Chapin, J. K., et al. (2000). Real-time prediction of hand trajectory by ensembles of cortical neurons in primates. *Nature* 408, 361–365. doi: 10.1038/35042582

Willett, F. R., Suminski, A. J., Fagg, A. H., and Hatsopoulos, N. G. (2013). Improving brain-machine interface performance by decoding intended future movements. *J. Neural. Eng.* 10, 026011. doi: 10.1088/1741-2560/10/2/026011

Wodlinger, B., Downey, J. E., Tyler-Kabara, E. C., Schwartz, A. B., Boninger, M. L., and Collinger, J. L. (2015). Ten-dimensional anthropomorphic arm control in a human brain-machine interface: Difficulties, solutions, and limitations. *J. Neural. Eng.* 12, 1–17. doi: 10.1088/1741-2560/12/1/016011

Wu, W., Black, M. J., Mumford, D., Gao, Y., Bienenstock, E., and Donoghue, J. P. (2004). Modeling and Decoding Motor Cortical Activity using a Switching Kalman Filter. *IEEE Trans. Biomed. Eng.* 51, 933–942. doi: 10.1109/TBME.2004.826666

Wu, W., Gao, Y., Bienenstock, E., Donoghue, J. P., and Black, M. J. (2006). Bayesian population decoding of motor cortical activity using a Kalman filter. *Neural. Comput.* 18, 80–118. doi: 10.1162/089976606774841585

Xu, K., Wang, Y., Zhang, S., Zhao, T., Wang, Y., Chen, W., et al. (2011). "Comparisons between linear and nonlinear methods for decoding motor cortical activities of monkey," in *2011 Annual International Conference of the IEEE Engineering in Medicine and Biology Society* (New Jersey: IEEE), 4207–4210.

Yu, B. M., Cunningham, J. P., Santhanam, G., Ryu, S. I., Shenoy, K. V., and Sahani, M. (2009). Gaussian-process factor analysis for low-dimensional single-trial analysis of neural population activity. *J. Neurophysiol.* 102, 614–635. doi: 10.1152/jn.90941.2008

Conflict of Interest: The authors declare that the research was conducted in the absence of any commercial or financial relationships that could be construed as a potential conflict of interest.

Advantages of publishing in Frontiers

OPEN ACCESS
Articles are free to read for greatest visibility and readership

FAST PUBLICATION
Around 90 days from submission to decision

HIGH QUALITY PEER-REVIEW
Rigorous, collaborative, and constructive peer-review

TRANSPARENT PEER-REVIEW
Editors and reviewers acknowledged by name on published articles

Frontiers
Avenue du Tribunal-Fédéral 34
1005 Lausanne | Switzerland

Visit us: www.frontiersin.org
Contact us: frontiersin.org/about/contact

REPRODUCIBILITY OF RESEARCH
Support open data and methods to enhance research reproducibility

DIGITAL PUBLISHING
Articles designed for optimal readership across devices

FOLLOW US
@frontiersin

IMPACT METRICS
Advanced article metrics track visibility across digital media

EXTENSIVE PROMOTION
Marketing and promotion of impactful research

LOOP RESEARCH NETWORK
Our network increases your article's readership